

**Interfacial Behavior and 2D Self-Assembly of Heteroatom-Doped
 π -Conjugated Surfactants**

Zahra Alinia

A Thesis
In the Department of
Chemistry and Biochemistry

Presented in Partial Fulfillment of the Requirements
for the Degree of
Doctor of Philosophy (Chemistry)
at Concordia University
Montréal, Québec, Canada

October 2024

© Zahra Alinia, 2024

CONCORDIA UNIVERSITY

School of Graduate Studies

This is to certify that the thesis prepared

By: Zahra Alinia

Entitled: Interfacial behavior and 2D self-assembly of heteroatom-doped π -conjugated surfactants

and submitted in partial fulfillment of the requirements for the degree of

Doctor of Philosophy (Chemistry)

complies with the regulations of the University and meets the accepted standards with respect to originality and quality.

Signed by the final examining committee:

_____ Chair
Dr. Paul Joyce

_____ External Examiner
Dr. Matthew Paige

_____ Arm's Length Examiner
Dr. Ayse Turak

_____ Examiner
Dr. Louis Cuccia

_____ Examiner
Dr. Ingo Salzmann

_____ Thesis Supervisor
Dr. Christine DeWolf

Approved by

Dr. Louis Cuccia, Graduate Program Director

2024/12/17

Dr. Pascale Sicotte, Dean of Faculty of Arts and Science

ABSTRACT

Interfacial behavior and 2D self-assembly of heteroatom-doped π -conjugated surfactants

Zahra Alinia, Ph. D.

Concordia University, 2024

The intrinsic photophysical properties of heteroatom-doped π -conjugated systems, which are essential for optimal electronic performance, necessitate the formation of well-ordered 2D thin films with structural stability. These thin films can be achieved by self-assembly using Langmuir and Langmuir-Blodgett (LB) techniques. Manipulation of molecular design and external conditions is explored to achieve controlled film morphology desirable for electronic applications. In this context, two classes of amphiphilic heteroatom-doped π -conjugated compounds are explored: phosphole-lipids and amphiphilic tetraazaporphyrins (TAPs).

Introduction of counterions to Langmuir films of phosphole-based lipids with charged dithienophospholium backbone showed that incorporation of halide salts significantly influences the intercalation between phosphole headgroups, thereby stabilizing monolayers and promoting the formation of well-ordered structures free from 3D aggregates. However, only the counterions with their size matching the space restriction in between the headgroups enhance the film organization and facilitate the desired monolayer formation. Characterization techniques, including atomic force microscopy (AFM) and grazing incidence X-ray diffraction (GIXD) confirm the formation of condensed phase and highlight the presence of hexagonally packed chains. Exploring the effects of aromatic additives on film structure of the same phosphole-lipids demonstrates that while such additives can influence the growth patterns and organization of 2D films, challenges remain in eliminating aggregate formation.

For the amphiphilic tetraazaporphyrins featuring octaalkylthio substitution, we focused on the influence of varying alkyl chain lengths on film morphology and orientation. Notably, TAPs with shorter alkyl chains yield homogeneous monolayers with spider-like conformation where the macrocycle is oriented face-on to the substrate. GIXD confirmed that the packing is not dominated by the pentyl chains, but rather by the organization of the rings (in a molecular lattice), resulting in an ordered condensed phase. However, TAPs with longer chains exhibit complex,

inhomogeneous LB films with combination of spider-like and interdigitated conformations observed by AFM, the latter attributed to the larger alkyl chains and confirmed by GIXD.

The findings of this research underscore the importance of tuning both molecular structure and external conditions to optimize the self-assembly of π -conjugated materials to enhance structural complexity and improve the functionality of the developed materials.

ACKNOWLEDGEMENTS

I would like to give my warmest thanks to people who have contributed to the success of my research and the completion of this thesis.

First and foremost, I would like to express my heartfelt gratitude to my supervisor, Dr. Christine DeWolf, for her guidance, support, and encouragement throughout my research journey. Her expertise and insights have been instrumental in shaping my work and fostering my academic growth.

I extend my appreciation to the members of my committee, Dr. Louis Cuccia and Dr. Ingo Salzmann, for their constructive feedback and valuable suggestions. Their diverse perspectives and critical evaluations have greatly enriched my thesis and enhanced my understanding of the subject matter.

I am also grateful to Dr. Hala Youssef, Dr. Renaud Milette Lamarche, Kailen, Mathieu, Janet, and Maryam for their support during my time in the lab. The stimulating discussions and teamwork we shared have made this research experience enjoyable and rewarding.

A special thanks to the wonderful Marika, as well as to the dedicated technical staff in our department -Neema, Jennifer, Khalil, Mihai, Vincent, and Kai- for the invaluable experiences and memorable moments shared.

My thanks go to my friends, who have provided support and encouragement throughout this process. Their motivation and understanding during challenging times have been a source of strength for me.

Lastly, I would like to express my deepest appreciation to my family for their unconditional love and support. Their belief in my abilities and their sacrifices have been crucial in my journey towards achieving this milestone in my life.

Thank you all for being a part of this significant chapter in my life.

CONTRIBUTION OF AUTHORS

Chapter 3. Tuning Electrostatics to Promote Ordered Monolayers of Phosphole-Lipids

This manuscript is published in *ACS Langmuir* with the following authors:

Zahra Alinia, Dandan Miao, Thomas Baumgartner, Christine E. DeWolf.

DOI: 10.1021/acs.langmuir.4c02962

Author contributions: Zahra Alinia conducted the conceptualization, investigation, formal analysis, validation, visualisation, writing (original draft, review and editing). Dr. Dandan Miao performed the synthesis of the phosphole-lipids. Dr. Thomas Baumgartner contributed to the molecular design of phosphole-lipids and assisted with the writing (review and editing). Dr. Christine DeWolf provided conceptualization, supervision, resources, project administration, and writing (review and editing). All authors reviewed the final manuscript and approved of the contents.

Chapter 4. Self-Assembly of Phosphole-Lipids in 2D Films: The Influence of π -Interactions and Steric Constraints

This manuscript is published in *RSC Applied Interfaces* with the following authors:

Zahra Alinia, Dandan Miao, Thomas Baumgartner, Christine E. DeWolf.

DOI: 10.1039/D4LF00361F

Author contributions: Zahra Alinia conducted the conceptualization, investigation, formal analysis, validation, visualisation, writing (original draft, review and editing). Dr. Dandan Miao performed the synthesis of the phosphole-lipids. Dr. Thomas Baumgartner contributed to the molecular design of phosphole-lipids and assisted with the writing (review and editing). Dr. Christine DeWolf provided conceptualization, supervision, resources, project administration, and writing (review and editing). All authors reviewed the final manuscript and approved of the contents.

Chapter 5. Amphiphilicity of Tetraazaporphyrins Containing Four Terminal Carboxylic Acid and Four Alkyl Groups Promotes Face-on Orientation in Langmuir Films

This manuscript is published in *ACS Langmuir* with the following authors:

Zahra Alinia, Elmahdy Abdulhamied, Serxho Selmani, Renaud Miclette Lamarche, S. Holger Eichhorn, Christine E. DeWolf

DOI: 10.1021/acs.langmuir.4c03800

Author contributions: This manuscript is a joint contribution from Dr. DeWolf's research group in Concordia University and Dr. Eichhorn's research group in University of Windsor and both Elmahdy Abdulhamied and Zahra Alinia have contributed equally to this manuscript and have been denoted as co-first authors.

Elmahdy Abdulhamied conducted the synthesis and associated spectroscopic confirmations, characterized the thermal properties and optical microscopy of the bulk materials. Zahra Alinia conducted all the interfacial characterization included in the manuscript. Both Elmahdy Abdulhamied and Zahra Alinia drafted their respective sections of the manuscript. Dr. DeWolf and Dr. Eichhorn provided conceptualization, supervision, resources, project administration, and manuscript writing (review and editing). Serxho Selmani developed the asymmetric synthesis route employed. Renaud Miclette Lamarche performed the preliminary assessment of the surface properties of the short-chain TAPs. All authors reviewed the final manuscript and approved of the contents.

Table of Contents

List of Figures	xii
List of Abbreviations.....	xvii
Chapter 1. Introduction	1
1.1. Organic π -conjugated materials: Advances, properties, and applications.....	1
1.1.1. Role of aromatic rings in tuning π -conjugated systems	1
1.1.2. Impact of heteroatom-doped aromatics on material performance	2
1.1.3. Addressing challenges in π -conjugated systems for device fabrication.....	3
1.2. Phosphole- and porphyrin-based π -conjugated systems: structural organization and functional applications	3
1.2.1. Phosphole-based π -conjugated systems	4
1.2.1.1. Phosphole-lipids.....	5
1.2.2. Porphyrins-based conjugated systems.....	7
1.2.2.1. Amphiphilic tetraazaporphyrins	9
1.3. Deposition techniques for π -conjugated materials: Achieving optimal thin films.....	10
1.3.1. Physical vapor deposition	11
1.3.2. Solution deposition	12
1.3.3. Langmuir-Blodgett deposition	13
1.4. Important internal and external impacts on Langmuir and LB film behavior and structure.....	14
1.4.1. The intra- and intermolecular interactions	14
1.4.1.1. Electrostatic interactions	15
1.4.1.2. π - π interaction:	16
1.4.2. External conditions impacting Langmuir and LB films.....	19
1.4.2.1. Temperature.....	19
1.4.2.2. pH.....	19

1.4.2.3. Ionic strength and specific ions in subphase	20
1.4.2.4. Spreading solvent.....	20
1.5. Research goals and thesis organization.....	20
Chapter 2. Experimental Techniques	22
2.1. Langmuir monolayers	22
2.1.1. Langmuir-Blodgett film balance	22
2.1.2. Compressibility	26
2.2. Brewster angle microscopy	27
2.3. Imaging Ellipsometry.....	28
2.4. Atomic force microscopy	30
2.4.1. AFM sample preparation.....	31
2.5. Surface-specific X-ray techniques	33
2.5.1. Grazing incidence x-ray diffraction (GIXD).....	34
2.5.2. Specular X-ray reflectivity.....	37
Chapter 3. Tuning Electrostatics to Promote Ordered Monolayers of Phosphole-Lipids	39
3.1. Abstract	39
3.2. Introduction.....	40
3.3. Materials and Methods.....	42
3.3.1. Solution and subphases	42
3.3.2. Surface pressure-molecular area isotherm	43
3.3.3. Brewster angle microscopy imaging (BAM)	43
3.3.4. Ellipsometry measurements	43
3.3.5. Atomic force microscopy imaging (AFM).....	44
3.3.6. Grazing incidence X-ray diffraction (GIXD) and X-ray reflectivity (XRR)	44

3.4. Results and Discussion	45
3.5. Conclusions.....	61
Chapter 4. Self-Assembly of Phosphole-Lipids in 2D Films: The Influence of π -Interactions and Steric Constraints	62
4.1. Abstract	62
4.2. Introduction.....	62
4.3. Materials and Methods.....	65
4.3.1. Solution and subphases	65
4.3.2. Surface pressure-molecular area isotherm	65
4.3.3. Brewster angle microscopy imaging (BAM)	65
4.3.4. Ellipsometry measurements	66
4.3.5. Atomic force microscopy imaging.....	66
4.3.6. Grazing incidence X-ray diffraction (GIXD) and X-ray reflectivity (XRR)	67
4.4. Results and Discussion	68
4.5. Conclusions.....	80
Chapter 5. Amphiphilicity of Tetraazaporphyrins Containing Four Terminal Carboxylic Acid and Four Alkyl Groups Promotes Face-on Orientation in Langmuir Films.....	82
5.1. Abstract	82
5.2. Introduction.....	83
5.3. Experimental Section	86
5.3.1. Chemicals and Materials.....	86
5.3.2. Methods.....	87
5.3.3. Material Properties	87
5.3.4. Langmuir and LB Films	87
5.4. Results and Discussion	90

5.4.1. Synthesis	90
5.4.2. Material Properties	91
5.4.3. Langmuir and LB Films	92
5.5. Conclusions	108
Chapter 6. Conclusions and Future Directions	109
6.1. Phosphole-based π -conjugated systems	110
6.2. Porphyrin-based π -conjugated systems	111
6.3. Future directions	112
6.3.1. Expanding findings on phosphole-based π -conjugated systems	113
6.3.2. Expanding findings on porphyrin-based π -conjugated systems	114
References	117
Appendix A. Supplementary information for Chapter 3	140
Appendix B. Supplementary information for Chapter 4	149
Appendix C. Supplementary information for Chapter 5	159

List of Figures

Figure 1.1 Chemical structure of aromatic-based conjugated systems of acenes (a), rubrene (b), and fullerene (c).....	2
Figure 1.2 Chemical structure of heteroatom-doped aromatic-based conjugated systems of P3HT (a), DPP (b), PEDOT(c), NDIs(d), and phthalocyanines(e).	3
Figure 1.3 Planar configuration of pyrrole versus the nonplanar configuration of phosphole, redrawn from Duffy et al. ³⁴ Based on theoretical calculations, the planar phosphole may exhibit higher aromaticity than thiophene or pyrrole. ³⁵	4
Figure 1.4 Chemical structure of phosphole-derivatives as building blocks of optoelectronics: thioxophospholes (a) ⁴⁷ , dithieno-4-keto-1,4-dihydrophosphinines (b) ⁴⁸ , dibenzophosphapentaphene (c) ⁴⁹ , and benzo[b]phosphole (d) ⁵⁰	5
Figure 1.5 Chemical structure of phosphole-based π -conjugated systems with a range of headgroup extension and counterions previously reported. ⁵⁴ The phospholium moiety provides the electronic character while the three alkoxy chains connected to the backbone through the benzyl ring offer the amphiphilic character.	6
Figure 1.6 Closed and open conformation of phosphole-lipid in solid state (left), conformational change at different concentrations in solution phase (middle), and the lamellar organization in the liquid-crystalline phase (right). For all structures, the counterion is bromide (image adapted from Ren et al.). ⁵⁴	7
Figure 1.7 Chemical structure of porphyrin with two types of substitution positions: eight <i>beta</i> positions on the pyrrolic rings and four <i>meso</i> positions on the methine bridges (the latter is shown in green).	8
Figure 1.8 Face-on orientation (left) and edge-on orientation (right). Each circle represents a cross-sectional area of an aromatic ring.	9
Figure 1.9 Chemical structure of TAPs previously studied. ⁷⁷ For the acid chains, n=3, 5, and 10, and for the alcohol chains, n=3,11 was evaluated.	10
Figure 1.10 Representative illustration of the physical vapor deposition technique (reproduced from Safavi et al.). ⁸⁹	11
Figure 1.11 Representative illustrations of different solution depositions (reproduced from Pasquarelli et al.). ¹⁰³	12
Figure 1.12 Representative illustration of roll-to-roll LB deposition technique (reproduced from Korpela et al.). ¹¹²	13
Figure 1.13 Schematic representation of DPPC monolayer interaction with bromide and sulfate anion (image reproduced from Li et al.). ¹²²	16
Figure 1.14 Schematic representative images of π -stacking orientation, from left: parallel stacking (sandwich), parallel displaced, edge-to-face, and T-shaped. The illustration on the right represents all other π - interactions including cation- π , anion- π , CH- π , and etc.	16
Figure 1.15 Parallel stacking of porphyrin rings with displacement to improve structural stability (redrawn from Hunter et al.). ¹²⁵	17
Figure 1.16 Chemical structure and packing orientation of azo-benzene derivatives (redrawn from Tang et al.). ¹²⁶	18

Figure 1.17 Chemical structure of meta-substituted dioctadecylaminobenzoquinones (a) and octadecyl gallate (b).	18
Figure 2.1 Schematic representation of surfactants with hydrophilic headgroup and different number of chains (tails).	22
Figure 2.2 Schematic representative of a Langmuir trough with two movable barriers and a Wilhelmy plate in middle.	23
Figure 2.3 Schematic representative surface pressure-molecular area isotherm with possible phases formed.	24
Figure 2.4 Schematic illustration of basic principle of BAM. The Brewster angle α is 53.15° , and n_1 and n_2 are refractive index of air and water, respectively.....	28
Figure 2.5 Schematic illustration of Atomic Force Microscopy, reproduced from ¹⁶⁴	30
Figure 2.6 Langmuir-Blodgett deposition (top) and Langmuir-Schaefer deposition (bottom) techniques. 33	
Figure 2.7 Principle of synchrotron-based X-ray scattering characterization techniques of GIXD and XRR (the image is modified from Stefaniu et al.). ¹⁷¹	34
Figure 2.8 Lattice structures in reciprocal space, including Bragg rods (a), and reciprocal space, tilt direction and unit cell for the common phases (b). The arrows define the tilt direction of the nearest neighbor (NN) or next nearest neighbor (NNN). For hexagonal unit cell of alkyl chain packing shown in (c), each circle corresponds to one alkyl chain, and the dark and pink dashed-line ovals represent a combination of packing for a double- and triple-chain surfactant, respectively.	35
Figure 2.9 Schematic representing the reciprocal disk, a top-down view of the chain lattice showing the chain tilt direction, and characteristic diffraction patterns (intensity integrated across Q_z and 2D contour plot) for the Langmuir monolayers at air-water interface (image is modified from Kaganer et al.). ¹⁷³	36
Figure 2.10 The layers (boxes) defined in Parratt method in addition to air and subphase: alkyl chains (top box) and headgroup (bottom box) (a), and representative model fit for the electron density profile for two-box model.....	38
Scheme 3.1 Chemical structure of previously reported phosphole-lipids. ⁵⁴	42
Figure 3.1 Surface pressure-molecular area isotherm of phosphole-lipid (molecule 1 of Scheme 3.1) on ultrapure water as a subphase, obtained at room temperature and compression rate of $5 \text{ cm}^2 \text{ min}^{-1}$	46
Figure 3.2 Repeated isotherm cycles for phosphole-lipid on ultrapure water as subphase without any waiting time after each cycle: (a) compression only up to surface pressure of 25 mN m^{-1} (below the plateau) and (b) full isotherm cycle.....	47
Figure 3.3 Normalized film area as a function of time for phosphole-lipid at constant surface pressures of 15 and 35 mN m^{-1} (below and above the plateau).	47
Figure 3.4 Surface pressure-molecular area isotherms of phosphole-lipid on an ultrapure water subphase as a function of the subphase temperature.....	48
Figure 3.5 Surface pressure-molecular area isotherms of phosphole-lipid as a function of lower (a) and higher (b) NaBr concentration in the subphase.....	49
Figure 3.6 Representative BAM images of the phosphole-lipid on water and different subphase concentrations of NaBr. The images corresponding to the surface pressures of the main phase transition plateau are aligned vertically and framed (pink). For 10 mM NaBr and 100 mM NaBr, the laser intensity	

increased to 70%; all other images were captured at 50%. The relative brightness levels of the images reflect the numbers of aggregates in the field of view for the specific molecular area.....	51
Figure 3.7 Representative AFM images of phosphole-lipid deposited onto mica by LB at different surface pressures from water and NaBr subphases (concentrations as indicated).....	53
Figure 3.8 Phosphole-lipid domain heights (a) and widths (b) measured from AFM images as a function of the NaBr concentration in the subphase. At least three locations from each of two independently prepared samples were measured (n>300 domains).	54
Figure 3.9 Ellipsometric measurements at the air-subphase interface as a function of lower (a) and higher (b) concentration of NaBr in the subphase.....	55
Figure 3.10 GIXD contour plot of X-ray diffraction intensity as a function of the Q_{xy} (in-plane) and Q_z (out-of-plane) vector components for the phosphole-lipid on 10 and 100 mM NaBr subphases.	56
Figure 3.11 Surface pressure-molecular area isotherms of phosphole-lipid as a function of (a) halide concentration, (b) NaCl concentration, and (c) NaI concentration in the subphase.....	58
Figure 3.12 AFM images of phosphole-lipid deposited onto mica by LB at two different surface pressures corresponding to below and above the phase transition plateau, for NaCl (top row) and NaI (bottom row), from two different subphase salt concentrations, 10 mM (left) and 100 mM (right) in the subphase.	59
Scheme 4.1 Chemical structure of previously reported phosphole-lipid with dithienophosphole headgroup (PL1), phosphole-lipid with benzo-fused dithienophosphole headgroup (PL2), ⁵⁴ dodecyl 4-hydroxybenzoate surfactant (C ₁₂ HB), and the aromatic molecules phenol, naphthalene, and 2-naphthol. 64	
Figure 4.1 Surface pressure-molecular area isotherm of PL1 as a function of phenol concentration in subphase. The isotherm for PL1 on water was previously reported, ²³⁸ and is repeated here for easier comparison.....	69
Figure 4.2 Representative BAM images of PL1 on water and different subphase concentrations of phenol. The images corresponding to the surface pressures of the main phase transition plateau are aligned vertically and framed (pink).....	70
Figure 4.3 Representative AFM images of PL1 deposited onto mica by LB at different surface pressures from water and phenol subphases (concentrations as indicated). All images are $50 \times 50 \mu\text{m}^2$, with height scale of 10 nm. The height scale was selected to enable visualization of the monolayer domains which are otherwise obscured by the large height of the aggregates (average aggregate heights are provided in Figure B1).	72
Figure 4.4 Ellipsometric measurements of PL1 at the air-subphase interface as a function of phenol concentration in the subphase. Each value represents the average of measurements made on three independently formed films. For each independent film, the $\delta\Delta$ is the average of 10 measurements of the same monolayer film at constant surface pressure.....	74
Figure 4.5 Surface pressure-molecular area isotherms of PL1 and lipid mixtures with 1:10 molar ratio of PL1: naphthalene and PL1: 2-naphthol (solid lines, pressure onset area $\sim 13 \text{ \AA}^2 \text{ molecule}^{-1}$). Inset: The same isotherms are replotted as a function of pure phosphole-lipid molecular area (dashed lines).	76
Figure 4.6 Surface pressure-molecular area isotherms of PL1, C ₁₂ HB, and their mixture with 1:1 molar ratio (structures shown in Scheme 4.1).	77
Figure 4.7 Surface pressure-molecular area isotherms of PL1, PL2, and their mixture with 1:1 molar ratio (structures shown in Scheme 4.1).	79

Figure 5.1 Schematic representation of the edge-on (left) and face-on (right) orientations of a macrocycle at air-water interface.	84
Figure 5.2 Proposed face-on conformers at the air-water interface of a previously reported octaacid TAP (left) with alkyl spacers of 10 methylene groups and the two tetraacid TAPs 4a (center) and 4b (right) reported here. Estimated chain lengths and TAP surface areas are taken from previous studies. ^{77,293–295} The side-chain and spacer lengths represent maximum values for fully extended (crystalline) alkyl chains. Side-chains in an amorphous state have a 10-20% shorter effective length. ⁷⁷	86
Scheme 5.1 Synthesis of TAPs as mixtures of four regioisomers.	90
Reaction conditions: a) flow reactor, diglyme, 1 equiv. BrC ₅ H ₁₁ or BrC ₁₂ H ₂₅ , 0 °C, 6 hrs; b) diglyme, 1.1 equiv. BrC ₅ H ₁₀ COOEt, 0 °C, 12 hrs; c) 1. Mg(OC ₃ H ₇) ₂ , 1-propanol, refl., Ar, 24 hrs; 2. THF/1 M HCl _{aq} , 0.5-1 hrs; d) THF/H ₂ O 95:5, 1 M NaOH _{aq} , refl., 24 hrs. Full synthetic details are provided in Appendix C, as are spectral characterizations of all prepared compounds (ATR FTIR, ¹ H NMR, ¹³ C NMR, HRMS and UV-VIS, Figures C1 to C26).	91
Figure 5.3 Surface pressure-molecular area and compressibility modulus plot (inset) of 4b at different subphase pH with a compression rate of 10 cm ² min ⁻¹ , 22 °C.	93
Figure 5.4 Schematic representation of possible interfacial orientation for 4b.	94
Figure 5.5 Representative BAM images (620 μm × 520 μm) of 4b at different subphase pH values of 4 (top), 6.5 (middle), and 11 (bottom) and surface pressures from 0.0 to 35.0 mN m ⁻¹ (brightness of -30% and contrast of +20% modification).	95
Figure 5.6 Ellipsometric measurements of 4b at the air-water interface at subphase pH 6.5 (a) and pH 11 (b) and for two different compression rates.	97
Figure 5.7 AFM images of 4b deposited onto mica at different surface pressures and subphase pHs: pH 6.5 (top) and pH 11 (bottom). Surface pressures from left to right are: 0.0 (a,f), 2.5 (b,g), 15.0 (c,h), 25.0 (d,i), and 35.0 (e,j) mN m ⁻¹	98
Figure 5.8 GIXD contour plots of X-ray diffraction intensity as a function of Q _{xy} (in-plane) and Q _z (out-of-plane) vector components for 4b: (a) pH 6.5, 15 mN m ⁻¹ ; (b) pH 6.5, 35 mN m ⁻¹ ; (c) pH 11, 15 mN m ⁻¹ ; and (d) pH 11, 31 mN m ⁻¹ . A rescaled image of 8c is shown in Figure C45.	99
Figure 5.9 Schematic representation of proposed height differences and thicknesses for the different regions observed by AFM for pH 6.5 and possible phase assignments (F: flat-on, F-F: flat-on atop flat-on). The dashed line represents the substrate (mica). The continuous phase height is shown by blue dashed arrows, and the relative heights measured from AFM are shown by black dashed arrows.	101
Figure 5.10 Surface pressure-molecular area isotherm and compressibility modulus plot (inset) of 4a at subphase pHs of 4, 6.5, and 11 at a compression rate of 10 cm ² min ⁻¹	102
Figure 5.11 Representative BAM images (620 μm × 520 μm) of 4a at a subphase pH of 6.5 and surface pressures from top-left: 0.0, 2.5, 5.0, 10.0, 17.5, 20.0, 25.0, and 35.0 mN m ⁻¹ . All images reported have been brightness reduced by 30% and contrast enhanced by 20%.	103
Figure 5.12 AFM images of 4a deposited onto mica at different surface pressures at a subphase pH of 6.5. Surface pressures from top left: (a) 0.0, (b) 2.5, (c) 5.0, (d) 15.0, (e) 25.0 and (f) 35.0 mN m ⁻¹	104
Figure 5.13 Ellipsometric measurements at air-water interface of 4a at subphase pH 6.5 at two different compression rates. Corresponding isotherms are shown in the inset.	105

Figure 5.14 GIXD contour plots of X-ray diffraction intensity as a function of Q_{xy} (in-plane) and Q_z (out-of-plane) vector components for 4a at subphase pH 6.5: (a) 5 mN m ⁻¹ , (b) 15 mN m ⁻¹ , (c) 27 mN m ⁻¹ , and (d) 35 mN m ⁻¹ . Top row: full range, bottom row: zoomed -in to a smaller Q_{xy} range.	106
Figure 5.15 Schematic representation of (a) possible interfacial orientations for 4a and (b) proposed orientation of the molecular lattice of the close-packed array of spider-like conformations. Each small square represents one porphyrin ring (1.1 nm length) where the different colors denote different molecular orientations. The large purple square represents the tetragonal unit cell, with the width of 1.96 nm, equal to the a-spacing value calculated from the fitting.	107
Figure 6.1 Summarized schematic representing the impact of counterion on phosphole-lipid film behavior.	110
Figure 6.2 Summarized schematic representing the impact of aromatic additives on phosphole-lipid film behavior.....	111
Figure 6.3 Summarized schematic representing the impact of alkyl chain length on TAPs monolayer film behavior.....	112
Figure 6.4 Chemical structure of phosphole-lipid 1, 3, and 4, previously reported. ⁵⁴	114

List of Abbreviations

2D	2-dimensional
3D	3-dimensional
AFM	atomic force microscopy
ASAP	atmospheric solids analysis probe ionization
BAM	Brewster angle microscopy
C	condensed phase
DPP	diketopyrrolepyrrole
DSSCs	dye-sensitized solar cells
fwhm	full width at half-maximum
GIXD	grazing incidence X-ray diffraction
HOMO	highest occupied molecular orbital
HOPG	highly oriented pyrolytic graphite
LB	Langmuir-Blodgett
LE	liquid-expanded
LS	Langmuir-Schaefer
LUMO	lowest unoccupied molecular orbital
MALDI	matrix assisted laser desorption ionization
OFETs	organic field effect transistors
OLEDs	organic light emitting diodes
OPVs	organic photovoltaics
OSCs	organic solar cells
NDIs	naphthalene diimides
Nd:YAG	neodymium-doped yttrium aluminum garnet
NN	nearest neighbor
NNN	next nearest neighbor
P3HT	poly(3-hexythiophene)
PEDOT	poly(3,4-ethylenedioxythiophene)
POM	polarized optical microscopy
PVD	physical vapor deposition
TAPs	tetraazaporphyrins

TGA	thermal gravimetric analysis
TR	transfer ratio
vdW	van der Waals
XRR	X-ray reflectivity

Chapter 1. Introduction

1.1. Organic π -conjugated materials: Advances, properties, and applications

The development of organic π -conjugated materials as fundamental components in semiconductors, storage devices, and other optoelectronic applications has achieved significant advancements over the past decade.¹⁻⁵ These materials have advantageous electronic and optical properties compared to the inorganic materials. Their lightweight nature, low-temperature processing requirements, lower production costs, and higher flexibility are among the properties that make them particularly desirable alternatives.⁶ In addition, their thermal stability and luminescence characteristics contribute to efficient performance.^{3,7,8} These organic π -conjugated systems have been utilized in manufacturing of commercial products in large scale, including cellphones, organic light emitting diodes (OLEDs),⁹ organic photovoltaics (OPVs),¹⁰ as well as other applications like transistors,¹¹ and lasers.^{12,13}

By modifying the chemical composition of these materials, particularly through alterations in the conjugation groups, it is possible to tune their electronic properties such as highest occupied molecular orbital (HOMO) and lowest unoccupied molecular orbital (LUMO) levels, which are one of the main defining factors for these materials' overall performance.^{3,14,15}

1.1.1. Role of aromatic rings in tuning π -conjugated systems

The incorporation of aromatic rings into organic π -conjugated materials can significantly impact their electronic properties by modifying the electron density (richness and distribution), and the polarizability of the molecular backbone. In addition, aromatic building blocks also offer synthetic flexibility and prominent stability for the final products.³ Figure 1.1 provides examples of aromatic rings commonly used in the building blocks of electronic and optoelectronic devices.

For instance, acenes, which are long linear molecules with varying number of rings, find applications in light-responsive materials. Pentacene (i.e., $n=3$ in Figure 1.1a) as an example is used as a donor block in OPV cells, oxygen sensing, photodynamic therapy, and drug delivery.¹⁶ Larger structures like rubrene have demonstrated good charge transport properties, making them suitable for use in OLEDs and chemiluminescence applications.^{17,18} The much larger molecules of

fullerenes and other C₆₀ derivatives mostly act as efficient acceptors in many OPV devices and have applications in capacitors, catalysts, and fuel cells.¹⁹

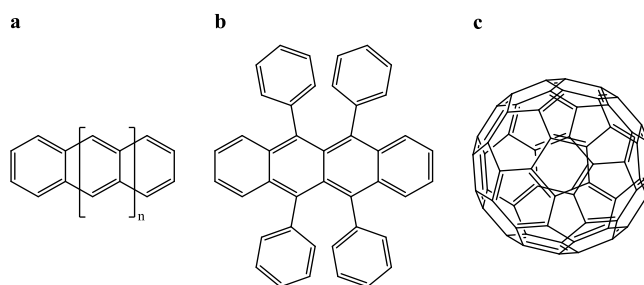


Figure 1.1 Chemical structure of aromatic-based conjugated systems of acenes (a), rubrene (b), and fullerene (c).

1.1.2. Impact of heteroatom-doped aromatics on material performance

Incorporating heteroatom-doped aromatic rings introduces distinct electronic properties. These properties include improved electron and charge mobility, and electrochemical and magnetic properties, which are difficult to achieve with carbon-based π -conjugated systems alone.²⁰ This allows for broader applications including ion batteries, supercapacitors, and electrochemical transistors. Figure 1.2 illustrates some of the commonly used heteroatom-doped aromatic rings that exhibit promising electronic and optical properties.

Heterocyclopentadienes like thiophene and pyrrole have been extensively studied and utilized in these systems in the past decades. For example, poly(3-hexythiophene (P3HT) is a widely used conjugated polymer that pairs well with fullerene acceptors.²¹ Other notable structures include diketopyrrolopyrrole (DPP), poly(naphthalene diimides) (NDIs), and Poly(3,4-ethylenedioxythiophene) (PEDOT), that have gained attention for their charge carrier mobility properties, high electron mobility, and stability.^{22–24} Macrocyclic compounds of phthalocyanines, known for their nonlinear optical and photoconductivity properties, stability and chemical versatility, have potential applications in areas such as photoacceptors, electroluminescent devices and solar cells.^{25–28}

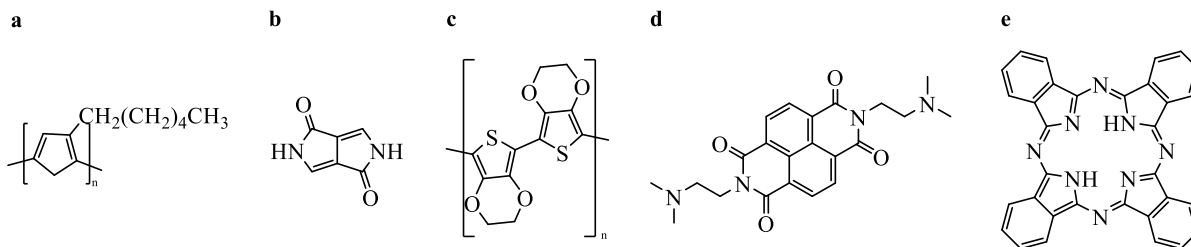


Figure 1.2 Chemical structure of heteroatom-doped aromatic-based conjugated systems of P3HT (a), DPP (b), PEDOT(c), NDIs(d), and phthalocyanines(e).

1.1.3. Addressing challenges in π -conjugated systems for device fabrication

One of the major challenges with π -conjugated systems is the strong π - π interactions, which often leads directly to the formation of solid-phase amorphous or crystalline structures.² These strong π - π interactions can result in formation of random or organized stacking or aggregation, reducing the solubility of the materials in organic solvents. Furthermore, unwanted and uncontrolled polymerization is another significant issue of working with π -conjugated systems. Despite the promising properties and potential applications of these π -conjugated materials, these challenges make it difficult to employ them in flexible optoelectronic devices by solution-based techniques.^{29,30}

A practical strategy to enhance solubility and reduce the possibility of polymerization is by adding alkyl chains to these π -conjugated materials. Introducing the alkyl chains also enhances the molecules' amphiphilic character, assisting with the self-assembly of the molecules. In addition, the interplay between the van der Waals (vdW) interactions of the hydrocarbon chains and the π - π interactions of the conjugated segments can impact the physical state of these materials. While weaker vdW forces favor a solid-state structure, stronger vdW interactions promote the formation of liquid-crystalline phase.²

1.2. Phosphole- and porphyrin-based π -conjugated systems: structural organization and functional applications

This thesis focuses on two specific classes of heterocyclopentadiene-based compounds: phosphole-based π -conjugated systems and porphyrin-based structures (with pyrrole as their

synthetic precursor). Both materials hold great potential for applications in electronic and optoelectronic devices.^{3,31} Their amphiphilic properties, conferred by alkylation, enable effective self-assembly. However, achieving a highly ordered structure still remains a challenge. This difficulty arises from the complex balance of different chemical moieties and the control over the intermolecular interactions. While the electronic and photophysical properties of these building blocks are critical for their performance, the focus of this work is on achieving well-oriented and structured films that can be employed in various applications.

1.2.1. Phosphole-based π -conjugated systems

Phosphole is considered a unique member of heterocyclopentadiene molecules due to its partial aromaticity.^{32,33} The nonplanar configuration of phosphorus atom (Figure 1.3) and the little overlap of its lone pair with the π -orbitals of the aromatic backbone and their poor interaction is the reason of this limited aromaticity.³⁴



Figure 1.3 Planar configuration of pyrrole versus the nonplanar configuration of phosphole, redrawn from Duffy et al.³⁴ Based on theoretical calculations, the planar phosphole may exhibit higher aromaticity than thiophene or pyrrole.³⁵

The nature of the ring substituents can influence the phosphole aromaticity. This impact becomes stronger by modification of the substituent linked to the phosphorus atom itself, with consequent effects on the optoelectronic properties of these compounds.^{32,36-39} For example, attachment of a bulky group such as phenyl to phosphorus atom shifts the tetrahedral geometry toward a more planar structure and enhances aromaticity.^{1,34,39-42}

The weak aromaticity of the phosphole compared to its counterparts like thiophene leads to distinct electronic delocalization.⁴³⁻⁴⁵ Phosphole displays a relatively high electron density and polarizable π -electrons. These unique properties make phosphole-based materials excellent candidates for applications requiring efficient ion, charge, and energy transfer.^{1,35,39,46}

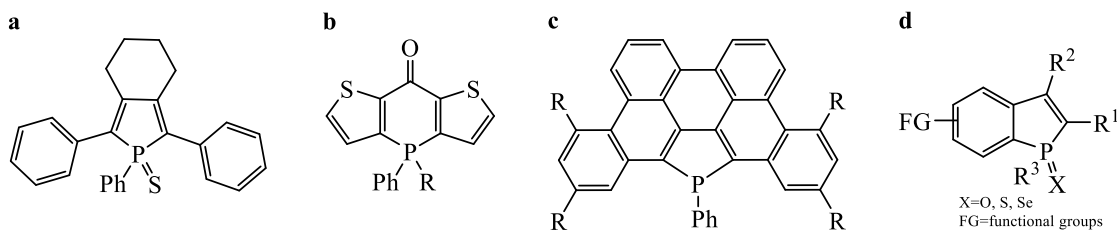


Figure 1.4 Chemical structure of phosphole-derivatives as building blocks of optoelectronics: thioxophospholes (a)⁴⁷, dithieno-4-keto-1,4-dihydrophosphinines (b)⁴⁸, dibenzophosphapentaphene (c)⁴⁹, and benzo[b]phosphole (d)⁵⁰.

Obtaining a well-structured and hierarchical arrangement of these phosphole-based building blocks relies on their cooperative and self-assembly properties. Well-ordered molecular arrangements are important for both electronic performance (e.g., efficient charge and energy transfer properties) and overall performance (including processing and durability).

Phosphole derivatives, such as those shown in Figure 1.4., are already in use as building blocks in electronic devices. Their amphiphilic nature can be further enhanced by combining them with hydrocarbon chains, forming organized one-, two-, or three-dimensional structures.^{51–53} For alkylated phosphole-derivatives, the conjugated phosphole backbone mainly governs the electronic and photophysical properties while the lipid-like behavior derived from the amphiphilic character can assist with their packing through self-assembly.⁵⁴

1.2.1.1. Phosphole-lipids

With this in mind, a series of phosphole-lipids, with a range of conjugation extension in the headgroup and a range a counterions with different sizes are synthesized and exhibited photophysical properties that were responsive to temperature and/or mechanical forces (Figure 1.5).⁵⁴ The orientation of these phospholium derivatives in both solid and solution phase relies on the dynamic and structural properties as well as their concentration in the phase under study. This impact is originally derived from the balance between the inter- and intramolecular π - π interactions and the electrostatic forces in the conjugated segment.⁵⁴ For example, phosphole-lipid exhibits two conformations of “closed” and “open” in the crystals obtained from evaporation of different solvents (Figure 1.6, solid). Similar observation is recorded for the solution phase. In the “closed” conformation at lower concentrations the benzyl groups are closer to the main phosphole moiety,

showing weak intramolecular interactions. At higher concentrations, the stronger intermolecular ionic and π - π interactions push this benzyl group away from the phosphole backbone, resulting in the formation of “open” conformation (Figure 1.6, solution).⁵⁴

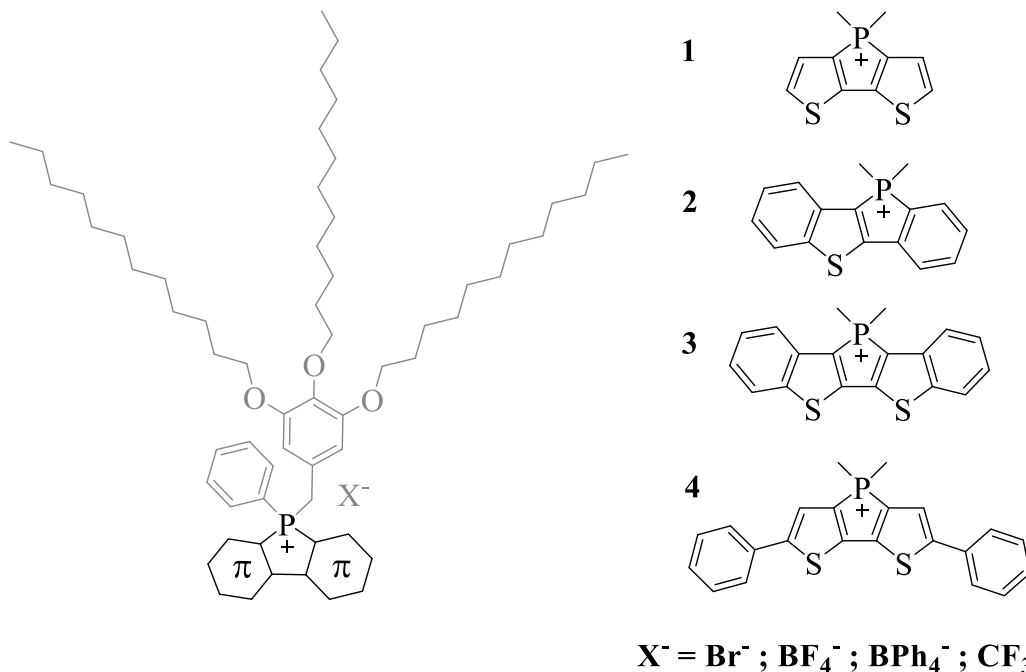


Figure 1.5 Chemical structure of phosphole-based π -conjugated systems with a range of headgroup extension and counterions previously reported.⁵⁴ The phospholium moiety provides the electronic character while the three alkoxy chains connected to the backbone through the benzyl ring offer the amphiphilic character.

The phosphole-lipid can be further modified by addition of fused aromatic rings to the phosphole core and extending the conjugation length (headgroups **2-4** in Figure 1.5). Although the increase in the conjugation length may be accompanied by stronger photophysical properties, the overextension of the conjugation may hinder the necessary intermolecular interactions and may require further adjustments in the length or number of the alkyl chains to maintain the amphiphilic character. For instance, for the same counterion (bromide), the smaller headgroup exhibits well-ordered lamellar organization through interdigitation of the alkyl chains. For bulkier conjugated backbone with a T-shape, as the headgroups become more distant, the alkyl chains are not close enough to show the same interdigitation (Figure 1.6, liquid crystalline).⁵⁴

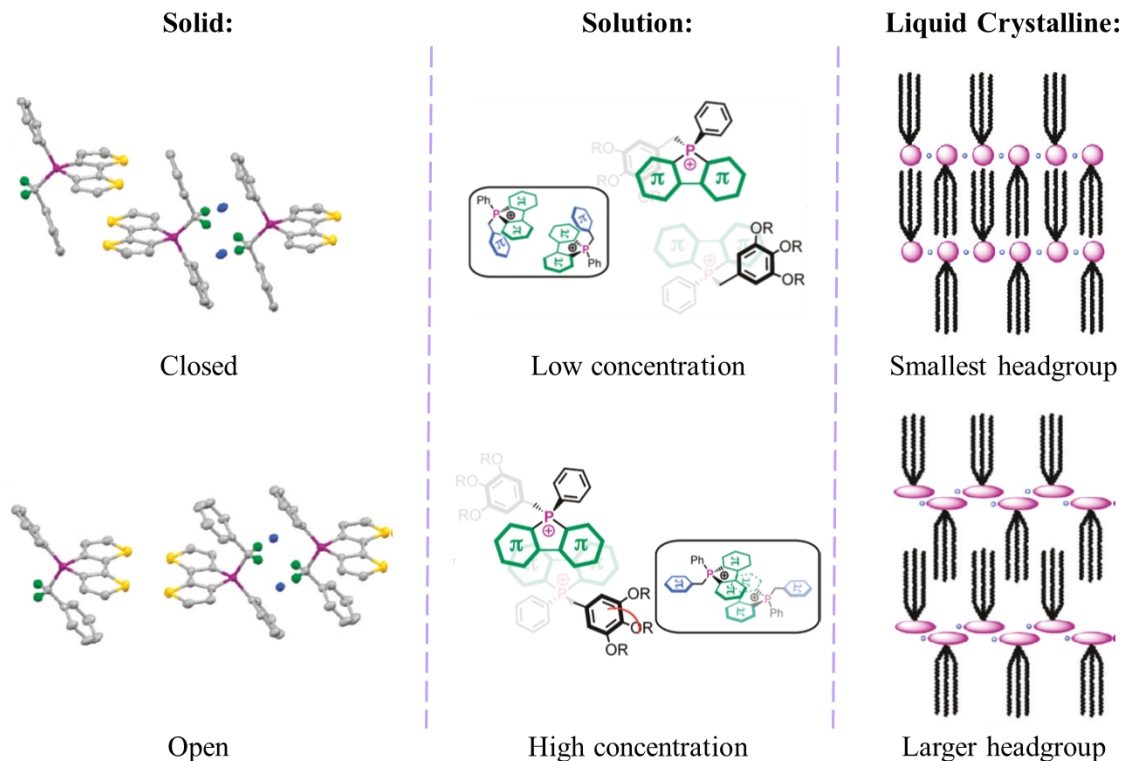


Figure 1.6 Closed and open conformation of phosphole-lipid in solid state (left), conformational change at different concentrations in solution phase (middle), and the lamellar organization in the liquid-crystalline phase (right). For all structures, the counterion is bromide (image adapted from Ren et al.).⁵⁴

While these larger phosphole-lipids with extension of conjugation are not considered macrocyclic compounds, their cross-sectional areas are similar to macrocyclic compounds like porphyrin or phthalocyanines.

1.2.2. Porphyrins-based conjugated systems

Porphyrins -aromatic heteroatom-doped macrocyclic compounds- are another multifunctional building blocks that have received attention for their applications in optoelectronic devices. For instance, the efficient capture of solar energy by porphyrins in the visible region of the spectrum makes them an ideal candidate for applications in dye-sensitized solar cells (DSSCs), a newer type of conventional organic solar cells (OSCs).^{31,55,56} The electronic properties of porphyrins are not

only limited to optoelectronic devices and porphyrin-based photosensitizers are also employed in photodynamic therapy and cancer treatments.^{31,57-59}

The photophysical properties of organic chromophores of porphyrins are mainly governed by number of heteroatoms and the conjugation degree present. Possessing unique size and shape, large surface area, and adjustable porosity make porphyrins resourceful member of heteroatom-doped macrocycles for a wide range of applications.^{60,61}

The chemical structure of porphyrin is shown in Figure 1.7. Porphyrin derivatives can be obtained and tailored by adding functional groups on the peripheral sites for specific and intended applications.^{62,63} For instance, the incorporation of fluorine enhances the conductivity in porphyrin complexes.^{62,64} Another approach is to have porphyrins in contact with metal ions to form metalloporphyrin complexes. The nature of the metal and the metal-porphyrin interactions can dictate the corresponding applications.^{31,65} For example, copper-porphyrin complexes exhibit promising properties to be employed in biomedical applications,⁶⁶ while nickel-porphyrin complexes are commonly employed in molecular thermometers, sensors or optical materials.⁶⁷⁻⁶⁹

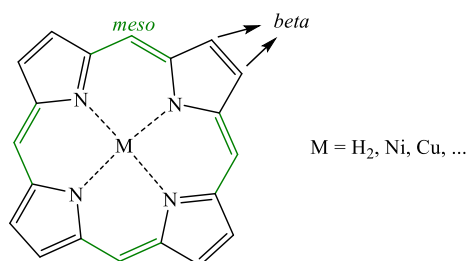


Figure 1.7 Chemical structure of porphyrin with two types of substitution positions: eight *beta* positions on the pyrrolic rings and four *meso* positions on the methine bridges (the latter is shown in green).

Tetraazaporphyrins (TAPs), are another variation of porphyrins that are formed by replacing the carbon atoms in the methine linkers with nitrogen atom. By this replacement, a highly π -conjugated ring with a narrower HOMO-LUMO gap and nonlinear optical properties is obtained.^{62,70,71}

As mentioned earlier for π -conjugated materials, and similar to the other macrocyclic compound of phthalocyanine, porphyrin derivatives tend to form aggregates due to the π - π interactions that

can hinder preferential molecular orientation and reduce performance.^{26,72–74} This aggregation may occur even at the air-water interface, complicating the formation of well-ordered structures.

To assist with the better molecular orientation in porphyrins self-assembly, and to reduce the possibility of aggregation, the hydrocarbon chains can be directly attached to the macrocycle (peripheral positions),^{26,75} or indirectly incorporated by considering a mixture of porphyrins with single-chain fatty acids such as stearic acid or arachidic acid.^{26,76}

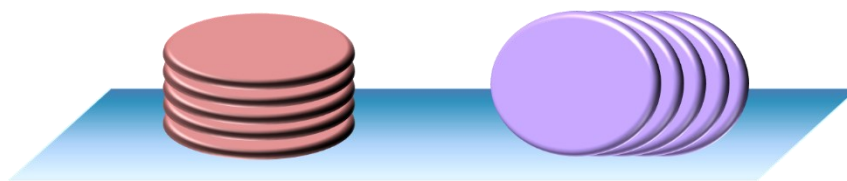


Figure 1.8 Face-on orientation (left) and edge-on orientation (right). Each circle represents a cross-sectional area of an aromatic ring.

There are two main orientations to consider regarding the organization of macrocyclic compounds such as porphyrin and their intermolecular interactions (Figure 1.8). In the edge-on orientation, the macrocycle rings are normal (completely perpendicular or in some cases, tilted) to the substrate or the subphase surface. In the face-on orientation, the rings are parallel to the substrate surface. Although face-on orientation may be the advantageous orientation considering the ring area is closer to the substrate that leads to variety of electronic properties, achieving it remains challenging as higher contribution of strong intermolecular π - π interactions compared to weaker porphyrin-substrate (subphase) interactions results in the edge-on orientation being the preferential orientation.

1.2.2.1. Amphiphilic tetraazaporphyrins

For the case of the amphiphilic tetraazaporphyrins, TAPs with eight side chains at peripheral positions (Figure 1.9) are studied.⁷⁷ The chain length has shown to play a critical role in the thermal stability and the molecular orientation of alkylated TAPs deposited films. As the side chains become longer, they provide and enhance the amphiphilic character. For example, for a range of carboxylic acid chains, the longer chains ($C_{10}COOH$) promote the formation of continuous monolayer, while shorter chains (C_3COOH and C_5COOH) result in the formation of fibrous

aggregates.⁷⁷ This can be due to fact that the longer aliphatic chains may compensate the mismatch of surface areas between the TAP ring ($\sim 120 \text{ \AA}^2$) and the eight acid chains ($\sim 190 \text{ \AA}^2$) better than the shorter chains. In this case, all acid chains in $C_{10}COOH$ are pointed down and form a homogenous film with a face-on orientation.

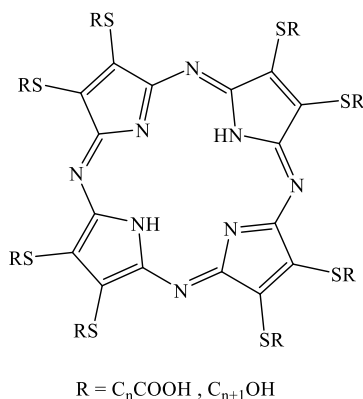


Figure 1.9 Chemical structure of TAPs previously studied.⁷⁷ For the acid chains, n=3, 5, and 10, and for the alcohol chains, n=3,11 was evaluated.

The chemical nature of the chain can also influence the molecular orientation. For example, for the same TAPs structure, although the face-on orientation is obtained with eight acid chains ($C_{10}COOH$), eight alcohol chains ($C_{11}OH$) lead to the edge-on orientation with cofacial interactions that may become tilted based on TAP-substrate interactions. The octaalcohol TAP does not show similar self-assembly properties reported for the octaacid TAP. This difference in molecular arrangements is due to the weaker intermolecular interaction of the hydroxyl groups, not retaining all the hydroxyl groups in the surface.⁷⁷

1.3. Deposition techniques for π -conjugated materials: Achieving optimal thin films

Obtaining electronic devices with high performance level relies on the quality and the structure of stacked films used in their construction. These stacked films comprise individual homogenous film layers that are fabricated in-plane, connected through an ideal inter-layer bonding in the z-direction.⁷⁸ An important key to obtain these individual homogeneous thin films with stability, proper functionality and duration is efficient and practical deposition technique. Different

deposition techniques are applied based on the chemical composition of the materials and the intended applications. It should be mentioned that although each deposition technique has its own benefits, the final film's quality, homogeneity, and consequently its performance remains mainly dependent on the material's inherent self-assembly properties.⁷⁸

1.3.1. Physical vapor deposition

Physical vapor deposition (PVD) involves condensing materials through evaporation or sublimation to form a thin film on a solid substrate (Figure 1.10). Being employed to fabricate thin films with liquid-crystalline order on substrate surfaces for OLEDs, OPV cells, and organic field effect transistors (OFETs) makes this technique a standard process in optoelectronics productions.^{12,79–82} PVD allows for the fabrication of a pure, high-density polymer thin film with nanometer-scale thickness control, as well as multilayered structures.⁸³ The PVD method can also be combined with other techniques (like UV irradiation) for intentional, controlled and/or patterned depositions.⁸⁴ Notably, PVD does not require solvents, which reduces contamination risks. Thermal evaporation, a specific low-cost type of PVD, is often employed for large-scale production of OLEDs.⁸⁵ However, thermal evaporation is time-consuming and requires vacuum conditions. High temperatures can also decompose sensitive materials before their sublimation occurs.⁸⁶ There are newer improvements on PVD to make it more compatible with temperature-sensitive π -conjugated materials, for example plasma-enhanced PVD or atomic layer deposition (ALD) can allow for lower-temperature deposition.^{87,88}

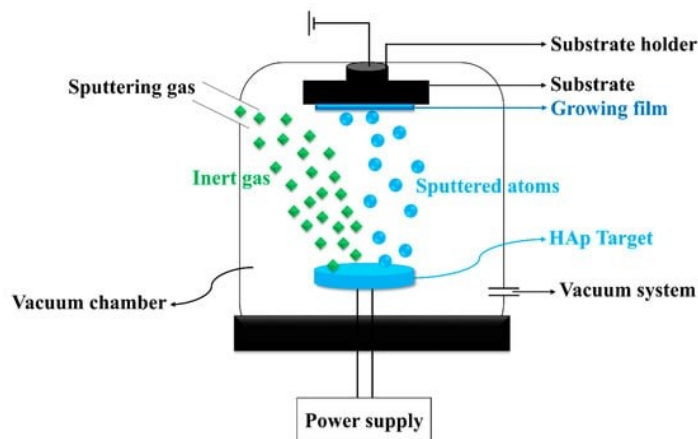


Figure 1.10 Representative illustration of the physical vapor deposition technique (reproduced from Safavi et al.).⁸⁹

1.3.2. Solution deposition

Another productive deposition technique with good control over film morphology is solution deposition, and as its name suggests, its success depends on the solubility of the materials.⁸⁶ The more conventional solution-based techniques include chemical bath deposition and electrodeposition that are low-cost and low-temperature, making them useful for solar cell production.⁹⁰ Electrochemical deposition allows for depositing insoluble materials onto conductive substrates with controlled film thickness.⁹¹⁻⁹³

Other solution deposition techniques include spin coating or dip coating, which generates reproducible thin films on a small scale.⁹⁴⁻⁹⁶ For larger-scale fabrications, methods such as screen printing, spray deposition, and inkjet printing are employed to produce high-density films.⁹⁷⁻¹⁰⁰ Figure 1.11 shows different solution deposition techniques.

Although solution deposition provides various technique options based on the intended application, requirements, and accessibility, these methods come with limitations. For example, dip coating may lead to high amount of solution waste, while the deposited film might still require further treatments, such as heating. Spin coating may result in energy waste with or without optimal success and spray coating may produce films with nonuniform thickness. There are ongoing advancements in solvent engineering and surface treatments to reduce these limitations, such as solvent-free printing or solvent additives that enhance solubility of materials.^{101,102} However, despite the drawbacks mentioned, solution deposition is a very popular method used in industry.

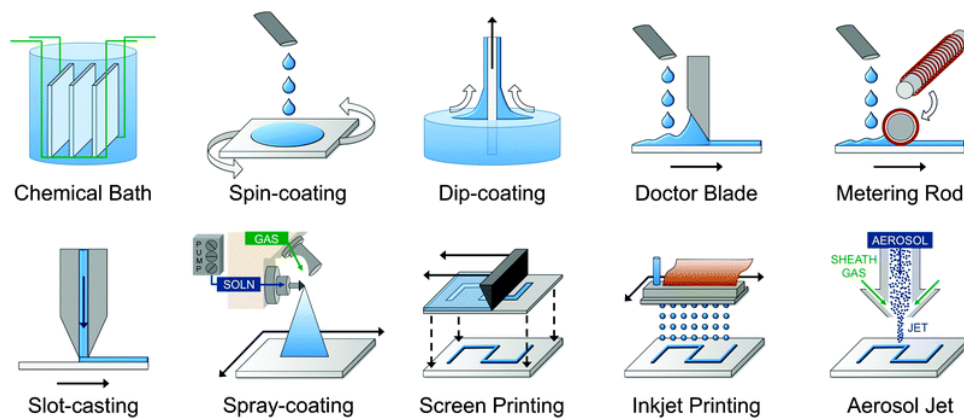


Figure 1.11 Representative illustrations of different solution depositions (reproduced from Pasquarelli et al.).¹⁰³

1.3.3. Langmuir-Blodgett deposition

Langmuir-Blodgett technique (LB) is a method based on molecular assembly developed in early 20th century. The LB method allows for deposition of subphase-insoluble materials from a liquid surface onto a solid substrate as a monolayer or multilayer (the latter can be obtained by repeated deposition). The precise control over the thickness and the homogeneity of the ultrathin film formed makes LB suitable for applications requiring high-quality well-ordered structures.

The molecular alignment and behavior of the LB films mainly depends on the chemical bonding, intermolecular interactions and external forces.^{104–108} While LB method is not commonly employed for large-scale productions, its potential to form well-ordered and high-density thin film structure makes it highly desirable for the fabrication of linear and nonlinear optical and storage devices with high-performance.^{105,107,109–111} Figure 1.12 shows an upscaled roll-to-roll LB deposition process in which the materials are deposited onto flexible substrates such as polyethylene in large areas, expanding the technique's potential applications.^{112–114}

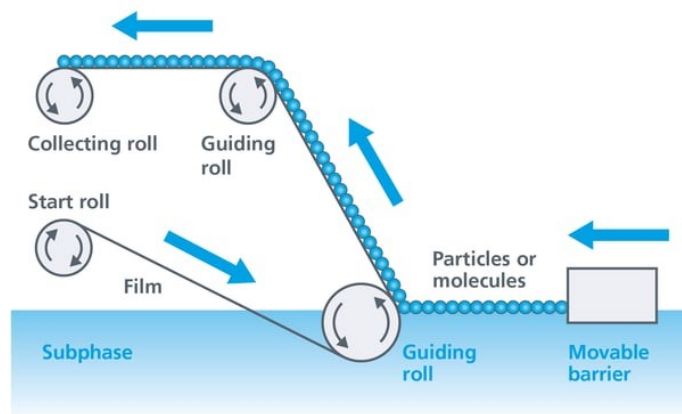


Figure 1.12 Representative illustration of roll-to-roll LB deposition technique (reproduced from Korpela et al.).¹¹²

LB deposition has limitations like any other technique. The long deposition time, instrumental sensitivity to temperatures, and restrictions on the substrate area are the main limitations for this technique. The area limitation is also a challenge for the roll-to-roll LB method, where the deposition depends on the trough length. The film quality and deposition reproducibility may also vary depending on the materials used, as challenges are reported for some chemicals, like graphene

oxide.¹¹⁵ There are ongoing modifications on LB method, such as automated LB systems, with controlled and continuous spreading to improve its scale capacity limitation. Additionally, hybrid deposition techniques that combine LB with other solution-based or vapor-based methods may enhance both the efficiency and quality of the resulting films.

To optimize the LB deposition and better control the arrangement of the thin film obtained, the properties of the Langmuir film of these materials at the air-liquid interface needs to be carefully characterized. Many materials, such as lipids, nanoparticles, polymers, proteins, and graphene derivatives form Langmuir films through self-assembly or insolubility at the air-water interface. The amphiphilic character of these molecules, along with noncovalent interactions, provides opportunities to tune deposition conditions and improve thin film properties. Further details on Langmuir films and the Langmuir-Blodgett deposition technique are provided in Chapter 2.

1.4. Important internal and external impacts on Langmuir and LB film behavior and structure

The formation and behavior of LB films can be tuned by the changes in the chemical composition of the materials and the intermolecular interactions within the self-assembled structure. The external experimental conditions also play a critical role in defining the organization of the film deposited on the substrate.

1.4.1. The intra- and intermolecular interactions

The self-assembly and behavior of monolayers, liquid crystals, and supramolecular structures are largely governed by noncovalent interactions within their chemical composition. These noncovalent interactions include ionic (electrostatic) interactions, hydrogen bonding, π -interactions, dipole interactions, and vdW interactions. The balance and the strength of these noncovalent interactions significantly impact the final molecular arrangement of the film.

For surfactants at air-water and air-solid interface, the vdW interactions mainly drive the packing of alkyl chains. The other interactions contribute to the headgroup interactions in contact with water (or other subphases). Potential hydrogen bonding with water molecules, electrostatic interactions for charged surfactants or subphases, and intermolecular π - π interactions between

aromatic headgroups are among the possible interactions to consider. The latter two are of particular relevance for the work here and will be reviewed below.

1.4.1.1. Electrostatic interactions

The ubiquitous electrostatic interactions, which have strong binding energies (overlapped with covalent bonds) and act over short and long distances, are essential in ionic bonding, often contributing to highly ordered crystalline structures.¹¹⁶ The charge present at the surface impacts the structural arrangements via the Coulombic force. The strength and the balance between electrostatic interactions and other noncovalent interactions at the interface governs phenomena such as phase aggregation, coalescence, and surface adsorption and deposition.¹¹⁷ This strong interaction can also be intentionally employed and manipulated as the main interaction in the ionic self-assembly process to fabricate nanostructured liquid crystals, fibers and nanotubes.¹¹⁸

In thin films at air-water or air-solid interface, electrostatic repulsion between similarly charged molecules can result in a reduced contribution of the line tension, the force acting to minimize the line of contact between different phases of the film. This balance can impact the stability, morphology and uniformity of the film. Strong repulsion can also lead to an expanded molecular arrangement, while higher line tension contributions would drive a more compact structure.^{119–121}

Impact of sodium and ammonium salts of different anions, commonly present in the sea surface and marine aerosols, on the surface organization of 1,2-dipalmitoyl-sn-glycero-3-phosphocholine (DPPC) lipid monolayer have been studied focusing on their implications for atmospheric aerosol nucleation. This study has shown that the addition of these salts disrupts the ordering in the lipid monolayer by expanding it. Although the nature and concentration of the anion directly impacts the lipid's surface morphology, these anions penetrate into the lipid monolayer only at higher surface concentrations of lipid. As shown in Figure 1.13, the presence of bromide causes defects in the interface, reducing the stability of DPPC monolayer, while addition of larger anion of sulfate with higher binding affinity for DPPC may result in transport of the lipid monolayer into the atmosphere as sea spray aerosol.¹²²

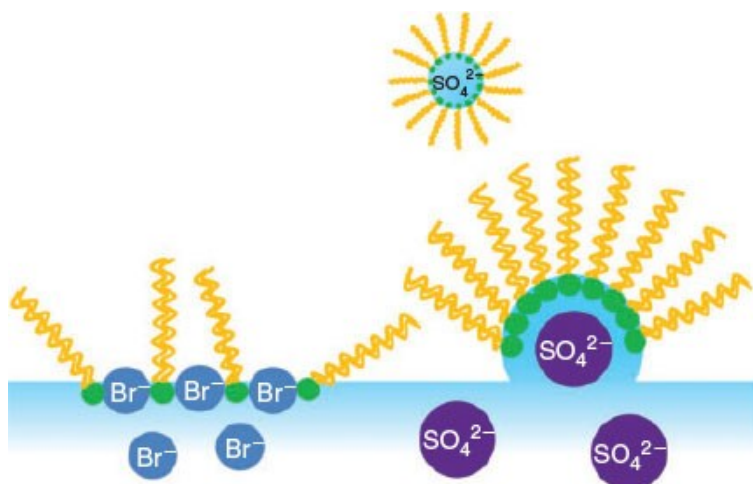


Figure 1.13 Schematic representation of DPPC monolayer interaction with bromide and sulfate anion (image reproduced from Li et al.).¹²²

1.4.1.2. π - π interaction:

π - π interactions are commonly found in both amorphous and crystalline solid materials. These interactions involve aromatic rings or conjugated double bonds and combined with other strong noncovalent interactions have prominent contributions in stabilization of structures such as double helical DNA orientation.¹²³ The strength of π - π interactions directly impacts the degree of molecular aggregation in various poly- and macrocyclic π -systems, while the orientation of π -stacking defines the direction in which the self-assembly and/or the aggregation will occur.¹²⁴ The π - π interactions between two aromatic rings can be observed in a face-to-face orientation (parallel or parallel displaced) or in an edge-to-face (or tilted) orientation (Figure 1.14).

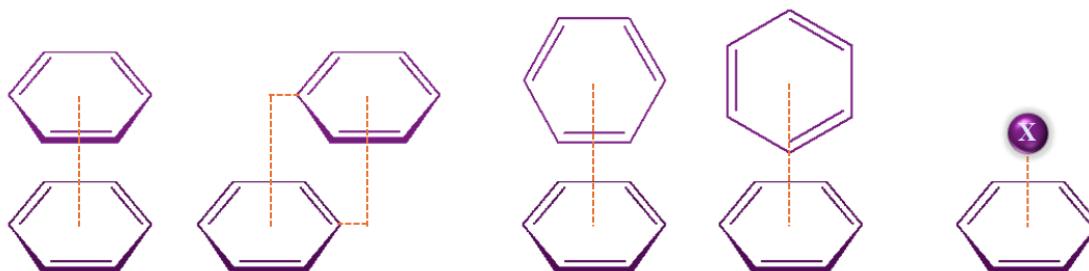


Figure 1.14 Schematic representative images of π -stacking orientation, from left: parallel stacking (sandwich), parallel displaced, edge-to-face, and T-shaped. The illustration on the right represents all other π - interactions including cation- π , anion- π , CH- π , and etc.

The presence of additional functional groups can alter the displacement and the tilt degree in π -stacking orientation to enhance the potential noncovalent interactions and to optimize the structural stability. For example, in the parallel stacking of porphyrins, the displacement of 3.5 Å and placing a pyrrole ring of one molecule above the π -cavity of the other reduces the π - π repulsions and strengthens the structural stability through vdW and electrostatic interactions (Figure 1.15).^{124,125}

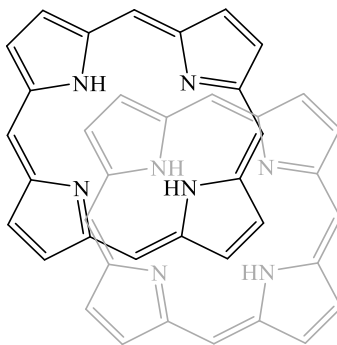


Figure 1.15 Parallel stacking of porphyrin rings with displacement to improve structural stability (redrawn from Hunter et al.).¹²⁵

Similarly, studies on a group of azo-benzene derivatives showed that the interplay between the π - π interactions and the dipole forces can result in different packing densities and aggregations. With weaker dipole coupling (acetyl substituent) and consequent domination of π - π stacking, a densely packed structure is observed (Figure 1.16, left). However, in presence of strong dipole interactions ($-\text{CN}$), the π - π stacking becomes displaced (staggered) and less dense (Figure 1.16, right). With the ending substituent such as $-\text{NO}_2$, although a more closed-packed structure is observed compared to CN , the dipole interaction is strong enough to slightly shift the packing to a staggered orientation (Figure 1.16, middle).¹²⁶

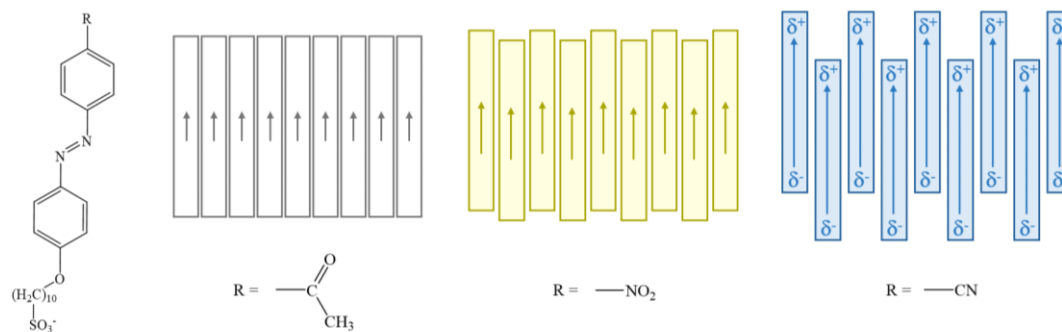


Figure 1.16 Chemical structure and packing orientation of azo-benzene derivatives (redrawn from Tang et al.).¹²⁶

Monolayer systems driven by π -interactions have been investigated by our research group. For instance, meta-substituted dioctadecylaminobenzoquinones (Figure 1.17a) exhibit cohesive monolayer with high degree of aggregation at air-water interface that is caused by the charge assisted hydrogen bonding and π -stacking.¹²⁷ Monolayers of octadecyl gallate (Figure 1.17b) also show that noncovalent interaction such as hydrogen bonding and π -stackings result in highly ordered headgroups in herringbone arrangements, accompanied by high aggregation. This strong headgroup interactions also impact the film morphology by reducing the contribution of the line tension, promoting the formation of dendritic domains (directional growth of condensed phase).¹²⁸

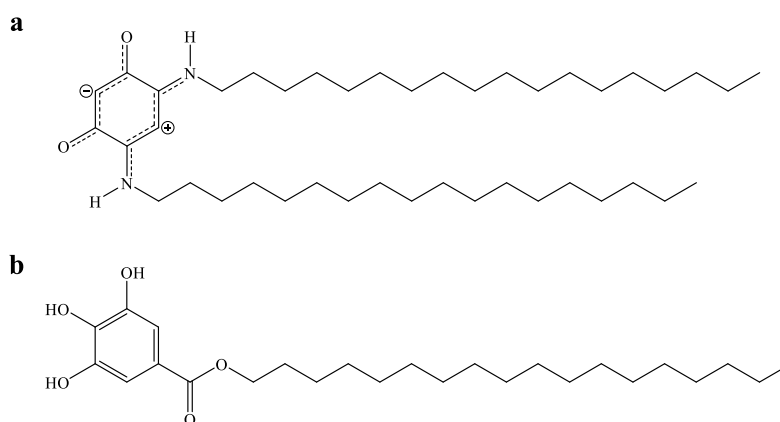


Figure 1.17 Chemical structure of meta-substituted dioctadecylaminobenzoquinones (a) and octadecyl gallate (b).

In addition to π - π interactions, cation- π and anion- π interactions can also influence the organizational stability of the materials and two-dimensional (2D) thin films containing aromatic rings. Electron-rich aromatic compounds attract cation species, while electron-deficient rings interact with anions.¹²⁹⁻¹³¹ The strength of these charge- π interactions is influenced by factors such as polarity, hydration behavior, electron affinity, and the environmental conditions such as pH, ionic strength, and solvent.¹³²⁻¹³⁴

1.4.2. External conditions impacting Langmuir and LB films

Several external factors can influence the formation, molecular arrangement, and behavior of the Langmuir and Langmuir-Blodgett films. The change in the subphase properties such as temperature, pH, ionic strength, and presence of other species are among these factors. The spreading solution can also affect the molecular arrangement of the Langmuir films.⁷⁸ A brief explanation of each is provided below.

1.4.2.1. Temperature

The change in the subphase temperature can alter the energy levels of individual phases that are formed along the surface pressure-molecular area isotherm and induce or accelerate specific phase transitions. Furthermore, this change can influence the film thickness and stability. For a given molecular area, by increasing the subphase temperature, an increase of the surface pressure may be observed as the surfactant monolayer is occupying larger average areas to accommodate the increase of its thermal motions.¹⁰⁵ At higher temperatures, increased molecular mobility may also lead to greater aggregation.^{105,135}

1.4.2.2. pH

The dominant effect of subphase pH is to alter the protonation state of the headgroup and thus influence charge interactions such as attraction or repulsion. The prominent change in headgroup's electrostatic interactions may overcome the existing packing orientation and change the LB film behavior and morphology. For instance, there are studies showing that higher pH levels may change the population of tilted-oriented regions and promote the formation of more stable and

smoother LB films, whereas lower pH levels may promote rougher and more distorted structures.¹³⁶⁻¹³⁸

1.4.2.3. Ionic strength and specific ions in subphase

The change in the ionic strength of the subphase, or the presence of specific ions, can also influence the intermolecular interactions in the Langmuir films. Factors like charge, electronegativity, polarization, and the change in the dipole moment impact the strength of the electrostatic interactions and charge screening effect, which can alter the molecular orientation, with higher tendency reported for formation of a ring-like or a coiled-shape structure.^{136,139} The ions-surfactant interaction can also change along the surface pressure-molecular area isotherm. At higher packing densities at smaller molecular areas, salts may be expelled from the monolayer plane, leading to changes in film structure.^{105,140}

1.4.2.4. Spreading solvent

The choice of spreading solvent is important in Langmuir film studies. The spreading solvent is required to be volatile and have a positive spreading coefficient on water surface as it directly affects the film morphology and homogeneity.^{104,105} Non-volatile or slow-evaporating solvents tend to form small, isolated islands at the air-water interface.¹⁴¹ Common spreading solvents include chloroform, hexane, dichloromethane, and tetrachloromethane. In addition to the spreading coefficient that impacts how well the surfactant is dispersed at the air-water interface, the water solubility of the spreading solvent can also impact the formation and stability of the Langmuir films.⁷⁸

1.5. Research goals and thesis organization

The focus of this thesis is to explore the Langmuir and Langmuir-Blodgett films of the two classes of optoelectronic building blocks mentioned earlier (phosphole-lipids and TAPs) and modify their film behavior through the modulation of the headgroup interactions and packing organizations that can be obtained by controlling the external conditions.

For phosphole-lipids with charged phosphonium headgroup and π -conjugation in the backbone, the impact of noncovalent interactions in the headgroup region are investigated. The electrostatic interactions are modulated via addition of ions (Chapter 3, supplementary information in Appendix A) and the π - π interactions are moderated by introducing the aromatics through different approaches (Chapter 4, supplementary information in Appendix B).

For macrocyclic compounds of TAPs, control over the environment pH allows for investigation of the impact of the protonation state of the carboxylic acids and the corresponding electrostatic interactions on the film organization and behavior. The length of the side alkyl chains and their impact on the Langmuir-Blodgett films orientation is also explored (Chapter 5, supplementary information in Appendix C).

The experimental techniques applied for all the surface characterizations are briefly presented in Chapter 2.

Chapter 2. Experimental Techniques

2.1. Langmuir monolayers

Langmuir monolayers (a single molecular layer formed from an insoluble surface-active molecule at air-liquid interface) were defined more than a century ago in order to study the interface systems and they remain attractive in interface-related science.^{142–145} These surface-active molecules (commonly labeled as surfactants) are made of hydrophobic alkyl chain(s) in balance with the hydrophilic headgroup and reduce the surface tension of water. Figure 2.1 shows a schematic representation of single-, double-, or triple-chain surfactants.

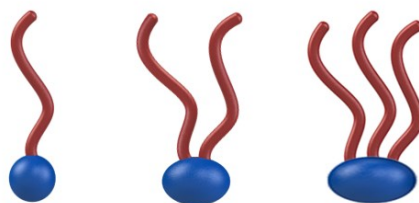


Figure 2.1 Schematic representation of surfactants with hydrophilic headgroup and different number of chains (tails).

2.1.1. Langmuir-Blodgett film balance

The Langmuir-Blodgett film balance (commonly referred as a Langmuir trough) is a technique to characterize the film behavior of the surfactants at the air-water interface. It comprises a Teflon trough with one or two movable Teflon barriers (Figure 2.2). Water (with pH adjustment, if needed), buffers (for physiological models), and salt solutions are among the commonly used subphases in the Langmuir trough. The surfactant or lipid solution is prepared in advance and spread onto the water subphase with a Hamilton syringe. The solvent used for spreading solution should be volatile (evaporate easily without dissolving into the subphase) and have high spreading coefficient to assure proper spreading of the lipid film onto the subphase.¹⁴⁶ For all the experiments reported in this thesis, ACS grade chloroform is used as the main spreading solvent for spreading solutions; methanol can be added to enhance solubility and reduce solution aggregation.

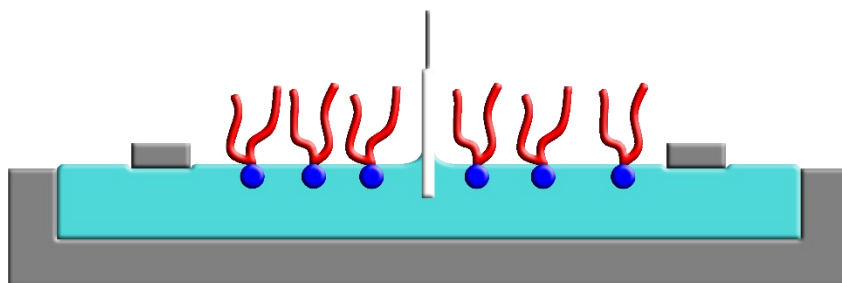


Figure 2.2 Schematic representative of a Langmuir trough with two movable barriers and a Wilhelmy plate in middle.

After spreading, and waiting for the solvent evaporation and monolayer equilibration, the barriers are closed at a chosen rate for the lateral compression of the monolayer films.¹⁴⁷ By compressing the monolayer, the accessible area for the molecules is decreasing that leads to the change of the surface tension. A Wilhelmy plate is used as a sensor to measure this change. The Wilhelmy plate pressure sensor used for all the experiments in this thesis is a 1 cm × 2 cm, Whatman No. 1 chromatography paper. The surface pressure, which is a difference between the surface tension of pure water and the surface tension of water in the presence of the monolayer film is measured as a function of available trough area through compression:

$$\pi = \gamma_0 - \gamma \quad \text{Equation 2.1}$$

Where π is the surface pressure, γ_0 and γ are the surface tension of pure water (72.8 mN m⁻¹ at room temperature) and surface tension of water in presence of the film, respectively.^{147,148}

By compression and reducing the surface area in between the trough barriers, the monolayers dispersed across the surface should adopt a phase that will further alter the surface tension of the water.

The surface pressure-molecular area isotherm of the surfactant is obtained with the Langmuir-Blodgett film balance, presenting the changes of the surface pressure (in mN m⁻¹) as a function of the surface area per molecule (in Å² molecule⁻¹) (Figure 2.3).¹⁴⁹ The monolayer film dispersed on the surface of water is a 2-dimensional (2D) analogous to the phases it adopts in the 3-dimensional (3D) bulk. At large accessible molecular areas -very large surface area relative to the number of

moles of surfactant spread- the surfactants adopt the gaseous phase, with similar characteristics of a 3D gas phase: surfactant molecules distant from the neighboring molecules, freely rotating with no or minimum intermolecular interactions observed.

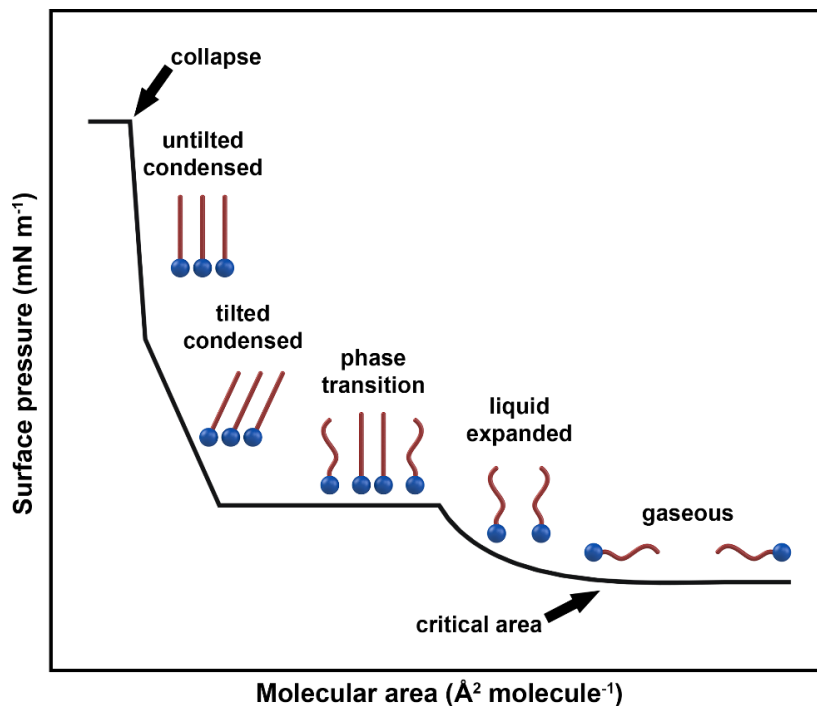


Figure 2.3 Schematic representative surface pressure-molecular area isotherm with possible phases formed.

Upon compression of the monolayer film and forcing the surfactants to interact, a phase transition may occur. The onset area is where the surface pressure shows an increase from 0 mN m^{-1} , indicative of coherent film coverage. The liquid-expanded phase (LE) is similar to the liquid phase observed in 3D: while the surfactants still have their high degree of conformational freedom, they are showing intermolecular interactions.

With further compression and interactions of the alkyl chains, a first-order phase transition, observable as a plateau in the isotherm, may be observed in the surface pressure-molecular area isotherm (depending on chain length and headgroup size – see below). Through this phase transition, the LE phase is converted to a condensed phase (C) without any change in the surface pressure as the area is decreasing (transition of liquid to the solid phase in 3D). In the condensed phases, the alkyl chains are fully extended and pack in an oriented fashion, as is seen in liquid-

crystalline state.¹⁵⁰ This condensed phase formed is defined by unit cell of the alkyl chains including their tilt from the normal and their tilt azimuth (i.e. the direction of tilt relative to the nearest neighbours). After the end of the plateau, for tilted phases, further compression reduces the tilt angle. In some cases, a subsequent second order tilting transition can be observed, wherein the direction of tilt azimuth changes or the molecules become untilted.¹⁵⁰ Note, that not all molecules will form a condensed phase, nor can all molecules be compressed to an untilted state.

The packing orientation of the chains that defines the tilting depends on the distance-dependent vdW interactions of carbon chains. The relative size of the hydrophobic moiety of chains versus the hydrophilic region of the headgroups is one of the controlling criteria of these interactions. If the headgroup is occupying larger surface area than the cross-sectional area occupied by the alkyl chains, the carbon chains may not interact with the neighboring chains when they are untilted, and they exhibit deviation from the normal to maximize favorable interactions. The relative size of the headgroup versus the chains can be modified by altering the number and length of the carbon chains as well as increasing the size of the headgroup itself. As an example for the former, for a well-known headgroup of phosphocholine lipids, when only two chains are present, higher surface pressures are needed to obtain fully upright orientation. When a third chain is added, the tilted to untilted phase transition occurs at larger molecular areas and lower surface pressure, and interestingly, by introducing the fourth alkyl chain, the untilted condensed phases are formed directly from the LE-C phase transition plateau.¹⁵¹

With further compression of the monolayer film, and mostly at relatively high surface pressures, the film collapses when it cannot remain in a monolayer plane. The collapse of the film can occur by the formation of multilayers or 3D aggregates at the air-water interface. The surfactants can also dissolve into the subphase through the collapse. Some surfactants may exhibit local collapse, which is represented by a decrease in the slope while the surface pressure continues to increase. While for other surfactants, no further change of surface pressure through compression is a demonstration of collapse. The collapse of fatty acids monolayer however is accompanied by a sharp decrease in the surface pressure.

As mentioned, not all surfactants form all the phases represented in Figure 2.3. For example, surfactants with unsaturation (usually cis-double bonds) in their alkyl chains do not form condensed phases at room temperature and may collapse from the LE phase without exhibiting

any LE-C phase transition. On the other hand, surfactants with strong intermolecular interactions may even exhibit a formation of condensed phase upon spreading and without any compression (i.e. at 0 mN m⁻¹ and large molecular areas).^{127,128}

It should also be noted that when the film is constantly compressed through an isotherm, it is not at equilibrium and kinetic effects may be observed. The surface pressure may differ based on the distance of the pressure sensor with respect to barriers for rigid films or the ones with larger headgroups.¹⁵² The surface pressure-molecular area isotherm may also alter based on the compression rate, waiting time for solvent evaporation and monolayer equilibration, the surface temperature, and the trough geometry. A slower compression rate may be a good alternative to avoid or reduce the kinetic impacts on the isotherm, as it provides longer time for the film to reorient through the isotherm, but it may also have negative impacts on the isotherm as it is accompanied by the subphase evaporation.

The Langmuir trough can be coupled with other techniques such as Brewster angle microscopy, IR spectroscopy, fluorescence microscopy or X-ray diffraction setup for further characterization of the monolayers.

2.1.2. Compressibility

The monolayer compressibility is one of the characteristics that defines the rigidity of the film as it provides information about the rheological and structural properties of the condensed monolayer,¹⁵³ as well as the in-plane elastic packing interactions.¹⁵⁴ The compressibility of the monolayer film is obtained from the surface pressure-molecular area isotherm:

$$C_s = -\frac{1}{A} \left(\frac{\partial A}{\partial \pi} \right)_T \quad \text{Equation 2.2}$$

Where A is the molecular area and π is the surface pressure. However, the surface compressional modulus (C_s^{-1}) is usually reported as a function of the surface pressure, to characterize the monolayer properties:¹⁵³

$$C_s^{-1} = -A \left(\frac{\partial \pi}{\partial A} \right)_T \quad \text{Equation 2.3}$$

Smaller C_s^{-1} values correspond to higher compressible films and larger ones mean the film is rigid and less compressible. Gaseous phase is the most compressible film while the rigid solid state with highest C_s^{-1} values is the least compressible of all. Although there are absolute values reported in literature as representative of a particular phases,¹⁵⁵ for the surfactants studied in this thesis, the relative change in the compressibility is evaluated as multiple phases can be present.

2.2. Brewster angle microscopy

Brewster angle microscopy (BAM) is one of the techniques performed to visualize the phase formation of the monolayer in real time at an air-water interface. With this technique, the morphology and the thickness of the film is evaluated.^{144,156,157}

This technique, invented in 1991,¹⁵⁶ exploits the reflective property of polarized light.¹⁵⁸ The Brewster angle of an interface is the incident angle at which p-polarized light does not reflect upon striking the interface, and is only transmitted (refracted through the medium). The Brewster angle can be determined by Snell's law and is dependent on the refractive index of the two media of the interface. For the air-water interface and at the wavelength of 532 nm, it is 53.15°.

$$\tan \alpha = \frac{n_2}{n_1} \quad \text{Equation 2.4}$$

Where α is the Brewster angle, n_1 and n_2 are the refractive index of the air (1.0003) and water (1.3333), respectively.¹⁵⁹

When the monolayer is present at the air-water interface, due to the different refractive index it has compared to water (resulted from the chemical composition of the film and its thickness) the p-polarized light will be reflected from the surface. Therefore, the monolayer film can be visually distinguished from the pure water subphase. Moreover, different phases have different optical properties which allows the morphology of the film to be visualized. A schematic illustration of this technique is shown in Figure 2.4.

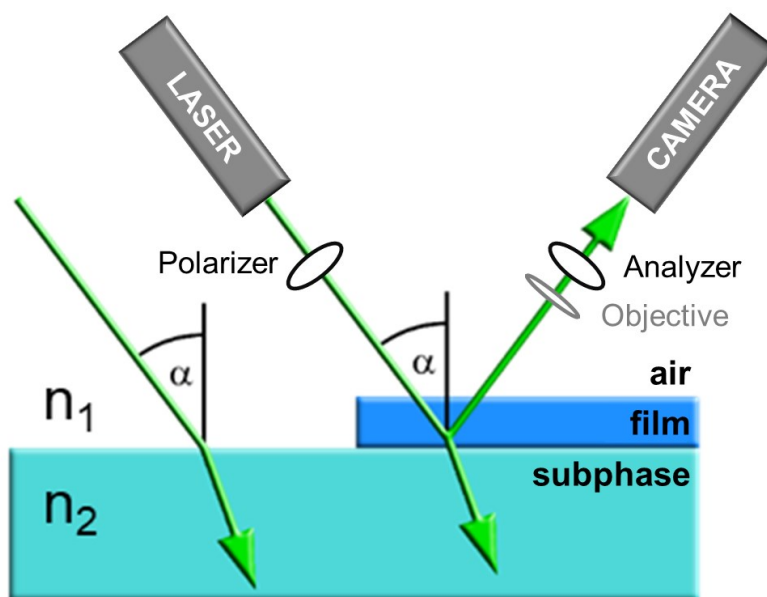


Figure 2.4 Schematic illustration of basic principle of BAM. The Brewster angle α is 53.15° , and n_1 and n_2 are refractive index of air and water, respectively.

For the Brewster angle microscope, an I-Elli2000 imaging ellipsometer (Nanofilm Technologies GmbH, Göttingen, Germany) equipped with a 50 mW Nd:YAG laser ($\lambda = 532$ nm) is used. A Langmuir trough is placed under this microscope and simultaneously records the surface pressure-molecular area isotherm during the BAM imaging experiment. The laser is directed through the first polarizer before striking the interface, to modify the polarization of the beam. The second polarizer, called the analyzer, will analyze the polarization of the light reflected from the monolayer (at air-water interface) before reaching the detector. The lateral resolution of this technique is 1-2 μm , due to the optical diffraction limit. However, it allows us to obtain information about the phases formed and domain shapes during monolayer compression.

2.3. Imaging Ellipsometry

Nulling ellipsometry exploits the optical properties of the polarized light by using the same microscope as BAM.^{160,161} The polarization of the light is impacted by the medium it strikes. For the case of the monolayer at the air-water interface, this change of the polarization depends on the physical properties of this thin film, including its refractive index and thickness. With the assumption that this thin film is homogeneously dispersed in the region under study and its

refractive index remains relatively constant, the film thickness becomes the main parameter that is determined.

The setup is similar to the BAM setup (Figure 2.4). The laser passes through a linear polarizer, followed by a compensator set at 45° , to generate elliptically (circular) polarized light. Upon reflecting from the air-water interface, this now linear polarized beam passes through the analyzer (the second polarizer) and is imaged using a CCD camera. The ellipsometric nulling condition is obtained when the minimum light is detected at the CCD camera. To reach this condition, the polarizer, compensator and analyzer angle are altered, which are directly related to the optical properties of the thin film studied. This polarization change is shown by the change in two polarization angles of Δ and Ψ . The angle Δ corresponds to the phase difference between the reflected p-polarized light and s-polarized light and provides information about the optical properties of the sample like refractive index and film thickness. The angle Ψ corresponds to the ratio of the amplitude of the reflected p-polarized light to the amplitude of the incident p-polarized light, and it provides information about the degree of the change in polarization state upon reflection from the sample surface.¹⁶² Studies show that Ψ does not change prominently by the film thickness for thin films ($\delta\Psi$ is about 0.1° and 0.3° for a 5 nm and 10 nm thick film with refractive index of 1.50, respectively). However, there is a linear correlation between the thin film thickness and the changes in Δ ($\delta\Delta$ is about 24° and 44° for a 5 nm and 10 nm thick film with refractive index of 1.50, respectively).¹⁶² Assuming that the monolayer film is homogeneous and using the fitting process embedded in the Imaging Ellipsometer software, the changes in these two polarization angles upon reflection are computed. For measurements at air-water interface and due to the important impact of vibration and optical modeling limitations, the changes in the change of the polarization angle of Δ are reported. The beam footprint is $572 * 768 \mu\text{m}^2$ for $20\times$ magnification and the measurements correspond to the average of the surface in this region of interest. By compressing the monolayer at the air-water interface, the film phase and its thickness change. Based on the molecular area in the isotherm and the size of the domains present, the region of interest may not represent only one phase, and the average of all phases is considered in the ellipsometric measurements. All the ellipsometric measurements reported in this thesis are performed at the air-water interface. At each measurement point, 10 measurements are obtained for the real time region of interest and $\delta\Delta$ measurements, and the standard deviation for each point is obtained. For each experiment, the measurement for the clean subphase before spreading the

surfactant is considered as the relative zero point, and all the $\delta\Delta$ measurements plotted are the relative changes to the subphase ($\delta\Delta = \Delta_{\text{film}} - \Delta_{\text{subphase}}$). The $\delta\Delta$ values are not evaluated by absolute values and their change though the isotherm and how they are impacted by the subphase nature is reported.

2.4. Atomic force microscopy

Atomic force microscopy (AFM) is a nonoptical scanning probe microscopy invented in 1986.¹⁶³ AFM is a powerful measurement tool which accurately evaluates surface topographical, optical and mechanical properties of deposited films on solid substrates, among other properties. The main advantages of this technique are the relatively simple process for sample preparation combined with high resolution, leading to its usage in characterization of nanomaterials.

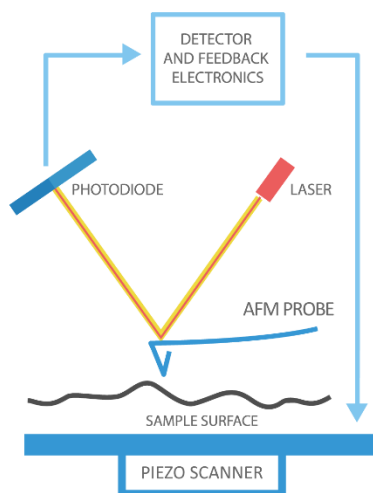


Figure 2.5 Schematic illustration of Atomic Force Microscopy, reproduced from ¹⁶⁴.

Figure 2.5 shows the setup that includes an AFM probe with a sharp tip which is attached to the free end of a spring cantilever. This probe scans over the sample surface in a raster pattern (rectangular array of regularly sampled values, known as pixels).¹⁶⁵ The AFM probes are mainly coated with a silicon/silicon nitride layer to reflect the laser beam. Any deflection in the cantilever caused by the height differences in the sample will alter the direction of the beam reflected from the back of the cantilever. This change will be tracked and detected by a position-sensitive photo detector. A piezoelectric ceramic scanner is placed beneath the sample holder and monitors the

relative coordination (both lateral and vertical direction) of the sample versus the AFM probe, while its vertical movement is controlled to maintain the tip-surface interaction force at a constant level. By recording the cantilever deflection in the vertical direction, the height scale 3D topography of the surface will be obtained.¹⁶⁶

The main modes of AFM include contact mode, noncontact mode, and tapping mode which has an overlap with the other two modes.¹⁶⁷ For all the AFM images reported in this thesis, PeakForce tapping mode was used, in which the probe taps the sample surface periodically. This mode provides recording of high-resolution AFM images regardless of the operator's experience as no cantilever tuning is mandatory.

For all the AFM images reported here, at least two separate samples were prepared and 5-8 spots on each sample were chosen for the imaging.

2.4.1. AFM sample preparation

AFM samples are obtained by depositing the thin-layer film on a solid substrate from the Langmuir trough. There are different solid supports used for AFM samples, covering both hydrophilic and hydrophobic substrates, including mica, silica, glass, highly oriented pyrolytic graphite (HOPG), Si wafers (the oxide layer is responsible for the hydrophilic interaction), and gold-, silver- and zinc-based substrates. For all the AFM samples presented in this thesis, and to retain the surfactants with hydrophilic headgroups down, mica has been used as the solid support. This negatively charged aluminum silicate substrate has an atomically smooth surface and only requires to be freshly cleaved by a sticky tape right before the sampling.

To transfer the monolayer film onto mica, the upstroke Langmuir-Blodgett (LB) deposition technique is used.¹⁶⁸ In this technique, the solid support (mica) is located into the subphase, perpendicular to the surface of the subphase, before spreading the surfactant. After spreading the surfactant and reaching the required surface pressure, as the barriers are actively compressing to keep the isotherm at the defined surface pressure, the arm holding the substrate is raised (upstroke) to withdraw the sample from the subphase and the monolayer film becomes deposited at a constant surface pressure. With this technique, we can control the deposition rate (the speed of the arm

pulling the mica up) to minimize the possibility of changing the morphology through the deposition. Also, we can measure the transfer ratio (TR) for each deposition:

$$\text{Transfer Ratio (TR)} = \frac{\text{Surface area loss of the subphase in the trough}}{\text{Surface area of the substrate}} \quad \text{Equation 2.5}$$

A transfer ratio of 1 implies an ideal transfer, and means that the loss of area from the surface matches the substrate area; i.e., a 1:1 transfer. When the material on the surface does not adhere very well to the substrate, they do not properly transfer to the solid support, and the molecules transferred have more space on the solid substrate and the transfer ratio will be lower than 1. However, the transfer ratios higher than 1 means that more materials that can fit onto the substrate area are transferred, and this may lead to a vertical growth on the substrate.

For the case of hydrophobic substrates, repeating deposition to obtain multilayers, or inducing a different orientation for the monolayer (chains attached to the substrate), this LB technique can be performed on the downstroke. The other deposition technique to consider (for both hydrophilic and hydrophobic substrates) is the Langmuir-Schaefer (LS) deposition method,^{105,169} in which, the substrate is located parallel to the subphase surface and is lowered from the air towards the subphase surface for film deposition. In the inverse LS method, the substrate is placed on the bottom of the trough, covered by subphase before spreading the surfactants, and by reaching the surface pressure, the substrate is pulled up or the subphase is aspirated from the trough well to have the thin film deposited. With LS method, we can transfer films onto larger substrates at higher rates with lower impact on the film morphology.^{105,170} However, due to the sudden change of surface area of the trough (through aspiration or moving the substrate), the transfer ratio cannot be calculated. The different placements of the substrate with respect to the Langmuir trough and their deposition directions for each technique are shown in Figure 2.6.

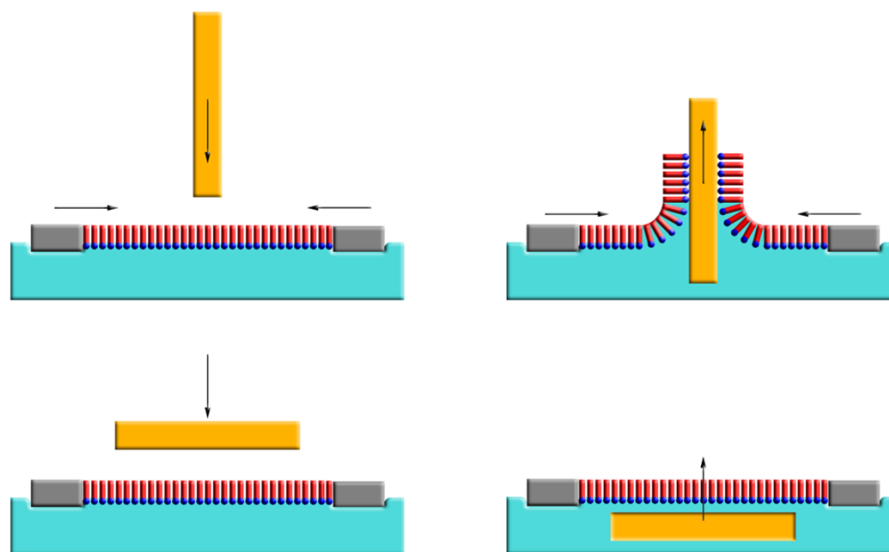


Figure 2.6 Langmuir-Blodgett deposition (top) and Langmuir-Schaefer deposition (bottom) techniques.

For all the AFM images reported in this thesis, the upstroke LB deposition is performed on mica as a substrate (Figure 2.6. top-right). The inverse LS deposition has also been performed to confirm that the morphology is independent of the deposition technique (Figure 2.6. bottom right).

2.5. Surface-specific X-ray techniques

The chemical structure of the present surface-active materials defines the structural orientation of the monolayer at the air-water interface.¹⁷¹ Synchrotron X-ray scattering is one of the important techniques that provides information about the structural organization of the materials at the molecular level. Non-crystalline packing of the monolayers mainly leads to a continuous scattering function (weaker X-ray scattering), while the crystalline packing leads to periodic scattering function (stronger X-ray scattering).¹⁷² As the conventional X-ray scattering may be weak for soft materials such as Langmuir monolayers at the air-water interface, the synchrotron-sourced X-ray is used for better probing the structural orientation.^{173,174} Figure 2.7 illustrates the principle behind the two main X-ray methods (Grazing incidence X-ray Diffraction (GIXD) and X-ray Reflectivity (XRR)) employed in this thesis.

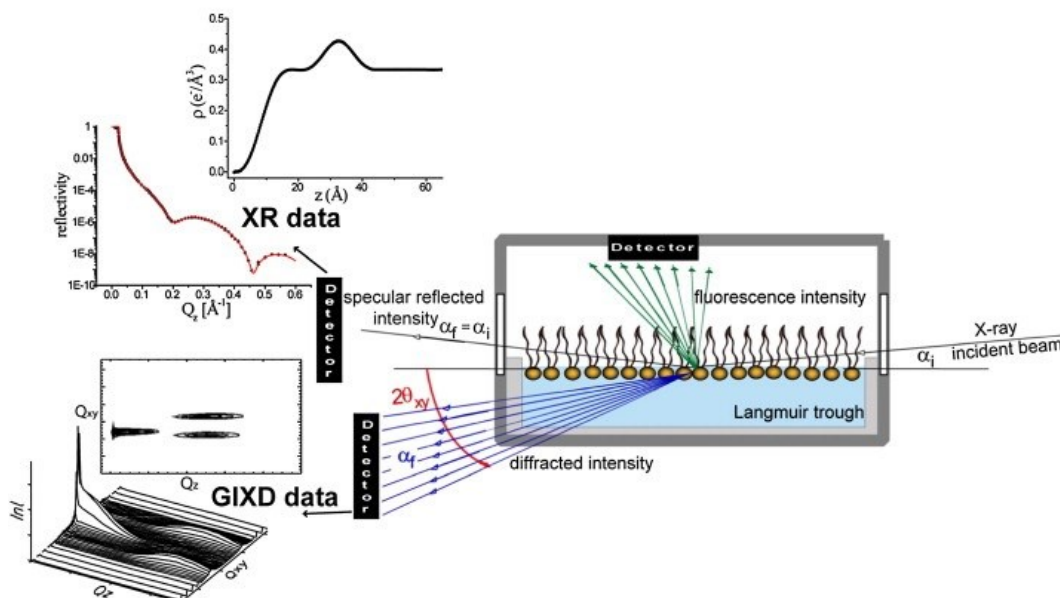


Figure 2.7 Principle of synchrotron-based X-ray scattering characterization techniques of GIXD and XRR (the image is modified from Stefaniu et al.).¹⁷¹

2.5.1. Grazing incidence x-ray diffraction (GIXD)

The crystallographic surface technique of GIXD is carried out at air-water interface and provides information about the lateral order of the thin film formed at the interface.

When the X-ray beam interacts with the monolayer film at an incident angle ($\alpha_i \sim 0.1^\circ$) below the critical angle (α_c) of the air-water interface, the beam is diffracted by the monolayer (the critical angle (α_c) is a function of the intensity of the x-ray beam). At this low incident angle, the X-ray has high surface sensitivity as it only penetrates into a few nanometers. This diffraction occurs along the X-ray component vectors of Q_{xy} and Q_z , and these components are defined as:^{172,175}

$$Q_{xy} = (2\pi/\lambda)[\cos^2(\alpha_i) + \cos^2(\alpha_f) - 2 \cos(\alpha_i) \cos(\alpha_f) \cos(2\theta_{xy})]^{1/2} = (4\pi/\lambda) \sin(2\theta_{xy}/2) \quad \text{Equation 2.6}$$

$$Q_z = (2\pi/\lambda)[\sin(\alpha_i) + \sin(\alpha_f)] = (2\pi/\lambda) \sin(\alpha_f) \quad \text{Equation 2.7}$$

The angles α_i , α_f , and θ_{xy} are shown in Figure 2.7. In the presence of organized monolayer with a lattice plane, the Bragg condition is met, and therefore, a Bragg diffraction peak is observed. Monolayer packing at the air-water interface represents a two-dimensional powder crystal. The 2D

lattice structure is represented as Bragg rods perpendicular to the plane and shown in a top-down view in Figure 2.8.

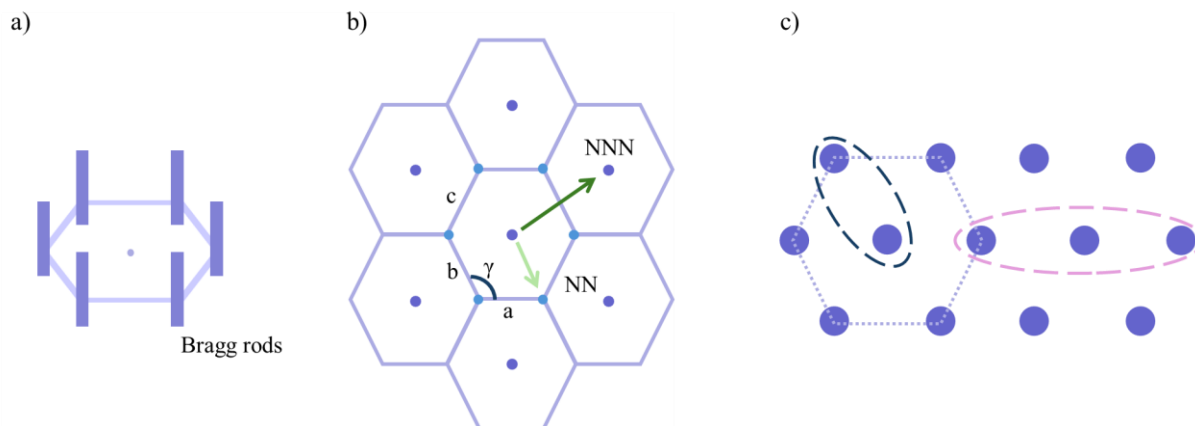


Figure 2.8 Lattice structures in reciprocal space, including Bragg rods (a), and reciprocal space, tilt direction and unit cell for the common phases (b). The arrows define the tilt direction of the nearest neighbor (NN) or next nearest neighbor (NNN). For hexagonal unit cell of alkyl chain packing shown in (c), each circle corresponds to one alkyl chain, and the dark and pink dashed-line ovals represent a combination of packing for a double- and triple-chain surfactant, respectively.

With GIXD, the relative position of the surfactants (mainly alkyl chain as they are dominating the packing) is defined by the deviation of these Bragg rods' position from the ideal hexagonal packing of the six first-order wave vectors with six reflections. As some of these reflections are partially or completely obstructed by water present in the trough, only the reflections in-plane and above the plane of the monolayer are recorded and those below the plane of the monolayer cannot be observed. Therefore, when a peak is located in-plane ($Q_z = 0$), only half of the peak is observed. The reciprocal disk represents the projection of the 2D reciprocal lattice onto the plane of the monolayer, capturing the in-plane scattering information. When the reciprocal disk orients parallel to the plane of the monolayer, there is no tilt, and all the alkyl chains are upright, and the six first-order peaks are in-plane and degenerate (Figure 2.9: Untilted).¹⁷³ When the molecules tilt (the reciprocal disk is not aligned in the plane of the monolayer), the degeneracy of peaks is disturbed, leading to the observation of out-of-plane peaks. The direction towards which the tilt occurs defines the peak patterns observed. With a tilt toward the nearest neighbor (NN), two degenerate

peaks are observed at nonzero values of Q_z (their mirror images below the surface) and two degenerate peaks remain at $Q_z=0$. In this case, the unit cell is distorted from hexagonal to a centered rectangular unit cell (Figure 2.9. NN tilt). The tilt toward the next nearest neighbor (NNN) also leads to the centered rectangular unit cell. However, all the peaks are moved out of plane with one doubly-degenerate and one nondegenerate peak (again, the mirror images of these three peaks are below the water surface) (Figure 2.9. NNN tilt). Lastly, if the tilt is toward somewhere between NN and NNN, three nondegenerate out-of-plane peaks above the water surface are observed with an oblique unit cell (Figure 2.9. Intermediate tilt).

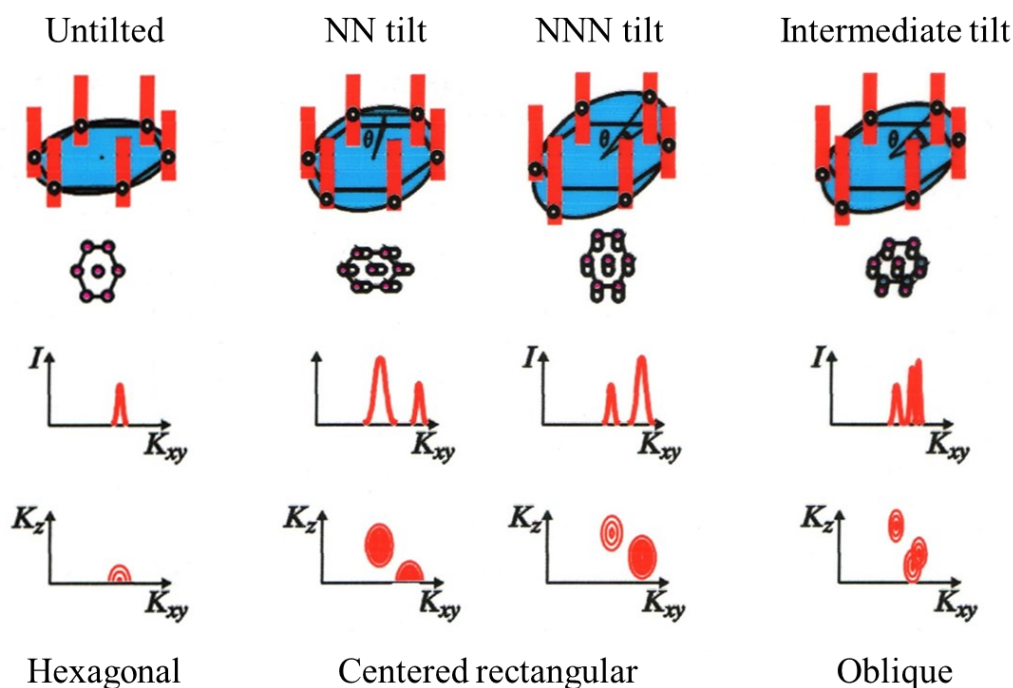


Figure 2.9 Schematic representing the reciprocal disk, a top-down view of the chain lattice showing the chain tilt direction, and characteristic diffraction patterns (intensity integrated across Q_z and 2D contour plot) for the Langmuir monolayers at air-water interface (image is modified from Kaganer et al.).¹⁷³

By defining the number and position of the peaks and respecting the selections rules defined for the fitting process, the information about the orientation of chains and unit cell parameters will be calculated.

The d-spacing is calculated using

$$d = \frac{2\pi}{Q_{xy}} \quad \text{Equation 2.8}$$

And with Scherrer formula^{173,176} and the full width at half maximum (fwhm) in both Q_{xy} (Lorentzian function) and Q_z (Gaussian function) direction, the lateral correlation length and vertical scattering length is measured:

$$\text{Lateral correlation length} \approx \frac{2}{FWHM} \quad \text{Equation 2.9}$$

$$\text{Vertical scattering length} \approx 0.9 \left[\frac{2\pi}{FWHM} \right] \quad \text{Equation 2.10}$$

As discussed by Kaganer et al., due to the lack of consensus on using these two equations and the discrepancy between them, different research groups may report characteristic lengths that differ by a factor of 3 for similar packing systems.¹⁷³ The lateral correlation length defines the length over which the crystalline packing is formed and can be different for different peaks. However, the vertical scattering length defines the thickness of this packing in z-direction and only one value is obtained for peaks originating from the same packing. For the majority of surfactants, as the headgroup interacts with water and may still freely rotate, the alkyl chains dominate the packing. Therefore, the calculated vertical scattering length must be compared to the extended alkyl chain length (maximum thickness possible).

2.5.2. Specular X-ray reflectivity

The other synchrotron-based X-ray scattering technique is specular X-ray reflectivity (XRR), and it provides information about the electron density of the monolayer film at air-water interface in a z-direction.¹⁷⁵ Upon directing the incident beam and its reflection to the detector, the intensity of the reflected beam normalized by the intensity of the incident beam is collected as a function of Q_z :

$$Q_z = 2k_0 \sin \alpha_i \quad \text{Equation 2.11}$$

Where Q_z is the vertical scattering vector, k_0 is the wave vector, and α_i is the incident angle.

This recorded normalized intensity will be further used to study the electron density $\rho(z)$ of the monolayer along its vertical structure at the air-water interface, averaged across the X-ray

footprint. This reflectivity data $R(Q_z)$ is normalized to the Fresnel reflectivity (R/R_F). The Fresnel reflectivity, $R_F(Q_z)$ is for when X-ray is reflected from an ideally flat air-water interface.

By fitting the scattering data obtained with Parratt method, the electron density profile of the monolayer is generated. In this method, a box model is considered to represent the continuous change in the electron density profile (Figure 2.10a). Each box is assigned with thickness and electron density based on the surfactant structure.¹⁷⁷ The thickness and electron density are adjusted through the fitting process to better represent the vertical structure of the thin film (Figure 2.10b). For greater detail, the reader is referred to Bu et al.¹⁷⁸

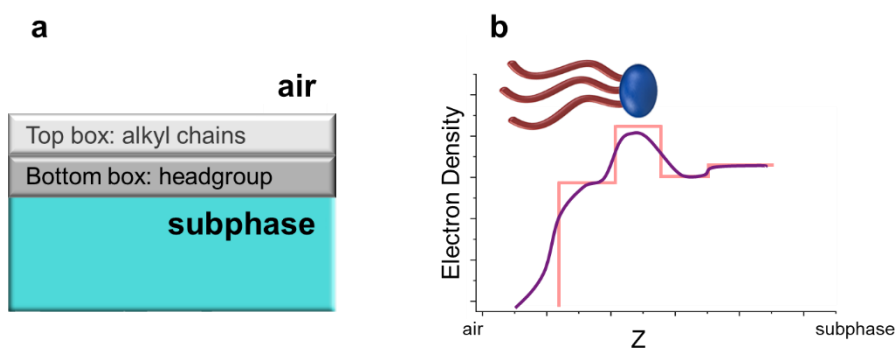


Figure 2.10 The layers (boxes) defined in Parratt method in addition to air and subphase: alkyl chains (top box) and headgroup (bottom box) (a), and representative model fit for the electron density profile for two-box model.

Chapter 3. Tuning Electrostatics to Promote Ordered Monolayers of Phosphole-Lipids

Zahra Alinia, Dandan Miao, Thomas Baumgartner, Christine E. DeWolf.

Published in *ACS Langmuir* (DOI: 10.1021/acs.langmuir.4c02962)

Supplementary information is provided in Appendix A.

3.1. Abstract

Heteroatom-doped π -conjugated systems have been exploited for electronic device applications. Phosphole-containing backbones are particularly intriguing with regard to electron delocalization and ultimately control over the photophysical, redox, and charge transfer characteristics. However, practical application of these materials commonly relies on well-structured, thin film architectures. Self-assembly offers a route to generate ordered 2D structures deposited on solid substrates. The orientation of these deposited films can be manipulated by the introduction of alkyl chains of varying length (to form phosphole-based lipids), and chemical modification of the phosphole-derived headgroup. External controls can also be considered to tune these films' properties; e.g., the electrostatic interactions within the film can be controlled by varying the environment with the addition of simple salt counterions. A series of lipids with phosphole-based π -conjugated headgroups have been designed and exhibit intramolecular conformational changes in response to external conditions. Herein the 2D film structure in Langmuir and Langmuir-Blodgett films is reported in the presence and absence of halide salts. The film morphology obtained from Brewster angle and atomic force microscopy shows the formation of a condensed phase but also 3D aggregates, and grazing incidence X-ray diffraction confirmed the presence of untilted, hexagonally packed chains. The size of the counterion influences its ability to intercalate between the phosphole headgroups, which ultimately provides a means to induce the formation of a well-ordered, single monolayer film without aggregates that can be transferred to the solid substrate.

3.2. Introduction

Heteroatom-doped π -conjugated systems have been reported as building blocks of various electronic and optoelectronic devices due to their electronic nature. HOMO-LUMO levels, effective conjugation length, electron-richness or -deficiency, and polarizability are among the key properties of these building blocks that can be controlled and finely tuned to obtain the high-performance materials with optimal features.^{3,12,179,180} These systems can include building blocks as small as thiophene in poly(3-hexylthiophene) commonly known as P3HT, up to macrocycles such as phthalocyanine, and have a wide range of applications from drug delivery and photodynamic therapy to electrochemical transistors,¹² thermoelectric devices,¹⁸¹ and lasers.¹³

Depending on their application, different techniques are used to deposit these materials. Physical vapor deposition is used to obtain organic semiconductors used in organic light-emitting diodes (OLEDs) and photovoltaic cells with high film density and controlled thickness and pattern.^{12,83,84} By contrast, solution deposition^{86,90} is mainly considered to control the morphology, whether for small areas with spin coating,^{182–185} or other coating techniques for larger areas. To obtain high-density films on large areas, spray coating is exploited.¹⁸⁶ And the low-cost thermal evaporation deposition is the choice to deposit OLEDs or organic solar cells on a large scale.⁸⁵

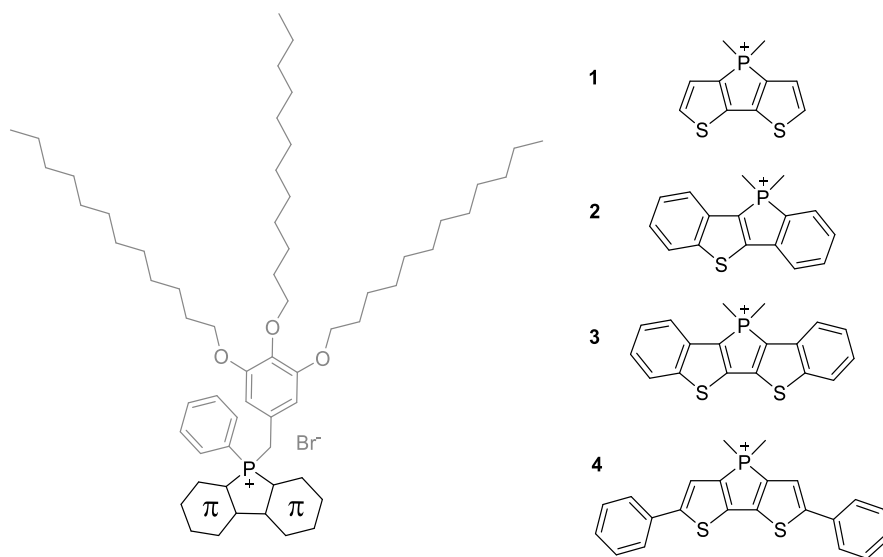
Although the Langmuir Blodgett deposition (LB) technique may have not been commonly used on a large scale, it nonetheless provides application-oriented control of the thin film thickness and morphology,^{74,187} and has received attention in areas like information storage or optical-related devices.^{78,109,110} This technique can be considered as a proper strategy for deposition of nontypical amphiphiles with application in sensors (flexible, wearable, or bio sensors)¹⁰⁴ or optoelectronic devices including photoresponsive soft materials.^{78,187,188} With LB, nanomaterials can be transferred on nonreactive substrates to obtain much thinner films compared to more conventional techniques while retaining the performance needed for battery applications.^{78,189} The LB technique can also be further modified for optimal transfer through incorporation of ions in the subphase (facilitating an ionic bridge between amphiphile polar heads and the solid support), and/or moderating the upstroke speed, temperature and pressure.^{104,190}

Phospholes have excellent features among heteroatom-doped aromatic rings, due to the pyramidal geometry around the phosphorus center leading to only weak aromaticity for the system, as well

as pronounced electron-acceptor features, that are distinctly different from those of their N-analogues.^{3,35,191} Their implementation also respects green chemistry with efficient and sustainable synthetic routes.¹⁹² With increased material density, electrochemical stability, electron-acceptor activity, and other photophysical properties, phospholes are considered an important building blocks of functional materials in supercapacitors and batteries, phosphorescent, pharmaceutical, or biomedical materials.^{179,180,193–195} When combined with alkyl chains, these surfactants, termed phosphole-lipids, can self-assemble to form organized structures and expand their unique properties that leads to variety of potential applications in material science, biomedical research, and surface modifications.^{196–198}

A series of phosphole-lipids with different conjugated scaffolds in the phosphole backbone have been reported by the Baumgartner group that combine variation of the electronic character of the headgroup with the cationic P-center, as well as three alkyl chains for their amphiphilic character (Scheme 3.1).⁵⁴ The addition of alkyl chains leads to well-ordered liquid-crystalline structures and interdigitated structures. Among different existing intermolecular interactions, the ionic interactions were reported as the main driving force stabilizing the liquid-crystalline phase.⁵⁴ These phosphole-lipids show good applications for organic electronics due to their high order and stability. Phospholes have already been reported to have suitable functional photophysical properties.¹⁹⁹ The overall fluorescence of phosphole-lipids is a function of the phosphole backbone conjugation, the counterion present, or the physical state of the system (stronger in the solid state due to aggregation-induced enhanced emission). It is, moreover, switchable using mechanical and thermal stimuli.^{198,200} These phosphole-lipids have headgroups with potential for π - π interactions and a bulky hydrophobic region, and the contributions of each need to be understood. It has been shown with smaller, phenolic headgroups that strong π -interactions can lead to highly organized headgroups and directional growth.^{127,128} Most surfactants comprise one or two alkyl chains with relatively few reports of three-chain surfactants.^{119,151,201,202} For phosphocholines, increasing the number of chains to three, and thus increasing the hydrophobicity of the lipids, has been shown to lower surface tension²⁰³ and form well-ordered monolayers at air-water interface.²⁰⁴ Lipids with three alkyl chains can also build micelles at lower concentrations and vesicles with greater stability.^{205,206} The higher number of alkyl chains may also increase the aggregation ability and affect the size and shape of domains formed.^{119,207}

Of the phosphole-lipids shown in Scheme 3.1, **1** has been shown to form highly ordered, lamellar liquid-crystalline structures.⁵⁴ It may be possible to replicate these ordered arrays in a two-dimensional single monolayer film produced via LB deposition. Herein, we characterize the phase monolayer behavior of this phosphole-lipid at both the air-water and air-solid interfaces.



Scheme 3.1 Chemical structure of previously reported phosphole-lipids.⁵⁴

3.3. Materials and Methods

3.3.1. Solution and subphases

4-Phenyl-4-(3,4,5-tris(dodecyloxy)benzyl)-4H-phospholo[3,2-*b*:4,5-*b'*]dithiophen-4-ium bromide (compound **1** in Scheme 3.1) was synthesized as previously reported⁵⁴ and will be referred to as phosphole-lipid for simplicity. Spreading solutions (0.6 - 1.1 mM) were prepared in chloroform (Certified ACS, approximately 0.75% ethanol as preservative) purchased from Fisher Scientific Company. For all subphases, ultrapure water with resistivity of 18.2 M Ω cm⁻¹ (pH 5.6 at 25 °C) was obtained from a Milli-Q HX 7080 water purification system (HC). For salt solutions as the subphase, NaBr (ACS reagent, \geq 99.0%), NaCl (ACS reagent, \geq 99.0%), and NaI (ACS reagent, \geq 99.5%) were purchased from Sigma-Aldrich and concentrations from \sim 1 μ M (10:1 molar ratio of counterion to lipid molecules) to 100 mM were prepared in ultrapure water.

3.3.2. Surface pressure-molecular area isotherm

The phosphole-lipid was spread by a 50 μL Hamilton syringe on ultrapure water/salt solutions as subphase in Langmuir film balance (from Nima Technology Ltd., Coventry, U.K.), with dimension of 7 cm by 42 cm, at room temperature (21.5 - 22.5 $^{\circ}\text{C}$). Ten minutes was allowed for complete solvent evaporation and relaxation of the surfactant for all the experiments. The monolayer was then compressed symmetrically at a compression rate of 5 - 10 $\text{cm}^2 \text{min}^{-1}$ (2.5 - 5.5 \AA^2 (molecule min^{-1}) - depending on the initial molecular area). Surface pressures were obtained and recorded by a filter paper (1 cm \times 2 cm, Whatman No. 1 chromatography paper) based Wilhelmy balance. To ensure reproducibility, at least three separate isotherms were obtained for all experiments from freshly prepared spreading solutions.

3.3.3. Brewster angle microscopy imaging (BAM)

An I-Elli2000 imaging ellipsometer (Nanofilm Technologies GmbH, Göttingen, Germany) equipped with a 50 mW Nd:YAG laser ($\lambda = 532 \text{ nm}$) was used to perform Brewster angle microscopy. The magnification was set at 20 \times with a lateral resolution of 1 μm . All images are obtained at an incident angle of 53.15 $^{\circ}$ (Brewster angle of water) with the laser output of 50% (analyzer, compensator, and polarizer set to 0 $^{\circ}$). Three separate BAM imaging experiments were performed for all of the systems.

3.3.4. Ellipsometry measurements

Measurement of the ellipsometric angle of ψ and Δ was performed by I-Elli2000 imaging ellipsometer. All ellipsometry measurements were obtained using a 20 \times magnification, incident angle of 50 $^{\circ}$, and laser output of 100%, while the compensator angle was set to 20 $^{\circ}$. Each measured value reported in the ellipsometric isotherm represents the average of 10 measurements of the same monolayer film at a constant surface pressure.

The initial angle of the analyzer and polarizer was set to 14 $^{\circ}$ and 20 $^{\circ}$, respectively, and later adjusted to have the reflection of the polarized beam eliminated. $\delta\Delta$ values ($\delta\Delta = \Delta_{\text{film}} - \Delta_{\text{subphase}}$) are reported in ellipsometric isotherms, representing how the ellipsometric angle Δ of the film is changing through the isotherm, relative to the ellipsometric angle Δ of the subphase alone. Film

thickness and refractive index are two separate monolayer film characteristics that have impact on $\delta\Delta$. Taking into account the film's relatively constant refractive index at the air-water interface, $\delta\Delta$ is taken to represent the change in the monolayer thickness upon compression.

3.3.5. Atomic force microscopy imaging (AFM)

For AFM sample deposition, Mica sheets V1 quality were purchased from Electron Microscopy Science and freshly cleaved before usage. Monolayers were transferred on mica on the upstroke at constant pressures by the Langmuir-Blodgett technique and dipping rate of 1 mm min^{-1} . With this technique, the transfer ratios (ratio of the monolayer surface area loss over the substrate surface area during deposition) were calculated. The AFM samples were kept for 30 minutes in ambient conditions to dry, and all imaging was performed in a 24-hour window. A Bruker multimode 8HR scanning probe microscope (Nanoscope 9.7, Digital Instruments, Santa Barbara, CA) was used to capture AFM images at the air-solid interface at room temperature. Peak-force tapping mode was used at a scan rate of 0.3-1 Hz with SCANASYST-AIR probes (silicon nitride cantilever, frequency 70 kHz, nominal spring constant 0.4 N m^{-1} , and tip radius 2 nm). Nanoscope software version 2.0 was used to perform all AFM image processing and analysis.

3.3.6. Grazing incidence X-ray diffraction (GIXD) and X-ray reflectivity (XRR)

All GIXD and XRR measurements at the air-water interface were carried out at 15-ID-C ChemMatCARS at the Advanced Photon Source (APS) in Argonne National Laboratory, with monochromatic X-rays and energy of 10 keV. A NIMA Langmuir trough with 340 cm^2 area with compression rate of the mobile barriers set at $2 - 5 \text{ cm}^2 \text{ min}^{-1}$ ($1 - 3 \text{ \AA}^2 (\text{molecule min})^{-1}$) was placed in the beam path in an airtight enclosure with Kapton windows which allowed for purging the atmosphere with helium. Raw data was extracted and processed using software developed by Wei Bu, beamline scientist at ChemMatCARS.

The following parameters were used for GIXD measurements:

X-ray beam wavelength: 1.239 \AA , incidence angle: 0.0906° , horizontal size: 20 mm, vertical size 120 mm, and beam footprint: 20 mm by 7.6 cm. The two-dimensional Swiss Light source PILATUS 100K set to single photon counting mode was used as a detector. To minimize intense

low-angle scattering, two sets of slits were used: one was placed in front of the detector (to control the beam footprint), and the other was located 280.0 mm from the sample. The GIXD data measured were plotted as contour plots of the intensity as a function of the horizontal (Q_{xy}) and the vertical (Q_z) scattering vector components. The lattice spacing d_{hk} was obtained from the in-plane diffraction data as $d_{hk} = 2\pi/q_{xy}^{hk}$, where the Miller indices h and k were used to index the Bragg peaks needed to calculate the unit cell parameters for the in-plane lattice.^{173,208} The Bragg rods and peaks were fitted with Gaussian and Lorentzian functions, respectively, using Origin lab graphing and analysis software. The full width at half-maximum values obtained from the corrected Bragg peaks and rods were used to obtain the in-plane correlation length and vertical scattering length through the Scherrer formula^{173,176}:

$$\text{Lateral correlation length} \approx \frac{2}{FWHM} \quad \text{Equation 3.1}$$

$$\text{Vertical scattering length} \approx 0.9 \left(\frac{2\pi}{FWHM} \right) \quad \text{Equation 3.2}$$

For XRR measurements, the X-ray intensity signal is collected as a function of vertical scattering component (Q_z) and the $R(Q_z)$ is normalized to the Fresnel reflectivity (R/R_F) (calculated for a sharp air-water interface with an ideal flat, water surface). The fitting process (Parratt method) includes defining a box model in which there is a thickness and electron density assigned to each box, in order to represent the vertical structure of the film averaged across the X-ray beam footprint. The resultant reflectivity profile is compared to the measured reflectivity and a monolayer electron density profile in a vertical direction is generated.

3.4. Results and Discussion

The surface pressure-molecular area isotherm of the phosphole-lipid on ultrapure water as subphase, at room temperature, and compression rate of $5 \text{ cm}^2 \text{ min}^{-1}$ ($2.6 \text{ \AA}^2 \text{ (molecule min)}^{-1}$) is shown in Figure 3.1. The isotherm shows a pressure onset at $135 \text{ \AA}^2 \text{ molecule}^{-1}$. The isotherm also exhibits a phase transition plateau at a relatively high surface pressure of around 30 mN m^{-1} compared to most commonly studied double and triple chain phospholipids.^{119,209} This results from a combination of a much larger headgroup and an increased number of alkyl chains. Studies have shown that increasing the number of alkyl chains from two to three to four for the same

phosphatidylcholine headgroup leads to a shift of phase transition pressure to higher values.¹¹⁹ The presence of the bulky hydrophobic part dominates the monolayer packing. The large moiety of three chains can also affect the fluid phase compressibility.¹⁵¹ The length of this plateau indicates a large reduction in the molecular area (reducing by half from $\sim 80 \text{ \AA}^2 \text{ molecule}^{-1}$ to less than $40 \text{ \AA}^2 \text{ molecule}^{-1}$). Such a large reduction has previously been attributed to the formation of multilayers.²¹⁰ Both the critical onset area and the plateau (surface pressure and length) are consistent with different compression rates and equilibration time (prior to compression) indicating the lack of kinetic effects on the isotherm (**Error! Reference source not found.**). A second transition is observed at $\sim 40 \text{ mN m}^{-1}$ which is impacted by the compression rate and equilibration time. The nature of this transition will be discussed later.

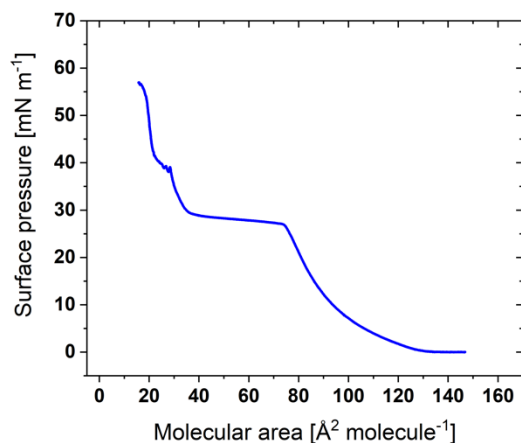


Figure 3.1 Surface pressure-molecular area isotherm of phosphole-lipid (molecule 1 of Scheme 3.1) on ultrapure water as a subphase, obtained at room temperature and compression rate of $5 \text{ cm}^2 \text{ min}^{-1}$.

Repeated compression-expansion cycles without any relaxation time between them are shown in Figure 3.2. These cycles are obtained for surface pressures up to 25 mN m^{-1} (before the main plateau, Figure 3.2a) and for the full isotherm range (Figure 3.2b). These cycles show that the isotherm is completely reversible up to the plateau. When compressed past the plateau, the onset area for each cycle is shifted to smaller values. This can be explained either by an irreversible film loss through the isotherm cycles or a slower and/or incomplete relaxation back to the 0 mN m^{-1} during the decompression.

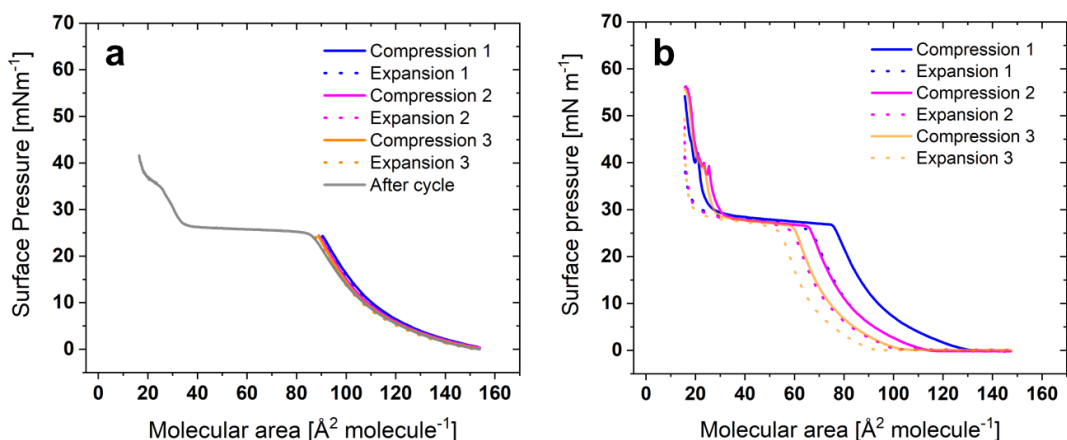


Figure 3.2 Repeated isotherm cycles for phosphole-lipid on ultrapure water as subphase without any waiting time after each cycle: (a) compression only up to surface pressure of 25 mN m⁻¹ (below the plateau) and (b) full isotherm cycle.

When the same compression-expansion cycle was performed with a 60-minute relaxation time between cycles, the shift of the onset area becomes smaller; i.e., compression 2 is shifted to slightly larger areas than expansion 1 (**Error! Reference source not found.**), confirming that a slow kinetic relaxation is responsible for the shift rather than an irreversible material loss. A study on triple-layer formation of a polymer surfactant with biphenyl mesogens showed similar cycle reversibility.²¹⁰

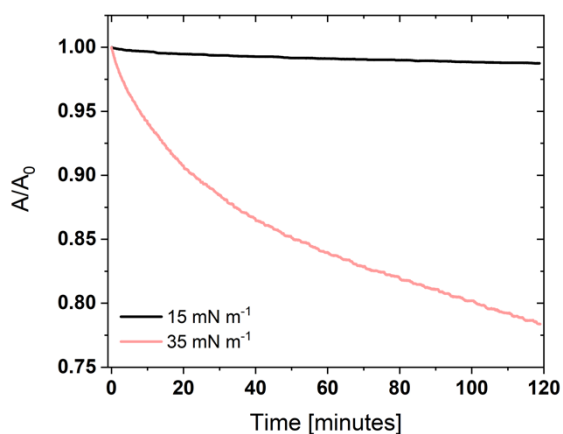


Figure 3.3 Normalized film area as a function of time for phosphole-lipid at constant surface pressures of 15 and 35 mN m⁻¹ (below and above the plateau).

This cycle reversibility is also exemplified through the area loss observed at constant surface pressure for two different surface pressures, namely before and after plateau. As shown in Figure 3.3, the monolayer film exhibits higher stability as a function of time below the plateau, but there is more than 10% area loss after 30 minutes at a constant surface pressure of 35 mN m⁻¹ (beyond the plateau). This area loss increases to about 15% after 60 minutes, indicative of film reorganization.

Figure 3.4 presents the effect of the subphase (water) temperature on the isotherm. Phospholipids usually show an increase in the plateau pressure and shortening of the plateau length with increasing temperature, due to the increased entropic component of the free energy, which results in the film remaining in the fluid phase up to higher surface pressures.^{153,209,211} For the phospholipid studied here, when the temperature increases from 22 to 28 °C, the phase transition is shifted to lower surface pressures, accompanied by an elongation of the phase transition plateau length. On the other hand, decreasing the temperature to 16 °C also results in a decrease in the plateau pressure but with a shortening of the plateau length. Thus, this suggests that the plateau is not associated with a simple liquid expanded (LE) - condensed (C) phase transition, and the possibility of a nonclassic (LE-C) and/or multiple overlapping phase transitions needs to be considered.

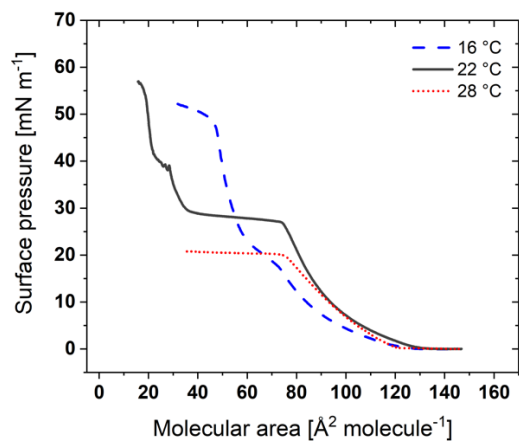


Figure 3.4 Surface pressure-molecular area isotherms of phosphole-lipid on an ultrapure water subphase as a function of the subphase temperature.

As ionic interactions were proposed to be the main driving force of lamellar structure formation in the liquid crystalline formed in bulk for this phosphole-lipid,⁵⁴ the intermolecular interactions

(electrostatic in particular) in the monolayer were evaluated. The phosphole-lipid has bromide as the counterion as synthesized; therefore, halide-containing subphases (NaCl, NaBr, and NaI) were studied. As bromide is already present as the counterion for the phosphole-lipid and has been shown to induce a lamellar structure in the bulk, the focus of this work is on bromide counterions.

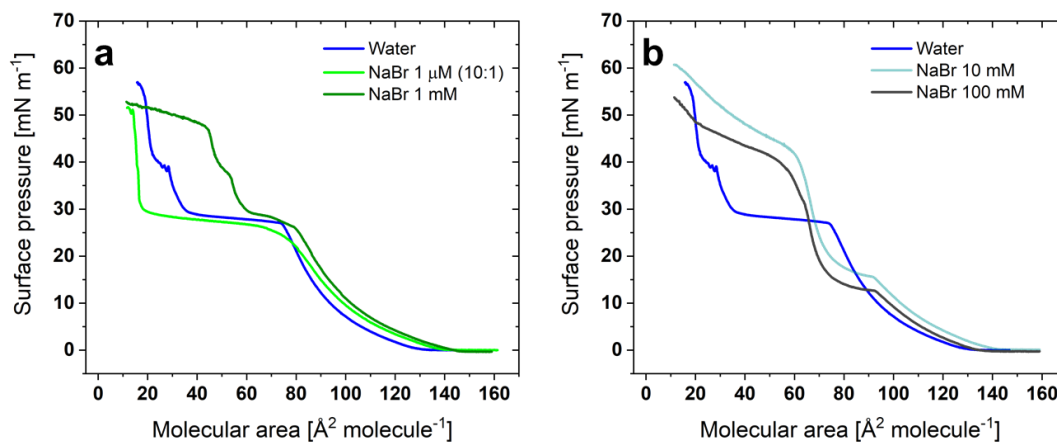


Figure 3.5 Surface pressure-molecular area isotherms of phosphole-lipid as a function of lower (a) and higher (b) NaBr concentration in the subphase.

The presence of salt can affect surface activities and bulk structures.^{212,213} Figure 3.5a shows that different concentrations of sodium bromide in the subphase lead to slightly larger pressure onset areas. The presence of counterions has been reported to expand the monolayer due to either insertion between the headgroups and, at high concentrations, increasing the electrostatic repulsion with adsorbed ions.^{122,214} In the case of condensed phases, such an expansion can transform the ordered phases into LE phase.^{213–215} It has been shown that ions of the Hofmeister series can have differential effects on the isotherm, and in particular the LE-C phase transition, of classical phospholipids; however, the film collapse was not affected, attributed to the ions being squeezed out of the monolayer before collapse.¹²² With the phosphole-lipid, the concentration of bromide noticeably alters the molecular area and surface pressure of the phase transition plateau and also affects how the monolayer collapses. At very low concentrations (1 μM NaBr, corresponding to a 10:1 molar ratio of bromide to the phosphole-lipid), the surface pressure at which the phase transition is occurring is not affected. However, it does lead to a larger area range for the plateau as it is elongated reaching smaller molecular areas. The minimum cross-sectional area for one

upright alkyl chain is 18.6 \AA^2 .¹⁷³ For both the water and 1 μM NaBr subphases, the phase transition plateau ends at molecular areas that are too small to accommodate the three alkyl chains in the plane of the monolayer. Therefore, the formation of multilayer or 3D aggregates must be taken into consideration. For example, for biphenyl mesogen polymer surfactants,²¹⁰ a plateau associated with the formation of a triple layer exhibited a relative area decrease to one third of the initial area at the start of the plateau. Additionally, the second transition has disappeared, which may be a consequence of the elongation of the main transition to very small molecular areas. Similarly, a 1 mM NaBr subphase has no impact on the surface pressure of the main or subsequent phase transitions. However, it alters the plateau length of the main phase transition, which occurs over a much shorter area range.

When higher concentrations of counterion are present in the subphase (10 and 100 mM, Figure 3.5b), the main phase transition is shifted to lower surface pressures and larger molecular areas. The plateau areas are more closely aligned with the area requirement for three chains. In order to better understand the nature of the two transitions, the film morphologies were studied by BAM (main transition) and AFM (both transitions).

BAM images to visualize the monolayer behavior at the air-subphase interface through the main phase transition plateau are shown in Figure 3.6. The pressures corresponding to the phase transition plateau are aligned vertically as the focus is on the monolayer film behavior change before and after this phase transition plateau. For water and lower concentrations of counterions present in the subphase (1 μM and 1 mM NaBr), there is no observation of condensed-phase domains formed across the plateau. Instead across the plateau, small, circular, very bright spots corresponding to aggregates begin to form. Compressing to lower molecular areas through the plateau leads to an increase in the number and brightness of these aggregates, with the latter corresponding to an increase in the aggregate height (and consequently film thickness). However, in the presence of higher concentrations of bromide (10 and 100 mM), no bright aggregates are observed and only a gradual increase on the film brightness after the phase transition is recorded.

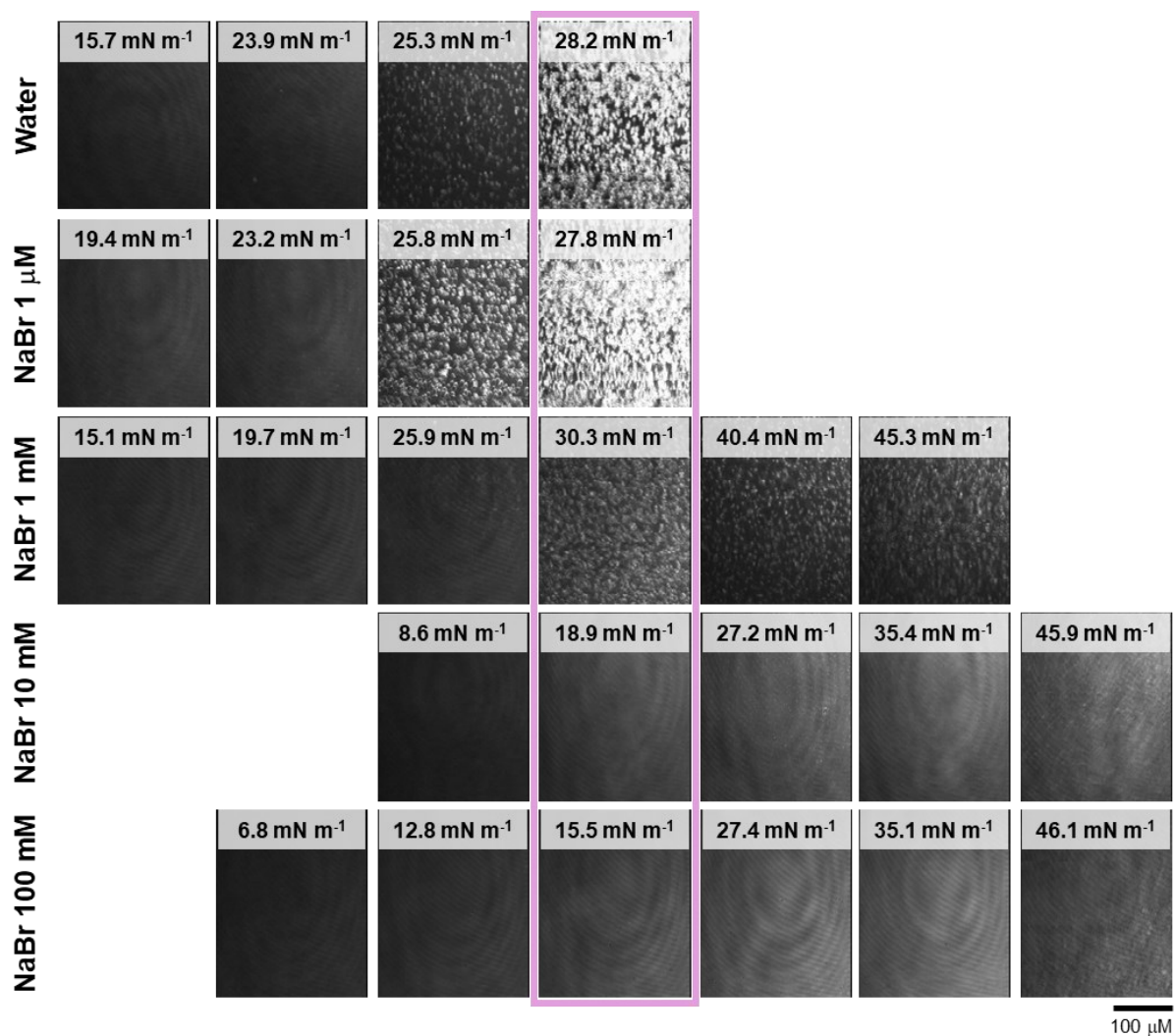


Figure 3.6 Representative BAM images of the phosphole-lipid on water and different subphase concentrations of NaBr. The images corresponding to the surface pressures of the main phase transition plateau are aligned vertically and framed (pink). For 10 mM NaBr and 100 mM NaBr, the laser intensity increased to 70%; all other images were captured at 50%. The relative brightness levels of the images reflect the numbers of aggregates in the field of view for the specific molecular area.

Both the solution and liquid-crystalline behavior for this phosphole-lipid show a propensity for π -stacking, which might be expected to generate a condensed phase. Other surfactants with the potential for π -interaction have shown large bright condensed-phase domains at the high molecular area, corresponding to the pressure of 0 mN m⁻¹, attributed to the strong intermolecular interactions between the headgroups, including π -stacking and charge-assisted hydrogen-bonding.^{127,128} The

phosphole-lipid's headgroup size and bulkier space requirement for the three alkyl chains could be responsible for the lack of condensed-phase domain observed by BAM. The larger hydrophobic volume may push the headgroups to large enough distances such that the distance-dependent headgroup interactions are not possible (or too weak) in the monolayer, where the interdigitation that enables lamellar phase to form in the bulk is precluded.

To determine whether condensed-phase domains form below the lateral resolution of the BAM, AFM imaging was employed. The AFM images obtained from deposition from water and different concentrations of NaBr are shown in Figure 3.7. For water as the subphase, a homogeneous film is observed for all surface pressures below the main phase transition. At the phase transition, circular 3D aggregates (bright spots) start to form and are randomly distributed throughout the sample.

After passing the main phase transition plateau, the AFM images show the coexistence of condensed-phase domains and 3D aggregates within the background matrix (Figure 3.7; water, 30 mN m^{-1}). The condensed-phase domains exhibit relatively circular shapes with rounded edges. The size and shape of domains are directly affected by the competition between the line tension and the electrostatic repulsion.¹¹⁹⁻¹²¹ When relatively high line tension exists at the domain boundary, like the ones for the phosphole-lipid on water, the domain-matrix interface is minimized, and circular-shaped domains are observed. It has been reported that going from double-chain to triple-chain systems for the same headgroup may lead to more circular-shaped domains, as the bulky hydrophobic chains are occupying more space compared to headgroup space per molecule.^{119,201} The domain and 3D-aggregate heights relative to the background matrix are on average 1.2 and 230 nm respectively (the maximum molecular length of the phosphole-lipid is about 2.5 nm). By further increasing the surface pressure, the condensed-phase domains increase in number while remaining circular, and eventually coalesce. The aggregates also increase in number but do not increase significantly in width. Beyond the second phase transition (40 mN m^{-1} and above), a second population of 3D aggregates is formed. These aggregates are much smaller ($0.3 \pm 0.1 \mu\text{m}$ compared to $1.9 \pm 0.2 \mu\text{m}$) and shorter ($13 \pm 7 \text{ nm}$ compared to $325 \pm 39 \text{ nm}$) than the previous ones already formed, and they are only observed on the domain-matrix interface, which may be the result of the excess free energy at the domain boundary.²¹⁶ Although the condensed-phase domains are approximately 1.8-2.6 μm in width (Figure 3.8b), which is at the limit of resolution

of the BAM, these may be obscured by the intensity of the extremely high aggregates that form concurrently. For all AFM samples obtained through and after the main phase transition for water, the transfer ratios are larger than one (**Error! Reference source not found.**), in agreement with the formation of multilayers or aggregates.

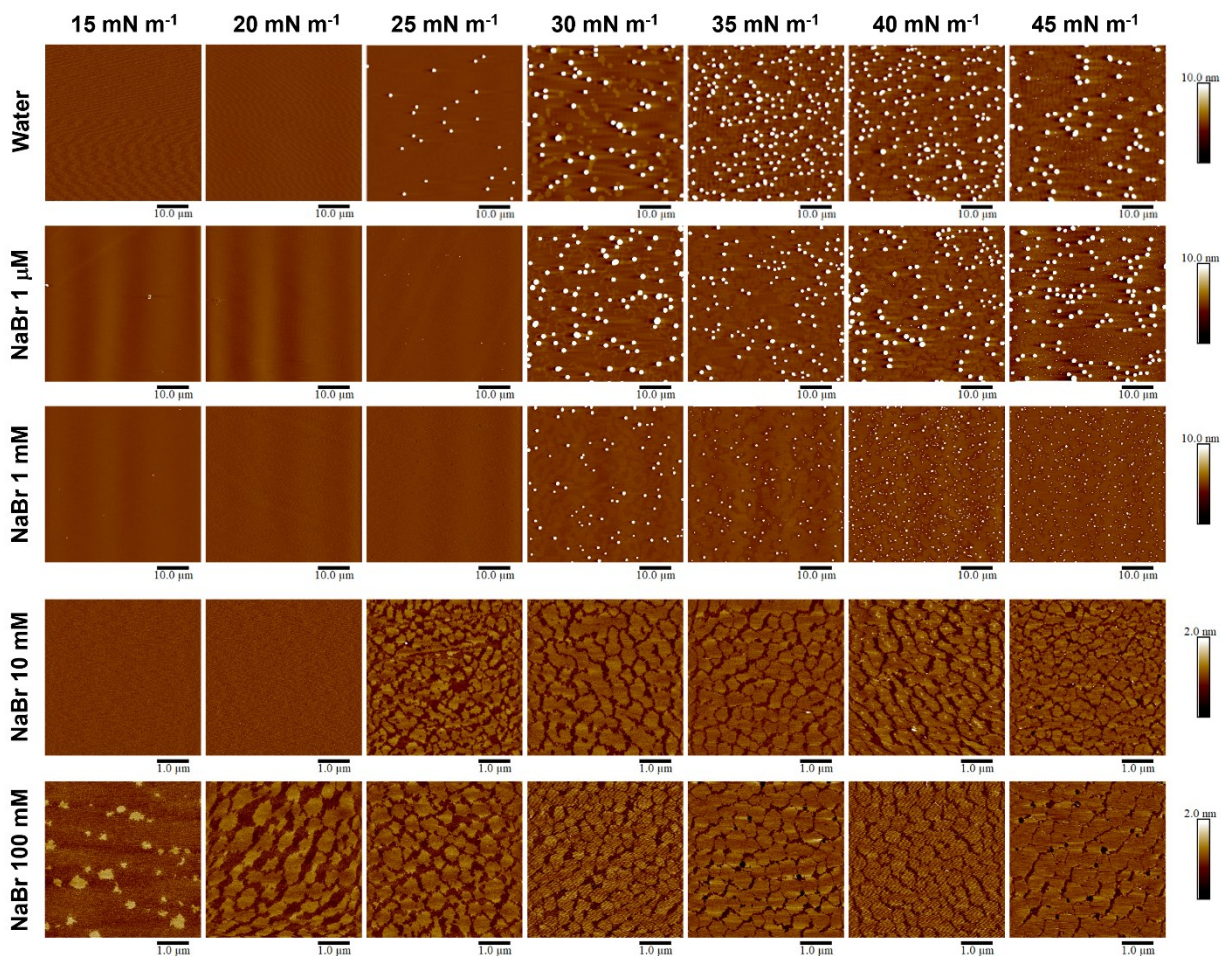


Figure 3.7 Representative AFM images of phosphole-lipid deposited onto mica by LB at different surface pressures from water and NaBr subphases (concentrations as indicated).

For lower concentrations of NaBr (Figure 3.7; second and third row), a similar trend in the formation of condensed-phase domains and 3D aggregates is observed. Focusing on the size of aggregates, it is clear that by introducing the counterion and increasing its concentration in the subphase, the width and height of the 3D aggregates decrease (**Error! Reference source not**

found.). Again, the transfer-ratio values at higher surface pressures agrees with the observation of 3D aggregates.

The AFM images for films transferred with higher concentrations of NaBr in the subphase are reported in smaller lateral and height scales compared to the previous ones (Figure 3.7, fourth and fifth row). The condensed-phase domain widths are noticeably decreased, and there is no record of 3D aggregates formation through or after the phase transition plateau. This change to smaller and less rounded domains that do not fully coalesce can be explained by the competition between line tension and electrostatic repulsion.^{119–121} With excess bromide, the electrostatic repulsion of the counterions dominates. The reduced line tension contribution favors smaller, nonrounded, and noncircular-shaped domains. Additionally, the domain height is reduced and becomes more consistent with a lower standard deviation (Figure 3.8a). Smaller transfer ratios for these subphases (before reaching the collapse area) agree with the absence of 3D aggregates (**Error! Reference source not found.**), as also observed by the BAM images. The isotherm plateau likewise exhibits larger and more realistic areas for a monolayer film. Thus, we postulate that presence of excess counterion in the subphase prevents the formation of the 3D materials and retains the phospholipid in the monolayer plane.

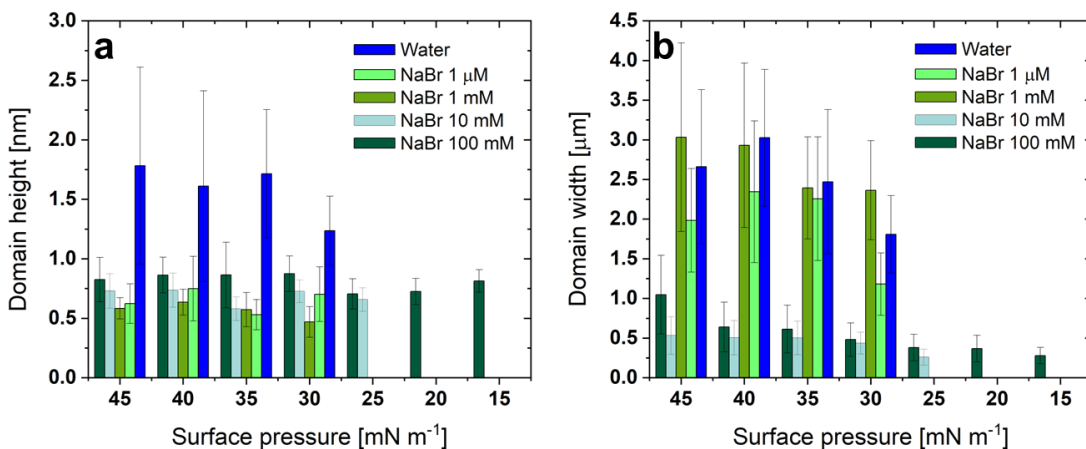


Figure 3.8 Phosphole-lipid domain heights (a) and widths (b) measured from AFM images as a function of the NaBr concentration in the subphase. At least three locations from each of two independently prepared samples were measured ($n > 300$ domains).

Ellipsometric measurements were performed on phosphole-lipid films at the air-subphase interface and are shown in Figure 3.9. The magnitude of change in the ellipsometric angle ($\delta\Delta$) normally represents changes in film thickness; however, differences in refractive index also contribute. Both water and the lowest concentration of NaBr present long plateaus, and we were unable to reach the end of the plateau in these experiments. There is an initial increase in magnitude for $\delta\Delta$ once the gaseous phase is passed, after which only a gradual increase in $\delta\Delta$ is observed. For 1 mM NaBr, the film initially exhibits the same trends and values but there is a small but distinct step change at 30 mN m^{-1} corresponding to the end of the main plateau (Figure 3.9a). A similar step change is observed for both of the higher concentrations of NaBr at their respective plateaus, and in the case of these films, the $\delta\Delta$ values after the plateau are slightly higher reflecting the greater coverage by the condensed-phase domains (Figure 3.9b). One might expect the $\delta\Delta$ value to be higher for the films with the aggregate formation. Given the films comprise multiple phases, the total $\delta\Delta$ reflects the combined contributions from each of these. Thus, the greater proportion of the lower background phase may decrease the impact of the presence of aggregates on $\delta\Delta$.

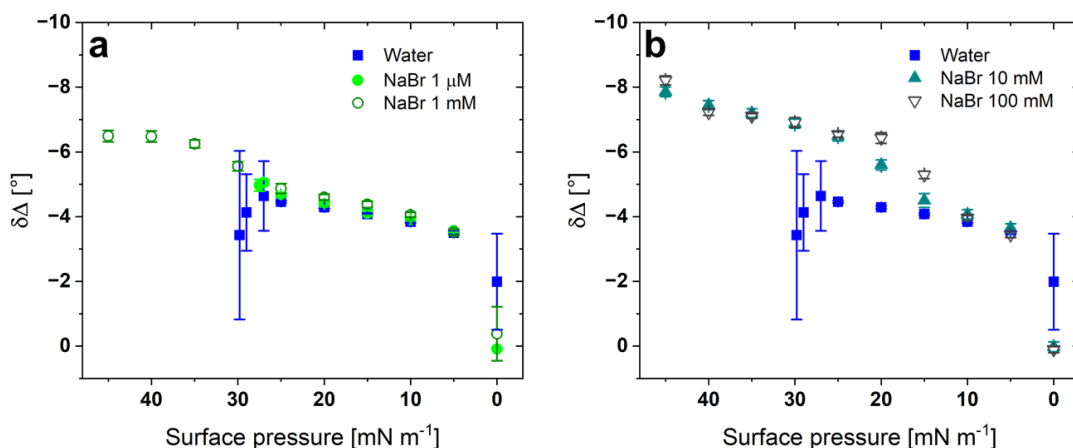


Figure 3.9 Ellipsometric measurements at the air-subphase interface as a function of lower (a) and higher (b) concentration of NaBr in the subphase.

Figure 3.10 shows the GIXD contour plot for the phosphole-lipid on 10 and 100 mM NaBr subphases and at different surface pressures. The first-order peaks were observed only for higher concentrations of NaBr and at pressures above the phase transition plateau (no diffraction peaks were observed at pressures below the plateau pressure, data not shown). Only one in-plane

diffraction peak is observed at a Q_{xy} value corresponding to an upright oriented alkyl chain packing with a hexagonal unit cell. For water and 1 mM NaBr, due to the shape of the isotherm, the highest surface pressure accessible was 26 mN m^{-1} (just before the end of the plateau), and no evidence of diffraction peaks were observed (**Error! Reference source not found.**), in agreement with the AFM imaging that showed that the domains only appear after the end of the plateau. The balance of the area requirements for chains and headgroups is well-known to determine the unit cell and chain tilt; for example, double chain phosphocholines are tilted due to the mismatch between the large headgroup and the chain cross-sectional areas and remain tilted throughout compression. However, adding a third chain leads to a transition from a tilted to an untilted, hexagonal phase at higher pressures. Adding a fourth alkyl chain leads to the direct formation at the plateau of untilted chains in a hexagonal unit cell.^{119,151} Herein we observe the direct phase transition from LE to the untilted condensed phase accompanied by the formation of 3D aggregates.

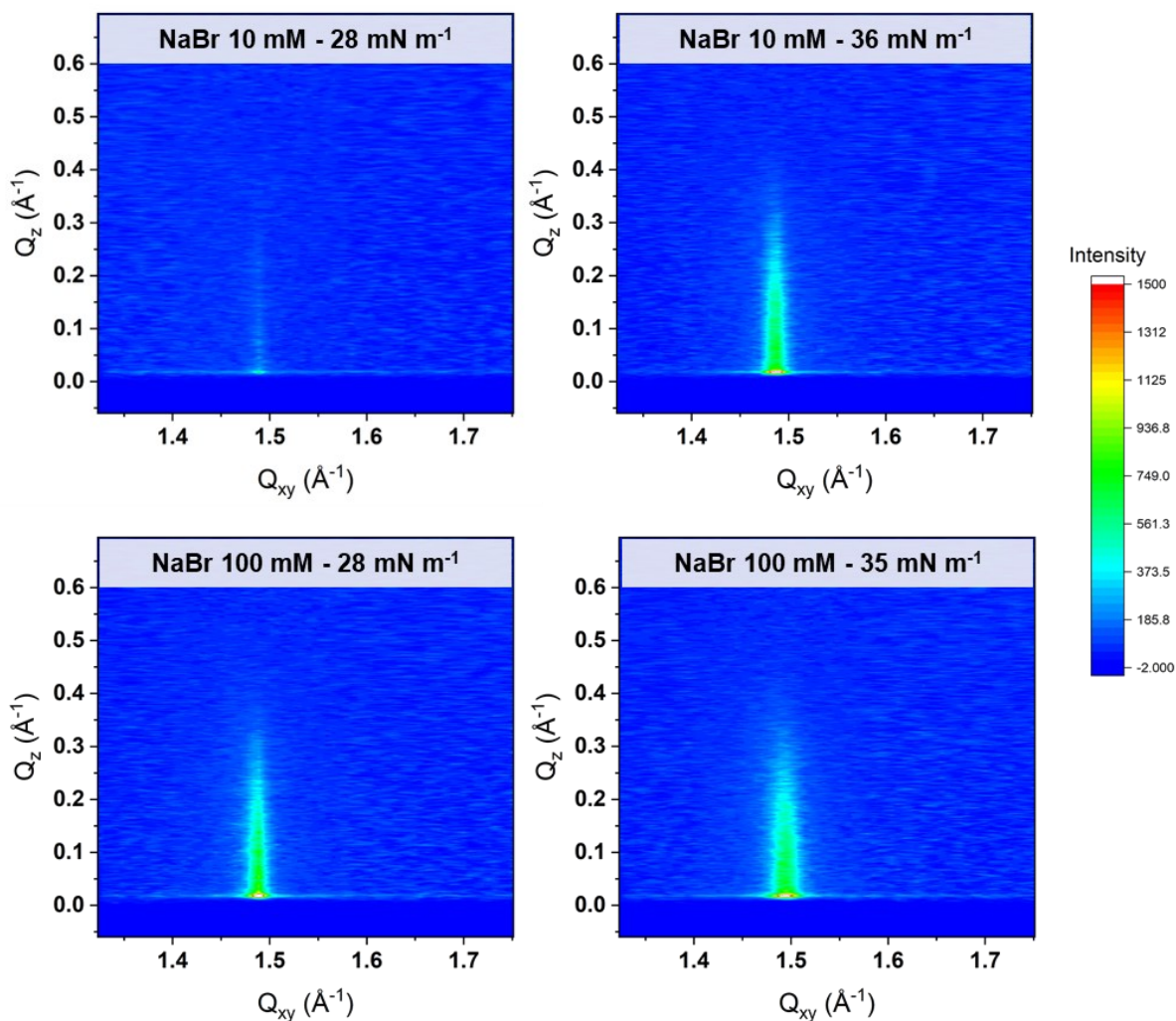


Figure 3.10 GIXD contour plot of X-ray diffraction intensity as a function of the Q_{xy} (in-plane) and Q_z (out-of-plane) vector components for the phosphole-lipid on 10 and 100 mM NaBr subphases.

Bragg peak and rod profiles with their corresponding fits are shown in Figures A5-A7 and peak positions and unit cell parameters are provided in **Error! Reference source not found..** For both of the higher NaBr concentrations, the full width at half-maximum (fwhm) of the peaks broadens as the surface pressure increases, indicating a loss of crystallinity. The peak at the lower surface pressure at 10 mM NaBr is distinctly weaker, attributed to the delayed onset of domain formation (higher surface pressure plateau); i.e., there is likely less condensed phase in the beam footprint. Additionally, as the surface pressure increases, the lateral correlation length decreases, suggesting that the domains initially form with optimal packing and that packing is perturbed as the film is

further compressed. This may also be correlated with the lack of full coalescence of the domains at higher surface pressures. By 45 mN m^{-1} (**Error! Reference source not found.**), the diffraction pattern for 100 mM NaBr shows a superposition of peaks associated with a monolayer and 3D ordered material, exemplified by the bending of peak along a Debye-Scherrer ring.^{127,217} Although no 3D aggregate was observed in AFM images at this surface pressure, this suggests that the film begins to collapse when held for extended periods at high surface pressures.

The calculated vertical scattering lengths are all smaller than the fully extended, 12-carbon alkyl chain length (1.54 nm). A lower length can be obtained when the alkyl chains are tilted, but in this case, a second out-of-plane peak would be generated, which is not observed. Given that all chains are untilted and in an upright packing, the full length of the chain is not participating in the crystalline packing. Two options can be considered: the molecules may stagger in z-placement relative to the plane of the interface, or due to their placement on the aromatic ring and the spatial restrictions imposed, the chains are only partially crystalline. Spatial constraints imposed by different linkages and position of branched chains have been reported to affect the diffraction, albeit the phase sequence rather than the vertical scattering length.¹⁵¹

The vertical structure of the film was probed by using X-ray reflectivity. All films were fit with a simple two-box model where the upper box corresponds to the chain regions and the lower box corresponds to the headgroups. An example of the fit to the X-ray reflectivity is provided in **Error! Reference source not found.** and the complete fitted parameters for all systems in **Error! Reference source not found.** As with the GIXD data, for water and the lowest concentration of NaBr, the end of the plateau could not be reached. Below the plateau, when only an LE phase is present, the films show a smaller thickness for the chain region than above the plateau where the film forms a condensed phase. The values for the latter are in good agreement with the vertical scattering lengths obtained from GIXD. As the condensed phase forms, the headgroup region also thickens which we attribute to a reorientation and staggering of the headgroups in response to the reduced area available. Such a conformational change was also reported for these lipids in solution as the concentration increased.⁵⁴

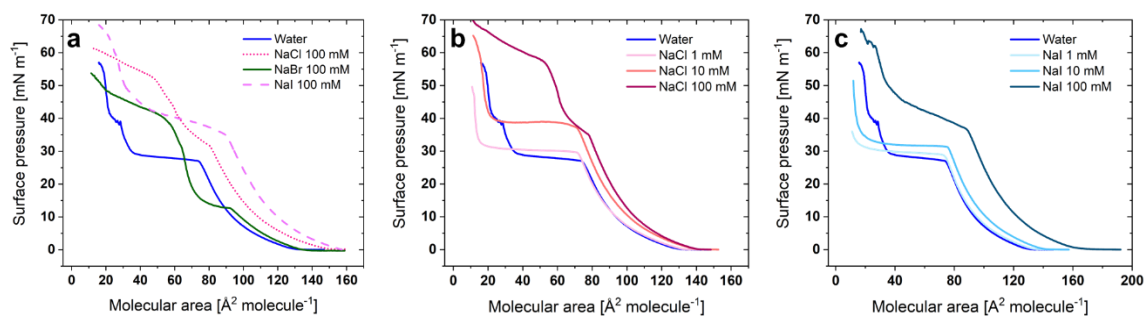


Figure 3.11 Surface pressure-molecular area isotherms of phosphole-lipid as a function of (a) halide concentration, (b) NaCl concentration, and (c) NaI concentration in the subphase.

As shown in Figure 3.11a, introducing other halide salts such as NaCl or NaI at the highest concentration of 100 mM does not have the same impact as NaBr, and it leads to a shift of the isotherm to higher molecular areas and an increase in the phase transition (plateau) surface pressure. The 100 mM NaCl shortens the molecular area range of the plateau, similar to NaBr 100 mM, while the 100 mM NaI does not alter the molecular area range, and only induces a shift to higher pressures.

For both halides, the 1 mM concentration has a slight effect, and significant effects are observed only after a threshold of 10 mM is reached, as is the case of NaBr. However, for this 10 mM concentration, although the shape of the isotherms is similar, NaCl has a greater impact resulting in a higher plateau surface pressure (Figure 3.11b,c).

The presence of the 3D aggregates in BAM imaging did not allow us to compare the formation of condensed-phase domains. Therefore, for NaCl and NaI, only the AFM images are reported here (Figure 3.12). For these two salts, and at each concentration, two surface pressures, corresponding to pressures below and above the phase transition plateau, are shown. 10 mM NaCl has a similar impact as low concentrations of NaBr: the 3D aggregates begin to appear right before the plateau, and there is a coexistence of condensed-phase domains and 3D aggregates at 45 mN m^{-1} , the latter distributed randomly across the image. However, for 100 mM NaCl and above the plateau (45 mN m^{-1}), the large 3D aggregates disappeared, and the image exhibits mainly a condensed phase with much smaller aggregates that only appear on the liquid expanded background. Unlike the domains formed in the presence of 100 mM NaBr, the lateral size of the domains formed with NaCl are similar to those formed on water; i.e., they maintain their larger size. For 10 mM NaI, although the

AFM image obtained at 30 mN m^{-1} shows the nucleation of condensed-phase domains, only 3D aggregates are observed above the plateau. At the higher concentration of 100 mM NaI , the only observation is the presence of 3D aggregates at both surface pressures below and above the phase transition plateau. The lack of condensed phase is in agreement with disruption of phospholipid condensed phases at high NaI concentrations, which has been attributed to adsorbed ions that affect the headgroup conformation and/or hydration.²¹⁴ At 1 mM , there is no significant difference in morphology with any of the halide salts (data not shown).

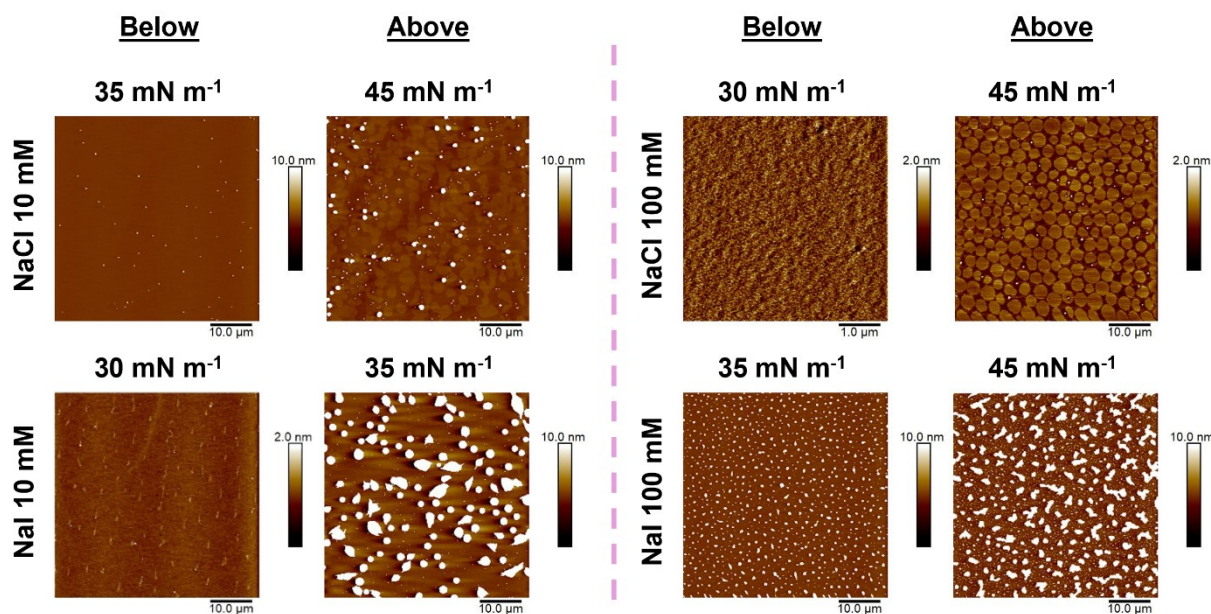


Figure 3.12 AFM images of phosphole-lipid deposited onto mica by LB at two different surface pressures corresponding to below and above the phase transition plateau, for NaCl (top row) and NaI (bottom row), from two different subphase salt concentrations, 10 mM (left) and 100 mM (right) in the subphase.

The X-ray intensity contour plot for the phosphole-lipid on a 100 mM NaCl subphase at 42 mN m^{-1} shows a single in-plane peak, corresponding to untilted carbon chains with a hexagonal unit cell (**Error! Reference source not found.**, unit cell parameters in **Error! Reference source not found.**). Again, the calculated vertical scattering length is smaller than the fully extended 12-carbon alkyl chain length, which has been discussed already. No diffraction peaks were observed for the phosphole-lipid on 100 mM NaI in agreement with the AFM imaging that shows a lack of condensed phase (data not shown). Fits for the X-ray reflectivity are given in **Error! Reference**

source not found. The halide anions are expected to be embedded in the headgroup region. The bromide anion gives the highest electron densities in the headgroup region, both below and above the plateau, which corresponds to the closer packing (smaller molecular areas) and the higher electron density of bromide compared to water. The lack of an increase in electron density of the headgroup region in the presence of iodide suggests that it does not reside between the headgroups.

One can expect ions to have differential effects on the monolayers as a function of the Hofmeister series, their size and their hydration shells, among others.^{122,218} For halide counterions, higher concentrations have been shown to stabilize the LE phase and thus shift the surface pressure higher for a given molecular area.²¹⁴ A key difference among these three anions (Cl⁻, Br⁻ and I⁻) is their ionic size. Comparing chloride and bromide, for chloride, the smallest of the three anions, a higher concentration in the subphase is needed to induce the retention of the phosphole-lipid in the plane of the monolayer. Both chloride and bromide are capable of fitting within the headgroup region and introducing favorable electrostatic interactions and both yield similar molecular arrangements, as evidenced by GIXD. On the other hand, iodide, the largest anion used, appears too large for the space available. Thus, as the film is compressed and intermolecular space restricted, the iodide is squeezed out from between the headgroup (although it can remain as an adsorbed ion), as was reported for phospholipids,¹²² allowing the aggregates to form. Shapovalov et al. showed deviations from the Gouy-Chapman model of the electrical double layer as a function of the film packing density and counterion size. Specifically smaller counterions that can penetrate into high charge density monolayers exhibit a preferential interaction without chemical specificity.²¹⁹ We can conclude that bromide has the optimal size for both the space constraints in the film and for maximizing the electrostatic interactions.

3.5. Conclusions

Combining a conjugated phosphole functionality with self-assembly in the form of a phosphole-lipid opens avenues for generating organized structures with tailored properties. Herein, the interfacial characterization showed that such phosphole-lipid can form well-ordered 2D films. These 2D films exhibit a plateau in the isotherms that does not correspond to a classical phase transition associated with a two-phase coexistence between a liquid-expanded and condensed phase, where the proportions of each phase vary along the plateau. Here, the condensed phase of

the phosphole-lipid forms only at the end of the plateau and is often coincidental with the formation of 3D aggregates. The addition of ions to the subphase offers the means to control the nature of the formed phases and the phosphole-lipid 2D film structure. However, the halide ion space requirement is a defining criterion that impacts the phosphole-lipid thin-film orientation. This space selectivity was confirmed by the ability of bromide to prevent the formation of 3D aggregates and to induce the formation of highly ordered monolayers of the phosphole-lipid. To achieve the same film structure, a higher concentration of chloride is required. On the other hand, iodide appears to be squeezed out from the headgroup layer through the compression and thus cannot remain intercalated between the headgroups at the surface pressures needed to form a condensed phase. Returning to the surface pressure-molecular area isotherms and the formation of 3D aggregates, the presence of an intercalated counterion can separate the simultaneous formation of the condensed phase and 3D aggregates through the plateau by postponing the latter to higher surface pressures. Therefore, it can be expected that any other external modification that shifts the two-phase transitions apart can lead to a formation of well-defined structured monolayers. This is essential for deposition of well-defined layers and the building of hierarchical structures required for electronic device applications.

Chapter 4. Self-Assembly of Phosphole-Lipids in 2D Films: The Influence of π -Interactions and Steric Constraints

Zahra Alinia, Dandan Miao, Thomas Baumgartner, Christine E. DeWolf.

Published in *RSC Applied Interfaces* (DOI: 10.1039/D4LF00361F)

Supplementary information is provided in Appendix B.

4.1. Abstract

Promising photophysical properties of π -conjugated phosphole-based materials make them appealing building blocks for electronic and optoelectronic devices. In practical terms, a well-ordered 2D film organization is required that can be obtained by deposition and/or self-assembly of thin films on a solid substrate. Manipulation of the existing noncovalent interactions within the films, via altering the chemical structure or environmental conditions to modify the molecular arrangements is one approach to control the electronic properties of these thin films. The inter- and intramolecular π - π interactions influencing the 2D film structure in Langmuir and Langmuir-Blodgett films of a series of lipids with phosphole-based, π -conjugated headgroups is explored in the presence and absence of aromatic additives. Brewster angle and atomic force microscopy demonstrated the simultaneous formation of 3D aggregates and a condensed phase. GIXD measurements confirmed that the 3D material formation should be hindered to promote the formation of an ordered 2D film. Different approaches were considered to manipulate the π - π interactions in the film: addition of small-molecule aromatics, mixtures of phosphole-lipids with phenolic surfactants, as well as conjugation extension of phosphole-lipid headgroup. Such π - π interactions can modify the directional growth of domains within 2D films, however, it is not strong enough to completely eliminate the 3D aggregate formation.

4.2. Introduction

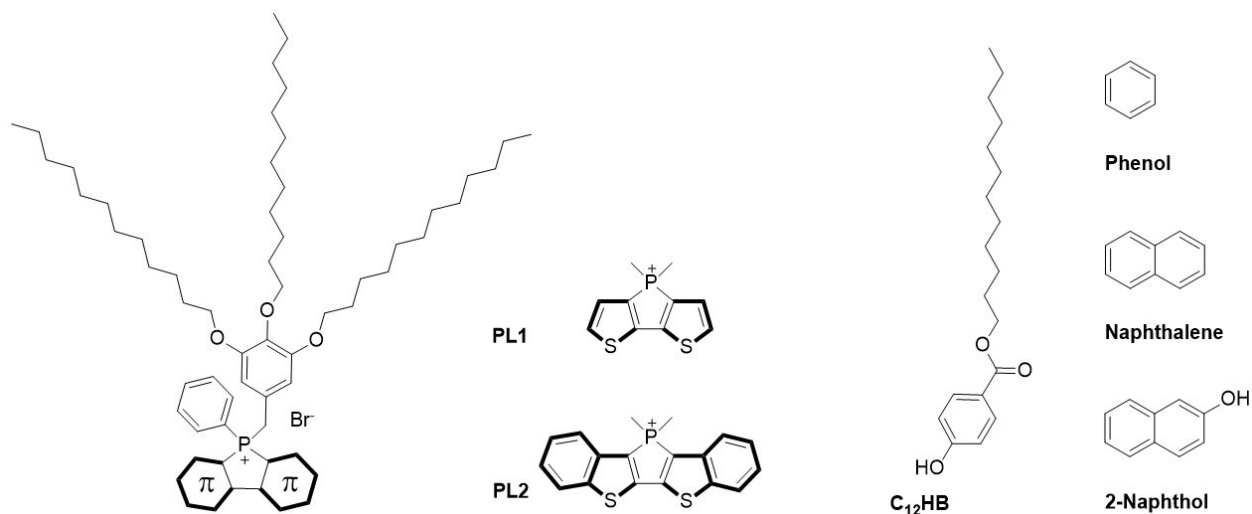
Polymeric materials with π -conjugated backbones have been used for electronic and optoelectronic applications for many years, where the photophysical performance depends on the molecular packing and crystallinity.^{220–224} Modification of the chemical structure through functional group

selection, altering the conjugation length and incorporation of heteroatoms, provides the means to tune the photophysical properties for the final product fabrications.^{3,12,179,225} With respect to heteroatoms in these materials, systems with backbones of aniline, pyrrole, or thiophene have been studied in depth.^{47,226–228} Phosphole, as the main phosphorus-based building block, has emerged in recent years as a unique member of this heteroatom-based group, as it displays partial aromaticity and high electron delocalization.¹⁹¹ The chemical properties of phosphole-based π -conjugated materials are a function of both the conformation of the phosphorus center and the conjugation of its substituents; these lead to unique multifunctional opportunities for optoelectronic device optimization including thermal stability, luminescence efficiency and charge-transport features.^{47,180,194,195,198} Rigid, fused-ring systems can be incorporated, extending the π -electron networks of the phospholes amplifying their light-emitting capacity.^{193,229,230} These building blocks can be accessed by flexible synthetic protocols and provide opportunities for functionalization of the phosphorus center, including metal coordination and alkylation.^{193,229} Furthermore, the ensuing π -interactions can decrease the electronic energy levels (HOMO-LUMO),^{54,231,232} and enhance the charge- and energy-transfer properties through intermolecular electronic coupling.^{233–235}

The molecular orientation can directly influence properties like charge-carrier transport or light-absorption efficiency. For example, phosphorus-based materials employing phosphinine building blocks show directional charge transfer derived from their organized solid-state packing.¹⁹⁴ Other properties like orientation-dependent ionization energies may be caused by packing-induced electronic energy levels.²²⁰ While the π - π interactions may strengthen the existing electrostatic and van der Waals interactions, they can also induce aggregation in solid-state and liquid-crystalline materials,^{124,236} which hinders the application of these building blocks. Aggregation becomes even more challenging as only a thin layer of these materials (on the nm scale) is needed for the majority of optoelectronic applications. For devices such as organic semiconductors and field-effect transistors, a major challenge remains the reproducible and controlled deposition of structurally well-defined thin films, as their charge-transfer properties are influenced by structure, orientation, and crystallinity.²²² Thus, the deposition technique and the external conditions play an important role for proper application properties.

The Langmuir-Blodgett deposition technique (LB) provides high control over the thin-film orientation and characterization. For proper LB deposition (from air-water to air-solid interfaces),

the phosphole-based materials should be surface-active, usually achieved via the addition of alkyl chains. For surfactants with π -interactions in the headgroup, the balance between the hydrophobic and hydrophilic properties impacts the film behavior at the air-water interface as it defines the packing configuration in the plane of the π system (edge-on or face-on).^{225,237} The chains also serve to promote liquid-crystalline over solid-phase formation. A series of phosphole-based surfactants (phosphole-lipid) with promising photophysical properties have been synthesized (Scheme 1).⁵⁴ Within this series, the smallest headgroup promotes well-ordered lamellar architectures (mainly impacted by ionic interactions), while the extension of π -conjugation (additional aromatic rings in the larger headgroup) leads to stronger emission and quantum yield at both solution and solid state.⁵⁴ We have recently reported the LB film behavior of the smallest headgroup of the series (**1**) in presence of halides.²³⁸ Herein, we characterize the monolayer behavior of these phosphole-lipids focusing on the intermolecular π -interaction (both from the extension of the headgroup conjugation and the introduction of additional aromatic moieties) and structure of the LB films formed.



Scheme 4.1 Chemical structure of previously reported phosphole-lipid with dithienophosphole headgroup (PL1), phosphole-lipid with benzo-fused dithienophosphole headgroup (PL2),⁵⁴ dodecyl 4-hydroxybenzoate surfactant (C₁₂HB), and the aromatic molecules phenol, naphthalene, and 2-naphthol.

4.3. Materials and Methods

4.3.1. Solution and subphases

Phosphole-lipids with dithienophosphole headgroup (PL1) and benzo-fused dithienophosphole headgroup (PL2) (Scheme 4.1) were synthesized as previously reported⁵⁴ and their spreading solutions (0.6 - 1.2 mM) were prepared in chloroform (Certified ACS, approximately 0.75% ethanol as preservative) purchased from Fisher Scientific. For all subphases, ultrapure water with resistivity of 18.2 M Ω cm⁻¹ (pH 5.6 at 25 °C) was obtained from a Milli-Q HX 7080 water purification system (HC). For solutions as the subphase, NaBr (ACS reagent, \geq 99.0%), NaCl (ACS reagent, \geq 99.0%), NaI (ACS reagent, \geq 99.5%), and phenol (ACS reagent, 99.0-100.5%) were purchased from Sigma-Aldrich and concentrations from \sim 1 μ M (10:1 molar ratio of counterion to lipid molecules) to 100 mM were prepared in ultrapure water as needed. For lipid mixture spreading solutions, dodecyl 4-hydroxybenzoate 98.0+% (C₁₂HB, Scheme 1) was purchased from Fisher Scientific and spreading solutions of PL1: C₁₂HB and PL2: C₁₂HB with different molar ratios were prepared.

4.3.2. Surface pressure-molecular area isotherm

Phosphole-lipids PL1 and PL2 were spread on ultrapure water and the other subphases in a Langmuir film balance (Nima Technology Ltd., Coventry, U.K.), with a maximum surface area of 300 cm². All measurements were made at room temperature (21.5 - 22.5 °C) and ten minutes were allowed for complete solvent evaporation and relaxation of the surfactant for all the experiments. A symmetrical compression rate of 5 - 10 cm² min⁻¹ (2.5 - 6.0 Å² (molecule min)⁻¹ - depending on the initial molecular area) was used. A filter-paper (1 cm \times 2 cm, Whatman No. 1 chromatography paper) based Wilhelmy plate was used to measure the surface pressure. To ensure the reproducibility, at least three separate isotherms were obtained for all experiments.

4.3.3. Brewster angle microscopy imaging (BAM)

An I-Elli2000 imaging ellipsometer (Nanofilm Technologies GmbH, Göttingen, Germany) equipped with a 50 mW Nd:YAG laser (λ = 532 nm) was used to perform Brewster angle microscopy. The magnification was set at 20 \times with lateral resolution of 1 μ m. All images were

obtained at an incident angle of 53.15° (Brewster angle of water) with the laser output of 50% (analyzer, compensator and polarizer set to 0°). Three separate BAM imaging experiments were performed for all systems.

4.3.4. Ellipsometry measurements

The I-Elli2000 was also used for measurement of the ellipsometric angles ψ and Δ with an incident angle of 50° , a laser output of 100%, and a compensator angle of 20° . Each value reported in the ellipsometric isotherm represents the average of measurements made on three independently formed films. For each independent film, the $\delta\Delta$ represents the average of 10 measurements of the same monolayer film at constant surface pressure.

The initial angles of analyzer and polarizer were set to 14 and 20° , respectively, and later adjusted to have the reflection of the polarized beam eliminated. $\delta\Delta$ values ($\delta\Delta = \Delta_{\text{film}} - \Delta_{\text{subphase}}$) are reported in ellipsometric isotherms, representing how the ellipsometric angle Δ of the film is changing through the isotherm, relative to the ellipsometric angle Δ of the subphase alone. Both film thickness and refractive index impact $\delta\Delta$, however, considering the relatively constant refractive index of the film at the air-water interface, $\delta\Delta$ is taken to represent the change in the monolayer thickness upon compression.

4.3.5. Atomic force microscopy imaging

For the AFM sample deposition, Mica sheets V1 quality were purchased from Electron Microscopy Science and freshly cleaved before usage. Monolayers were transferred onto the mica on the upstroke at constant pressures by Langmuir-Blodgett technique and dipping rate of 1 mm min^{-1} and the transfer ratios (ratio of the monolayer surface area loss over the substrate surface area during deposition) calculated. The AFM samples were allowed to dry for 30 minutes in ambient conditions followed by imaging within a 24-hour window. A Bruker multimode 8HR scanning probe microscope (Nanoscope 9.7, Digital Instruments, Santa Barbara, CA) was used to capture AFM images at the air-solid interface at room temperature. Peak-force tapping mode was used at a scan rate of 0.3-1 Hz with SCANASYST-AIR probes (silicon nitride cantilever, frequency

70 kHz, nominal spring constant 0.4 N m^{-1} , and tip radius 2 nm). Nanoscope software version 2.0 was used to perform all AFM image processing and analysis.

4.3.6. Grazing incidence X-ray diffraction (GIXD) and X-ray reflectivity (XRR)

All GIXD and XR measurements at the air-water interface were conducted at 15-ID-C ChemMatCARS at the Advanced Photon Source (APS) in Argonne National Laboratory, with monochromatic X-rays and energy of 10 keV. A Nima Langmuir trough with 340 cm^2 area with compression rate of the mobile barriers set at $2 - 5 \text{ cm}^2 \text{ min}^{-1}$ ($1 - 4 \text{ \AA}^2 (\text{molecule} \cdot \text{min})^{-1}$) was placed in the beam path in an air-tight enclosure with Kapton windows which allowed for purging the atmosphere with helium. The raw data were extracted and processed using software developed by Wei Bu, beamline scientist at ChemMatCARS.

The following parameters were used for GIXD measurements:

X-ray beam wavelength: 1.239 \AA , incidence angle: 0.0906° , horizontal size: 20 mm, vertical size: 120 mm, beam footprint: 20 mm by 7.6 cm. The two-dimensional Swiss Light source PILATUS 100K set to single-photon counting mode was used as detector. To minimize intense low-angle scattering, two sets of slits were used, one was placed in front of the detector (to control the beam footprint), and the other was located 280.0 mm from the sample. The GIXD data measured were plotted as contour plots of the intensity as a function of the horizontal (Q_{xy}) and the vertical (Q_z) scattering vector components. The lattice spacing d_{hk} was obtained from the in-plane diffraction data as $d_{hk} = 2\pi/q_{xy}^{hk}$, where the Miller indices h and k were used to index the Bragg peaks needed to calculate the unit cell parameters for the in-plane lattice.^{173,208} The Bragg rods and peaks were fitted with Gaussian and Lorentzian function, respectively, using Origin lab graphing and analysis software. The full-width-at-half-maximum values obtained from the corrected Bragg peaks and rods were used to obtain the in-plane correlation length and vertical scattering length through Scherrer formula^{173,176}:

$$\text{Lateral correlation length} \approx \frac{2}{FWHM} \quad \text{Equation 4.1}$$

$$\text{Vertical scattering length} \approx 0.9 \left(\frac{2\pi}{FWHM} \right) \quad \text{Equation 4.2}$$

For XRR measurements, the X-ray intensity signal is collected as a function of vertical scattering component (Q_z) and the $R(Q_z)$ is normalized to the Fresnel reflectivity (R/R_F) (calculated for a sharp air-water interface with an ideal flat, water surface). The fitting process (Parratt method) includes defining a box model in which there is a thickness and electron density assigned to each box, in order to represent the vertical structure of the film averaged across the X-ray beam footprint. The resultant reflectivity profile is compared to the measured reflectivity and a monolayer electron density profile in a vertical direction is generated.

4.4. Results and Discussion

While ionic interactions were proposed to be the main driving force of lamellar structure formation in the liquid crystalline formed in bulk for phosphole-lipid (**PL1**),⁵⁴ other intermolecular interactions such as π -interactions have been proposed to impact the formation and stability of these structures. With a headgroup comprising a conjugated π -system, an alkoxy benzyl connector between the alkyl chains and the dithienophospholium unit, the intermolecular interactions of these phosphole-lipids can be influenced by the presence of other aromatic rings to the environment or extension of the conjugation length.

Our first approach to tailoring the π -interactions of the thin film at the air-water interface involves introduction of aromatics via the subphase. The surface pressure-molecular area isotherms of the **PL1** on an ultrapure water and different concentrations of phenol in the subphase, at room temperature are shown in Figure 4.1. As previously reported, the isotherm of **PL1** on ultrapure water exhibits a pressure onset at $135 \text{ \AA}^2 \text{ molecule}^{-1}$, and a main phase transition plateau around 30 mN m^{-1} , corresponding to a transition from the liquid-expanded phase (LE) to the simultaneous formation of 3D aggregates and condensed-phase domains, followed by a second transition at $\sim 40 \text{ mN m}^{-1}$ at which a second population of 3D aggregates formed.²³⁸

The presence of phenol in the subphase at its lowest concentration ($\sim 1 \text{ \mu M}$, corresponding to 10:1 molar ratio of phenol to phosphole-lipid) leads to the same pressure onset area and phase transition plateau surface pressure ($136 \text{ \AA}^2 \text{ molecule}^{-1}$ and $\sim 30 \text{ mN m}^{-1}$, respectively). However, the area reduction through the plateau is larger in presence of 1 \mu M phenol, leading to the observation of the second transition at smaller molecular areas and at $\sim 40 \text{ mN m}^{-1}$. Increasing the subphase phenol concentration to 1 mM does not alter pressure onset area, however, the phase transition plateau is

shifted to a lower surface pressure of $\sim 25 \text{ mN m}^{-1}$. The phase-transition onset is noticeably less sharp and more rounded. Further increasing the phenol concentration (10 mM) leads to a slight increase of the pressure onset area of the isotherm ($\sim 145 \text{ \AA}^2 \text{ molecule}^{-1}$) and a further decrease in the phase transition plateau pressure ($\sim 21 \text{ mN m}^{-1}$). At concentrations of 1 and 10 mM, phenol is theoretically in excess in the subphase (i.e., all bound to the film), but it is only the presence of 100 mM phenol that leads to the elongation of LE phase and the shift of the pressure onset to much larger areas ($\sim 240 \text{ \AA}^2 \text{ molecule}^{-1}$). The 100 mM phenol subphase also exhibits the lowest phase transition plateau surface pressure at $\sim 18 \text{ mN m}^{-1}$.

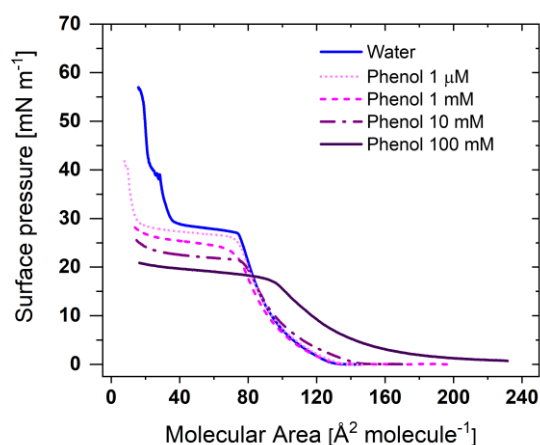


Figure 4.1 Surface pressure-molecular area isotherm of PL1 as a function of phenol concentration in subphase. The isotherm for PL1 on water was previously reported,²³⁸ and is repeated here for easier comparison.

This noticeable shift in the pressure onset area is likely the result of the higher concentration driving a greater partitioning of phenol to the headgroup region such that it can interdigitate between the phosphole headgroups and shift the lipids further apart. The consequence of the interdigitation is to reduce the chain-chain interactions that are dominated by short-range van der Waals interactions (and hence film organization) and to promote the formation of 3D aggregates, which correlates with the decrease in the phase transition plateau pressure. The formation of 3D aggregates through the phase transition is expected for all concentrations of phenols, as the plateau reaches molecular areas smaller than a minimum cross-sectional area required for three alkyl chain.^{173,238} In contrast to the subphase counterions,²³⁸ the presence of the single aromatic ring of

phenol with the same concentration in the subphase does not have a significant impact on the phosphole-lipid **PL1** isotherm.

Phenol was initially chosen as a small aromatic ring, with practical water solubility²³⁹ to be used as a subphase solution. However, it may be that the phenol – phosphole-lipid interactions are weak compared to the existing headgroup interactions, including electrostatics and intra- or interlipid interactions, and consequently at low concentrations, it may only remain adsorbed at the headgroup surface rather than penetrating into the film.

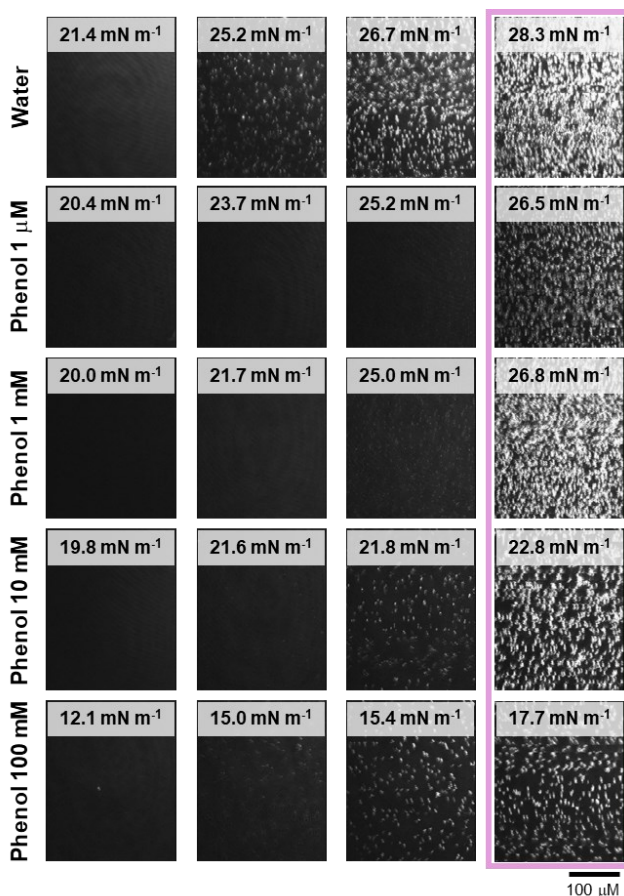


Figure 4.2 Representative BAM images of PL1 on water and different subphase concentrations of phenol. The images corresponding to the surface pressures of the main phase transition plateau are aligned vertically and framed (pink).

Figure 4.2 presents the BAM images of a **PL1** monolayer on water and different concentrations of phenol in the subphase. For better comparison of the film changes relative to the isotherm, the

BAM images corresponding the phase transition plateau surface pressures are aligned vertically. The BAM images are relatively similar for all subphases (in the absence or presence of phenol at different concentrations); bright and small 3D aggregates appear, forming as the film begins to reach the plateau. With further compression, these aggregates grow in number and brightness. The increase in the contrast (brighter aggregates) corresponds to an increase in height difference (film thickness).

The AFM images obtained for films formed by LB deposition from water and different concentrations of phenol are shown in Figure 4.3. For both water and the lowest concentration of phenol (Figure 4.3; first and second rows), the formation of relatively circular domains accompanied by the 3D aggregates begin at the end of the phase transition plateau (30 mN m^{-1}). The number of domains and aggregates increase at higher surface pressures, and beyond the second phase transition, a second population of 3D aggregates is observed that are much smaller in height and width, and only form on the domain/background boundary (45 mN m^{-1}). As the number of 3D aggregates increases, this leads to higher transfer ratios (**Error! Reference source not found.**)

With 1 mM phenol (Figure 4.3; third row), the domains initially adopt an elongated, ribbon-like shape (30 mN m^{-1}) that are narrower than the domains formed at the same surface pressure with water and the lowest phenol concentration. These ribbons vary in length and degree of branching and cover approximately 10-15% of the image area. However, as the surface pressure increases and the domains are pushed to higher area coverage ($\sim 50\%$ at 35 mN m^{-1} and $\sim 65\%$ at 40 mN m^{-1}), their shape becomes more rounded, and they begin to coalesce (with both quasi-circular domains and residual ribbons observable).

With 10 mM phenol (fourth row), due to the shape of the isotherm, we could only obtain AFM images for one surface pressure beyond the phase transition plateau. The domains observed at this surface pressure (30 mN m^{-1}) are even narrower than the ones for films deposited from a 1 mM phenol subphase. With 100 mM phenol, we could no longer pass the plateau to record the formation of condensed-phase domains. The only observation is the formation of 3D aggregates at the surface pressure of 20 mN m^{-1} , in the phase transition plateau.

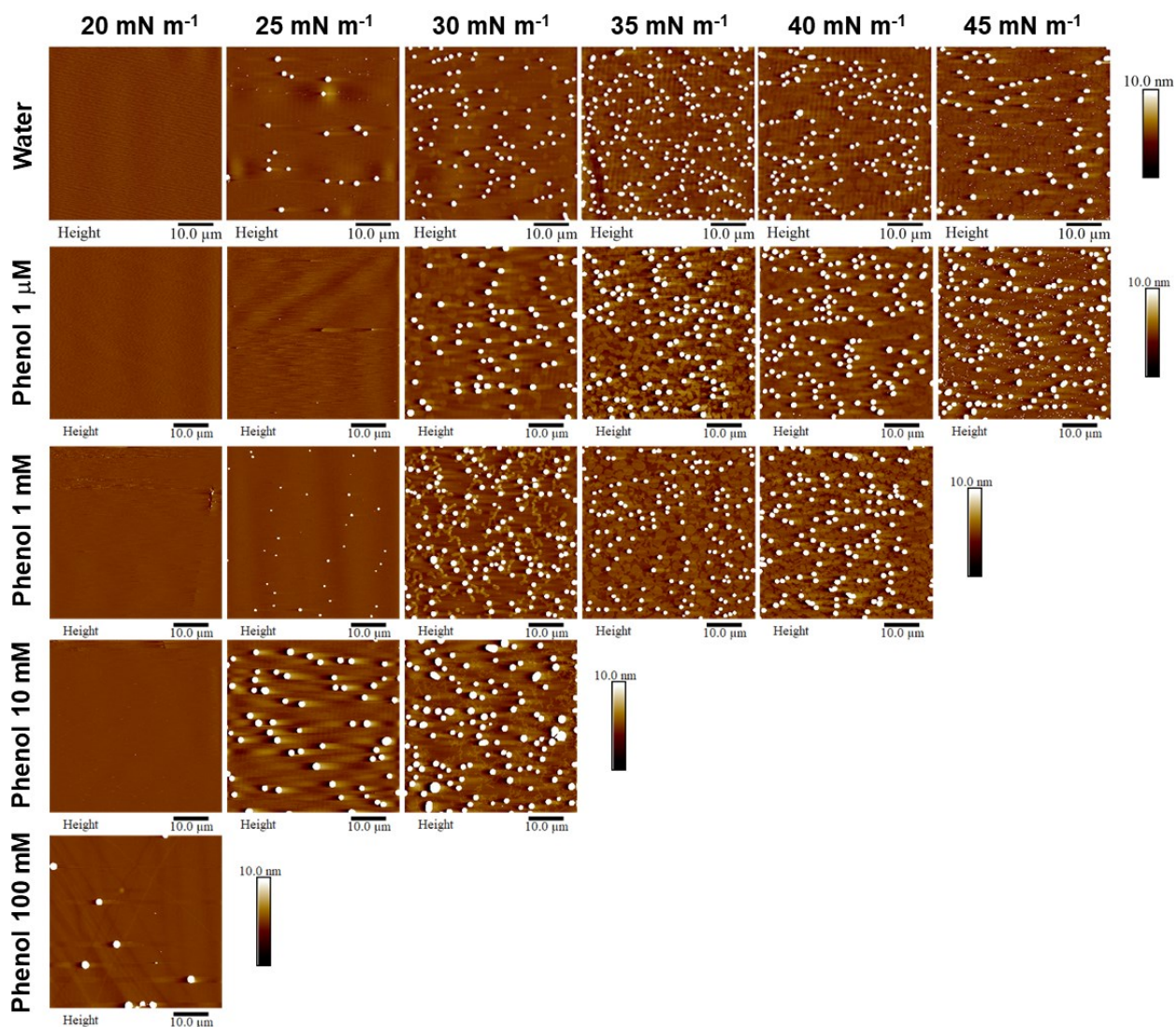


Figure 4.3 Representative AFM images of PL1 deposited onto mica by LB at different surface pressures from water and phenol subphases (concentrations as indicated). All images are $50 \times 50 \mu\text{m}^2$, with height scale of 10 nm. The height scale was selected to enable visualization of the monolayer domains which are otherwise obscured by the large height of the aggregates (average aggregate heights are provided in Figure B1).

For all concentrations of phenol, the impact on the formation of domains and 3D aggregates is not as prominent as was observed with halide counterions with the same concentration (altered electrostatic interactions).²³⁸ Specifically, the presence of phenol does not help to form a uniform film, nor does it limit 3D aggregation, as was observed for the addition of bromide.²³⁸ In other

aromatic compounds such as *para*-azoxyanisole with two aromatic rings, electrostatic interactions have been reported as the main driving force of the liquid-crystalline packing.²⁴⁰ Additionally, wherein high concentrations of halides significantly decreased domain heights,²³⁸ no specific trend in the change of height for domains or 3D aggregates as a function of phenol concentration could be discerned (**Error! Reference source not found.**). Note that the aggregate heights range from < 50 nm to almost 400 nm, with a large aggregate height variation for given conditions, despite their consistency in shape and lateral dimensions (attributed to line tension, given the three chains and a large hydrophobic volume. However, unlike the addition of halides, increasing concentrations of phenol leads to domain elongation (see the AFM images for surface pressure of 30 mN m⁻¹ in Figure 4.3). This elongation appears as ribbon-like domains that are first observed at concentrations > 1 mM phenol, which is in agreement with the first observation of a shift in the pressure onset area in the isotherms, suggesting that at these concentrations the penetration of the phenol begins to impact the headgroup organization.

Any interaction that alters the balance of intermolecular forces in the monolayer can disturb the competition between line tension and electrostatic repulsion and result in the domain shape change.^{119–121} The narrowing of the domains as the phenol concentration increases, may be the result of an increase of the inter-headgroup (intermolecular) distance as the phenol moieties localize between the headgroups, leading to the formation of smaller domains (similar to how electrostatic repulsion would alter the shape of domains). The concurrent formation of extended and elongated domains may derive from the π - π interactions of phenol and aromatic rings of **PL1**; as the surfactant molecules align in the presence of phenol, oriented domain growth is observed. Nittmann described the formation of dendritic domains as an early stage of domain growth due to lattice anisotropy, but competitive interactions eventually lead to round domains.²⁴¹ However, persistent directional growth has been reported for other surfactant headgroups exhibiting π -stacking interactions, albeit the directional growth in such systems was more prominent with the formation of dendritic domains.^{127,128} π - π Stacking in surfactants has been reported to provoke long-range orientational order through edge-to-face arrangements of aryl rings in the headgroup region and further packing of the chains.²⁴² In many cases, where nondirectional interactions dominate, this stage is not observed, and domains appear rounded from the onset. In this case, the strong, directional interactions, the elongated domains become more circular only at higher surface pressures. Such directional and oriented domain growth may be intentionally invoked through

crystallization with the aim of better controlling the charge transfer properties and electrical conductivity in electronic devices.²⁴³

Figure 4.4 shows the ellipsometric measurements performed on **PL1** films at the air-subphase interface for the 1 mM and 100 mM phenol concentrations. The change in magnitude of $\delta\Delta$ normally correlates to changes in film thickness (assuming the refractive index is relatively constant). At all surface pressures, the lower concentration of phenol leads to larger $\delta\Delta$ magnitudes, with the greatest difference at a surface pressure of 0 mN m⁻¹. However, as the films are compressed to the phase transition plateau, the $\delta\Delta$ magnitudes at the air-subphase interface, and consequently the film thickness, for both phenol concentrations converge. It should be mentioned that the lower $\delta\Delta$ values for 100 mM phenol may only be the result of the isotherm shape: as the isotherm is shifted to larger molecular areas and with the larger lateral space, the phosphole-lipids should form thinner films at the same surface pressure. Both phenol concentrations follow the same trend $\delta\Delta$ upon compression, as previously reported for a water subphase.²³⁸

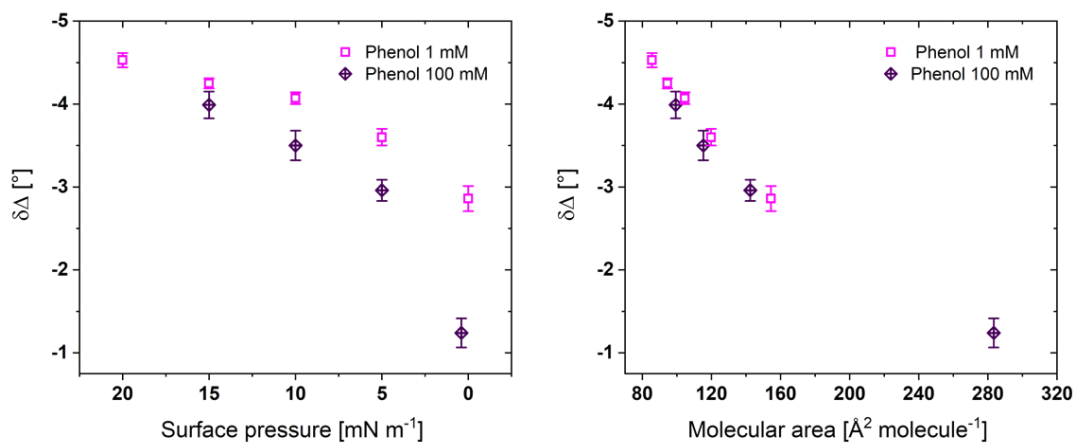


Figure 4.4 Ellipsometric measurements of PL1 at the air-subphase interface as a function of phenol concentration in the subphase. Each value represents the average of measurements made on three independently formed films. For each independent film, the $\delta\Delta$ is the average of 10 measurements of the same monolayer film at constant surface pressure.

For Figure 4.4, the values of $\delta\Delta$ are only reported up to the phase transition (the full $\delta\Delta$ -molecular area ellipsometric isotherms for all four phenol concentrations are shown in **Error! Reference source not found.**). The ellipsometric isotherm for 1 μ M phenol is similar, including larger errors,

to that on a water subphase.²³⁸ The errors decrease substantially with higher phenol concentrations, suggesting that phenol, while not impacting the absolute heights of domains or aggregates, does create a more uniform distribution of phases within the region of interest that is measured. Although the 3D aggregates begin to form upon reaching the phase transition plateau, the ellipsometric measurements do not show an increase in the $\delta\Delta$ magnitude, however the formation of 3D aggregates leads to nonuniformity (multiple phases with different thicknesses) and increased errors in the measurement. The $\delta\Delta$ value represents the average measurement of the film at the region of study, and a larger area covered by the thinner background may balance the thickness increase due to the other higher phases present. For the 10 mM phenol subphase, the film could be compressed beyond the plateau and a significant increase in $\delta\Delta$ could then be observed.

GIXD measurements at 18 mN m^{-1} (below the plateau) and 26 mN m^{-1} (in the plateau) were carried out for **PL1** with the 10 mM phenol subphase since this is the first concentration at which the surface pressure-area isotherm shifts to higher molecular areas. It was not possible to compress the film beyond the plateau for a higher surface pressure measurement. No diffraction signal was observed at either surface pressure (**Error! Reference source not found.**) confirming that the condensed phase forms only after the end of the plateau.

The vertical structure of the film at the same surface pressures was also probed using X-ray reflectivity. The reflectivity was fit with a simple two-box model where the upper box corresponds to the chain region and the lower box to the headgroups. The fits to the X-ray reflectivity are shown in **Error! Reference source not found.** and the fitted parameters are provided in **Error! Reference source not found.**. The presence of phenol in the subphase does not alter the thickness or electron density of either region. This is in good agreement with ellipsometry that shows similar values of $\delta\Delta$ for all phenol concentrations indicative of similar total film thicknesses.

To evaluate, if the size of the aromatic ring present has an impact on the ability of the molecule to intercalate between headgroups and therefore the headgroup packing, naphthalene and 2-naphthol were introduced. Strong interactions have been reported when sodium 2-naphthalenesulfonate was mixed with aromatic surfactants, where the π - π interaction and edge-to-face stackings formed enhanced the naphthalene insertion and led to ordered conformations with less space requirements.^{244,245} As both naphthalene and 2-naphthol have lower solubility than phenol in water, they were cospread with the phosphole-lipid. The chloroform-based lipid mixtures of 1:10 molar

ratio of phosphole-lipid: aromatic hydrocarbons were separately prepared (to match the $\sim 1 \mu\text{M}$ concentration phenol in subphase) and the surface pressure-molecular area isotherms of two lipid mixtures were obtained (Figure 4.5, solid lines). Both lipid mixtures exhibit a pressure onset area of around $13 \text{ \AA}^2 \text{ molecule}^{-1}$, followed by a phase transition at slightly lower surface pressures than the film on a water subphase ($\sim 24 \text{ mN m}^{-1}$). These pressure onset areas are too small for even a single chain surfactant with a small headgroup. When the same isotherms are replotted as a function of molecular area of a pure phosphole-lipid (dashed line, Figure 4.5, inset), they show the same pressure onset area as the water subphase. Although the conjugation of naphthalene or 2-naphthol may be expected to generate stronger interactions and better bridging between the headgroups, their size may not be optimal for penetration into the intermolecular space and disruption of the existing strong intra- and intermolecular interactions. Consequently, despite being cospread, the naphthalene and 2-naphthol do not appear to remain intercalated within the film. Considering that all of the naphthalene or 2-naphthol must then dissolve into the subphase, the total concentration of naphthalene or 2-naphthol would be approximately $1 \mu\text{M}$, which is still below their respective solubility limits of 0.241 mM and 5.24 mM .^{246,247} That said, similar to phenol at high concentrations, the isotherms exhibit a rounding of the plateau and a shift of the plateau to lower surface pressures, indicating that some of the naphthol or naphthalene may be surface bound (adsorbed).

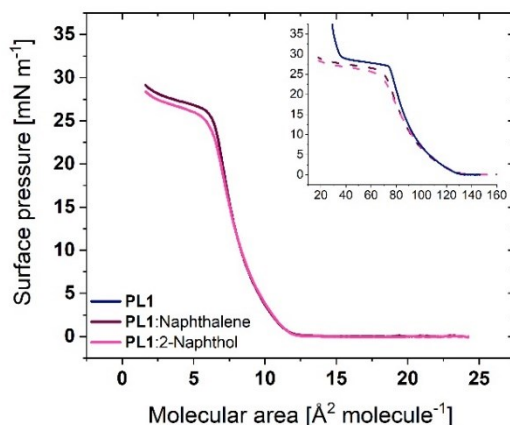


Figure 4.5 Surface pressure-molecular area isotherms of PL1 and lipid mixtures with 1:10 molar ratio of PL1: naphthalene and PL1: 2-naphthol (solid lines, pressure onset area $\sim 13 \text{ \AA}^2 \text{ molecule}^{-1}$). Inset: The same isotherms are replotted as a function of pure phosphole-lipid molecular area (dashed lines).

As the phenol and naphthalene solutions used in this work were within their solubility range in water, and it cannot be expected that all of the aromatic hydrocarbon molecules would remain at the subphase surface. Another approach to retain the aromatic species at the air-water interface, in the plane of phosphole-lipids, is to cospread another surfactant with an aromatic headgroup and similar alkyl chain length. For this approach, a lipid mixture of **PL1** with the phenolic surfactant dodecyl 4-hydroxybenzoate (**C₁₂HB** in Scheme 1) was studied. As shown in Figure 4.6, the surface pressure-molecular area isotherm of a 1:1 molar ratio lipid mixture of **PL1**:**C₁₂HB** is found in between the isotherms of each individual surfactant, with a phase transition plateau shifted to lower surface pressures than **PL1**. Although the 1:1 isotherm exhibits a negative excess area of $-4.6 \pm 0.1 \text{ \AA}^2 \text{ molecule}^{-1}$ (indicative of attractive interactions), the BAM images (**Error! Reference source not found.a**) and ellipsometric measurements (**Error! Reference source not found.b**) show no significant differences to those of the phosphole-lipid (i.e., no formation of domains and bright 3D aggregates that begin to form upon reaching the phase transition plateau and similar $\delta\Delta$ values).

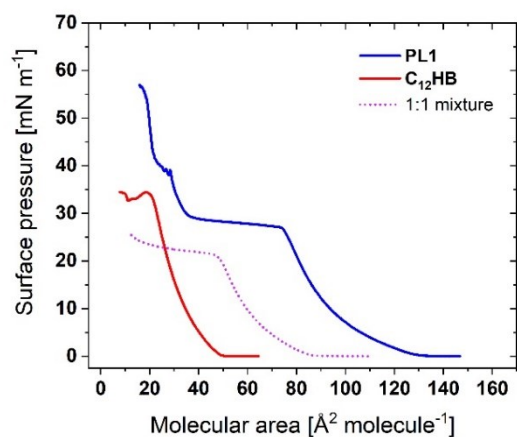


Figure 4.6 Surface pressure-molecular area isotherms of **PL1**, **C₁₂HB**, and their mixture with 1:1 molar ratio (structures shown in Scheme 4.1).

The AFM images (**Error! Reference source not found.c**) show that the condensed-phase domains still begin to form at the end of plateau (25 mN m^{-1}) accompanied by the formation of the 3D aggregates. The main difference observed is that the domains are slightly bigger in width and lower in height for the lipid mixture compared to **PL1** and upon reaching higher surface pressures the

condensed-phase domains of the lipid mixture coalesce to form larger domains (that was not observed for **PL1**). Additionally, even at these high surface pressures, significantly fewer aggregates are observed. Thus, the addition of a cosurfactant reduces the extent of aggregation but does not eliminate it and unlike high concentrations of bromide, the condensed phase formation and aggregate formation still occur simultaneously (i.e., the plateaus are not separated).

Error! Reference source not found. shows isotherms and AFM images for both 10:1 and 1:10 ratios of **PL1:C₁₂HB**. The 10:1 mixture is dominated by the **PL1** properties as would be expected, with similar isotherms and morphologies. The 1:10 mixture exhibits a plateau at higher surface pressures than **PL1** (surface pressures commensurate with the collapse of **C₁₂HB**) and a homogeneous film even at these high surface pressure (up to 35 mN m⁻¹). Thus, increased proportions of **C₁₂HB** prevent aggregation. Further study would be required to determine an optimal amount of **C₁₂HB** to promote retention in the plane of the film while still generating the desired film optoelectronic properties.

GIXD measurements were carried out for 1:1 lipid mixture of **PL1:C₁₂HB** on water subphase at 17 mN m⁻¹ (below the plateau) and 23 mN m⁻¹ (in the plateau). Again, it was not possible to compress the film beyond the plateau precluding measurements at higher surface pressures. No diffraction signal was observed at either surface pressure (data not shown). Thus, the condensed phase forms only after the end of the plateau. The vertical structure of the lipid mixture film at the same surface pressures was also probed using X-ray reflectivity. The presence of phenolic surfactant of **C₁₂HB** in the in the plane of phosphole-lipid at the air-water interface does not impact the length or electron density of chain and headgroup regions (**Error! Reference source not found.**).

The final approach employed to modify π -interactions in the phosphole-lipids Langmuir films is the extension the conjugation length in their headgroup (**PL2** in Scheme 4.1). This extension of the conjugation has been shown to alter the photophysical properties in both the solid and solution phases. The intermolecular π - π interactions of this larger scaffold have been reported to cause a large red-shift in emission wavelength for **PL2** in the solid state compared to **PL1**. Although **PL2** shows an organized orientation in the liquid-crystalline phase, the alkyl chain interdigitation and ionic interactions of the headgroups are not as strong as those reported for **PL1**, due to the larger

space requirements for the headgroup that increases the intermolecular distance and the layer thickness in liquid-crystalline phase.⁵⁴

The surface pressure-molecular area isotherm of **PL2** is shown in Figure 4.7. Although the headgroup is larger for **PL2**, its isotherm exhibits only a slight decrease in pressure onset area ($\sim 6 \text{ \AA}^2 \text{ molecule}^{-1}$). This small change in onset area may be due to the dominance of three alkyl chains in the area requirements at low surface pressures. The impact of the headgroup becomes more significant at higher surface pressures. With the larger headgroup, the phase transition plateau begins at slightly larger molecular areas and lower surface pressures. Also, the isotherm does not reach surface pressures beyond the plateau, indicative of the stronger influence of aggregate formation as opposed to condensed phase formation in the isotherm. This lack of condensed phase is confirmed by BAM and AFM imaging and ellipsometry shows a similar trend along the isotherm as observed for **PL1** (**Error! Reference source not found.**). Both the solution and liquid-crystalline phases for **PL2** show evidence of inter- and intraheadgroup π -stacking which might be expected to generate a condensed phase.⁵⁴ Studies of lipids with nonaromatic headgroups have shown that an increase in the size of the headgroup relative to the alkyl chain cross-sectional area weakens the packing of the alkyl chains, increases the tilt angle, and decreases the monolayer thickness.²⁴⁸

A 1:1 mixture of **PL1** and **PL2** exhibits a pressure onset area that is slightly larger than either **PL1** or **PL2** and positive excess areas throughout the isotherm ($+5.3 \pm 0.2 \text{ \AA}^2 \text{ molecule}^{-1}$) indicative of repulsive interactions, which may be the result a mismatch of the headgroup space requirements. The isotherm is most similar to that of **PL2** suggesting that the larger phosphole-lipid headgroup can dominate the film properties.

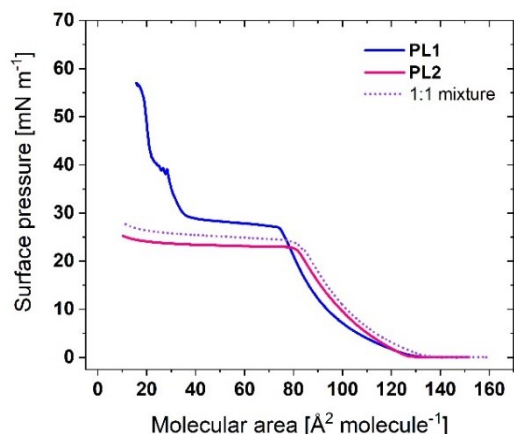


Figure 4.7 Surface pressure-molecular area isotherms of **PL1**, **PL2**, and their mixture with **1:1** molar ratio (structures shown in Scheme 4.1).

PL2 has been probed in the same range of subphases, including halide counterions and phenolic structures (**Error! Reference source not found.**). The notable outcomes of these studies are that the films of **PL2** lose their selectivity towards bromide counterions (i.e., there is no differentiation based on the halide selected), have reduced shifts upon incorporation of phenol, and exhibit small positive excess areas with naphthalene and 2-naphthol.

The presence of both aromatic rings and charged species can promote the possibility of charge- π interactions, and further impact the molecular orientation and structure.^{129–131} Factors like the aromatics' electron richness, or the components' polarity and electron affinity, and environmental factors such as pH or ionic strength have been reported as the defining elements for such charge- π interactions.^{132–134} Despite the wealth of potential interactions in the phosphole films studies here, it appears that the headgroup size may be the principal factor of **PL2** behavior with halide subphases. The headgroup size can also explain the shortening of the LE phase for **PL2** compared to **PL1** with 100 mM phenol subphase.

4.5. Conclusions

The impact of intra- and intermolecular interactions and arrangement of conjugated phosphole-based materials on the performance of the electronic devices provide opportunities for tailoring their self-assembly and organization and thus improving the final product functionality. Herein,

interfacial characterization of the phosphole-lipids showed that an ordered 2D film (condensed phase) only begins to form after a nonclassical phase transition in the isotherms. However, obtaining a well-ordered film remains a challenge as the plateau is also associated with the formation of 3D aggregates.

For better control over the formation of the desired ordered, 2D thin films, various aromatic additives were introduced to modify the π -interactions for which phosphole-lipid headgroup size, intermolecular space requirements, and the balance between all the noncovalent interactions play a key role. Introducing the single aromatic ring of phenol in the subphase (particularly, at higher concentrations) alters the growth pattern of the domains. However, the resultant interactions are not sufficient to retain the phosphole-lipid in the monolayer plane or prevent the formation of aggregation. Although the phenol-phosphole π -interactions showed the capacity to control the film formation through directional domain growth.

The polycyclic, fused rings of naphthalene and 2-naphthol did not remain intercalated between the headgroups when cospread with phosphole-lipids. However, anchoring the aromatic ring to the interface, via cospreading a mixture of the phosphole-lipid and a phenolic surfactant, reduced the formation of 3D aggregates while also generating larger domains. The extension of the conjugation in the headgroup, on the other hand, resulted in the loss of selectivity towards halide counterions, as the larger headgroup space requirements may lead to larger pores available. The larger area required for headgroups relative to the chains hinders the optimal packing and no domain formation was recorded. Although the conjugation extension generates promising photophysical properties (increased quantum yield and intensity), the larger headgroup induces a loss of distance-dependent (chain-chain) interactions and insufficient π -interactions to yield an organized film. It may be possible to achieve a well-ordered, aggregate-free thin films required for organic electronics through a combined approach of tuning headgroup interactions for both strong electrostatic interactions (via counterions) and weaker π -interactions (via phenolic surfactants). LB films offer a unique path to investigate and control molecular organization due to the precise control over monolayer assembly, critical in the design of 2D thin films for applications in optoelectronics. However, achieving a balance between headgroup interactions, chain packing, and noncovalent interactions (such as π -interactions) remains a significant challenge to forming uniform, well-ordered, aggregate-free thin films. By introducing additives and mixtures, such as

aromatic compounds and phenolic surfactants, we explored approaches to intentionally tune and direct molecular orientation and enhance interfacial order. This strategy supports the broader efforts in the field to engineer self-assembled systems with tailored structures and functions from the bottom-up. These understandings highlight the potential of combining molecular design and control over environmental conditions to optimize film organization, offering a pathway to eliminate aggregate formation and promote ordered domain growth, critical for functional self-assembled architectures.

Chapter 5. Amphiphilicity of Tetraazaporphyrins Containing Four Terminal Carboxylic Acid and Four Alkyl Groups Promotes Face-on Orientation in Langmuir Films

Zahra Alinia, Elmahdy Abdulhamied, Serxho Selmani, Renaud Milette Lamarche, S. Holger Eichhorn, Christine E. DeWolf

Zahra Alinia and Elmahdy Abdulhamied contributed equally to the paper.

Published in *ACS Langmuir* (DOI: 10.1021/acs.langmuir.4c03800)

Supplementary information is provided in Appendix C.

5.1. Abstract

Control over the orientation of polycyclic aromatic dyes in thin films is paramount for tailoring their optical, electronic, and mechanical properties. Their supramolecular assembly in deposited films is tuned here by converting the macrocyclic dyes into large amphiphiles. Two octaalkylthio-substituted tetraazaporphyrins (TAPs) with one 5-carboxypentyl and one pentyl or dodecyl chain per pyrrole ring were synthesized as statistical mixtures of four regioisomers. The unsymmetrically substituted maleodinitrile precursors were prepared in good yields with a flow reactor. Neither the tetraester pre-cursor TAPs nor the tetraacid TAPs show mesomorphism and both belong to the small class of porphyrin derivatives that display isotropic liquid phases at or close to room temperature. Interfacial properties of the two amphiphilic tetraacids were probed using Langmuir films on aqueous subphases at different pH values and Langmuir-Blodgett (LB) films transferred onto mica substrates. The tetraacid with the longer dodecyl chains forms inhomogeneous films comprising a combination of monolayer, stacked macrocycles with interdigitated chains and 3D structures, with the latter favored at higher sub-phase pH and higher surface pressures. In contrast, the LB films of the tetraacid with the shorter pentyl chains yielded relatively homogeneous monolayers. The combination of atomic force microscopy imaging and packing correlations elucidated by grazing incidence X-ray diffraction suggests that these form spider-like conformation, with the macrocycles close-packed and oriented parallel to the substrate (face-on).

This difference in molecular packing is attributed to a possible intramolecular mixing of 5-carboxypentyl and pentyl chains that gives a better match between the footprints of the macrocycle, acid groups, and alkyl groups. The longer dodecyl chains are too large for filling the space between 5-carboxypentyl chains (mixing) and too small for filling the footprint of a TAP macrocycle. We demonstrate that by judicious tailoring of the chain length and subphase conditions, the desirable homogeneous film of face-on oriented macrocycles can be formed.

5.2. Introduction

Porphyrins are heterocyclic organic compounds with unique electronic and optical properties, resulting from their large conjugated π -systems.^{249–251} These characteristics have made porphyrins central to applications in photosynthetic research, sensor technologies, biomedical imaging, and energy harvesting.^{31,252–256} The significance of porphyrins in these fields originates from their role in natural systems, such as in the photosynthetic apparatus and hemoproteins, where they play critical roles in energy transfer and oxygen transport, respectively.^{257,258} Structurally, porphyrins consist of four pyrrole units connected by methine bridges, forming a planar conjugated macrocycle. Their photophysical characteristics, particularly strong absorption in the visible spectrum, make them ideal candidates for light-harvesting and photodynamic applications.^{59,256,259,260} Furthermore, the ability to functionalize porphyrins at various positions enables fine-tuning of their amphiphilic balance, a crucial parameter for assembling them into stable, well-organized films.^{61,62}

While the photophysical and electronic properties of porphyrin are essential for these applications, the success of porphyrin-based devices also depends on achieving precise molecular orientation and alignment.²⁴⁹ This orientation is particularly critical for applications in thin-film electronics, where face-on or edge-on arrangements at the interface can influence electronic properties, as well as charge transfer and light absorption (orientations shown in Figure 1).^{261–263} A major challenge lies in overcoming the tendency of porphyrins to generate stacks in solution and at interfaces, often dominated by strong cofacial interactions.^{264,265}



Figure 5.1 Schematic representation of the edge-on (left) and face-on (right) orientations of a macrocycle at air-water interface.

Deposition techniques such as solution-processing or vacuum deposition may require complex conditions, or limit the device performance as films with heterogeneous orientation and noncoherent packing can be formed.^{266,267} Langmuir and Langmuir-Blodgett (LB) film deposition techniques can be employed to tune porphyrin assembly at the air-water interface.^{105,107,110} With this technique, amphiphilic porphyrin molecules can form monolayers with distinct molecular orientations at an air-water interface. LB deposition allows these films to be transferred onto solid substrates as single- or multilayer, with control over thickness and molecular orientation. This approach enables the fabrication of 2D thin films with highly ordered, homogeneous structures, suitable for optoelectronic and sensing applications where alignment and consistency are crucial.¹⁰⁵ For instance, in photovoltaic devices, the ability to create ordered LB films with face-on orientation improves charge transfer and device efficiency.²⁶⁸ In biomedical applications, LB films offer a means of producing stable, organized films of porphyrins for photodynamic therapy and bioimaging.^{104,268} The controlled orientation and density of porphyrin molecules at the substrate can enhance the efficiency of singlet oxygen generation, a critical parameter in therapeutic effectiveness.^{269,270}

With the aim of developing sensors and catalysts, previous LB studies with porphyrin derivatives employing nonamphiphilic compounds, have shown ineffective LB properties due to spontaneous aggregation.^{265,271,272} Even for those derivatives forming monolayers, the porphyrin macrocycles were often oriented edge-on or tilted at the interfaces.²⁷³ For example, the TiO metalated phthalocyanines form monolayers with a tilted orientation of the macrocycle as polar axial TiO group increases the amphiphilicity and reduces macrocycle cofacial interactions.²⁶ Such edge-on and tilted orientations may enhance optical absorption at specific wavelengths due to π - π stacking and charge-transfer between layers,²⁷⁴ however the face-on orientation would allow for better electronic interactions with the substrate and possible analytes and reagents.²⁷⁵⁻²⁷⁸ The orientation

in Langmuir and LB films can be moderated through mixing with surfactants (e.g. insoluble monolayer forming fatty acids),^{26,279} or incorporating a central ion.^{280–282} Anchoring the macrocycle through directed attachment of polar moieties or a single alkyl chain has also been employed to control the orientation and aggregation.^{283–285} However, directing a uniform face-on orientation within the films, without aggregation, remains a challenge.

Octaalkylthio-substituted tetraazaporphyrins (TAPs), a class of porphyrins with specific structural features provide a synthetic platform for developing amphiphilic organic dyes that can be tailored to preferentially align with a face-on orientation of the macrocycle at the interface.^{286,287} In contrast to phthalocyanines and tetraphenyl porphyrins, properties of TAPs are not only dominated by the macrocycle but can be widely varied by different substituents and central metal ions.^{288,289} Our previous work on octaacid TAPs showed that the alterations of the acid chains length impact the film homogeneity and orientation.⁷⁷ In order to generate sufficient amphiphilicity for the formation of stable Langmuir and LB films with a face-on orientation, the aliphatic spacer chains between the terminal carboxylic acid groups and TAP core must be at least 10 methylene groups long (Figure 2).⁷⁷ A limitation that hampers the use of TAPs lies in the incompatibility between the surface area of the TAP macrocycle (roughly 120 Å²) and the eight carboxylic acid groups (~192 Å²), reducing the stability of the face-on orientation.^{77,290} Another limitation remains the strong self-aggregation and island formation, causing defect-rich monolayers, that is the result of the high dimerization enthalpy of carboxylic acids (50–80 kJ/mol in the gas phase)²⁹¹ compared to an adsorption energy of 28 kJ/mol²⁹² for a carboxylic headgroup at the air–water interface. Although complete deprotonation of the carboxylic acid groups reduces self-aggregation, the octacarboxylate TAPs become soluble in aqueous solutions. The best LB properties are obtained when only half of the carboxylic acid groups are protonated whereas no stable condensed Langmuir monolayers are observed for fully protonated octa–acid TAPs.⁷⁷

Presented here is a new molecular design that aims to address the common limitations in achieving consistent film quality and orientation. Each pyrrole ring of the TAP is substituted with one alkylthio group and one terminal carboxylic acid group, attached via pentamethylenethio linkers. This less symmetric TAP structure, while more challenging to synthesize than symmetrical derivatives, offers expanded molecular design options for balancing the hydrophilicity and hydrophobicity. This balance is essential for controlling the desired and preferential macrocycle

orientation and optimizing the potential performance of porphyrin-based LB films in various practical fields.

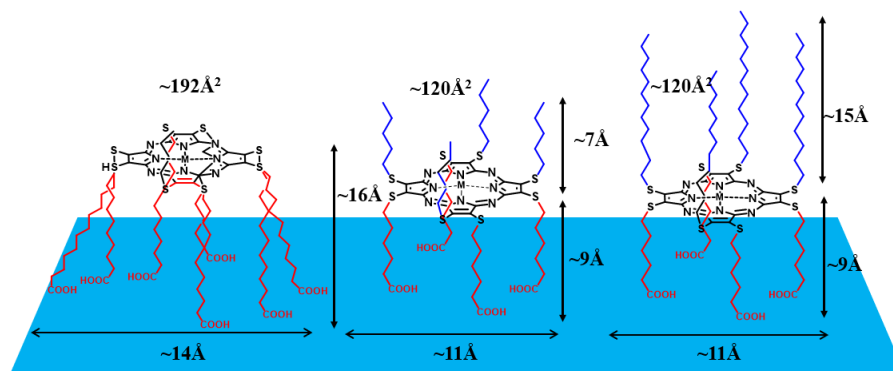


Figure 5.2 Proposed face-on conformers at the air-water interface of a previously reported octaacid TAP (left) with alkyl spacers of 10 methylene groups and the two tetraacid TAPs **4a** (center) and **4b** (right) reported here. Estimated chain lengths and TAP surface areas are taken from previous studies.^{77,293–295} The side-chain and spacer lengths represent maximum values for fully extended (crystalline) alkyl chains. Side-chains in an amorphous state have a 10-20% shorter effective length.⁷⁷

5.3. Experimental Section

Synthesis. All synthetic procedures along with spectroscopic data are provided in Appendix C.

5.3.1. Chemicals and Materials

The starting reagent, disodium 1,2-dicyanoethylene-1,2-dithiolate **1**, was prepared according to literature procedures.^{296,297} 1-Propanol and methanol were dried over 4 and 3 Å molecular sieves, respectively, and dry and air-free dichloromethane, tetrahydrofuran, and diethyl ether were obtained from a solvent purification system (Innovative Technology Inc. MA, USA, Pure-Solv 400). All other reagents and solvents were used as received unless stated otherwise. Analytical thin-layer chromatography and column chromatography were performed on aluminum-backed silica gel 60 plates and with SiliaFlash F60 silica gel, respectively, from Silicycle.

5.3.2. Methods

The flow reactor consisted of a dual syringe pump that was injected into tubing with an inner diameter of 1 mm. Tubing of a total volume of 10 mL (1273 cm in length) was coiled around a copper cylinder that was submerged in a heating or cooling bath. NMR spectra were recorded on Bruker AVANCE 300 and Bruker AVANCE III spectrometers operating at 300 and 500 MHz, respectively. NMR data acquisition and processing were performed with Topspin 2.1 software. Since the TAP compounds are mixtures of up to four different regioisomers, NMR spectra show more peaks than just for the most abundant regioisomer and the low symmetry of some regioisomers may also generate additional peaks. Peak assignments are given for all peaks. Infrared spectra (ATR) of neat samples were recorded on a Bruker Alpha FT-IR Spectrometer. Frequencies are given in reciprocal centimeters (cm^{-1}) for selected absorbance peaks. High-resolution mass spectra were obtained by matrix assisted laser desorption ionization, chemical ionization, and atmospheric solid analysis probe ionization operated in positive modes. Solution UV-vis absorption spectra were recorded on a Varian Cary 50 spectrophotometer and corrected for solvent absorption.

5.3.3. Material Properties

Thermal properties of esters **3a,b** and acids **4a,b** were probed by polarized optical microscopy, differential scanning calorimetry (DSC), and thermal gravimetric analysis (TGA). These measurements were conducted on an Olympus BX51 light microscope that is equipped with an Instec heating stage, and a DSC Discovery 2500 and TGA Discovery 5500 from TA Instruments.

5.3.4. Langmuir and LB Films

Spreading solutions (0.5 - 1 mM for **4b** and ~0.5 mM for **4a**) were prepared in chloroform (Certified ACS, approximately 0.75% ethanol as a stabilizer, Fisher Scientific). To avoid aggregation and to obtain a longer solution lifetime, 5% v/v Methanol (ACS reagent, $\geq 99.8\%$, Sigma-Aldrich) was added to all solutions. For all subphases, ultrapure water with a resistivity of $18.2 \text{ M}\Omega \text{ cm}^{-1}$ (pH 5.6 at 25°C) was obtained from a Milli-Q HX 7080 (HC) water purification system. The pH of the subphase was adjusted (pH 4, 6.5, and 11) using HCl and NaOH solutions.

NaCl (ACS reagent, $\geq 99.0\%$) was purchased from Sigma-Aldrich and 1 mM solutions were prepared in ultrapure water.

TAPs **4a,b** were spread on ultrapure water as a subphase (pH adjusted, as described above) at room temperature (21.5-22.5 °C) in a Langmuir film balance (Nima Technology Ltd., Coventry, U.K.), with dimensions of 7 cm by 42 cm. All surface pressure–molecular area isotherms, LB transfers and ellipsometry measurements were obtained on this Langmuir trough. Ten minutes were allowed for solvent evaporation and monolayer equilibration for all experiments. The monolayer was compressed symmetrically at a compression rate of 2-10 cm² min⁻¹ (1-10 Å² (molecule min)⁻¹, depending on the initial molecular area). Surface pressures were obtained using a filter paper (1 cm × 2 cm, Whatman No. 1 chromatography paper) based Wilhelmy balance. To ensure reproducibility, three separate isotherms were obtained for all experiments. The compressibility modulus was calculated using:¹⁵⁴

$$C_s^{-1} = -A \left(\frac{\partial \pi}{\partial A} \right)_T \quad \text{Equation 5.1}$$

where A is the molecular area, π is the surface pressure, and T is the temperature.

Brewster Angle Microscopy (BAM) was carried out with an autonulling imaging ellipsometer (NANOFILM-EP4, Accurion GmbH, Göttingen, Germany) equipped with a 50 mW internal solid-state laser (Laser-stabilized Xenon arc lamp) with a wavelength of 658 nm. All images at the air-water interface were obtained using a 10× magnification ultra objective with a lateral resolution of 1-2 μm . The experiment was performed at the Brewster angle of water (53.15°) and laser output of 30%, with the analyzer, compensator, and polarizer set to 0°. The Langmuir film balance (KSV NIMA LB series, Biolin Scientific Oy, Finland) with dimensions of 7.5 cm by 73.5 cm with a roughened platinum plate as a Wilhelmy balance was used for all BAM imaging. All experiments were performed at room temperature and a compression rate of 7.5 cm² min⁻¹ (equivalent to 2-4 Å² (molecule min)⁻¹). Two separate isotherms were obtained to ensure that the BAM images are reproducible. All images reported have been brightness reduced by 30% and contrast enhanced by 20%.

Measurement of the ellipsometric angles Ψ and Δ was performed using an imaging ellipsometer (I-Elli2000 imaging ellipsometer Nanofilm Technologies GmbH, Göttingen, Germany) equipped with a 50 mW Nd:YAG laser ($\lambda = 532$ nm). All ellipsometry measurements were performed using

a 10× magnification at an incident angle of 50° and a laser output of 100%, while the compensator angle was set to 20°. The initial angle of the analyzer and polarizer was set to 14° and 20°, respectively, and later adjusted to have the reflection of the polarized beam eliminated. $\delta\Delta$ values ($\delta\Delta = \Delta_{\text{film}} - \Delta_{\text{subphase}}$) are reported as ellipsometric isotherms, representing how the ellipsometric angle Δ of the film is changing through the isotherm. Film thickness and refractive index are two separate monolayer film characteristics that have an impact on $\delta\Delta$. Taking into account the film's relatively constant refractive index at the air-water interface, $\delta\Delta$ may represent the change in the monolayer thickness following the compression. The NIMA film balance was used for the ellipsometric measurements along the isotherm and the film was held at constant surface pressure during the measurement period. Each $\delta\Delta$ value reported is the average of measurements made on three independently formed films. For each independent film, $\delta\Delta$ represents the average of 10 ellipsometric measurements made at each surface pressure.

For atomic force microscopy (AFM) sample deposition, V1 quality mica sheets were purchased from Electron Microscopy Sciences and cleaved right before usage. Monolayers were transferred on mica on the upstroke at constant pressures by the LB technique and a dipping rate of 1 mm min⁻¹, followed by a 30-minute drying in ambient conditions. The transfer ratios (ratio of the monolayer surface area loss over the substrate surface area during deposition) were measured and values >1 were attributed to the presence of multilayered structures. A Bruker multimode 8HR scanning probe microscope (Nanoscope 9.7, Digital Instruments, Santa Barbara, CA) was used to capture AFM images at the air/solid interface at room temperature (in a 24-hour window after sample preparation). Peak-force tapping mode at a scan rate of 0.3-1 Hz was used with SCANASYST-AIR probes (Silicon nitride cantilever, frequency 70 kHz, nominal spring constant 0.4 N m⁻¹, and tip radius 2 nm). Nanoscope software version 2.0 was used to perform image processing and analysis on condensed-phase domain heights and widths. At least two separate samples per surface pressure were prepared and for each sample three different areas were imaged using AFM.

All grazing incidence X-ray diffraction (GIXD) measurements at the air/water interface were carried out at 15-ID-C ChemMatCARS at the Advanced Photon Source (APS) in the Argonne National Laboratory, with the following parameters: X-ray beam wavelength, 1.239 Å; incidence angle, 0.0906 °; horizontal size, 20 mm; vertical size, 120 mm; and beam footprint, 20 mm by 7.6 cm. The two-dimensional Swiss Light source PILATUS 100 K set to single photon counting mode

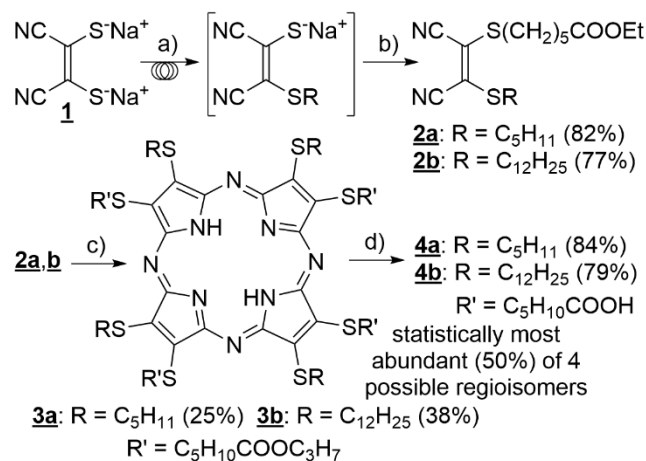
was used as a detector. To minimize intense low-angle scattering, two sets of slits were used: one was placed in front of the detector (to control the beam footprint), and the other was located 280.0 mm from the sample. A NIMA Langmuir trough with an area of 340 cm² and a compression rate of the mobile barriers set at 2-5 cm² min⁻¹ (1-3 Å² (molecule min)⁻¹) was placed in the beam path in an airtight enclosure with Kapton windows which allowed for purging the atmosphere with helium. The GIXD data measured were plotted as contour plots of the intensity as a function of the horizontal (Q_{xy}) and the vertical (Q_z) scattering vector components.^{173,208} The lattice spacing d_{hk} was obtained from the in-plane diffraction data as $d_{hk} = 2\pi/q_{xy}^{hk}$, where the Miller indices h and k were used to index the Bragg peaks needed to calculate the unit cell parameters for the in-plane lattice. Raw data was extracted and patched using software developed by Wei Bu, beamline scientist at ChemMatCARS. The Bragg rods and peaks were fitted with Gaussian and Lorentzian functions, respectively, using Origin lab graphing and analysis software.

5.4. Results and Discussion

5.4.1. Synthesis

While the dialkylation of sodium maleonitriledithiolate **1** is straightforward the stepwise alkylation with two different alkyl bromides has been proven difficult because of the low solubility of **1** especially in aprotic polar organic solvents. In fact, to the best of our knowledge this is the first report of a maleonitrile with two different alkylthio groups (Scheme 5.1). We chose a flow reactor and diglyme as the solvent for the preparation of the monoalkylated intermediate that was directly converted to maleonitriles **2a,b**. The flow conditions most importantly allowed for a local 1:1 molar ratio of 1-bromopentane and **1** that reduced the formation of symmetric dialkylated side-products from about 50% to less than 20%.

Scheme 5.1 Synthesis of TAPs as mixtures of four regioisomers.



Reaction conditions: a) flow reactor, diglyme, 1 equiv. BrC₅H₁₁ or BrC₁₂H₂₅, 0 °C, 6 hrs; b) diglyme, 1.1 equiv. BrC₅H₁₀COOEt, 0 °C, 12 hrs; c) 1. Mg(OC₃H₇)₂, 1-propanol, refl., Ar, 24 hrs; 2. THF/1 M HCl_{aq.}, 0.5-1 hrs; d) THF/H₂O 95:5, 1 M NaOH_{aq.}, refl., 24 hrs. Full synthetic details are provided in Appendix C, as are spectral characterizations of all prepared compounds (ATR FTIR, ¹H NMR, ¹³C NMR, HRMS and UV-VIS, Figures C1 to C26).

Previously reported conditions were employed for the cyclization of compounds **2** to TAPs **3a,b** and their ester hydrolysis to the final products **4a,b**. Cyclization to compounds **3a,b** is expected to give 4 different regioisomers with a statistical ratio of 4:2:1:1 (Scheme S1) of which the isomer formed with 50% probability is shown in Scheme 5.1. Separation of these isomers by chromatography is not straightforward and the isomer mixture is expected to be less prone to aggregation and crystallization, which is an advantage for the LB studies. ¹³C NMR spectra of compounds **3a,b** and **4a,b** show the peaks of more than one regioisomer and the lower symmetry of some regioisomers may also generate additional peaks. In addition, ¹H NMR spectra were broadened by aggregation, which was the worst for TAPs **4a,b**. Reasonable ¹³C NMR spectra were obtained at temperatures between 50 and 60 °C.

5.4.2. Material Properties

Thermal properties of TAPs **3a,b** and **4a,b** were studied by polarized optical microscopy, TGA, and DSC (Figures C27 to C38). Tetraester **3a** melts at 14 °C (onset) but does not crystallize on cooling at a rate of 10 °C min⁻¹. It does crystallize on heating below its melting temperature (cold crystallization). Tetraester **3b** is the only compound that reversibly melts (31 °C) and crystallizes

(14 °C) on cooling. Both TAPs are viscous isotropic liquids at room temperature on cooling. Surprisingly, tetraacids **4a,b** did not crystallize despite the potential for strong hydrogen bonding between carboxylic acid groups. Instead, tetraacid **4a** is a viscous isotropic liquid at room temperature and shows no thermal transitions between -60 and 90 °C. Tetraacid **4b** is an isotropic glass at room temperature with glass transitions at 47 and 44 °C on heating and cooling, respectively. Thermal stability was estimated as a 5% mass loss in the TGA measurements which gave the values 113 °C, 125 °C, 138 °C, and 168 °C, for **3a**, **3b**, **4a**, and **4b**, respectively.

Porphyrin derivatives of this size are usually not isotropic liquids but solids at room temperature. The first such examples were reported rather recently.^{298,299} Crystallization of both tetraesters and tetraacids is hindered by the presence of up to four regioisomers and their lower symmetry compared to a TAP with 8 identical substituents. Formation of a crystalline lattice was fully suppressed in tetraacids **4a,b**. This may be reasoned with strong intermolecular H-bonding between carboxylic acid groups that prevents the molecules from moving to their appropriate lattice places. The bulky ester and strongly interacting acid groups at the periphery of the alkyl chains also interfere with the formation of discotic mesophases that were reported for octaalkylthio- and octa(oligoethyleneoxy)thio-substituted TAP derivatives.^{293,295}

Decomposition temperatures for **3a,b**, and **4a,b** are well below 200 °C, which is low for TAPs but in line with values reported for TAP derivatives that contain peripheral carboxylic acid and hydroxyl groups.⁷⁷ Unexpectedly, the tetraesters are less stable than the tetraacids and the derivatives with dodecyl chains are more thermally stable than the compounds with pentyl chains. However, the latter observation may just be caused by higher evaporation temperatures for fragments with longer chains formed at a lower temperature. In any case, the estimated decomposition temperatures are well above the values used in the studies reported here.

5.4.3. Langmuir and LB Films.

Surface pressure-molecular area isotherms of **4b** at room temperature and at compression rate of 10 cm² min⁻¹ are shown in Figure 5.3. At the lowest pH (pH 4) where all four acid chains are protonated, the pressure onset is around 250 Å² molecule⁻¹. The molecular design generates a number of possible film structures that must be considered when interpreting the surface characterization. A summary of these is presented in Figure 4. The pressure onset is in reasonable

agreement with the molecular area occupied by the ring in a face-on orientation (i.e., the ring portion of the molecule lying parallel to the water surface). Initially a slow increase in pressure upon compression for the film is observed until a pressure of around 17 mN m^{-1} is reached at which point a phase transition plateau begins. Beyond the plateau the pressure rises more steeply until the film collapses at a pressure of 40 mN m^{-1} .

At a higher pH of 6.5, where one to two of the acid chains is deprotonated based on the titration of octaacid TAPs,⁷⁷ the isotherm shape is similar to the one at pH 4 except that the surface pressure onset is shifted to smaller molecular areas of $200\text{-}210 \text{ \AA}^2 \text{ molecule}^{-1}$.

At pH 11, where all the acidic chains are deprotonated, the surface pressure only starts to increase at much smaller molecular areas ($130 \text{ \AA}^2 \text{ molecule}^{-1}$), despite the anticipated increase in charge repulsion. The molecular area is too small to accommodate the molecule face-on in a monolayer, and the formation of multilayers and/or aggregates must be considered, especially given that the area at collapse is close to $20 \text{ \AA}^2 \text{ molecule}^{-1}$. To confirm that the isotherm shift is due to deprotonation and not an effect of changing the ionic strength, the isotherm was repeated on the 1 mM NaCl subphase, and no shift was observed (**Error! Reference source not found.**).

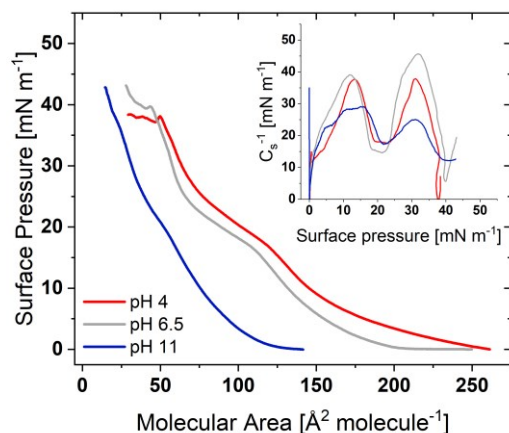


Figure 5.3 Surface pressure-molecular area and compressibility modulus plot (inset) of 4b at different subphase pH with a compression rate of $10 \text{ cm}^2 \text{ min}^{-1}$, $22 \text{ }^\circ\text{C}$.

The phase transition plateau is longer and broader (in terms of surface pressures) for the lower pH subphases but ends at the same approximate surface pressure (as is more evident from the plot of compressibility modulus, C_s^{-1} , as a function of surface pressure, **Error! Reference source not**

found. (inset)). This suggests that there may be a kinetic effect. To probe this, the isotherms were repeated at lower compression rates, providing the film more time to accommodate the change in the area through reorganization (**Error! Reference source not found.**).

When **4b** is fully deprotonated (pH 11) and the compression rate is reduced, the isotherm exhibits a small shift to smaller molecular areas at low pressures but eventually converges with the isotherm at higher compression rates at high pressures. For pH 6.5, the effect of reducing the compression rate is more prominent: the isotherm exhibits a significant shift to smaller molecular areas, and consequently, the plateau is contracted so that again the isotherms of the two compression rates converge at high surface pressures. Notably the higher-pressure plateaus (around 40 mN m^{-1}) for the fully or partially protonated forms (pH 4 and pH 6.5), show a characteristic shape which is associated with a kinetically controlled transition and overcompression of the film.³⁰⁰

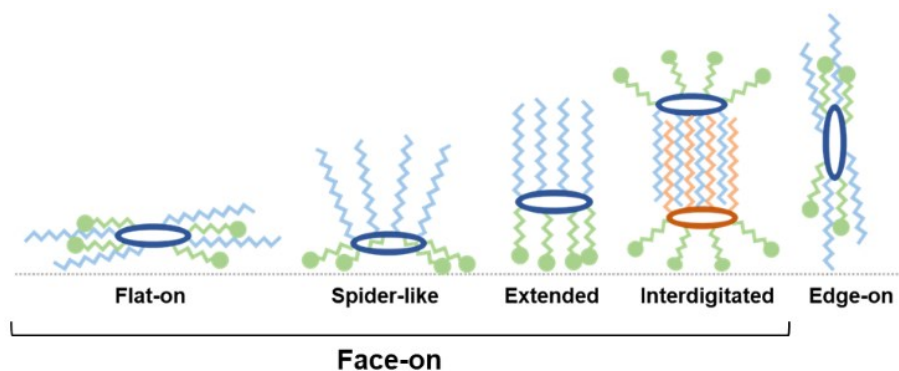


Figure 5.4 Schematic representation of possible interfacial orientation for 4b.

The compressibility moduli for these films at both compression rates are shown in **Error! Reference source not found.** (inset) and **Error! Reference source not found.b.** Below the first plateau the compressibility moduli are in the same range for both $10 \text{ cm}^2 \text{ min}^{-1}$ and $2 \text{ cm}^2 \text{ min}^{-1}$, but pH 11 at the faster compression rate exhibits a distinctly lower maximum compressibility modulus than the (partially or fully) protonated forms. Above this plateau, there is a significant difference in the maximum compressibility modulus for the two compression rates at both pH values, wherein the fully deprotonated form always exhibits a lower compressibility modulus.

At low compression rates, the film is less compressible (higher compressibility modulus) for the protonated forms, with the maximum compressibility modulus increasing from $40\text{-}45 \text{ mN m}^{-1}$ (10

$\text{cm}^2 \text{min}^{-1}$) to $90\text{-}100 \text{ mN m}^{-1}$ ($2 \text{ cm}^2 \text{min}^{-1}$). At pH 11, although the isotherms appear similar, the plateau is less distinct and converges with the collapse at the lower compression rate.

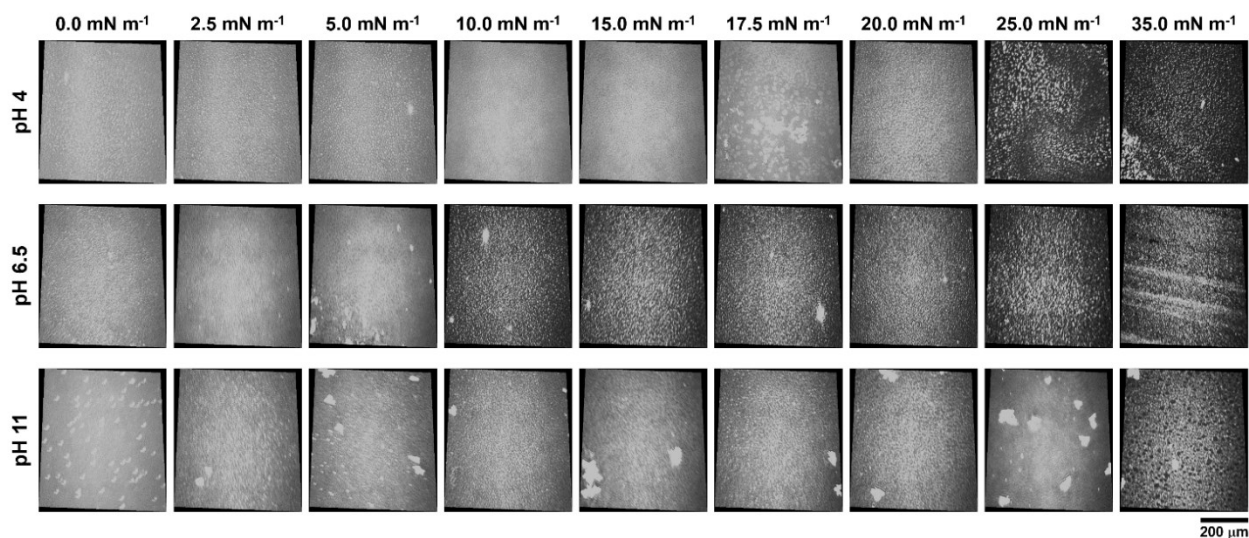


Figure 5.5 Representative BAM images ($620 \mu\text{m} \times 520 \mu\text{m}$) of **4b at different subphase pH values of 4 (top), 6.5 (middle), and 11 (bottom) and surface pressures from 0.0 to 35.0 mN m^{-1} (brightness of -30% and contrast of +20% modification).**

BAM imaging was used to understand the phase transitions that are occurring for **4b** at different pH subphases (Figure 5.5). To allow better equilibration, a slow compression rate was selected. The geometry of the BAM trough is different, and this difference in geometry induced a distinct isotherm shape change at pH 6.5 (**Error! Reference source not found.**), the origin of which may be associated with the distance of the surface pressure sensor relative to the barriers where compression is first occurring. Such geometric influences have been reported for some rigid monolayer systems.¹⁵² As will be discussed, the same phase transitions occur as with the other trough geometry, albeit at different surface pressures. This likely occurs only for pH 6.5 due to the partial protonation state, wherein the degree of protonation throughout the film may be directly affected by the compression process.

For all systems at very high molecular areas and immediately after spreading, phase coexistence of bright domains within a darker continuous phase is observed, confirming the existence of strong intermolecular interactions even at 0.0 mN m^{-1} surface pressure. At low pressures, regions of higher and lower densities of domains can be observed. When the terminal acids are all or mostly

protonated (pH 4 and pH 6.5, respectively), these domains remain small as the film is compressed and the only obvious change after the phase transition plateau is the increase in contrast, indicative of a greater difference in thickness, which occurs at the end of the plateau (between 20 and 25 mN m⁻¹ for pH 4, between 6 and 10 mN m⁻¹ for pH 6.5). Some very bright spots are observed that likely correspond to aggregate formation.

Even when all acid chains are deprotonated at pH 11, the same strong intermolecular interactions exist, driving domain formation at high molecular areas. In addition, the aggregates are larger in diameter and occur at much lower surface pressures. The change in contrast appears more gradual and across a greater range of surface pressures, from 17 mN m⁻¹ to 35 mN m⁻¹ which is also reflected in the isotherm, wherein the transition is less distinct. Comparing the BAM images at 35 mN m⁻¹ for all pH subphases, it is clear that when the acids are deprotonated (charged), the domains formed are less discrete and interconnected.

Ellipsometry measurements were carried out on pH 6.5 and 11 subphases, at both low and high compression rates, and are shown in Figure 5.6. The kinetic effects are observable in the stepwise isotherm used for ellipsometric measurements (**Error! Reference source not found.**), where the decrease in the surface area at a constant pressure is greater for higher compression rates. After the plateau, the isotherms begin to converge, as the majority of the molecular rearrangements have occurred at the lower surface pressures. Higher errors are reported for surface pressures corresponding to the gaseous-condensed phase coexistence and the plateau, both of which represent regions of greater inhomogeneity.

The more negative $\delta\Delta$ values reflect a film that is thicker on average. At pH 6.5, the $\delta\Delta$ values at both compression rates show a gradual increase in magnitude up to the plateau, followed by a relatively constant value. At lower compression rates where the film has more time for reorganization, the films consistently exhibit a larger average thickness. At pH 11, for any given surface pressure, the magnitude of $\delta\Delta$ is greater than the equivalent film at pH 6.5 and these values increase more steeply above 25 mN m⁻¹. Again, the slower compression rate yields a thicker film, however the error bars for the slow compression rate have significantly increased at this pH. Considering the BAM images, we propose that the greater density of large aggregates that may be in the region of interest for the measurements contributes to this error.

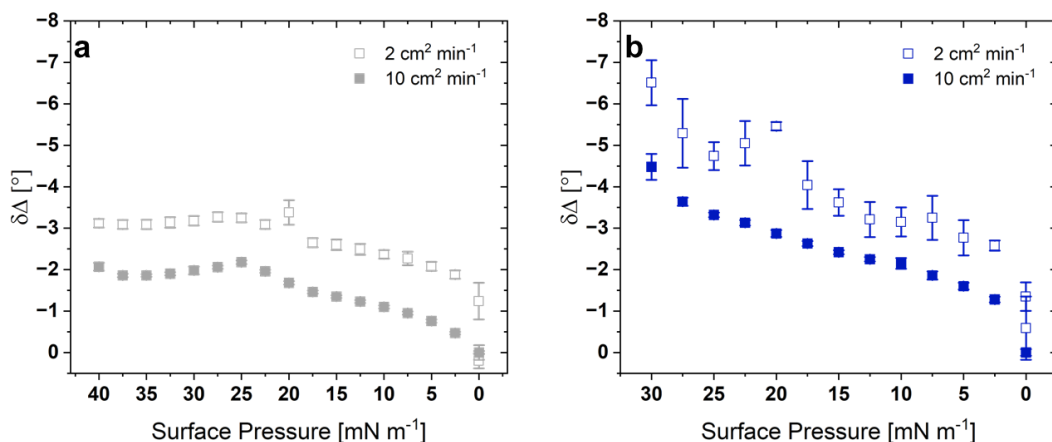


Figure 5.6 Ellipsometric measurements of 4b at the air-water interface at subphase pH 6.5 (a) and pH 11 (b) and for two different compression rates.

AFM imaging was used to evaluate the morphology of **4b** deposited from different pH subphases (Figure 5.7) where the film compression rate was $10 \text{ cm}^2 \text{ min}^{-1}$. For both pH values, at very high molecular areas and immediately after spreading, formation of bright domains distributed throughout the continuous phase is observed. (Figure 5.7a,f).

At large molecular areas and surface pressure of 0.0 mN m^{-1} for both pH values, there are two distinct populations of domains that differ in their height with respect to the continuous phase (a histogram representation of height differences and height profiles is provided in [Error! Reference source not found.](#)). When mostly protonated (pH 6.5), the larger domains are also taller than the very small diameter domains. When all of the acids are deprotonated (pH 11), the shorter domains are much larger in diameter. Both domain phases are slightly taller at higher pH ([Error! Reference source not found.](#)). Additionally, at pH 11, the periodic formation of aggregated material can be observed in some images (data not shown). This may explain the unusually low onset area at this pH.

As the film is compressed, at 2.5 mN m^{-1} (Figure 5.7b,g), although the relative heights are not changing ([Error! Reference source not found.](#)), the density of the higher domains has increased at the expense of the shorter domains. At higher pH, both domain types continue to coexist and both grow in diameter. By 15 mN m^{-1} , just below the plateau, at both pH values, there is only one population of domains by height, although the diameter distribution appears to remain bimodal

(Figure 5.7c,h). At this pressure, small aggregates that are much taller begin to appear. Beyond the plateau, the only major difference is the increased density of aggregates that can be observed; the height difference of the domains to the continuous phase remains about 1 nm. Comparing pH 6.5 and pH 11 above the plateau, the aggregates are more dispersed at pH 6.5 and appear to form at the edges of the domains, while at pH 11, the aggregates are clustered with no clear preference for location (Figure 7d,e,i,j).

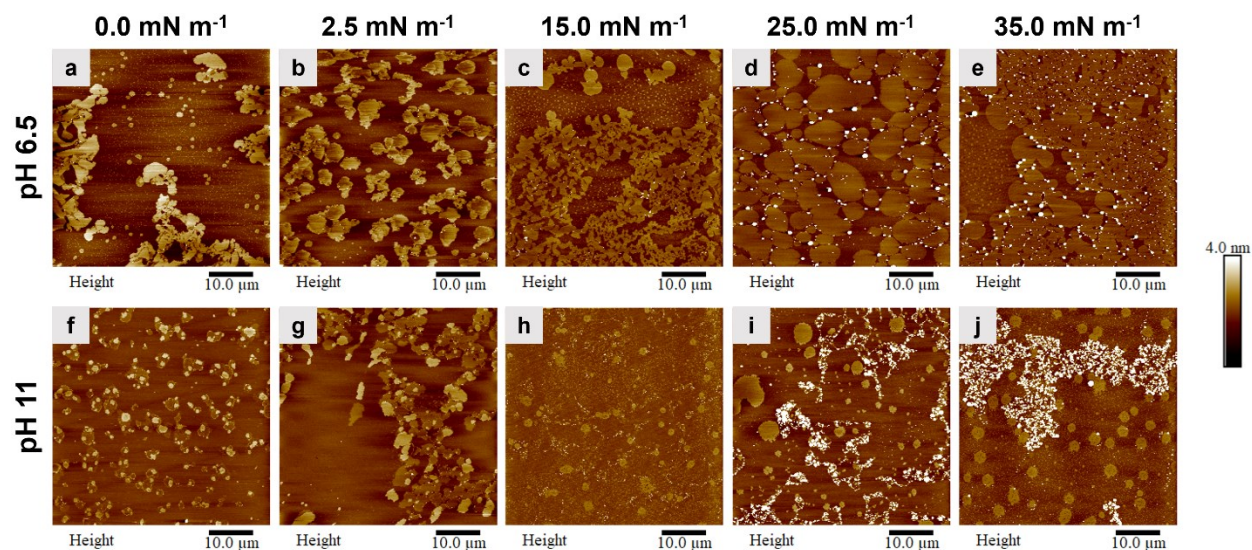


Figure 5.7 AFM images of 4b deposited onto mica at different surface pressures and subphase pHs: pH 6.5 (top) and pH 11 (bottom). Surface pressures from left to right are: 0.0 (a,f), 2.5 (b,g), 15.0 (c,h), 25.0 (d,i), and 35.0 (e,j) mN m^{-1} .

The deprotonation of the acid chains can generate intra- and intermolecular charge repulsion. The change in the balance of charge repulsion and line tension may explain the smaller domains at pH 11.^{119–121} This charge repulsion can also lead to greater chain extension and the resultant height increase of the domains.

GIXD measurements were carried out at two surface pressures before and after the phase transition plateau for both pHs. At pH 6.5 and 15 mN m^{-1} (Figure 5.8a), two peaks are observed, one in-plane and the second one out-of-plane. The positions of the peaks indicate a centered rectangular unit cell with Nearest-Neighbor (NN) tilting of the alkyl chains. The fitting and unit cell parameters are provided in [Error! Reference source not found.](#). Both peak positions in Q_{xy} and the vertical

correlation length correspond to packing of the alkyl chains. At higher surface pressure (35 mN m⁻¹, Figure 5.8b), only one strong first-order peak is observed at $Q_z = 0 \text{ \AA}^{-1}$, representing a hexagonal unit cell with untilted chain packing.

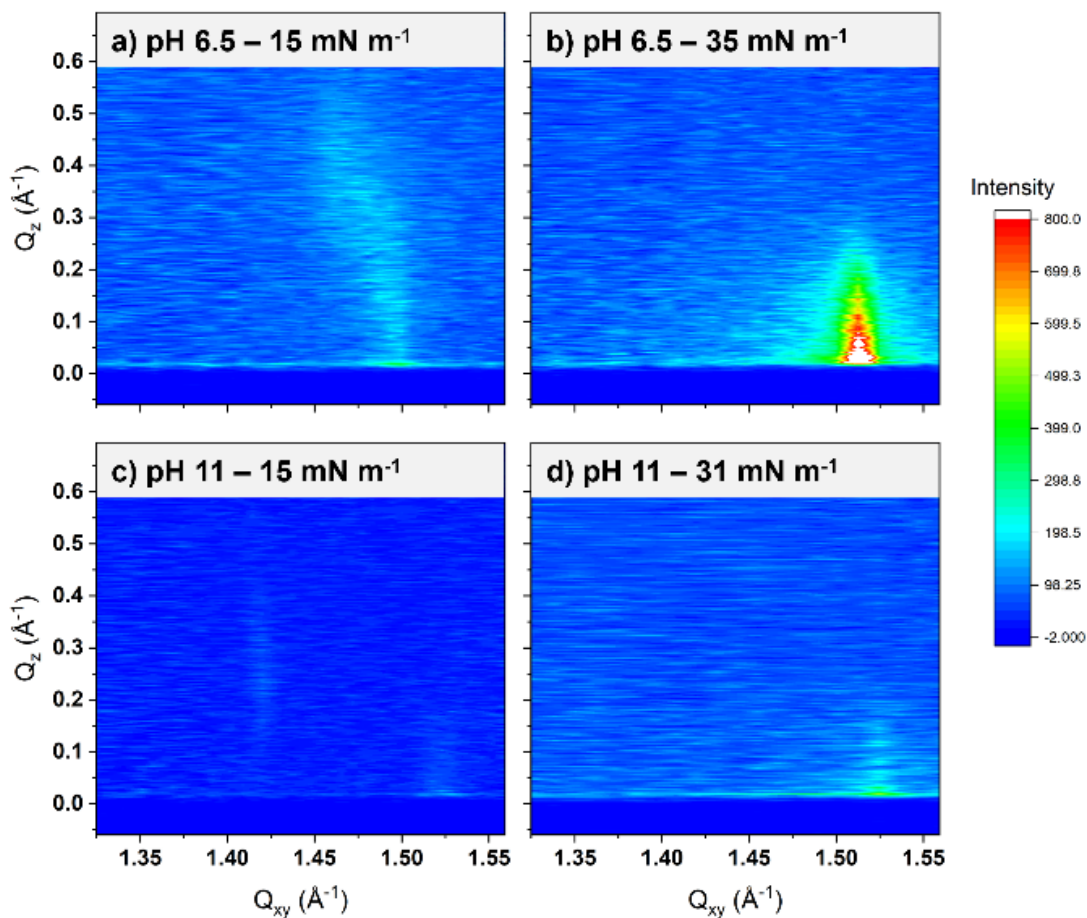


Figure 5.8 GIXD contour plots of X-ray diffraction intensity as a function of Q_{xy} (in-plane) and Q_z (out-of-plane) vector components for 4b: (a) pH 6.5, 15 mN m⁻¹; (b) pH 6.5, 35 mN m⁻¹; (c) pH 11, 15 mN m⁻¹; and (d) pH 11, 31 mN m⁻¹. A rescaled image of 8c is shown in [Error! Reference source not found.](#)

When deprotonated and at a surface pressure of 15 mN m⁻¹, two peaks are observed that are weakly correlated (Figure 5.8c) and that are spread further apart in Q_{xy} . Again, the pattern corresponds to a centered rectangular unit cell with a NN tilt. At 31 mN m⁻¹, after the phase transition and close to the collapse area, there is only one in-plane peak (Figure 5.8d), corresponding to a hexagonal

unit cell with untilted chains. Comparing pH 6.5 and pH 11, the peaks for pH 11 are much weaker in intensity at both surface pressures correlating to a lower coverage of the condensed phase in the region of interest in agreement with the AFM images.

The vertical correlation values obtained for all four diffraction measurements match an alkyl chain length of about 10-13 carbons, in an acceptable range compared to the 12 carbons present in **4b**. But, as the ring area ($\sim 1.2 \text{ nm}^2$) is larger than the cross-sectional area of four alkyl chains per molecule ($\sim 0.8 \text{ nm}^2$), and these diffraction patterns cannot be assigned to a single monolayer packing of **4b** in a spider-like or extended shape (different structure orientations of **4b** were shown in Figure 5.4). The edge-on orientation is not expected to yield crystalline chains. Thus, we propose that the most probable structural orientation for these diffraction patterns would be an interdigitated structure. In order to maximize intermolecular interactions leading to the condensed phase observed and minimize the chain-ring area mismatch, we propose that the rings are staggered (rather than an explicit dimer formation).

The maximum length of the interdigitated structure can be estimated at 3 nm assuming extended C_{12} chains, the thickness of two porphyrin rings, and noncrystalline C_5 chains. From AFM for the structures obtained at pH 6.5, the average relative height above the continuous phase for the condensed phase at surface pressures of 15 and 35 mN m^{-1} is about 1.0 nm, which implies that the continuous phase is about 2 nm thick (a scratch test by AFM confirmed that the continuous (background) phase is not simply the mica substrate). This thickness of the continuous phase is too small for the **4b** molecules to be flat-on. The spider-like conformation would be expected to generate more fluid alkyl chains and would be thicker than the flat-on but may not be sufficient to fully account for this thickness (Figure 5.9). One option to explain the thickness may be a spider conformation sitting atop a flat-on underlying monolayer. This would also be a possible stacked molecule precursor for the formation of the interdigitated structure as the film is compressed.

Considering now the AFM images obtained for surface pressures of 2.5 mN m^{-1} , the condensed phase domains were measured to be around 1.6 nm above the continuous phase. We propose that the domains comprise the spider atop a flat-on monolayer, but that the continuous phase at these lower surface pressures is the simple flat-on orientation. At 0.0 mN m^{-1} the same two structures are observed with an additional intermediate height structure that is 0.6 nm above the continuous phase which could correlate to the thickness of two flat-on structures (considering the GIXD result,

there is no evidence that the ring positions are correlated). Again, the latter could be considered as the precursor to the spider atop a flat-on monolayer.

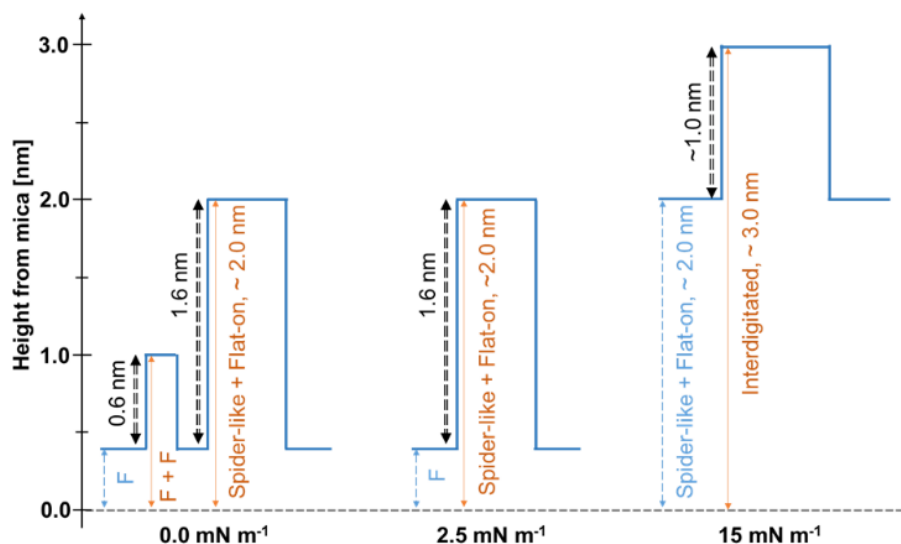


Figure 5.9 Schematic representation of proposed height differences and thicknesses for the different regions observed by AFM for pH 6.5 and possible phase assignments (F: flat-on, F-F: flat-on atop flat-on). The dashed line represents the substrate (mica). The continuous phase height is shown by blue dashed arrows, and the relative heights measured from AFM are shown by black dashed arrows.

The same trend in height differences is observed for films deposited at pH 11 except that (a) the heights obtained are slightly larger by about 0.1 nm, which may result from greater chain extension due to electrostatic repulsion, and (b) the lower domains (attributed to two flat-on molecules) are still observed at 2.5 mN m⁻¹.

Control over the homogeneity of the porphyrin organization and the formation of a condensed monolayer was not afforded to compound **4b** by variation of the pH. An alternative approach to modification of the external parameter is to tailor the TAP molecular structure, in this case, via altering the alkyl chain length. To this end, the C₁₂ chains were replaced with C₅ chains in **4a**, which allows for intramolecular mixing between pentyl chains and acid spacer chains because of their identical length. So, the structurally less amphiphilic **4a** may form more homogeneous films than compound **4b**.

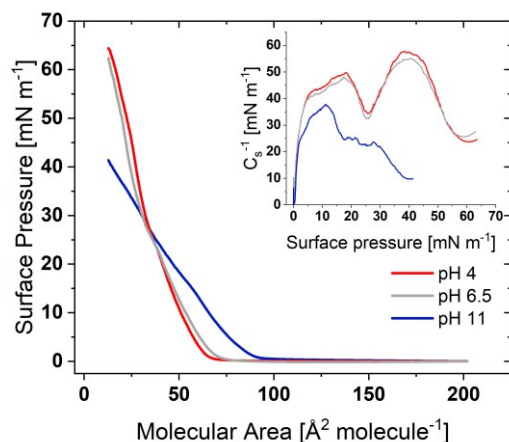


Figure 5.10 Surface pressure-molecular area isotherm and compressibility modulus plot (inset) of 4a at subphase pHs of 4, 6.5, and 11 at a compression rate of 10 cm² min⁻¹.

The surface pressure-molecular area isotherms of **4a** at room temperature, at different pH subphases and a compression rate of 10 cm² min⁻¹, are shown in Figure 5.10. At pH 4 and 6.5, the isotherm presents a surface pressure onset of approximately 75 Å² molecule⁻¹ which would correspond to tightly packed rings (see Error! Reference source not found.). As pH 4 and 6.5 present identical isotherms and given the similarity of **4b** at these two surface pressures, only pH 6.5 films were studied in detail. The pressure onset is followed by a sharp increase in the surface pressure with a change of slope starting at 20 mN m⁻¹. The slope change is subtle but is clearly evident from the compressibility modulus (Error! Reference source not found. (inset)). The maximum compressibility modulus is 57 mN m⁻¹ which is slightly higher than that of the **4b** which reached a maximum of 46 mN m⁻¹. At pH 11, the onset area for **4a** is higher, the slope change occurs at a lower surface pressure, and the compressibility modulus is lower at all surface pressures, all of which may be due to electrostatic repulsion.

BAM images of **4a** at pH 6.5 shown in Figure 5.11 were obtained at the slower compression rate of 7.5 cm² min⁻¹ (matching the compression rate for **4b**). At high molecular areas and 0.0 mN m⁻¹, a significant coverage with condensed-phase domains can be observed. By 2.5 mN m⁻¹, there is a continuous condensed phase with some residual holes. By 5 mN m⁻¹ the film is uniform, and this uniformity persists up to collapse. No bright spots or aggregates were observed at any surface pressure before collapse.

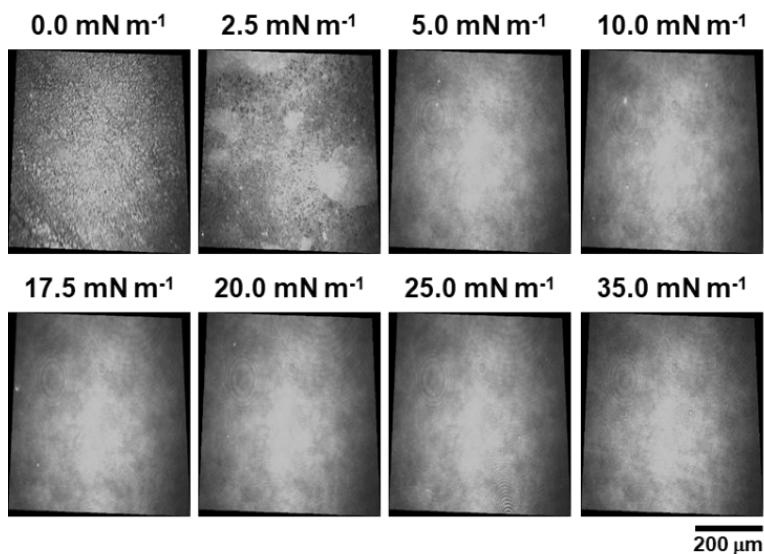


Figure 5.4 Representative BAM images ($620\ \mu\text{m} \times 520\ \mu\text{m}$) of **4a** at a subphase pH of 6.5 and surface pressures from top-left: 0.0, 2.5, 5.0, 10.0, 17.5, 20.0, 25.0, and 35.0 mN m^{-1} . All images reported have been brightness reduced by 30% and contrast enhanced by 20%.

The AFM images of **4a** transferred by LB from a pH 6.5 subphase to a mica substrate are shown in Figure 5.12. At very high molecular areas and immediately after spreading as well as at 2.5 mN m^{-1} , there are regions that appear completely covered with the condensed phase (with or without holes) and others that show domains surrounded by what is presumably the gaseous phase (Figure 5.12a,b). At both surface pressures, the average height of the domains is 1.4 nm. The average depth of the holes is 1.2 nm, but with small diameter holes, these measurements can be underestimated due to the tip geometry.

Notably, at both surface pressures, some of the domain structures grow in a line fiber-like shape that appears to be chains of connected small circular domains. At 5 and 15 mN m^{-1} , the film is mostly homogeneous with residual holes and periodic aggregates appearing which may be the consequence of the deposition as they are not observed by BAM. The transfer ratios for surface pressures below the phase transition plateau (Figure 5.12a-d) are between 1.0 and 1.3, indicating that the structures observed via AFM are a reasonable representation of the structures at the air-water interface. The depth of the background holes stays relatively constant at around 1-1.2 nm.

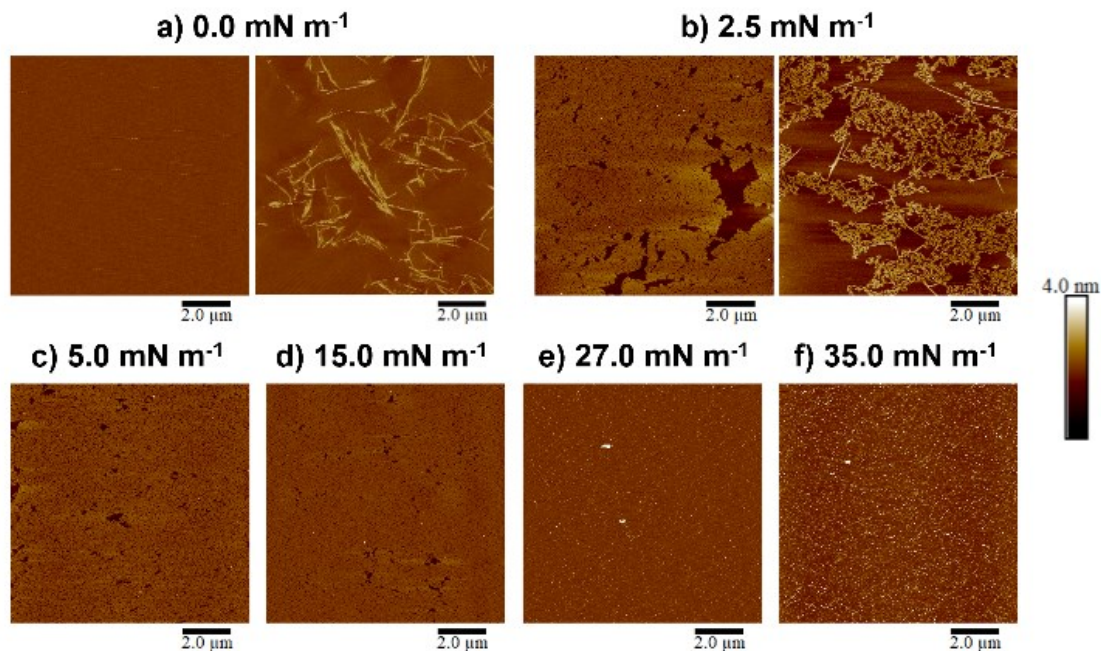


Figure 5.5 AFM images of **4a** deposited onto mica at different surface pressures at a subphase pH of 6.5. Surface pressures from top left: (a) 0.0, (b) 2.5, (c) 5.0, (d) 15.0, (e) 25.0 and (f) 35.0 mN m^{-1} .

Beyond the kink in the isotherm; i.e., at surface pressures above 20 mN m^{-1} , no residual holes can be observed, and the monolayer is fully continuous (Figure 5.12e). After this transition, there is the formation of very small bright spots that have a relative height of 1.2 nm above the condensed phase but with significantly increased height variability. The relative height of these structures increases to 1.9 nm when reaching the surface pressure of 35 mN m^{-1} (Figure 5.12f). At these higher surface pressures, the transfer ratio increases to 3.0 - 3.3, showing that more material is transferred, and indicating multilayer or aggregate formation.

AFM images were also obtained for **4a** films transferred from a pH 11 subphase (**Error! Reference source not found.**). At 0.0 mN m^{-1} and high molecular areas ($150 \text{ \AA}^2 \text{ molecule}^{-1}$), domains with a low height differential (0.2-0.3 nm) from the background can be discerned, but there is already evidence of aggregate material forming. After the pressure onset, the underlying film is relatively homogeneous, and the aggregates increase in lateral coverage as the pressure increases. By 33 mN m^{-1} , the larger aggregates are accompanied by a new population of aggregates that are smaller both vertically and laterally. The aggregate morphology is very similar to that

observed for **4b** at the same pH and in fact, the isotherms are nearly coincidental (**Error! Reference source not found.**). This suggests that charge repulsion plays a strong role in determining the formation of aggregates, regardless of the chain lengths.

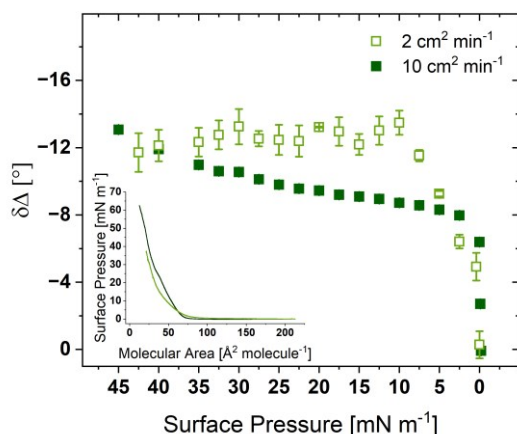


Figure 5.6 Ellipsometric measurements at air-water interface of 4a at subphase pH 6.5 at two different compression rates. Corresponding isotherms are shown in the inset.

Given that the film at pH 6.5 shows the desired homogeneity for thin film applications, ellipsometric measurements were performed at both compression rates and are shown in Figure 5.13. At higher compression rates and as the film is compressed beyond 0.0 mN m^{-1} , there is a gradual increase in the magnitude of $\delta\Delta$, and the $\delta\Delta$ values are higher than any obtained for **4b**. This indicates that the average thickness of the shorter-chain film is larger than that of **4b**, which is likely due to the greater coverage of the condensed phase from the onset; i.e., the lack of significant gaseous regions (flat-on conformation) means an overall thicker film. The extremely small error bars are also indicative of a uniform and coherent film, in agreement with BAM and AFM images. As the surface pressure increases beyond the kink where multilayered/aggregated material appears, the $\delta\Delta$ values begin to increase more steeply. At a lower compression rate where there is more time for reorganization, the isotherm exhibits a small shift in molecular area and the pressure onset appears more rounded. The corresponding ellipsometry measurements show an increase to larger $\delta\Delta$ values upon compression beyond 0.0 mN m^{-1} , exhibiting a larger average thickness. As observed with **4b** at pH 11, the increase in the error bars may reflect a greater proportion of aggregates at this slower compression rate. Notably, for **4a**, the $\delta\Delta$ values converge

at 35 mN m^{-1} , the surface pressure at which aggregate formation was observed by AFM. Thus, the increase in thickness and the errors suggest that at a slower compression rate, the film tends to form aggregates.

The GIXD measurements for **4a** at pH 6.5 are carried out at four different surface pressures (Figure 5.14). Two different sets of peaks are observed for all four surface pressures: one at $Q_{xy} \sim 0.37 \text{ \AA}^{-1}$, corresponding to the ring-ring interactions (Figure 5.14 - second row), and the other at $Q_{xy} 1.4\text{--}1.5 \text{ \AA}^{-1}$ and Q_z out-of-plane with weak correlation, corresponding to the alkyl chain packing (note that for **4b**, a full Q_{xy} scan from 0.3 to 2.4 \AA^{-1} showed no additional peaks, data not shown). As the alkyl chain packing is weak ([Error! Reference source not found.](#)), it was not possible to definitively fit the peaks, and thus only the results of the porphyrin ring packing will be discussed here.

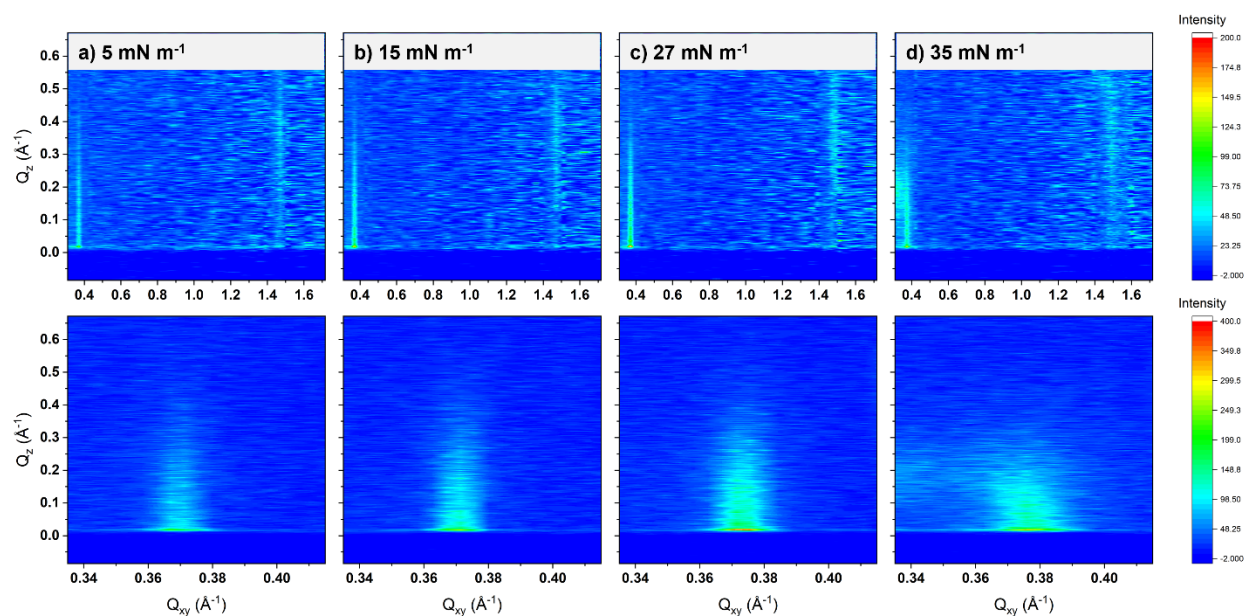


Figure 5.7 GIXD contour plots of X-ray diffraction intensity as a function of Q_{xy} (in-plane) and Q_z (out-of-plane) vector components for **4a** at subphase pH 6.5: (a) 5 mN m^{-1} , (b) 15 mN m^{-1} , (c) 27 mN m^{-1} , and (d) 35 mN m^{-1} . Top row: full range, bottom row: zoomed -in to a smaller Q_{xy} range.

The peaks at smaller Q_{xy} are all in-plane, indicating a hexagonal unit cell with untilted packing. As the surface pressure increases above the kink in the isotherm, the peak begins to broaden, indicative of lower lateral correlation lengths (decreasing from 111 to 77 nm). At the highest

surface pressure measured (35 mN m^{-1}), an additional peak appears out-of-plane, and the main peak begins to bend which we attribute to the formation of the multilayered aggregates, in agreement with the ellipsometry measurements. From the fwhm in the Q_z direction, the vertical correlation lengths all range from 0.8 to 1.2 nm which is in agreement with the film thickness from AFM. The fitting and unit cell parameters are provided in [Error! Reference source not found.](#)

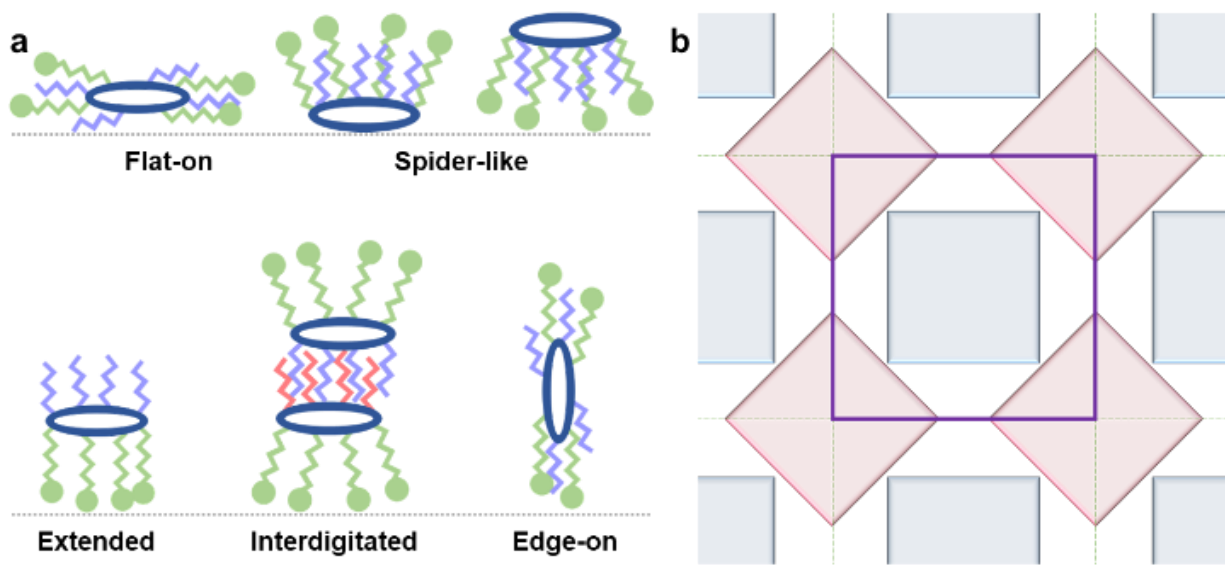


Figure 5.8 Schematic representation of (a) possible interfacial orientations for 4a and (b) proposed orientation of the molecular lattice of the close-packed array of spider-like conformations. Each small square represents one porphyrin ring (1.1 nm length) where the different colors denote different molecular orientations. The large purple square represents the tetragonal unit cell, with the width of 1.96 nm, equal to the a-spacing value calculated from the fitting.

Considering the d-spacing of around 1.7 nm, this corresponds to an a-spacing (center-to-center distance of 1.96 nm), which is far too large for alkyl chain packing. However, the vertical correlation length of approximately 1 nm is too large to be attributed to the porphyrin ring alone (approximate ring thickness of 0.4 nm). An interdigitated structure would generate a longer correlation length and strongly correlated alkyl chain peaks ($Q_{xy} 1.4\text{-}1.5 \text{ \AA}^{-1}$), neither of which are observed (possible interfacial orientations shown in Figure 5.15a). Although the vertical correlation length would agree with the ring diameter for an edge-on orientation, it cannot account for the low Q_{xy} position or the weakly crystalline chains. Thus, we attribute the peaks to a

molecular lattice of spider-like conformations and propose that the molecules form a close-packed array as depicted in Figure 5.15b. This is in agreement with the molecular area at the surface pressure onset, which is close to the minimum area for the porphyrin ring.

5.5. Conclusions

A synthetic approach to achieving octaalkylthio-substituted TAPs with two different substituents on each pyrrole ring is presented. Attachment of 4 alkyl groups and 4 hexanoic ester or acid groups lowers their melting points below room temperature, a rare property for porphyrin derivatives.

In terms of film structure, the length of the alkyl chains has a much more profound effect on the film properties than changing the pH of the subphase, although film morphologies can be altered by a combined adjustment of surface pressure and pH. Both compounds **4a** and **4b** generate films, in which the TAP macrocycle adopts a face-on orientation but also exhibit a transition in the surface pressure-molecular area isotherm that corresponds to growth of the film out-of-plane either as aggregates or as multilayers. The chain mismatch generated by mixing dodecyl and 5-carboxypentyl chains leads to the formation of dimers with interdigitated dodecyl chains. These dimers exhibit well-ordered chain regions but the interdigitation remains inhomogeneous across the surface. On the other hand, matching the chain lengths of the acid and alkyl-terminated chains enables formation of homogeneous Langmuir and LB films in a spider-like conformation attributed to a better fit between the macrocycle footprint and the space requirements of the carboxylic acid groups and alkyl chains. In this case, aggregate formation is delayed until much higher surface pressures enabling deposition of a homogeneous, face-on oriented film.

Chapter 6. Conclusions and Future Directions

This research investigates the Langmuir film organization and structural stability at the air-water interface to control the conditions for optimal film transfer and deposition onto the solid substrate while obtaining highly ordered and hierarchical structures with desired characteristics. The findings of this thesis highlight the critical factors within molecular design that impact self-assembly and play an important role in controlling the properties of two distinct classes of conjugated materials with potential applications in electronic devices. For the heteroatom-doped π -conjugated amphiphilic compounds explored here, the interplay of intra- and intermolecular interactions, including π -interactions, electrostatic forces, and the size of the molecular headgroups and the use of additives, was shown to be essential in tuning the film morphology, organization, and stability. This study demonstrates the importance of optimizing both molecular structure and external conditions to achieve the precise organization and performance needed for advanced optoelectronic and electronic devices.

Both investigated compounds, phosphole-lipids and the alkylated TAPs, exhibit promising self-assembly behavior due to their noncovalent interactions such as π - π interactions as well as amphiphilic characteristics. However, a significant challenge remains in obtaining highly ordered, aggregate-free 2D thin film structures, as strong intermolecular π - π interactions often leads to the direct formation of solid-phase amorphous or crystalline structures.² These strong interactions in these π -conjugated compounds lead them to undergo uncontrolled stacking, aggregation, and polymerization, limiting their utility, despite their promising properties and potential applications.^{29,30}

The BAM and AFM images confirmed that the aggregation, mainly governed by π - π interactions, is a challenge for the Langmuir and LB films of these conjugated surfactants, too. While considering different chemical moieties of these π -conjugated compounds (charged moieties, conjugation and π -interactions, counterion/hydrogen-bonding interactions, chain-chain interactions) and the control over the intermolecular interactions may complicate the structural optimization process, it might provide more alteration flexibilities that we can employ to potentially achieve well-ordered aggregate-free 2D films.

Considering the different inter- and intramolecular interactions within these surfactants and in order to overcome this challenge and obtain well-ordered 2D LB films, both external conditions and chemical composition of these π -conjugated compounds were tuned to achieve the optimal conditions for the formation of hierarchical structures required for electronic and optoelectronic applications.

6.1. Phosphole-based π -conjugated systems

The synthetic flexibility of the phosphole-lipids with their charged headgroups provided the opportunity to explore the impact of ionic interactions and conjugation extension on the Langmuir and LB film organization and behavior. This exploration aimed to optimize the structure of the deposited films for the intended applications. The successful incorporation of phosphole backbone's electronic functionality into self-assembled structures -with the assistance of the amphiphilic nature of their alkyl chains- demonstrated that 2D phosphole-lipid films can be achieved with tunable properties through control of the counterion (both size and concentration), summarized in Figure 6.1. The ability of bromide ions to stabilize well-ordered monolayers without the formation of 3D aggregates is particularly significant for the development of thin-film electronics, offering a promising strategy for building layered architectures.

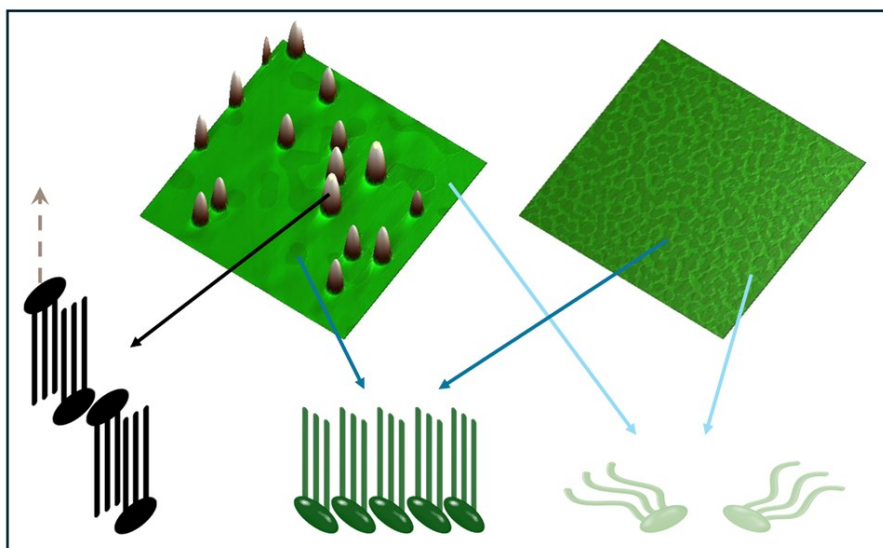


Figure 6.1 Summarized schematic representing the impact of counterion on phosphole-lipid film behavior.

The introduction of aromatic additives to modulate the π -interactions and self-assembly within the phosphole-lipids showed that while additives like phenol influenced the growth pattern of the domains, challenges remained in obtaining aggregate-free, highly ordered 2D films. An improvement to limit the formation of aggregates was obtained by introduction of aromatic additives such as phenolic surfactants. By this approach, the impact of aromatic rings interactions with phosphole-lipids increase as they are kept at the interface (summarized schematic is shown in Figure 6.2). However, the introduction of phenolic surfactants did not lead to obtaining completely aggregate-free 2D films.

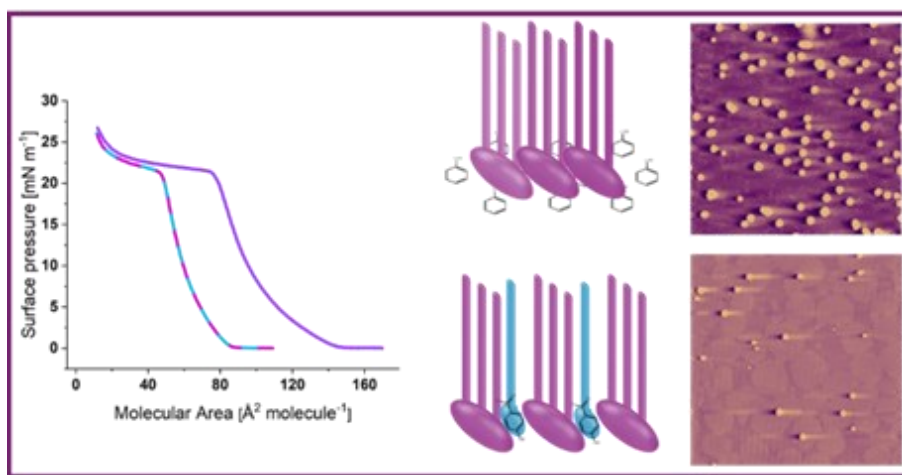


Figure 6.2 Summarized schematic representing the impact of aromatic additives on phosphole-lipid film behavior.

A potential route for enhancing the film order and reducing the aggregation lies in the strategic combination of strong electrostatic interactions (via counterions) with weaker π -interactions (via phenolic additives or surfactants). This route offers a potential pathway to mitigate aggregation and produce the well-organized films required for functional electronic applications.

6.2. Porphyrin-based π -conjugated systems

The combination of alkyl and acid chains in porphyrin-based systems like TAPs not only enhances their self-assembly properties but also allows for deeper evaluation of the impact of protonation state of the carboxylic acids on the monolayer film orientation at both air-water and air-solid

interfaces. Furthermore, the synthetic possibility of achieving structures with varying length of alkyl chains allowed us to optimize the molecular packing in the structure while preserving the macrocycle electronic properties governed by its core.

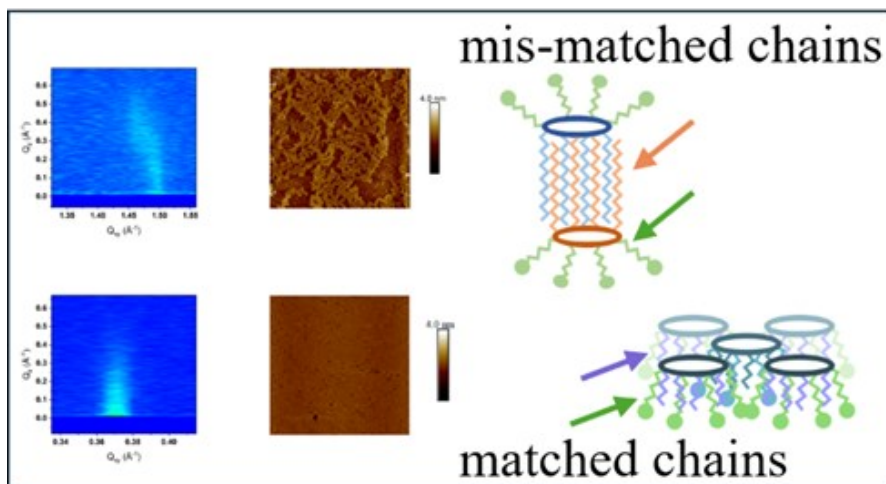


Figure 6.3 Summarized schematic representing the impact of alkyl chain length on TAPs monolayer film behavior.

The study of the TAPs derivatives with varying alkyl chain lengths at different subphase pH revealed that the chain length has a more profound effect on Langmuir and LB film properties than the subphase pH (and consequently charge). The shorter alkyl chains facilitate improved molecular packing and promote homogeneous films. In contrast, longer chains led to inhomogeneous interdigitation, which altered the overall film morphology (Figure 6.3). These findings highlight the importance and need of optimizing chain length and the molecular footprint (relative cross-sectional area of the ring compared to the chains) to achieve the desired surface properties.

6.3. Future directions

Both phosphole- and porphyrin-based π -conjugated compounds exhibit promising structural and electronic properties, making them ideal candidates for further developments to enhance their usage in a broader range of optoelectronic applications. Expanding the investigations on external conditions and how they impact structural orientation, and behavior could offer easier and cost-effective solutions for production processes. The chemical composition of these compounds could

also be modified through the incorporation of more complex polycyclic compounds or functionalized aromatic groups to promote stronger and/or directional inter- and intramolecular interactions, including π -stacking interactions.

6.3.1. Expanding findings on phosphole-based π -conjugated systems

The introduction of bromide as the main counterion and the other halides of chloride and iodide is investigated. As electrostatic interactions exhibit a more prominent impact on the monolayer packing, the use of a wider variety of counterions beyond halides could be explored. This could include the size of the counterion as well as the control over their charge and hydration shell. Such variations can significantly impact how they penetrate into the plane of the phosphole-lipid, intercalate within the molecular arrangement and influence the film organization. Exploring the other counterions that were considered for the synthesis of these phosphole-lipids, such as tetrafluoroborate (BF_4^-), tetraphenylborate (BPh_4^-), and trifluoromethanesulfonate (CF_3SO_3^-) is a choice to consider. Despite potential structural challenges posed by bulkier headgroups, replacing bromide with tetraphenylborate enhances the photophysical properties, particularly in the solid state.⁵⁴ Introducing divalent counterions or structures with more than one binding group that can act as a bridge between the headgroups might be worth considering to assist with anchoring the phosphole-lipids in the interface and hinder the formation of multilayers. A range of structures such as amines (i.e., ethylenediamine), polyols (i.e., ethylene glycol, glycerol), carboxylic acids (i.e., citric acid, maleic acid) and thiol-based structures (i.e., 1,2-ethanedithiol) can act as a cross-linker. This physical cross-linking in the film may alter or enhance the existing electronic properties of the thin deposited films.

Although ionic interactions demonstrated stronger impact, the directional domain growth heavily depends on the strength of the π - π interactions. Thus, introducing a combination of aromatic additives and ionic species could be a promising option for future research on the phosphole-lipids deposited film orientation and behavior. This combined effect can be explored through different approaches. An aromatics and ionic species can be both added to the subphase. An aromatic surfactant can be co-spread with phosphole-lipid on a salt solution as subphase. Also, charged aromatic additives (or surfactants) could be added into the subphase or co-spread with the phosphole-lipids. Comparing the addition of charged aromatic surfactants and the addition of

separate charged species and aromatic additives together and how differently they would influence the phosphole-lipid film organization and behavior provide insight into how different interactions affect phosphole-lipid film stability and organization.

Phosphole-lipids **1** and **3** were the focus of the study in chapters 2 and 3. Regarding the π - π interactions in the headgroup and the extension of the conjugation, phosphole-lipid **4** could be a viable alternative for further Langmuir and LB film study of phosphole-lipids. The bulky phosphole-lipid **4** with extended conjugation, exhibit stronger photophysical properties, including mechanical photoluminescence response in the solid state.⁵⁴ Based on the observations for phosphole-lipid **3**, the potential challenge would be the large size of the headgroup and reduced counterion selectivity. However, a main difference between **3** and **4** is that the conjugation extension in **4** is through a nonfused ring which assists with preserving the structural flexibility (Figure 6.1).⁵⁴ This difference may overcome some of the anticipated limitations in the Langmuir and LB film studies and promote well-oriented 2D films.

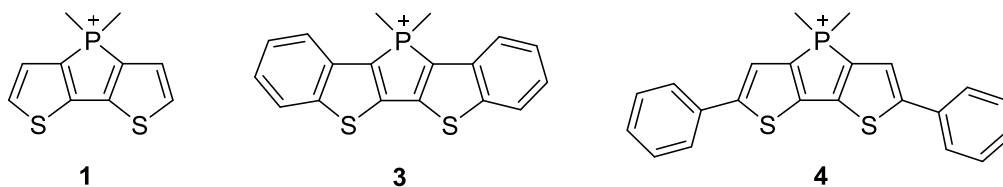


Figure 6.4 Chemical structure of phosphole-lipid 1, 3, and 4, previously reported.⁵⁴

6.3.2. Expanding findings on porphyrin-based π -conjugated systems

The high number of side chains in TAPs provide opportunities to explore the balance between the alkyl chains and carboxylic acid chains. For the synthesis of both short (C_5) and long (C_{12}) alkyl chains investigated here, equal number of alkyl and acid chains were considered. The other possible options to explore would be reducing the number of acid chains that could promote stronger alkyl chain interactions and enhance the molecular packing (stronger GIXD peaks). However, a potential challenge to consider is that reducing the carboxylic acid-water interactions may result in the formation of the edge-on orientation that may not be the preferential arrangement for optoelectronic applications.

The chemical composition of these side chains can be modified (if synthetically accessible) to promote the preferential ordered structures. For example, replacing the carboxylic acid endings by other hydrophilic functional groups such as amines, carbonyls, or hydroxyl groups may be explored without changing the alkyl chain length.

Further insights on the impact of alkyl chains number and lengths on the TAPs Langmuir and LB films structures can be obtained by co-spreading them with single chain fatty acids of the relatively same length. For example, stearic acid with 18 carbons would be a good choice to be co-spread with the longer chain TAP studied (C_{12}). Working with different molar ratios could help to optimize the cross-sectional area of chains relative to the core in order to obtain better film organization. In addition to co-spreading TAPs with fatty acids, a mixture of TAPs with aromatic surfactants can be explored. An aromatic additive/surfactant with functional groups to provide sufficient hydrophilic interactions may anchor the TAPs core in plane (closer to subphase/substrate) and promote an in-plane molecular arrangement.

Similar to the phosphole-lipids study, introducing charged additives and molecules that may serve as crosslinker might assist with anchoring the rings parallel to the subphase and substrate, promoting the face-on orientation in a monolayer film.

A different and challenging approach to achieve homogenous thin films for TAPs would be to focus on the controlled growth of 3D aggregates instead of preventing their formation. The aggregates observed in AFM images for both long and short chain TAPs at both pHs exhibited relatively similar height. Thus, a controlled deposition to promote an oriented aggregates (such as interdigitated arrangement in a lamellar organization) may allow for formation of thicker, but homogenous films. A deeper conceptualization and design evaluation are required to characterize the film and control the orientation of the stacked layers.

Lastly, incorporating metals into the core of TAP macrocycles presents a promising option to enhance their electronic properties and influence their orientation and behavior in Langmuir and LB films. Having metals combined with π -conjugated porphyrin macrocycle may allow for wider range of characterization techniques to be employed to explore the Langmuir and LB films of TAPs derivatives. For example, UV-Vis reflection spectroscopy and/or X-ray fluorescence can be employed for Langmuir films of metalloporphyrin. Grazing incidence wide angle X-ray scattering technique (GIWAXS), scanning tunneling microscopy (STM), scanning electron microscopy

(SEM) or transmission electron microscopy (TEM), and surface-enhanced Raman spectroscopy (SERS) are among the techniques that can be employed for easier surface characterizations of the LB films of porphyrins in presence of metals.

For the deposited 2D films of heteroatom-doped π -conjugated compounds studied in this thesis, only mica was used as the substrate. To broaden the study and include the characterization of deposited thin films regarding their electronic properties, other substrates such as silicon wafers or highly oriented pyrolytic graphite (HOPG) might be chosen. In addition, to enhance the headgroup-substrate interactions for charged phosphonium headgroups in phosphole-lipids or charged TAPs at different subphase pHs, a charged substrate may promote higher order through deposition rather than a neutral one.

In summary, introduction of additives, the use of surfactant mixtures, and modifications to the chemical composition to tune the intermolecular interactions presents an exciting avenue for future research aimed at optimizing the structural organization of the 2D films of heteroatom-doped π -conjugated compounds as building blocks of optoelectronic devices. The contributions of these modifications and their influence on the thin film orientation have a direct or indirect impact on the 2D films electronic properties. Although these impacts were not the primary focus of this thesis, they hold significant potential for future exploration of heteroatom-doped π -conjugated compounds and their applications in electronic and optoelectronic devices.

References

- (1) Hissler, M.; Dyer, P. W.; Réau, R. Linear Organic π -Conjugated Systems Featuring the Heavy Group 14 and 15 Elements. *Coord. Chem. Rev.* **2003**, *244* (1-2), 1–44. [https://doi.org/10.1016/S0010-8545\(03\)00098-5](https://doi.org/10.1016/S0010-8545(03)00098-5).
- (2) Lu, F.; Nakanishi, T. Alkyl- π Engineering in State Control toward Versatile Optoelectronic Soft Materials. *Sci. Technol. Adv. Mater.* **2015**, *16*, 014805. <https://doi.org/10.1088/1468-6996/16/1/014805>.
- (3) Crassous, J.; Réau, R. π -Conjugated Phosphole Derivatives: Synthesis, Optoelectronic Functions and Coordination Chemistry. *Dalton Trans.* **2008**, *48*, 6865–6875. <https://doi.org/10.1039/b810976a>.
- (4) Hall, N. Focus Article: Twenty-Five Years of Conducting Polymers. *Chem. Commun.* **2003**, *1*, 1–4. <https://doi.org/10.1039/b210718j>.
- (5) Skotheim, T. A.; Elsenbaumer, R. L.; Reynolds, J. R. *Handbook of Conducting Polymers Marcel*; Marcel Dekker: New York, 1998.
- (6) Ostroverkhova, O. Organic Optoelectronic Materials: Mechanisms and Applications. *Chem. Rev.* **2016**, *116* (22), 13279–13412. <https://doi.org/10.1021/acs.chemrev.6b00127>.
- (7) Burroughes, J. H.; Bradley, D. D. C.; Brown, A. R.; Marks, R. N.; Mackay, K.; Friend, R. H.; Burns, P. L.; Holmes, A. B. Light-Emitting Diodes Based on Conjugated Polymers. *Nature* **1990**, *347* (6293), 539–541. <https://doi.org/10.1038/347539a0>.
- (8) Baldo, M. A.; O'Brien, D. F.; You, Y.; Shoustikov, A.; Sibley, S.; Thompson, M. E.; Forrest, S. R. Highly Efficient Phosphorescent Emission from Organic Electroluminescent Devices. *Nature* **1998**, *395* (6698), 151–154. <https://doi.org/10.1038/25954>.
- (9) Zou, S.-J.; Shen, Y.; Xie, F.-M.; Chen, J.-D.; Li, Y.-Q.; Tang, J.-X. Recent Advances in Organic Light-Emitting Diodes: Toward Smart Lighting and Displays. *Mater. Chem. Front.* **2020**, *4* (3), 788–820. <https://doi.org/10.1039/C9QM00716D>.
- (10) Hedley, G. J.; Ruseckas, A.; Samuel, I. D. W. Light Harvesting for Organic Photovoltaics. *Chem. Rev.* **2017**, *117* (2), 796–837. <https://doi.org/10.1021/acs.chemrev.6b00215>.
- (11) Horowitz, G. Organic Field-Effect Transistors. *Adv. Mater.* **1998**, *10* (5), 365–377. [https://doi.org/10.1002/\(SICI\)1521-4095\(199803\)10:5%3C365::AID-ADMA365%3E3.0.CO;2-U](https://doi.org/10.1002/(SICI)1521-4095(199803)10:5%3C365::AID-ADMA365%3E3.0.CO;2-U)
- (12) Bagchi, K.; Ediger, M. D. Controlling Structure and Properties of Vapor-Deposited Glasses of Organic Semiconductors: Recent Advances and Challenges. *J. Phys. Chem. Lett.* **2020**, *11* (17), 6935–6945. <https://doi.org/10.1021/acs.jpcclett.0c01682>.
- (13) Sandanayaka, A. S. D.; Matsushima, T.; Bencheikh, F.; Terakawa, S.; Potscavage, W. J.; Qin, C.; Fujihara, T.; Goushi, K.; Ribierre, J. C.; Adachi, C. Indication of Current-Injection Lasing from an Organic Semiconductor. *Appl. Phys. Express* **2019**, *12* (6). <https://doi.org/10.7567/1882-0786/ab1b90>.
- (14) Babudri, F.; Farinola, G. M.; Naso, F. Synthesis of Conjugated Oligomers and Polymers: The Organometallic Way. *J. Mater. Chem.* **2004**, *14* (1), 11. <https://doi.org/10.1039/b309515k>.

- (15) Drain, C. M.; Varotto, A.; Radivojevic, I. Self-Organized Porphyrinic Materials. *Chem. Rev.* **2009**, *109* (5), 1630–1658. <https://doi.org/10.1021/cr8002483>.
- (16) Çaldıran, Z.; Erkem, Ü.; Baltakesmez, A.; Biber, M. Effects of the PENTACENE as Doping Material on the Power Conversion Efficiency of P3HT:PCBM Based Ternary Organic Solar Cells. *Physica B Condens. Matter* **2021**, *607*, 412859. <https://doi.org/10.1016/j.physb.2021.412859>.
- (17) Wang, Z.; Lou, Y.; Naka, S.; Okada, H. High Efficiency Rubrene Based Inverted Top-Emission Organic Light Emitting Devices with a Mixed Single Layer. *J. Lumin.* **2010**, *130* (7), 1198–1202. <https://doi.org/10.1016/j.jlumin.2010.02.021>.
- (18) Orosz, G.; Givens, R. S.; Schowen, R. L. Chemiluminescence Arising from the Interaction of Rubrene with Intermediates Derived from Hydrogen Peroxide and Bis(2,4-Dinitrophenyl) Oxalate (DNPO): Quantum Yield and Carbondioxide Yield. *Anal. Chim. Acta* **1992**, *266* (2), 219–223. [https://doi.org/10.1016/0003-2670\(92\)85046-9](https://doi.org/10.1016/0003-2670(92)85046-9).
- (19) Kausar, A. Breakthroughs of Fullerene in Optoelectronic Devices—An Overview. *Hyb. Adv.* **2024**, *6*, 100233. <https://doi.org/10.1016/j.hybadv.2024.100233>.
- (20) Yamaguchi, S.; Akiyama, S.; Tamao, K. Colorimetric Fluoride Ion Sensing by Boron-Containing π -Electron Systems. *J. Am. Chem. Soc.* **2001**, *123* (46), 11372–11375. <https://doi.org/10.1021/ja015957w>.
- (21) Aygül, U.; Hintz, H.; Egelhaaf, H.-J.; Distler, A.; Abb, S.; Peisert, H.; Chassé, T. Energy Level Alignment of a P3HT/Fullerene Blend during the Initial Steps of Degradation. *J. Phys. Chem. C* **2013**, *117* (10), 4992–4998. <https://doi.org/10.1021/jp4004642>.
- (22) Hambsch, M.; Erdmann, T.; Chew, A. R.; Bernstorff, S.; Salleo, A.; Kiriy, A.; Voit, B.; Mannsfeld, S. C. B. Increased Charge Carrier Mobility and Molecular Packing of a Solution Sheared Diketopyrrolopyrrole-Based Donor–Acceptor Copolymer by Alkyl Side Chain Modification. *J. Mater. Chem. C* **2019**, *7* (12), 3665–3674. <https://doi.org/10.1039/C8TC06255B>.
- (23) Choi, J.; Kim, K.-H.; Yu, H.; Lee, C.; Kang, H.; Song, I.; Kim, Y.; Oh, J. H.; Kim, B. J. Importance of Electron Transport Ability in Naphthalene Diimide-Based Polymer Acceptors for High-Performance, Additive-Free, All-Polymer Solar Cells. *Chem. Mater.* **2015**, *27* (15), 5230–5237. <https://doi.org/10.1021/acs.chemmater.5b01274>.
- (24) Fan, X.; Stott, N. E.; Zeng, J.; Li, Y.; Ouyang, J.; Chu, L.; Song, W. PEDOT:PSS Materials for Optoelectronics, Thermoelectrics, and Flexible and Stretchable Electronics. *J. Mater. Chem. A* **2023**, *11* (35), 18561–18591. <https://doi.org/10.1039/D3TA03213B>.
- (25) Grobosch, M.; Schmidt, C.; Kraus, R.; Knupfer, M. Electronic Properties of Transition Metal Phthalocyanines: The Impact of the Central Metal Atom (d^5 - d^{10}). *Org. Electron* **2010**, *11* (9), 1483–1488. <https://doi.org/10.1016/j.orgel.2010.06.006>.
- (26) Del Caño, T.; Aroca, R.; De Saja, J. A.; Rodriguez-Mendez, M. L. Langmuir - Blodgett Mixed Films of Titanyl(IV) Phthalocyanine and Arachidic Acid. Molecular Orientation and Film Structure. *Langmuir* **2003**, *19* (9), 3747–3751. <https://doi.org/10.1021/la020825h>.
- (27) Law, K. Yee. Organic Photoconductive Materials: Recent Trends and Developments. *Chem. Rev.* **1993**, *93* (1), 449–486. <https://doi.org/10.1021/cr00017a020>.

- (28) Tsuzuki, T.; Shirota, Y.; Rostalski, J.; Meissner, D. The Effect of Fullerene Doping on Photoelectric Conversion Using Titanyl Phthalocyanine and a Perylene Pigment. *Sol. Energy Mater. Sol. Cells* **2000**, *61* (1), 1–8. [https://doi.org/10.1016/S0927-0248\(99\)00091-4](https://doi.org/10.1016/S0927-0248(99)00091-4).
- (29) Moonen, P. F.; Yakimets, I.; Huskens, J. Fabrication of Transistors on Flexible Substrates: From Mass-Printing to High-Resolution Alternative Lithography Strategies. *Adv. Mater.* **2012**, *24* (41), 5526–5541. <https://doi.org/10.1002/adma.201202949>.
- (30) Lei, T.; Pei, J. Solution-Processed Organic Nano- and Micro-Materials: Design Strategy, Growth Mechanism and Applications. *J. Mater. Chem.* **2012**, *22* (3), 785–798. <https://doi.org/10.1039/C1JM14599A>.
- (31) Shi, Y.; Zhang, F.; Linhardt, R. J. Porphyrin-Based Compounds and Their Applications in Materials and Medicine. *Dyes Pigm.* **2021**, *188*, 109136. <https://doi.org/10.1016/j.dyepig.2021.109136>.
- (32) Wang, Z.; Gelfand, B. S.; Dong, P.; Trudel, S.; Baumgartner, T. Tuning the Aggregation-Induced Enhanced Emission Behavior and Self-Assembly of Phosphole-Lipids. *J. Mater. Chem. C* **2016**, *4* (14), 2936–2944. <https://doi.org/10.1039/c5tc03311j>.
- (33) Baumgartner, T.; Réau, R. Organophosphorus π -Conjugated Materials. *Chem. Rev.* **2006**, *106* (11), 4681–4727. <https://doi.org/10.1021/cr040179m>.
- (34) Duffy, M. P.; Delaunay, W.; Bouit, P. A.; Hissler, M. π -Conjugated Phospholes and Their Incorporation into Devices: Components with a Great Deal of Potential. *Chem. Soc. Rev.* **2016**, *45* (19), 5296–5310. <https://doi.org/10.1039/c6cs00257a>.
- (35) Nyulászi, L. Aromaticity of Phosphorus Heterocycles. *Chem. Rev.* **2001**, *101* (5), 1229–1246. <https://doi.org/10.1021/cr990321x>.
- (36) Baumgartner, T.; Neumann, T.; Wirges, B. The Dithieno[3,2-*b*:2',3'-*d*]Phosphole System: A Novel Building Block for Highly Luminescent Π -Conjugated Materials. *Angew. Chem. Int. Ed.* **2004**, *43* (45), 6197–6201. <https://doi.org/10.1002/anie.200461301>.
- (37) Katritzky, A. R.; Rees, C. W. *Comprehensive Heterocyclic Chemistry*; Elsevier science, 1984. <https://doi.org/10.1016/C2009-0-15932-9>.
- (38) Mathey, F. The Organic Chemistry of Phospholes. *Chem. Rev.* **1988**, *88* (2), 429–453. <https://doi.org/10.1021/cr00084a005>.
- (39) Delaere, D.; Dransfeld, A.; Nguyen, M. T.; Vanquickenborne, L. G. Theoretical Study of the Structure - Property Relationship in Phosphole Monomers. *J. Org. Chem.* **2000**, *65* (9), 2631–2636. <https://doi.org/10.1021/jo991373p>.
- (40) Quin, L. D.; Keglevich, G.; Ionkin, A. S.; Kalgutkar, R.; Szalontai, G. Phospholes with Reduced Pyramidal Character from Steric Crowding. 1. Synthesis and NMR Characterization of 1-(2,4-Di-*Tert* -Butyl-6-Methylphenyl)-3-Methylphosphole. *J. Org. Chem.* **1996**, *61* (22), 7801–7807. <https://doi.org/10.1021/jo960640d>.
- (41) Keglevich, G.; Böcskei, Z.; Keserü, G. M.; Újszászy, K.; Quin, L. D. 1-(2,4,6-Tri-*Tert* -Butylphenyl)-3-Methylphosphole: A Phosphole with a Significantly Flattened Phosphorus Pyramid Having Pronounced Characteristics of Aromaticity. *J. Am. Chem. Soc.* **1997**, *119* (22), 5095–5099. <https://doi.org/10.1021/ja970463d>.

- (42) Nyulaszi, L.; Keglevich, G.; Quin, L. D. Phospholes with Reduced Pyramidal Character from Steric Crowding. 2. Photoelectron Spectral Evidence for Some Electron Delocalization in 1-(2,4-Di-*Tert*-Butyl-6-Methylphenyl)-3-Methylphosphole. *J. Org. Chem.* **1996**, *61* (22), 7808–7812. <https://doi.org/10.1021/jo9606416>.
- (43) Delaere, D.; Nguyen, M. T.; Vanquickenborne, L. G. Structure–Property Relationships in Phosphole Oligomers: A Theoretical Insight. *J. Organomet. Chem.* **2002**, *643–644*, 194–201. [https://doi.org/10.1016/S0022-328X\(01\)01274-8](https://doi.org/10.1016/S0022-328X(01)01274-8).
- (44) Susumu, K.; Therien, M. J. Decoupling Optical and Potentiometric Band Gaps in π -Conjugated Materials. *J. Am. Chem. Soc.* **2002**, *124* (29), 8550–8552. <https://doi.org/10.1021/ja0203925>.
- (45) Roncali, J. Synthetic Principles for Bandgap Control in Linear π -Conjugated Systems. *Chem. Rev.* **1997**, *97* (1), 173–206. <https://doi.org/10.1021/cr950257t>.
- (46) Schleyer, P. von R.; Maerker, C.; Dransfeld, A.; Jiao, H.; van Eikema Hommes, N. J. R. Nucleus-Independent Chemical Shifts: A Simple and Efficient Aromaticity Probe. *J. Am. Chem. Soc.* **1996**, *118* (26), 6317–6318. <https://doi.org/10.1021/ja960582d>.
- (47) Su, H. C.; Fadhel, O.; Yang, C. J.; Cho, T. Y.; Fave, C.; Hissler, M.; Wu, C. C.; Réau, R. Toward Functional π -Conjugated Organophosphorus Materials: Design of Phosphole-Based Oligomers for Electroluminescent Devices. *J. Am. Chem. Soc.* **2006**, *128* (3), 983–995. <https://doi.org/10.1021/ja0567182>.
- (48) He, X.; Lin, J. Bin; Kan, W. H.; Baumgartner, T. Phosphinine Lipids: A Successful Marriage between Electron-Acceptor and Self-Assembly Features. *Angew. Chem. Int. Ed.* **2013**, *52* (34), 8990–8994. <https://doi.org/10.1002/anie.201303729>.
- (49) Bouit, P.-A.; Escande, A.; Szűcs, R.; Szieberth, D.; Lescop, C.; Nyulászi, L.; Hissler, M.; Réau, R. Dibenzophosphapentaphenes: Exploiting P Chemistry for Gap Fine-Tuning and Coordination-Driven Assembly of Planar Polycyclic Aromatic Hydrocarbons. *J. Am. Chem. Soc.* **2012**, *134* (15), 6524–6527. <https://doi.org/10.1021/ja300171y>.
- (50) Wu, B.; Santra, M.; Yoshikai, N. A Highly Modular One-Pot Multicomponent Approach to Functionalized Benzo[b]Phosphole Derivatives. *Angew. Chem. Int. Ed.* **2014**, *53* (29), 7543–7546. <https://doi.org/10.1002/anie.201404019>.
- (51) Diring, S.; Camerel, F.; Donnio, B.; Dintzer, T.; Toffanin, S.; Capelli, R.; Muccini, M.; Ziessel, R. Luminescent Ethynyl–Pyrene Liquid Crystals and Gels for Optoelectronic Devices. *J. Am. Chem. Soc.* **2009**, *131* (50), 18177–18185. <https://doi.org/10.1021/ja908061q>.
- (52) Ajayaghosh, A.; Praveen, V. K.; Vijayakumar, C. Organogels as Scaffolds for Excitation Energy Transfer and Light Harvesting. *Chem. Soc. Rev.* **2008**, *37* (1), 109–122. <https://doi.org/10.1039/B704456A>.
- (53) He, X.; Lin, J. Bin; Kan, W. H.; Dong, P.; Trudel, S.; Baumgartner, T. Molecular Engineering of “Click”-Phospholes towards Self-Assembled Luminescent Soft Materials. *Adv. Funct. Mater.* **2014**, *24* (7), 897–906. <https://doi.org/10.1002/adfm.201302294>.
- (54) Ren, Y.; Kan, W. H.; Henderson, M. A.; Bomben, P. G.; Berlinguette, C. P.; Thangadurai, V.; Baumgartner, T. External-Stimuli Responsive Photophysics and Liquid Crystal Properties of Self-

- Assembled “Phosphole-Lipids.” *J. Am. Chem. Soc.* **2011**, *133* (42), 17014–17026. <https://doi.org/10.1021/ja206784f>.
- (55) Cárdenas-Jirón, G.; Borges-Martínez, M.; Mera-Adasme, R.; Pino-Rios, R. Quantum Chemical Studies of Porphyrin- and Expanded Porphyrin-based Systems and Their Potential Applications in Nanoscience. *Latin America Research Review. Int J. Quantum Chem.* **2019**, *119* (2) e25821. <https://doi.org/10.1002/qua.25821>.
- (56) Tang, C. W.; Albrecht, A. C. Photovoltaic Effects of Metal–Chlorophyll-a–Metal Sandwich Cells. *J. Chem. Phys.* **1975**, *62* (6), 2139–2149. <https://doi.org/10.1063/1.430780>.
- (57) Singh, S.; Aggarwal, A.; Bhupathiraju, N. V. S. D. K.; Arianna, G.; Tiwari, K.; Drain, C. M. Glycosylated Porphyrins, Phthalocyanines, and Other Porphyrinoids for Diagnostics and Therapeutics. *Chem. Rev.* **2015**, *115* (18), 10261–10306. <https://doi.org/10.1021/acs.chemrev.5b00244>.
- (58) Lanzilotto, A.; Kyropoulou, M.; Constable, E. C.; Housecroft, C. E.; Meier, W. P.; Palivan, C. G. Porphyrin-Polymer Nanocompartments: Singlet Oxygen Generation and Antimicrobial Activity. *J. Biol. Inorg. Chem.* **2018**, *23* (1), 109–122. <https://doi.org/10.1007/s00775-017-1514-8>.
- (59) Akbar, A.; Khan, S.; Chatterjee, T.; Ghosh, M. Unleashing the Power of Porphyrin Photosensitizers: Illuminating Breakthroughs in Photodynamic Therapy. *J. Photochem. Photobiol. B* **2023**, *248*, 112796. <https://doi.org/10.1016/j.jphotobiol.2023.112796>.
- (60) Wang, F.; Li, C.; Cheng, J.; Yuan, Z. Recent Advances on Inorganic Nanoparticle-Based Cancer Therapeutic Agents. *Int. J. Environ. Res. Public Health* **2016**, *13* (12), 1182. <https://doi.org/10.3390/ijerph13121182>.
- (61) Lovejoy, K. S.; Lippard, S. J. Non-Traditional Platinum Compounds for Improved Accumulation, Oral Bioavailability, and Tumor Targeting. *Dalton Trans.* **2009**, No. 48, 10651. <https://doi.org/10.1039/b913896j>.
- (62) Rusanov, A. I.; Chizhova, N. V.; Likhonina, A. E.; Mamardashvili, N. Z. Synthesis, Structures, and Spectral Properties of Octa(2,6-Difluorophenyl)Tetraazaporphyrin and Its Cu(II) and Ni(II) Complexes. *Russ. J. Inorg. Chem.* **2023**, *68* (8), 979–987. <https://doi.org/10.1134/S0036023623601137>.
- (63) Chumakov, D. E.; Khoroshutin, A. V.; Anisimov, A. V.; Kobrakov, K. I. Bromination of Porphyrins (Review). *Chem. Heterocycl. Compd.* **2009**, *45* (3), 259–283. <https://doi.org/10.1007/s10593-009-0277-8>.
- (64) Stuzhin, P. A.; Goryachev, M. Yu.; Ivanova, S. S.; Nazarova, A.; Pimkov, I.; Koifman, O. I. Perfluorinated Porphyrazines 1: Synthesis and UV-Vis Spectral Study of Perfluorinated Octaphenylporphyrazine and Its Indium(III) Complex. *J. Porphyr. Phthalocyanines* **2013**, *17* (08n09), 905–912. <https://doi.org/10.1142/S1088424613500892>.
- (65) Adler, A. D.; Longo, F. R.; Kampas, F.; Kim, J. On the Preparation of Metalloporphyrins. *J. Inorg. Nucl. Chem.* **1970**, *32* (7), 2443–2445. [https://doi.org/10.1016/0022-1902\(70\)80535-8](https://doi.org/10.1016/0022-1902(70)80535-8).
- (66) Liu, J.-J.; Wang, J.; Chen, Q.-Y.; Chen, F.; Wang, G.-J. Photoresponsive Nanoarchitectonics Based on Copper-Porphyrins for Near-Infrared-Enhanced Bacterial Treatment. *ACS Omega* **2024**, *9* (23), 24513–24519. <https://doi.org/10.1021/acsomega.4c00496>.

- (67) Mamardashvili, N. Zh.; Koifman, O. I. Porphyrin-Calix[4]Arenes. *Russ. J. Org. Chem.* **2005**, *41* (6), 787–806. <https://doi.org/10.1007/s11178-005-0247-2>.
- (68) Lupton, J. M. A Molecular Thermometer Based on Long-Lived Emission from Platinum Octaethyl Porphyrin. *Appl. Phys. Lett.* **2002**, *81* (13), 2478–2480. <https://doi.org/10.1063/1.1509115>.
- (69) Engeser, M.; Fabbrizzi, L.; Licchelli, M.; Sacchi, D. A Fluorescent Molecular Thermometer Based on the Nickel(II) High-Spin/Low-Spin Interconversion. *Chem. Commun.* **1999**, *13*, 1191–1192. <https://doi.org/10.1039/a901931f>.
- (70) Tasso, T. T.; Furuyama, T.; Mack, J.; Nyokong, T.; Kobayashi, N. Synthesis and Photophysical Investigation of Tetraazaporphyrin Substituted with Aggregation-Induced Emission (AIE) Active Moieties. *Eur. J. Inorg. Chem.* **2015**, *2015* (33), 5516–5522. <https://doi.org/10.1002/ejic.201500726>.
- (71) He, J.; Benkö, G.; Korodi, F.; Polívka, T.; Lomoth, R.; Åkermark, B.; Sun, L.; Hagfeldt, A.; Sundström, V. Modified Phthalocyanines for Efficient Near-IR Sensitization of Nanostructured TiO₂ Electrode. *J. Am. Chem. Soc.* **2002**, *124* (17), 4922–4932. <https://doi.org/10.1021/ja0178012>.
- (72) Palacin, S. Phthalocyanines in Langmuir and Langmuir–Blodgett Films: From Molecular Design to Supramolecular Architecture. *Adv. Colloid Interface Sci.* **2000**, *87* (2–3), 165–181. [https://doi.org/10.1016/S0001-8686\(99\)00043-3](https://doi.org/10.1016/S0001-8686(99)00043-3).
- (73) Chen, Y.; Li, A.; Huang, Z.-H.; Wang, L.-N.; Kang, F. Porphyrin-Based Nanostructures for Photocatalytic Applications. *Nanomaterials* **2016**, *6* (3), 51. <https://doi.org/10.3390/nano6030051>.
- (74) Ishihara, K. M.; Tian, F. Semiconducting Langmuir–Blodgett Films of Porphyrin Paddle-Wheel Frameworks for Photoelectric Conversion. *Langmuir* **2018**, *34* (51), 15689–15699. <https://doi.org/10.1021/acs.langmuir.8b03236>.
- (75) Fouriaux, S.; Armand, F.; Araspin, O.; Ruau-del-Teixier, A.; Maya, E. M.; Vazquez, P.; Torres, T. Effect of the Metal on the Organization of Tetraamidometallophthalocyanines in Langmuir–Blodgett Films. *J. Phys. Chem.* **1996**, *100* (42), 16984–16988. <https://doi.org/10.1021/jp961225s>.
- (76) Gaffo, L.; Constantino, C. J. L.; Moreira, W. C.; Aroca, R. F.; Oliveira, O. N. Atomic Force Microscopy and Micro-Raman Imaging of Mixed Langmuir–Blodgett Films of Ytterbium Bisphthalocyanine and Stearic Acid. *Langmuir* **2002**, *18* (9), 3561–3566. <https://doi.org/10.1021/la011234e>.
- (77) Ahmida, M.; Dufour, S.; Li, H. S.; Kayal, H.; Schmidt, R.; Dewolf, C. E.; Eichhorn, S. H. Face- and Edge-on Orientations of Octa-Acid and -Alcohol Substituted Tetraazaporphyrins in Langmuir and Langmuir-Blodgett Monolayers. *Soft Matter* **2013**, *9* (3), 811–819. <https://doi.org/10.1039/c2sm27064a>.
- (78) Lin, C.; Chen, Q.; Yi, S.; Wang, M.; Regen, S. L. Polyelectrolyte Multilayers on PTMSP as Asymmetric Membranes for Gas Separations: Langmuir-Blodgett versus Self-Assembly Methods of Anchoring. *Langmuir* **2014**, *30* (3), 687–691. <https://doi.org/10.1021/la404660f>.
- (79) Yokoyama, D. Molecular Orientation in Small-Molecule Organic Light-Emitting Diodes. *J. Mater. Chem.* **2011**, *21* (48), 19187. <https://doi.org/10.1039/c1jm13417e>.

- (80) Menke, S. M.; Luhman, W. A.; Holmes, R. J. Tailored Exciton Diffusion in Organic Photovoltaic Cells for Enhanced Power Conversion Efficiency. *Nat. Mater.* **2013**, *12* (2), 152–157. <https://doi.org/10.1038/nmat3467>.
- (81) Park, B.; In, I.; Gopalan, P.; Evans, P. G.; King, S.; Lyman, P. F. Enhanced Hole Mobility in Ambipolar Rubrene Thin Film Transistors on Polystyrene. *Appl. Phys. Lett.* **2008**, *92* (13). <https://doi.org/10.1063/1.2904964>.
- (82) Zheng, Y.-Q.; Zhang, J.; Yang, F.; Komino, T.; Wei, B.; Zhang, J.; Wang, Z.; Pu, W.; Yang, C.; Adachi, C. Influence of Deposition Substrate Temperature on the Morphology and Molecular Orientation of Chloroaluminum Phthalocyanine Films as Well the Performance of Organic Photovoltaic Cells. *Nanotechnology* **2015**, *26* (40), 405202. <https://doi.org/10.1088/0957-4484/26/40/405202>.
- (83) Otsuki, E.; Sato, H.; Kawakami, A.; Taka, H.; Kita, H.; Usui, H. Vapor Deposition Polymerization of Vinyl Compounds and Fabrication of OLED Having Double Emissive Layers. *Thin Solid Films* **2009**, *518* (2), 703–706. <https://doi.org/10.1016/j.tsf.2009.07.073>.
- (84) Muroyama, M.; Saito, I.; Yokokura, S.; Tanaka, K.; Usui, H. Selective Patterning of Organic Light-Emitting Diodes by Physical Vapor Deposition of Photosensitive Materials. *Jpn. J. Appl. Phys.* **2009**, *48* (4 PART 2). <https://doi.org/10.1143/JJAP.48.04C163>.
- (85) Wasa, K.; Kitabatake, M.; Adachi, H. Thin Film Processes. In *Thin Film Materials Technology*; Wasa, K.; Kitabatake, M.; Adachi, H., Eds.; William Andrew Publishing: 2004; pp 17–69. <https://doi.org/10.1016/B978-081551483-1.50003-4>.
- (86) Allwright, E.; Berg, D. M.; Djemour, R.; Steichen, M.; Dale, P. J.; Robertson, N. Electrochemical Deposition as a Unique Solution Processing Method for Insoluble Organic Optoelectronic Materials. *J. Mater. Chem. C* **2014**, *2* (35), 7232–7238. <https://doi.org/10.1039/c4tc01134a>.
- (87) Li, M.; Liu, D.; Wei, D.; Song, X.; Wei, D.; Wee, A. T. S. Controllable Synthesis of Graphene by Plasma-Enhanced Chemical Vapor Deposition and Its Related Applications. *Adv. Sci.* **2016**, *3* (11). <https://doi.org/10.1002/advs.201600003>.
- (88) Sun, S.; Zhang, G.; Gauquelin, N.; Chen, N.; Zhou, J.; Yang, S.; Chen, W.; Meng, X.; Geng, D.; Banis, M. N.; Li, R.; Ye, S.; Knights, S.; Botton, G. A.; Sham, T.-K.; Sun, X. Single-Atom Catalysis Using Pt/Graphene Achieved through Atomic Layer Deposition. *Sci. Rep.* **2013**, *3* (1), 1775. <https://doi.org/10.1038/srep01775>.
- (89) Safavi, M. S.; Walsh, F. C.; Surmeneva, M. A.; Surmenev, R. A.; Khalil-Allafi, J. Electrodeposited Hydroxyapatite-Based Biocoatings: Recent Progress and Future Challenges. *Coatings* **2021**, *11* (1), 110. <https://doi.org/10.3390/coatings11010110>.
- (90) Pauporté, T.; Lincot, D. Electrodeposition of Semiconductors for Optoelectronic Devices: Results on Zinc Oxide, *Electrochim. Acta* **2000**, *45* (20), 3345–3353. [https://doi.org/10.1016/S0013-4686\(00\)00405-9](https://doi.org/10.1016/S0013-4686(00)00405-9).
- (91) Lincot, D. Electrodeposition of Semiconductors. *Thin Solid Films* **2005**, *487* (1–2), 40–48. <https://doi.org/10.1016/j.tsf.2005.01.032>.
- (92) Buschmann, W. E.; Paulson, S. C.; Wynn, C. M.; Girtu, M. A.; Epstein, A. J.; White, H. S.; Miller, J. S. Reversed (Negative) Magnetization for Electrochemically Deposited High- T_c Thin Films of

- Chromium Hexacyanide Magnets. *Chem. Mater.* **1998**, *10* (5), 1386–1395. <https://doi.org/10.1021/cm970773v>.
- (93) Samantilleke, A. P.; Sahal, M.; Ortiz, L.; Cerqueira, M. F.; Marí, B. Flexible CuInSe₂ Photovoltaic Cells Fabricated by Non-Vacuum Techniques. *Thin Solid Films* **2011**, *519* (21), 7272–7275. <https://doi.org/10.1016/j.tsf.2011.01.373>.
- (94) Hu, Z.; Zhang, J.; Xiong, S.; Zhao, Y. Performance of Polymer Solar Cells Fabricated by Dip Coating Process. *Sol. Energy Mater. Sol. Cells* **2012**, *99*, 221–225. <https://doi.org/10.1016/j.solmat.2011.12.002>.
- (95) Shang, H.; Fan, H.; Shi, Q.; Li, S.; Li, Y.; Zhan, X. Solution Processable D-A-D Molecules Based on Triphenylamine for Efficient Organic Solar Cells. *Sol. Energy Mater. Sol. Cells* **2010**, *94* (3), 457–464. <https://doi.org/10.1016/j.solmat.2009.11.005>.
- (96) Lin, Y.; Cheng, P.; Liu, Y.; Zhao, X.; Li, D.; Tan, J.; Hu, W.; Li, Y.; Zhan, X. Solution-Processable Small Molecules Based on Thieno[3,4-c]Pyrrole-4,6-Dione for High-Performance Solar Cells. *Sol. Energy Mater. Sol. Cells* **2012**, *99*, 301–307. <https://doi.org/10.1016/j.solmat.2011.12.018>.
- (97) Shaheen, S. E.; Radspinner, R.; Peyghambarian, N.; Jabbour, G. E. Fabrication of Bulk Heterojunction Plastic Solar Cells by Screen Printing. *Appl. Phys. Lett.* **2001**, *79* (18), 2996–2998. <https://doi.org/10.1063/1.1413501>.
- (98) Azarova, N. A.; Owen, J. W.; McLellan, C. A.; Grimminger, M. A.; Chapman, E. K.; Anthony, J. E.; Jurchescu, O. D. Fabrication of Organic Thin-Film Transistors by Spray-Deposition for Low-Cost, Large-Area Electronics. *Org. Electron.* **2010**, *11* (12), 1960–1965. <https://doi.org/10.1016/j.orgel.2010.09.008>.
- (99) Hoth, C. N.; Choulis, S. A.; Schilinsky, P.; Brabec, C. J. High Photovoltaic Performance of Inkjet Printed Polymer:Fullerene Blends. *Adv. Mater.* **2007**, *19* (22), 3973–3978. <https://doi.org/10.1002/adma.200700911>.
- (100) Krebs, F. C.; Jørgensen, M.; Norrman, K.; Hagemann, O.; Alstrup, J.; Nielsen, T. D.; Fyenbo, J.; Larsen, K.; Kristensen, J. A Complete Process for Production of Flexible Large Area Polymer Solar Cells Entirely Using Screen Printing—First Public Demonstration. *Sol. Energy Mater. Sol. Cells* **2009**, *93* (4), 422–441. <https://doi.org/10.1016/j.solmat.2008.12.001>.
- (101) Ohyama, A.; Hirata, N.; Oguma, N.; Ichikawa, M. Solvent-Free Printing Process for Organic Transistors Using a Naphthalene Diimide Bearing Long Alkyl Chains. *Org. Electron.* **2018**, *63*, 300–304. <https://doi.org/10.1016/j.orgel.2018.09.038>.
- (102) McDowell, C.; Abdelsamie, M.; Toney, M. F.; Bazan, G. C. Solvent Additives: Key Morphology-Directing Agents for Solution-Processed Organic Solar Cells. *Adv. Mater.* **2018**, *30* (33). <https://doi.org/10.1002/adma.201707114>.
- (103) Pasquarelli, R. M.; Ginley, D. S.; O’hayre, R. Solution Processing of Transparent Conductors: From Flask to Film. *Chem. Soc. Rev.* **2011**, *40* (11), 5406–5441. <https://doi.org/10.1039/c1cs15065k>.
- (104) Oliveira, O. N.; Caseli, L.; Ariga, K. The Past and the Future of Langmuir and Langmuir-Blodgett Films. *Chem. Rev.* **2022**, *122* (6), 6459–6513. <https://doi.org/10.1021/acs.chemrev.1c00754>.

- (105) Lin, H.; Zheng, Y.; Zhong, C.; Lin, L.; Yang, K.; Liu, Y.; Hu, H.; Li, F. Controllable-Assembled Functional Monolayers by the Langmuir-Blodgett Technique for Optoelectronic Applications. *J. Mater. Chem. C* **2024**, *12* (4), 1177–1210. <https://doi.org/10.1039/d3tc03591c>.
- (106) Ariga, K.; Yamauchi, Y.; Mori, T.; Hill, J. P. 25th Anniversary Article: What Can Be Done with the Langmuir-Blodgett Method? Recent Developments and Its Critical Role in Materials Science. *Adv. Mater.* **2013**, *25* (45), 6477–6512. <https://doi.org/10.1002/adma.201302283>.
- (107) Bodik, M.; Jergel, M.; Majkova, E.; Siffalovic, P. Langmuir Films of Low-Dimensional Nanomaterials. *Adv. Colloid Interface Sci.* **2020**, *283*, 102239. <https://doi.org/10.1016/j.cis.2020.102239>.
- (108) Wang, Z.; Kang, Y.; Zhao, S.; Zhu, J. Self-Limiting Assembly Approaches for Nanoadditive Manufacturing of Electronic Thin Films and Devices. *Adv. Mater.* **2020**, *32* (3), 1806480. <https://doi.org/10.1002/adma.201806480>.
- (109) Kim, H.; Mattevi, C.; Kim, H. J.; Mittal, A.; Mkhoyan, K. A.; Riman, R. E.; Chhowalla, M. Optoelectronic Properties of Graphene Thin Films Deposited by a Langmuir-Blodgett Assembly. *Nanoscale* **2013**, *5* (24), 12365–12374. <https://doi.org/10.1039/c3nr02907g>.
- (110) Nguyen, D. M.; Mayer, T. M.; Hubbard, S. F.; Singer, K. D.; Mann, J. A.; Lando, J. B. Polar Polymeric Langmuir-Blodgett Films for Optical Applications. *Macromolecules* **1997**, *30* (20), 6150–6157. <https://doi.org/10.1021/ma961256l>.
- (111) Makiura, R. Creation of Metal–Organic Framework Nanosheets by the Langmuir-Blodgett Technique. *Coord. Chem. Rev.* **2022**, *469*, 214650. <https://doi.org/10.1016/j.ccr.2022.214650>.
- (112) Korpela, J. *What is Roll-to-Roll Langmuir-Blodgett deposition?* <https://www.biolinscientific.com/blog/what-is-roll-to-roll-langmuir-blodgett-deposition> Accessed on 2024 08 08.
- (113) Parchine, M.; McGrath, J.; Bardosova, M.; Pemble, M. E. Large Area 2D and 3D Colloidal Photonic Crystals Fabricated by a Roll-to-Roll Langmuir–Blodgett Method. *Langmuir* **2016**, *32* (23), 5862–5869. <https://doi.org/10.1021/acs.langmuir.6b01242>.
- (114) Xu, L.; Tetreault, A. R.; Khaligh, H. H.; Goldthorpe, I. A.; Wettig, S. D.; Pope, M. A. Continuous Langmuir-Blodgett Deposition and Transfer by Controlled Edge-to-Edge Assembly of Floating 2D Materials. *Langmuir* **2019**, *35* (1), 51–59. <https://doi.org/10.1021/acs.langmuir.8b03173>.
- (115) Holm, A.; Wrasman, C. J.; Kao, K.-C.; Riscoe, A. R.; Cargnello, M.; Frank, C. W. Langmuir–Blodgett Deposition of Graphene Oxide—Identifying Marangoni Flow as a Process That Fundamentally Limits Deposition Control. *Langmuir* **2018**, *34* (33), 9683–9691. <https://doi.org/10.1021/acs.langmuir.8b00777>.
- (116) Premarathna, K. S. D.; Rajapaksha, A. U.; Sarkar, B.; Kwon, E. E.; Bhatnagar, A.; Ok, Y. S.; Vithanage, M. Biochar-Based Engineered Composites for Sorptive Decontamination of Water: A Review. *Chem. Eng. J.* **2019**, *372*, 536–550. <https://doi.org/10.1016/j.cej.2019.04.097>.
- (117) Adameczyk, Z.; Warszyński, P. Role of Electrostatic Interactions in Particle Adsorption. *Adv. Colloid Interface Sci.* **1996**, *63*, 41–149. [https://doi.org/10.1016/0001-8686\(95\)00281-2](https://doi.org/10.1016/0001-8686(95)00281-2).

- (118) Faul, C. F. J.; Antonietti, M. Ionic Self-Assembly: Facile Synthesis of Supramolecular Materials. *Adv. Mater.* **2003**, *15* (9), 673–683. <https://doi.org/10.1002/adma.200300379>.
- (119) Brezesinski, G.; Dietrich, A.; Dobner, B.; Möhwald, H. Morphology and Structures in Double-, Triple- and Quadruple-Chain Phospholipid Monolayers at the Air/Water Interface. In *Trends in Colloid and Interface Science IX*; Appell, J., Porte, G., Eds.; Progress in Colloid & Polymer Science; Steinkopff, 1995; vol 98. <https://doi.org/10.1007/BFb0115249>.
- (120) Helm, C. A.; Möhwald, H. Equilibrium and Nonequilibrium Features Determining Superlattices in Phospholipid Monolayers. *J. Phys. Chem.* **1988**, *92* (5), 1262–1266. <https://doi.org/10.1021/j100316a050>.
- (121) McConnell, H. M. Structures and Transitions in Lipid Monolayers at the Air-Water Interface. *Annu. Rev. Phys. Chem.* **1991**, *42* (1), 171–195. <https://doi.org/10.1146/annurev.pc.42.100191.001131>.
- (122) Li, S.; Du, L.; Wang, W. Impact of Anions on the Surface Organisation of Lipid Monolayers at the Air-Water Interface. *Environ. Chem.* **2017**, *14* (7), 407–416. <https://doi.org/10.1071/EN17147>.
- (123) Hunter, C. A. Sequence-Dependent DNA Structure. *J. Mol. Biol.* **1993**, *230* (3), 1025–1054. <https://doi.org/10.1006/jmbi.1993.1217>.
- (124) Abraham, R. J.; Eivazi, F.; Pearson, H.; Smith, K. M. Mechanisms of Aggregation in Metalloporphyrins: Demonstration of a Mechanistic Dichotomy. *J. Chem. Soc. Chem. Commun.* **1976**, 17, 698. <https://doi.org/10.1039/c39760000698>.
- (125) Hunter, C. A.; Sanders, J. K. M. The Nature of π - π Interactions. *J. Am. Chem. Soc.* **1990**, *112* (14), 5525–5534. <https://doi.org/10.1021/ja00170a016>.
- (126) Tang, Z.; Johal, M. S.; Scudder, P.; Caculitan, N.; Magyar, R. J.; Tretiak, S.; Wang, H. L. Study of the Non-Covalent Interactions in Langmuir-Blodgett Films: An Interplay between π - π and Dipole-Dipole Interactions. *Thin Solid Films* **2007**, *516* (1), 58–66. <https://doi.org/10.1016/j.tsf.2007.04.149>.
- (127) Behyan, S.; Gritzalis, D.; Schmidt, R.; Kebede, E.; Cuccia, L. A.; Dewolf, C. Structural Organization and Phase Behaviour of: Meta -Substituted Dioctadecylaminobenzoquinones at the Air/Water Interface. *Phys. Chem. Chem. Phys.* **2019**, *21* (5), 2345–2350. <https://doi.org/10.1039/c8cp07186a>.
- (128) Milette Lamarche, R.; Dewolf, C. Strong Headgroup Interactions Drive Highly Directional Growth and Unusual Phase Co-Existence in Self-Assembled Phenolic Films. *Appl. Mater. Interfaces* **2019**, *11* (48), 45354–45363. <https://doi.org/10.1021/acsami.9b16958>.
- (129) Giese, M.; Albrecht, M.; Rissanen, K. Experimental Investigation of Anion- π Interactions – Applications and Biochemical Relevance. *Chem. Commun.* **2016**, *52* (9), 1778–1795. <https://doi.org/10.1039/C5CC09072E>.
- (130) Chifotides, H. T.; Dunbar, K. R. Anion- π Interactions in Supramolecular Architectures. *Acc. Chem. Res.* **2013**, *46* (4), 894–906. <https://doi.org/10.1021/ar300251k>.
- (131) Dougherty, D. A. The Cation- π Interaction. *Acc. Chem. Res.* **2013**, *46* (4), 885–893. <https://doi.org/10.1021/ar300265y>.

- (132) Chen, J.; Peng, Q.; Liu, J.; Zeng, H. Mussel-Inspired Cation- π Interactions: Wet Adhesion and Biomimetic Materials. *Langmuir* **2023**, *39* (49), 17600–17610. <https://doi.org/10.1021/acs.langmuir.3c02818>.
- (133) Akamatsu, M.; Kimura, A.; Yamanaga, K.; Sakai, K.; Sakai, H. Anion- π Interaction at the Solid/Water Interfaces. *Chem. Commun.* **2021**, *57* (38), 4650–4653. <https://doi.org/10.1039/d1cc01186c>.
- (134) Akamatsu, M.; Yamanaga, K.; Tanaka, K.; Kanehara, Y.; Sumita, M.; Sakai, K.; Sakai, H. Anion- π Interactions in Monolayers Formed by Amphiphilic Electron-Deficient Aromatic Compounds at Air/Water Interfaces. *Langmuir* **2023**, *39* (16), 5833–5839. <https://doi.org/10.1021/acs.langmuir.3c00127>.
- (135) Ding, Y.; Wen, G.; Chrysostomou, V.; Pispas, S.; Jiang, K.; Sun, Z.; Li, H. Aggregation Behavior of the Strong Amphiphilic Cationic Diblock Polyelectrolytes at the Air/Water Interface. *J. Appl. Polym. Sci.* **2022**, *139* (18). <https://doi.org/10.1002/app.52079>.
- (136) Ji, W.; Zhao, W.; Li, W.; Wang, Y.; Wang, J.; Lan, D. Hydrodynamic Process in the Langmuir-Blodgett Film Method. *Langmuir* **2020**, *36* (47), 14461–14469. <https://doi.org/10.1021/acs.langmuir.0c02975>.
- (137) Roy, D.; Naskar, B.; Bala, T. Exploring Langmuir-Blodgett Technique to Investigate Effect of Various Subphase Conditions on Monolayers Formed by Amphiphilic Block Co-Polymers Tetronic 701 and Tetronic 90R4. *Colloids Surf. A* **2021**, *625*, 126924. <https://doi.org/10.1016/j.colsurfa.2021.126924>.
- (138) Peñacorada, F.; Reiche, J.; Dietel, R.; Zetzsche, T.; Stiller, B.; Knobloch, H.; Brehmer, L. Monolayers and Multilayers of Uranyl Arachidate 2. Influence of the Subphase PH on the Structure and Stability of Langmuir-Blodgett Films. *Langmuir* **1996**, *12* (5), 1351–1356. <https://doi.org/10.1021/la950709x>.
- (139) Claro, P. C. dos S.; Coustet, M. E.; Diaz, C.; Maza, E.; Cortizo, M. S.; Requejo, F. G.; Pietrasanta, L. I.; Ceolín, M.; Azzaroni, O. Self-Assembly of PBzMA-b-PDMAEMA Diblock Copolymer Films at the Air-Water Interface and Deposition on Solid Substrates via Langmuir-Blodgett Transfer. *Soft Matter* **2013**, *9* (45), 10899. <https://doi.org/10.1039/c3sm52336e>.
- (140) Paul, S.; Pearson, C.; Molloy, A.; Cousins, M. A.; Green, M.; Kolliopoulou, S.; Dimitrakakis, P.; Normand, P.; Tsoukalas, D.; Petty, M. C. Langmuir-Blodgett Film Deposition of Metallic Nanoparticles and Their Application to Electronic Memory Structures. *Nano Lett.* **2003**, *3* (4), 533–536. <https://doi.org/10.1021/nl034008t>.
- (141) Honig, D.; Overbeck, G. A.; Mobius, D. Morphology of Pentadecanoic Acid Monolayers at the Air/Water Interface Studied by BAM. *Adv. Mater.* **1992**, *4* (6), 419–424. <https://doi.org/10.1002/adma.19920040610>.
- (142) Giner-Casares, J. J.; Brezesinski, G.; Möhwald, H. Langmuir Monolayers as Unique Physical Models. *Curr. Opin. Colloid Interface Sci.* **2014**, *19* (3), 176–182. <https://doi.org/10.1016/j.cocis.2013.07.006>.
- (143) Krägel, J.; Derkatch, S. R.; Miller, R. Interfacial Shear Rheology of Protein-Surfactant Layers. *Adv. Colloid Interface Sci.* **2008**, *144* (1–2), 38–53. <https://doi.org/10.1016/j.cis.2008.08.010>.

- (144) Vollhardt, D.; Fainerman, V. B. Characterisation of Phase Transition in Adsorbed Monolayers at the Air/Water Interface. *Adv. Colloid Interface Sci.* **2010**, *154* (1–2), 1–19. <https://doi.org/10.1016/j.cis.2010.01.003>.
- (145) Ferri, J. K.; Kotsmar, C.; Miller, R. From Surfactant Adsorption Kinetics to Asymmetric Nanomembrane Mechanics: Pendant Drop Experiments with Subphase Exchange. *Adv. Colloid Interface Sci.* **2010**, *161* (1–2), 29–47. <https://doi.org/10.1016/j.cis.2010.08.002>.
- (146) Harkins, W. D.; Feldman, A. FILMS. THE SPREADING OF LIQUIDS AND THE SPREADING COEFFICIENT. *J. Am. Chem. Soc.* **1922**, *44* (12), 2665–2685. <https://doi.org/10.1021/ja01433a001>.
- (147) Langmuir, I. THE CONSTITUTION AND FUNDAMENTAL PROPERTIES OF SOLIDS AND LIQUIDS. II. LIQUIDS. ¹. *J. Am. Chem. Soc.* **1917**, *39* (9), 1848–1906. <https://doi.org/10.1021/ja02254a006>.
- (148) Martin, P.; Szablewski, M. *Langmuir-Blodgett Troughs Operating Manual*, 6th ed.; Grunfeld, F., Ed.; Nima Technology Ltd: Coventry, 2001.
- (149) Petty, M. C. *Langmuir-Blodgett Films*; Cambridge University Press: Cambridge, 1996. <https://doi.org/10.1017/CBO9780511622519>.
- (150) Kaganer, V. M.; Loginov, E. B. Crystallization Phase Transitions and Phase Diagram of Langmuir Monolayers. *Phys. Rev. Lett.* **1993**, *71* (16), 2599–2602. <https://doi.org/10.1103/PhysRevLett.71.2599>.
- (151) Dahmen-Levison, U.; Brezesinski, G.; Möhwald, H. Monolayer Structures of Triple-Chain Phosphatidylcholines as Substrates for Phospholipases. *Colloids and Surfaces* **2000**, *171*, 97–103. [https://doi.org/10.1016/S0927-7757\(99\)00540-3](https://doi.org/10.1016/S0927-7757(99)00540-3).
- (152) Schmidt, R.; DeWolf, C. E. Monolayer Behavior of 1,2-Dipalmitoylglycerol, a Synthetic Lipid with Strong Cohesive Properties. *Langmuir* **2004**, *20* (8), 3284–3288. <https://doi.org/10.1021/la036099f>.
- (153) Vollhardt, D.; Fainerman, V. B. Progress in Characterization of Langmuir Monolayers by Consideration of Compressibility. *Adv. Colloid Interface Sci.* **2006**, *127* (2), 83–97. <https://doi.org/10.1016/j.cis.2006.11.006>.
- (154) Smaby, J. M.; Kulkarni, V. S.; Momsen, M.; Brown, R. E. The Interfacial Elastic Packing Interactions of Galactosylceramides, Sphingomyelins, and Phosphatidylcholines. *Biophys. J.* **1996**, *70* (2), 868–877. [https://doi.org/10.1016/S0006-3495\(96\)79629-7](https://doi.org/10.1016/S0006-3495(96)79629-7).
- (155) Hutchinson, E. *Chemistry: Interfacial Phenomena*. J. T. Davies and E. K. Rideal. Academic Press, New York, Ed. 2, 1963. 494 Pp. \$15. *Science* **1963**, *142* (3595), 1052–1052. <https://doi.org/10.1126/science.142.3595.1052.a>.
- (156) Hénon, S.; Meunier, J. Microscope at the Brewster Angle: Direct Observation of First-Order Phase Transitions in Monolayers. *Rev. Sci. Instrum.* **1991**, *62* (4), 936–939. <https://doi.org/10.1063/1.1142032>.
- (157) Roldán-Carmona, C.; Giner-Casares, J. J.; Pérez-Morales, M.; Martín-Romero, M. T.; Camacho, L. Revisiting the Brewster Angle Microscopy: The Relevance of the Polar Headgroup. *Adv. Colloid Interface Sci.* **2012**, *173*, 12–22. <https://doi.org/10.1016/j.cis.2012.02.002>.

- (158) Hönig, D.; Möbius, D. Reflectometry at the Brewster Angle and Brewster Angle Microscopy at the Air-Water Interface. *Thin Solid Films* **1992**, *210–211*, 64–68. [https://doi.org/10.1016/0040-6090\(92\)90169-C](https://doi.org/10.1016/0040-6090(92)90169-C).
- (159) Hecht, E.; Zajac, A. *Optics*; Addison-Wesley, 1974.
- (160) Bass, M.; DeCusatis, C.; Enoch, J. M.; Lakshminarayanan, V.; Li, G.; McDonald, C.; Mahajan, V. N.; Stryland, E. Van. *Handbook of Optics, Volume I: Geometrical and Physical Optics, Polarized Light, Components and Instruments(Set)*, 3rd ed.; McGraw Hill Professional, 2009; Vol. I.
- (161) Garcia-Caurel, E.; De Martino, A.; Gaston, J.-P.; Yan, L. Application of Spectroscopic Ellipsometry and Mueller Ellipsometry to Optical Characterization. *Appl. Spectrosc.* **2013**, *67* (1), 1–21. <https://doi.org/10.1366/12-06883>.
- (162) Desbat, B.; Castano, S. Brewster Angle Microscopy and Imaging Ellipsometry. In *Encyclopedia of Biophysics*; Springer: Berlin, Heidelberg, 2013; pp 196–200.
- (163) Binnig, G.; Quate, C. F.; Gerber, Ch. Atomic Force Microscope. *Phys. Rev. Lett.* **1986**, *56* (9), 930–933. <https://doi.org/10.1103/PhysRevLett.56.930>.
- (164) What is Atomic Force Microscopy (AFM). <https://www.nanoandmore.com/what-is-atomic-force-microscopy>, Accessed on 2024 08 13.
- (165) Rao, A.; Gnecco, E.; Marchetto, D.; Mougins, K.; Schönenberger, M.; Valeri, S.; Meyer, E. The Analytical Relations between Particles and Probe Trajectories in Atomic Force Microscope Nanomanipulation. *Nanotechnology* **2009**, *20* (11), 115706. <https://doi.org/10.1088/0957-4484/20/11/115706>.
- (166) Alvarez, L.; Siqueiros, J. Atomic Force Microscopy. In *Microscopy: Advances in Scientific Research and Education*; Mendez-Vilas, A. Ed.; FORMATEX, 2014; pp 605–609.
- (167) Asmatulu, R.; Khan, W. S. Characterization of Electrospun Nanofibers. In *Synthesis and Applications of Electrospun Nanofibers*; Asmatulu, R.; Khan, W. S. Ed.; Elsevier, 2019; pp 257–281. <https://doi.org/10.1016/B978-0-12-813914-1.00013-4>.
- (168) Roberts, G. *Langmuir-Blodgett Films*; Roberts, G., Ed.; Springer US, 1990. <https://doi.org/10.1007/978-1-4899-3716-2>.
- (169) Langmuir I, Schaefer VJ, Wrinch DM. BUILT-UP FILMS OF PROTEINS AND THEIR PROPERTIES. *Science*. **1937**, *85* (2194), 76–80. <https://doi.org/10.1126/science.85.2194.76-a>.
- (170) Tredgold, R. H. Spreading It Out. *Nature* **1991**, *354* (6349), 120–120. <https://doi.org/10.1038/354120a0>.
- (171) Stefaniu, C.; Brezesinski, G. X-Ray Investigation of Monolayers Formed at the Soft Air/Water Interface. *Curr. Opin. Colloid Interface Sci.* **2014**, *19* (3), 216–227. <https://doi.org/10.1016/j.cocis.2014.01.004>.
- (172) Ezquerra, T. A.; Garcia-Gutierrez, M.; Nogales, A.; Gomez, M. *Applications of Synchrotron Light to Scattering and Diffraction in Materials and Life Sciences*; Springer: Berlin Heidelberg, 2009.
- (173) Kaganer, V. M.; Möhwald, H.; Dutta, P. Structure and Phase Transitions in Langmuir Monolayers. *Rev. Mod. Phys.* **1999**, *71* (3), 779–819. <https://doi.org/10.1103/RevModPhys.71.779>.

- (174) Miller, D. M. R. *Novel Methods to Study Interfacial Layers, Volume 11*, 1st ed.; Elsevier, 2001; Vol. 11.
- (175) Jensen, T. R.; Balashev, K.; Bjørnholm, T.; Kjaer, K. Novel Methods for Studying Lipids and Lipases and Their Mutual Interaction at Interfaces. Part II. Surface Sensitive Synchrotron X-Ray Scattering. *Biochimie* **2001**, *83* (5), 399–408. [https://doi.org/10.1016/S0300-9084\(01\)01265-2](https://doi.org/10.1016/S0300-9084(01)01265-2).
- (176) Alami, E.; Beinert, G.; Marie, P.; Zana, R. Alkanediyl-a,o-Bis (Dimet Hylalkylammonium Bromide) Surfactants. 3. Behavior at the Air-Water Interface. *Langmuir* **1993**, *9* (6), 1456-1467. <https://doi.org/10.1021/la00030a006>.
- (177) Parratt, L. G. Surface Studies of Solids by Total Reflection of X-Rays. *Phys. Rev.* **1954**, *95* (2), 359–369. <https://doi.org/10.1103/PhysRev.95.359>.
- (178) Bu, W.; Schlossman, M. L. Synchrotron X-Ray Scattering from Liquid Surfaces and Interfaces. In *Synchrotron Light Sources and Free-Electron Lasers: : Accelerator Physics, Instrumentation and Science Applications*; Jaeschke, E. J.; Khan, S.; Schneider, J. R.; Hastings, J. B., Ed.; Springer International Publishing, 2020; pp 1897–1933. https://doi.org/10.1007/978-3-030-23201-6_45.
- (179) Feng, X.; Bai, Y.; Liu, M.; Li, Y.; Yang, H.; Wang, X.; Wu, C. Untangling the Respective Effects of Heteroatom-Doped Carbon Materials in Batteries, Supercapacitors and the ORR to Design High Performance Materials. *Energy Environ. Sci.* **2021**, *14* (4), 2036–2089. <https://doi.org/10.1039/d1ee00166c>.
- (180) Stolar, M.; Baumgartner, T. Phosphorus-Containing Materials for Organic Electronics. *Chem. Asian J.* **2014**, *9* (5), 1212–1225. <https://doi.org/10.1002/asia.201301670>.
- (181) Russ, B.; Glauddell, A.; Urban, J. J.; Chabinye, M. L.; Segalman, R. A. Organic Thermoelectric Materials for Energy Harvesting and Temperature Control. *Nat. Rev. Mater.* **2016**, *1*, 16050. <https://doi.org/10.1038/natrevmats.2016.50>.
- (182) Chang, C. C.; Pai, C. L.; Chen, W. C.; Jenekhe, S. A. Spin Coating of Conjugated Polymers for Electronic and Optoelectronic Applications. *Thin Solid Films* **2005**, *479* (1–2), 254–260. <https://doi.org/10.1016/j.tsf.2004.12.013>.
- (183) Ganesh, V.; Haritha, L.; Manthrammel, M. A.; Shkir, M.; AlFaify, S. An Impact of La Doping Content on Physical Properties of NiO Films Facilely Casted through Spin-Coater for Optoelectronics. *Physica B Condens. Matter* **2020**, *582*, 411955. <https://doi.org/10.1016/j.physb.2019.411955>.
- (184) Arif, M.; Shkir, M.; Ganesh, V.; Singh, A.; Algarni, H.; AlFaify, S. A Significant Effect of Ce-Doping on Key Characteristics of NiO Thin Films for Optoelectronics Facilely Fabricated by Spin Coater. *Superlattices Microstruct.* **2019**, *129*, 230–239. <https://doi.org/10.1016/j.spmi.2019.03.025>.
- (185) Sugumaran, S.; Bellan, C. S., B. Dip and Spin Coated Nanoscale Transparent PMMA Thin Films for Field Effect Thin Film Transistors and Optoelectronic Devices. *J. Optoelectron. Adv. M.* **2013** *15* (3-4), 139-144. <https://www.researchgate.net/publication/255696412>.
- (186) Routledge, T. J.; Lidzey, D. G.; Buckley, A. R. Ultrasonic Spray Coating as an Approach for Large-Area Polymer OLEDs: The Influence of Thin Film Processing and Surface Roughness on Electrical Performance. *AIP Adv* **2019**, *9* (1), 015330. <https://doi.org/10.1063/1.5082791>.

- (187) Ariga, K. Don't Forget Langmuir-Blodgett Films 2020: Interfacial Nanoarchitectonics with Molecules, Materials, and Living Objects. *Langmuir* **2020**, *36* (26), 7158–7180. <https://doi.org/10.1021/acs.langmuir.0c01044>.
- (188) Era, M.; Takada, N. Squeezed-Out Technique to Prepare High-Quality PbBr-Based Layered Perovskite Langmuir-Blodgett Films Applicable to Cavity Polariton Devices. *Langmuir* **2019**, *35* (37), 12224–12228. <https://doi.org/10.1021/acs.langmuir.9b00473>.
- (189) Liu, Q.; Hao, Z.; Liao, X.; Pan, X.; Li, S.; Xu, L.; Mai, L. Langmuir–Blodgett Nanowire Devices for In Situ Probing of Zinc-Ion Batteries. *Small* **2019**, *15* (30), 1902141. <https://doi.org/10.1002/sml.201902141>.
- (190) Lee, Y. L.; Lin, J. Y.; Chang, C. H. Thermodynamic Characteristics and Langmuir-Blodgett Deposition Behavior of Mixed DPPA/DPPC Monolayers at Air/Liquid Interfaces. *J. Colloid Interface Sci.* **2006**, *296* (2), 647–654. <https://doi.org/10.1016/j.jcis.2005.09.050>.
- (191) Baumgartner, T. Insights on the Design and Electron-Acceptor Properties of Conjugated Organophosphorus Materials. *Acc. Chem. Res.* **2014**, *47* (5), 1613–1622. <https://doi.org/10.1021/ar500084b>.
- (192) Brahmachari, G. Organophosphorus Chemistry, In *Green synthetic approaches in organophosphorus chemistry: recent developments with energy-efficient protocols*; Allen, D. W., Loakes, D., Tebby, J. C., Eds.; The Royal Society of Chemistry, 2016; Vol 45, pp 438–491. <https://doi.org/10.1039/9781782626930-00438>.
- (193) Romero-Nieto, C.; Baumgartner, T. Dithieno[3,2-*b*:2',3'-*d*]Phospholes: A Look Back at the First Decade. *Synlett.* **2013**, *24* (08), 920–937. <https://doi.org/10.1055/s-0032-1317804>.
- (194) He, X.; Chen, L.; Baumgartner, T. Modified Viologen- and Carbonylpyridinium-Based Electrodes for Organic Batteries. *ACS Appl. Mater. Interfaces* **2024**, *16* (37), 48689–48705. <https://doi.org/10.1021/acsami.3c09856>.
- (195) Yamaguchi, S.; Fukazawa, A.; Taki, M. Phosphole *P*-Oxide-Containing π -Electron Materials: Synthesis and Applications in Fluorescence Imaging. *J. Syn. Org. Chem. Japan* **2017**, *75* (11), 1179–1187. <https://doi.org/10.5059/yukigoseikyokaishi.75.1179>.
- (196) Sanji, T.; Shiraishi, K.; Tanaka, M. Sugar-Phosphole Oxide Conjugates as “Turn-on” Luminescent Sensors for Lectins. *ACS Appl. Mater. Interfaces* **2009**, *1* (2), 270–273. <https://doi.org/10.1021/am800224r>.
- (197) Lukáč, M.; Devínsky, F.; Pisárčik, M.; Papapetropoulou, A.; Bukovský, M.; Horváth, B. Novel Phospholium-Type Cationic Surfactants: Synthesis, Aggregation Properties and Antimicrobial Activity. *J. Surfactants Deterg.* **2017**, *20* (1), 159–171. <https://doi.org/10.1007/s11743-016-1908-6>.
- (198) Wang, Z.; Baumgartner, T. Organophosphorus Avenues toward Self-Assembled Conjugated Soft Materials. *The Chemical Record* **2015**, *15* (1), 199–217. <https://doi.org/10.1002/tcr.201402061>.
- (199) Hay, C.; Hissler, M.; Fischmeister, C.; Rault-Berthelot, J.; Toupet, L.; Nyulászi, L.; Réau, R. Phosphole-Containing π -Conjugated Systems: From Model Molecules to Polymer Films on Electrodes. *Chem. Eur. J.* **2001**, *7* (19), 4222–4236. [https://doi.org/10.1002/1521-3765\(20011001\)7:19<4222::AID-CHEM4222>3.0.CO;2-3](https://doi.org/10.1002/1521-3765(20011001)7:19<4222::AID-CHEM4222>3.0.CO;2-3).

- (200) Ren, Y.; Kan, W. H.; Thangadurai, V.; Baumgartner, T. Bio-Inspired Phosphole-Lipids: From Highly Fluorescent Organogels to Mechanically Responsive FRET. *Angew. Chem. Int. Ed.* **2012**, *51* (16), 3964–3968. <https://doi.org/10.1002/anie.201109205>.
- (201) Dietrich, A.; Möhwald, H.; Rettig, W.; Brezesinski, G. Polymorphism of a Triple-Chain Lecithin in Two- and Three-Dimensional Systems. *Langmuir* **1991**, *7* (3), 539–546. <https://doi.org/10.1021/la00051a021>.
- (202) Leporatti, S.; Bringezu, F.; Brezesinski, G.; Möhwald, H. Condensed Phases of Branched-Chain Phospholipid Monolayers Investigated by Scanning Force Microscopy. *Langmuir* **1998**, *14* (26), 7503–7510. <https://doi.org/10.1021/la980838o>.
- (203) Zhu, Y.-P.; Masuyama, A.; Ichi Kirito, Y.; Okahara, M.; Rosen, M. J. Preparation and Properties of Glycerol-Based Double- or Triple-Chain Surfactants with Two Hydrophilic Ionic Groups. *J. Am. Oil Chemists Soc.* **1992**, *69*, 626–632. <http://dx.doi.org/10.1007/BF02635800>.
- (204) Sumida, Y.; Oki, T.; Masuyama, A.; Maekawa, H.; Nishiura, M.; Kida, T.; Nakatsuji, Y.; Ikeda, I.; Nojima, M. π -A Isotherms for Triple-Chain Amphiphiles Bearing Two or Three Hydroxyl Groups. Effect of the Backbone Structure on the Adsorption Behavior of the Molecules on the Surface. *Langmuir* **1998**, *14* (26), 7450–7455. <https://doi.org/10.1021/la980814h>.
- (205) Sumida, Y.; Masuyama, A.; Takasu, M.; Kida, T.; Nakatsuji, Y.; Ikeda, I.; Nojima, M. Behavior of Self-Organized Molecular Assemblies Composed of Phosphatidylcholines and Synthetic Triple-Chain Amphiphiles in Water. *Langmuir* **2000**, *16* (21), 8005–8009. <https://doi.org/10.1021/la000694p>.
- (206) Sumida, Y.; Masuyama, A.; Maekawa, H.; Takasu, M.; Kida, T.; Nakatsuji, Y.; Ikeda, I.; Nojima, M. Stable Vesicles Made from New Triple-Chain Amphiphiles: Long-Term Stability toward Leakage of the Trapped Substances. *Chem. Commun.* **1998**, 2385–2386. <https://doi.org/10.1039/A806903D>.
- (207) Ngyugen, H.; McNamee, C. E. Determination and Comparison of How the Chain Number and Chain Length of a Lipid Affects Its Interactions with a Phospholipid at an Air/Water Interface. *J. Phys. Chem. B* **2014**, *118* (22), 5901–5912. <https://doi.org/10.1021/jp500840a>.
- (208) Jacquemain, D.; Leveiller, F.; Weinbach, S. P.; Lahav, M.; Leiserowitz, L.; Kjaer, K.; Als-Nielsen, J. Crystal Structure of Self-Aggregates of Insoluble Aliphatic Amphiphilic Molecules at the Air-Water Interface. An x-Ray Synchrotron Study. *J. Am. Chem. Soc.* **1991**, *113* (20), 7684–7691. <https://doi.org/10.1021/ja00020a034>.
- (209) Toimil, P.; Prieto, G.; Miñones, J.; Sarmiento, F. A Comparative Study of F-DPPC/DPPC Mixed Monolayers. Influence of Subphase Temperature on F-DPPC and DPPC Monolayers. *Phys. Chem. Chem. Phys.* **2010**, *12* (40), 13323–13332. <https://doi.org/10.1039/c0cp00506a>.
- (210) Nieuwhof, R. P.; Kimkes, P.; Marcelis, A. T. M.; Sudhölter, E. J. R.; Opitz, R.; De Jeu, W. H. Langmuir and Langmuir-Blodgett Films of Side-Chain Liquid-Crystalline Poly(Maleic Acid-Alt-1-Alkene)s. *Langmuir* **2001**, *17* (1), 78–85. <https://doi.org/10.1021/la000960z>.
- (211) Möhwald, H. In *Phospholipids Handbook*; Cevc, G., Ed.; CRC Press: New York, 1993; pp 579–602. <https://doi.org/10.1201/9780203743577>.

- (212) Dong, B.; Li, N.; Zheng, L.; Yu, L.; Inoue, T. Surface Adsorption and Micelle Formation of Surface Active Ionic Liquids in Aqueous Solution. *Langmuir* **2007**, *23* (8), 4178–4182. <https://doi.org/10.1021/la0633029>.
- (213) Stefaniu, C.; Brezesinski, G.; Möhwald, H. Langmuir Monolayers as Models to Study Processes at Membrane Surfaces. *Adv. Colloid Interface Sci.* **2014**, *208*, 197–213. <https://doi.org/10.1016/j.cis.2014.02.013>.
- (214) Aroti, A.; Leontidis, E.; Dubois, M.; Zemb, T.; Brezesinski, G. Monolayers, Bilayers and Micelles of Zwitterionic Lipids as Model Systems for the Study of Specific Anion Effects. *Colloids Surf. A Physicochem. Eng. Asp.* **2007**, *303* (1–2), 144–158. <https://doi.org/10.1016/j.colsurfa.2007.03.011>.
- (215) Avazbaeva, Z.; Sung, W.; Lee, J.; Phan, M. D.; Shin, K.; Vaknin, D.; Kim, D. Origin of the Instability of Octadecylamine Langmuir Monolayer at Low PH. *Langmuir* **2015**, *31* (51), 13753–13758. <https://doi.org/10.1021/acs.langmuir.5b03947>.
- (216) Smith, R. K.; Lewis, P. A.; Weiss, P. S. Patterning Self-Assembled Monolayers. *Prog. Surf. Sci.* **2004**, *75* (1–2), 1–68. <https://doi.org/10.1016/j.progsurf.2003.12.001>.
- (217) Banerjee, R.; Sanyal, M. K.; Bera, M. K.; Gibaud, A.; Lin, B.; Meron, M. Reversible Monolayer-to-Crystalline Phase Transition in Amphiphilic Silsesquioxane at the Air-Water Interface. *Sci. Rep.* **2015**, *5* (1), 8497. <https://doi.org/10.1038/srep08497>.
- (218) Pegram, L. M.; Record, M. T. Hofmeister Salt Effects on Surface Tension Arise from Partitioning of Anions and Cations between Bulk Water and the Air-Water Interface. *J. Phys. Chem. B* **2007**, *111* (19), 5411–5417. <https://doi.org/10.1021/jp070245z>.
- (219) Shapovalov, V. L.; Brezesinski, G. Breakdown of the Gouy - Chapman Model for Highly Charged Langmuir Monolayers: Counterion Size Effect. *J. Phys. Chem. B* **2006**, *110* (20), 10032–10040. <https://doi.org/10.1021/jp056801b>.
- (220) Zhang, J.; Wang, M.; Yang, Z.; Zhang, X. Highly Flexible and Stretchable Strain Sensors Based on Conductive Whisker Carbon Nanotube Films. *Carbon* **2021**, *176*, 139–147. <https://doi.org/10.1016/j.carbon.2021.01.130>.
- (221) Price, L. S.; Price, S. L. Packing Preferences of Chalcones: A Model Conjugated Pharmaceutical Scaffold. *Cryst. Growth Des.* **2022**, *22* (3), 1801–1816. <https://doi.org/10.1021/acs.cgd.1c01381>.
- (222) Gómez, P.; Cerdá, J.; Más-Montoya, M.; Georgakopoulos, S.; Da Silva, I.; García, A.; Ortí, E.; Aragón, J.; Curiel, D. Effect of Molecular Geometry and Extended Conjugation on the Performance of Hydrogen-Bonded Semiconductors in Organic Thin-Film Field-Effect Transistors. *J. Mater. Chem. C* **2021**, *9* (33), 10819–10829. <https://doi.org/10.1039/d1tc01328a>.
- (223) Yao, Z.-F.; Wang, J.-Y.; Pei, J. Control of π - π Stacking via Crystal Engineering in Organic Conjugated Small Molecule Crystals. *Cryst. Growth Des.* **2018**, *18* (1), 7–15. <https://doi.org/10.1021/acs.cgd.7b01385>.
- (224) Thakuria, R.; Nath, N. K.; Saha, B. K. The Nature and Applications of π - π Interactions: A Perspective. *Cryst. Growth Des.* **2019**, *19* (2), 523–528. <https://doi.org/10.1021/acs.cgd.8b01630>.

- (225) Park, J. Y.; Advincula, R. C. Nanostructured Thin Films from Amphiphilic Molecules. In *Nanocoatings and Ultra-Thin Films*; Hamdy Makhlof A. S.; Tiginyanu, I., ed.; Woodhead Publishing, 2011; pp 24–56. <https://doi.org/10.1533/9780857094902.1.24>.
- (226) Kraft, A.; Grimsdale, A. C.; Holmes, A. B. Electroluminescent Conjugated Polymers - Seeing Polymers in a New Light. *Angew. Chem. Int. Ed.* 1998, 37 (4), 402–428. [https://doi.org/10.1002/\(SICI\)1521-3773\(19980302\)37:4<402::AID-ANIE402>3.0.CO;2-9](https://doi.org/10.1002/(SICI)1521-3773(19980302)37:4<402::AID-ANIE402>3.0.CO;2-9).
- (227) Kulkarni, A. P.; Tonzola, C. J.; Babel, A.; Jenekhe, S. A. Electron Transport Materials for Organic Light-Emitting Diodes. *Chem. Mater.* 2004, 16 (23), 4556–4573. <https://doi.org/10.1021/cm0494731>.
- (228) Yan, H.; Lee, P.; Armstrong, N. R.; Graham, A.; Evmenenko, G. A.; Dutta, P.; Marks, T. J. High-Performance Hole-Transport Layers for Polymer Light-Emitting Diodes. Implementation of Organosiloxane Cross-Linking Chemistry in Polymeric Electroluminescent Devices. *J. Am. Chem. Soc.* 2005, 127 (9), 3172–3183. <https://doi.org/10.1021/ja044455q>.
- (229) Matano, Y.; Miyajima, T.; Fukushima, T.; Kaji, H.; Kimura, Y.; Imahori, H. Comparative Study on the Structural, Optical, and Electrochemical Properties of Bithiophene-Fused Benzo[*c*]Phospholes. *Chem. Euro. J.* 2008, 14 (27), 8102–8115. <https://doi.org/10.1002/chem.200801017>.
- (230) Makioka, Y.; Hayashi, T.; Tanaka, M. Poly[2,7-(9-Oxo-9-Phosphafluorenylene)-*alt-co*-(1,4-Arylene)]s: Phosphorus-Containing π -Conjugated Polymers. *Chem. Lett.* 2004, 33 (1), 44–45. <https://doi.org/10.1246/cl.2004.44>.
- (231) Hatano, T.; Kato, T. A Columnar Liquid Crystal Based on Triphenylphosphine Oxide—Its Structural Changes upon Interaction with Alkaline Metal Cations. *Chem. Commun.* 2006, No. 12, 1277. <https://doi.org/10.1039/b514520a>.
- (232) Kimura, M.; Hatano, T.; Yasuda, T.; Morita, J.; Akama, Y.; Minoura, K.; Shimomura, T.; Kato, T. Photoluminescent Liquid Crystals Based on Trithienylphosphine Oxides. *Chem. Lett.* 2009, 38 (8), 800–801. <https://doi.org/10.1246/cl.2009.800>.
- (233) Ren, Y.; Baumgartner, T. Dually Switchable Heterotetracenes: Addressing the Photophysical Properties and Self-Organization of the P-S System. *J. Am. Chem. Soc.* 2011, 133 (5), 1328–1340. <https://doi.org/10.1021/ja108081b>.
- (234) Curtis, M. D.; Cao, J.; Kampf, J. W. Solid-State Packing of Conjugated Oligomers: From π -Stacks to the Herringbone Structure. *J. Am. Chem. Soc.* 2004, 126 (13), 4318–4328. <https://doi.org/10.1021/ja0397916>.
- (235) Kim, E.-G.; Coropceanu, V.; Gruhn, N. E.; Sánchez-Carrera, R. S.; Snoeberger, R.; Matzger, A. J.; Brédas, J.-L. Charge Transport Parameters of the Pentathienoacene Crystal. *J. Am. Chem. Soc.* 2007, 129 (43), 13072–13081. <https://doi.org/10.1021/ja073587r>.
- (236) West, A. Intermolecular Forces and Solvation. In *Interface Science and Technology*; Elsevier B.V., 2017; Vol. 21, pp 49–130. <https://doi.org/10.1016/B978-0-12-801970-2.00002-1>.
- (237) Mcquade, D. T.; Kim, J.; Swager, T. M. Two-Dimensional Conjugated Polymer Assemblies: Interchain Spacing for Control of Photophysics. *J. Am. Chem. Soc.* 2000, 122 (24), 5885–5886. <https://doi.org/10.1021/ja000553+>.

- (238) Alinia, Z.; Miao, D.; Baumgartner, T.; DeWolf, C. E. Tuning Electrostatics to Promote Ordered Monolayers of Phosphole-Lipids. *Langmuir* **2024**. <https://doi.org/10.1021/acs.langmuir.4c02962>.
- (239) Southworth, G. R.; Keller, J. L. Hydrophobic Sorption of Polar Organics by Low Organic Carbon Soils. *Water Air Soil Pollut.* **1986**, *28*, 239-248. <https://doi.org/10.1007/BF00583490>.
- (240) Mendoza Huizar, L. H.; Rios-Reyes, C. H.; García Sanchez, E. A Theoretical Study of the Intermolecular Interactions in the P-Azoxyanisole Liquid Crystal. *J. Mol. Liq.* **2014**, *199*, 530–537. <https://doi.org/10.1016/j.molliq.2014.10.005>.
- (241) Nittmann, J.; Eugene Stanley, H. Tip Splitting without Interfacial Tension and Dendritic Growth Patterns Arising from Molecular Anisotropy. *Nature*, **1986**, *321*, 663-668.
- (242) Jurak, M.; Szafran, K.; Cea, P.; Martín, S. Analysis of Molecular Interactions between Components in Phospholipid-Immunosuppressant-Antioxidant Mixed Langmuir Films. *Langmuir* **2021**, *37* (18), 5601–5616. <https://doi.org/10.1021/acs.langmuir.1c00434>.
- (243) Jimison, L. H.; Toney, M. F.; McCulloch, I.; Heeney, M.; Salleo, A. Charge-Transport Anisotropy Due to Grain Boundaries in Directionally Crystallized Thin Films of Regioregular Poly(3-Hexylthiophene). *Adv. Mater.* **2009**, *21* (16), 1568–1572. <https://doi.org/10.1002/adma.200802722>.
- (244) Zhao, L.; Zhang, H.; Wang, W. π - π Stacking Interaction in Mixed Surfactant Solutions Assembled by Cationic Surfactant and Organic Salt with a Naphthalene Nucleus. *J. Mol. Liq.* **2017**, *240*, 14–20. <https://doi.org/10.1016/j.molliq.2017.05.048>.
- (245) Neumann, C. F.; Sigel, H. Ternary Complexes in Solution. XVIII. The Stability Enhancement of Nucleotide-Containing Charge-Transfer Adducts through the Formation of a Metal Ion Bridge, *J. Am. Chem. Soc.* **1974**, *96*, 2750-2756.
- (246) Pearlman, R. S.; Yalkowsky, S. H.; Banerjee, S. Water Solubilities of Polynuclear Aromatic and Heteroaromatic Compounds. *J. Phys. Chem. Ref. Data* **1984**, *13* (2), 555–562. <https://doi.org/10.1063/1.555712>.
- (247) Yalkowsky, S. H.; He, Y.; Jain, P. *Handbook of Aqueous Solubility Data*; CRC Press, Boca Raton, 2016. <https://doi.org/10.1201/EBK1439802458>.
- (248) Madrid, E.; Horswell, S. L. Effect of Headgroup on the Physicochemical Properties of Phospholipid Bilayers in Electric Fields: Size Matters. *Langmuir* **2013**, *29* (5), 1695–1708. <https://doi.org/10.1021/la304455d>.
- (249) Jurow, M.; Schuckman, A. E.; Batteas, J. D.; Drain, C. M. Porphyrins as Molecular Electronic Components of Functional Devices. *Coord. Chem. Rev.* **2010**, *254* (19–20), 2297–2310. <https://doi.org/10.1016/j.ccr.2010.05.014>.
- (250) Hu, C.; Jiang, D.; Zhang, Y.; Gao, H.; Zeng, Y.; Khaorapapong, N.; Liu, Z.; Yamauchi, Y.; Pan, M. Porphyrins-Based Multidimensional Nanomaterials: Structural Design, Modification and Applications. *Coord. Chem. Rev.* **2025**, *523*, 216264. <https://doi.org/10.1016/j.ccr.2024.216264>.
- (251) Hill, J. P.; Shrestha, L. K.; Ishihara, S.; Ji, Q.; Ariga, K. Self-Assembly: From Amphiphiles to Chromophores and Beyond. *Molecules.* **2014**, *19* (6), 8589–8609. <https://doi.org/10.3390/molecules19068589>.

- (252) Paolesse, R.; Nardis, S.; Monti, D.; Stefanelli, M.; Di Natale, C. Porphyrinoids for Chemical Sensor Applications. *Chem. Rev.* **2017**, *117* (4), 2517–2583. <https://doi.org/10.1021/acs.chemrev.6b00361>.
- (253) Li, L.-L.; Diao, E. W.-G. Porphyrin-Sensitized Solar Cells. *Chem. Soc. Rev.* **2013**, *42* (1), 291–304. <https://doi.org/10.1039/C2CS35257E>.
- (254) Yella, A.; Lee, H.-W.; Tsao, H. N.; Yi, C.; Chandiran, A. K.; Nazeeruddin, Md. K.; Diao, E. W.-G.; Yeh, C.-Y.; Zakeeruddin, S. M.; Grätzel, M. Porphyrin-Sensitized Solar Cells with Cobalt (II/III)-Based Redox Electrolyte Exceed 12 Percent Efficiency. *Science* **2011**, *334* (6056), 629–634. <https://doi.org/10.1126/science.1209688>.
- (255) Xu, J.; Zeng, F.; Wu, H.; Hu, C.; Wu, S. Enhanced Photodynamic Efficiency Achieved via a Dual-Targeted Strategy Based on Photosensitizer/Micelle Structure. *Biomacromolecules* **2014**, *15* (11), 4249–4259. <https://doi.org/10.1021/bm501270e>.
- (256) Son, H.-J.; Jin, S.; Patwardhan, S.; Wezenberg, S. J.; Jeong, N. C.; So, M.; Wilmer, C. E.; Sarjeant, A. A.; Schatz, G. C.; Snurr, R. Q.; Farha, O. K.; Wiederrecht, G. P.; Hupp, J. T. Light-Harvesting and Ultrafast Energy Migration in Porphyrin-Based Metal–Organic Frameworks. *J. Am. Chem. Soc.* **2013**, *135* (2), 862–869. <https://doi.org/10.1021/ja310596a>.
- (257) Everse, J. Heme Proteins. In *Encyclopedia of Biological Chemistry*; Elsevier, 2004; pp 354–361. <https://doi.org/10.1016/B0-12-443710-9/00304-5>.
- (258) Ptaszek, M. Rational Design of Fluorophores for In Vivo Applications. In *Progress in Molecular Biology and Translational Science*; Academic Press, 2013; pp 59–108. <https://doi.org/10.1016/B978-0-12-386932-6.00003-X>.
- (259) Zheng, W.; Shan, N.; Yu, L.; Wang, X. UV–Visible, Fluorescence and EPR Properties of Porphyrins and Metalloporphyrins. *Dyes Pigm.* **2008**, *77* (1), 153–157. <https://doi.org/10.1016/j.dyepig.2007.04.007>.
- (260) Kou, J.; Dou, D.; Yang, L. Porphyrin Photosensitizers in Photodynamic Therapy and Its Applications. *Oncotarget* **2017**, *8* (46), 81591–81603. <https://doi.org/10.18632/oncotarget.20189>.
- (261) Adachi, K.; Hirose, T.; Matsuda, K. The Polymorphism of Porphyrin 2D Assemblies at the Liquid–Graphite Interface: The Effect of a Polar Solvent Additive and a Flexible Spacer on the Face-on and Edge-on Type Molecular Arrangements. *Chem. Commun.* **2019**, *55* (60), 8836–8839. <https://doi.org/10.1039/C9CC02579K>.
- (262) Piot, L.; Marie, C.; Feng, X.; Müllen, K.; Fichou, D. Hierarchical Self-Assembly of Edge-On Nanocolumnar Superstructures of Large Disc-Like Molecules. *Adv. Mater.* **2008**, *20* (20), 3854–3858. <https://doi.org/10.1002/adma.200801428>.
- (263) Sakano, T.; Higashiguchi, K.; Matsuda, K. Comparison of Molecular Conductance between Planar and Twisted 4-Phenylpyridines by Means of Two-Dimensional Phase Separation of Tetraphenylporphyrin Templates at a Liquid–HOPG Interface. *Chem. Commun.* **2011**, *47* (29), 8427. <https://doi.org/10.1039/c1cc12041g>.
- (264) Ding, X.; Wei, S.; Bian, H.; Zhu, L.; Xia, D. Insights into the Self-Aggregation of Porphyrins and Their Influence on Asphaltene Aggregation. *Energy Fuels* **2021**, *35* (15), 11848–11857. <https://doi.org/10.1021/acs.energyfuels.1c00652>.

- (265) Eichhorn, S. H.; Abdulhamied, E. Self-Organization of Porphyrins and Phthalocyanines in Two and Three Dimensions. In *Handbook of Porphyrin Science*; World Scientific, 2016; pp 173–232. https://doi.org/10.1142/9789813149625_0003.
- (266) Auwärter, W.; Écija, D.; Klappenberger, F.; Barth, J. V. Porphyrins at Interfaces. *Nat. Chem.* **2015**, *7* (2), 105–120. <https://doi.org/10.1038/nchem.2159>.
- (267) Wang, S.; Peng, L.; Sun, H.; Huang, W. The Future of Solution Processing toward Organic Semiconductor Devices: A Substrate and Integration Perspective. *J. Mater. Chem. C Mater* **2022**, *10* (35), 12468–12486. <https://doi.org/10.1039/D2TC02316D>.
- (268) Gu, W.; Li, Q.; Wang, R.; Zhang, L.; Liu, Z.; Jiao, T. Recent Progress in the Applications of Langmuir–Blodgett Film Technology. *Nanomaterials* **2024**, *14* (12), 1039. <https://doi.org/10.3390/nano14121039>.
- (269) Harvey, P. D.; Stern, C.; Gros, C. P.; Guillard, R. The Photophysics and Photochemistry of Cofacial Free Base and Metallated Bisporphyrins Held Together by Covalent Architectures. *Coord. Chem. Rev.* **2007**, *251* (3–4), 401–428. <https://doi.org/10.1016/j.ccr.2006.06.009>.
- (270) Wang, X.; Lv, H.; Sun, Y.; Zu, G.; Zhang, X.; Song, Y.; Zhao, F.; Wang, J. New Porphyrin Photosensitizers—Synthesis, Singlet Oxygen Yield, Photophysical Properties and Application in PDT. *Spectrochim. Acta Part A* **2022**, *279*, 121447. <https://doi.org/10.1016/j.saa.2022.121447>.
- (271) Ricciardi, G.; Belviso, S.; Giancane, G.; Tafuro, R.; Wagner, T.; Valli, L. Floating Films of a Nonamphiphilic Porphyrine at the Air-Water Interface and LS Multilayer Construction and Optical Characterization. *J. Phys. Chem. B* **2004**, *108* (23), 7854–7861. <https://doi.org/10.1021/jp036695i>.
- (272) Peñacorada, F.; Souto, J.; Saja, J. A. D.; Brehmer, L. Brewster Angle Microscopy and Surface Potential Measurements of Langmuir-Blodgett Films of Zinc Tri(Tert-Butyl)-4-Sulphophthalocyanine. In *Applied Surface Science*; Elsevier, 2005; Vol. 246, pp 425–429. <https://doi.org/10.1016/j.apsusc.2004.11.047>.
- (273) Valli, L. Phthalocyanine-Based Langmuir–Blodgett Films as Chemical Sensors. *Adv. Colloid Interface Sci.* **2005**, *116* (1–3), 13–44. <https://doi.org/10.1016/j.cis.2005.04.008>.
- (274) Dong, S.; Tian, H.; Song, D.; Yang, Z.; Yan, D.; Geng, Y.; Wang, F. The First Liquid Crystalline Phthalocyanine Derivative Capable of Edge-on Alignment for Solution Processed Organic Thin-Film Transistors. *Chem. Commun.* **2009**, *21*, 3086. <https://doi.org/10.1039/b822819a>.
- (275) Zhou, K.; Wu, Y.; Liu, Y.; Zhou, X.; Zhang, L.; Ma, W. Molecular Orientation of Polymer Acceptor Dominates Open-Circuit Voltage Losses in All-Polymer Solar Cells. *ACS Energy Lett.* **2019**, *4* (5), 1057–1064. <https://doi.org/10.1021/acsenergylett.9b00416>.
- (276) Liang, Q.; Duan, M.; Geng, Z.; Zhang, M.; Xu, W.; Geng, H.; He, Z.; Liu, J. Regulation of Molecular Orientation in Organic Solar Cells. *Chem. Eng. J.* **2024**, *488*, 150783. <https://doi.org/10.1016/j.cej.2024.150783>.
- (277) Mulay, S. V.; Dishy, O.; Fang, Y.; Niazi, M. R.; Shimon, L. J. W.; Perepichka, D. F.; Gidron, O. A Macrocyclic Oligofuran: Synthesis, Solid State Structure and Electronic Properties. *Chem. Sci.* **2019**, *10* (37), 8527–8532. <https://doi.org/10.1039/C9SC03247A>.

- (278) Javaid, S.; Lee, G. The Impact of Molecular Orientation on Carrier Transfer Characteristics at a Phthalocyanine and Halide Perovskite Interface. *RSC Adv.* **2021**, *11* (50), 31776–31782. <https://doi.org/10.1039/D1RA05909B>.
- (279) Li, X.; Xu, W.; Itoh, T.; Ikehata, A.; Zhao, B.; Li, B.; Ozaki, Y. Effects of a Central Metal on the Organization of 5,10,15,20-Tetra-(p-Chlorophenyl)-Rare Earth Porphyrin Hydroxyl Compound at the Air/Water Interface and in Langmuir-Blodgett Films. *J. Colloid Interface Sci.* **2005**, *284* (2), 582–592. <https://doi.org/10.1016/j.jcis.2004.10.053>.
- (280) Zhou, Y.; Wang, B.; Zhu, M.; Hou, J. G. Observation of Co-Existence of ‘Face-on’ and ‘Edge-on’ Stacking Styles in a Porphyrin Monolayer. *Chem. Phys. Lett.* **2005**, *403* (1–3), 140–145. <https://doi.org/10.1016/j.cplett.2005.01.006>.
- (281) Nikiforov, M. P.; Zerweck, U.; Milde, P.; Loppacher, C.; Park, T.-H.; Uyeda, H. T.; Therien, M. J.; Eng, L.; Bonnell, D. The Effect of Molecular Orientation on the Potential of Porphyrin–Metal Contacts. *Nano Lett.* **2008**, *8* (1), 110–113. <https://doi.org/10.1021/nl072175d>.
- (282) Tomita, K.; Shioya, N.; Shimoaka, T.; Wakioka, M.; Hasegawa, T. Control of Supramolecular Organizations by Coordination Bonding in Tetrapyridylporphyrin Thin Films. *Chem. Commun.* **2022**, *58* (13), 2116–2119. <https://doi.org/10.1039/D1CC06169K>.
- (283) Graewe, L.; Hupfer, M. L.; Schulz, M.; Mohammed, A.; Gross, Z.; Presselt, M. Supramolecular Control of Photonic Response and Sensing of Nitricoxide Using Iron(III) Corrole Monolayers and Their Stacks. *ChemPlusChem* **2023**, *88* (3). <https://doi.org/10.1002/cplu.202200260>.
- (284) Shokurov, A. V.; Alexandrova, A. V.; Shcherbina, M. A.; Bakirov, A. V.; Rogachev, A. V.; Yakunin, S. N.; Chvalun, S. N.; Arslanov, V. V.; Selektor, S. L. Supramolecular Control of the Structure and Receptor Properties of an Amphiphilic Hemicyanine Chromoionophore Monolayer at the Air/Water Interface. *Soft Matter* **2020**, *16* (43), 9857–9863. <https://doi.org/10.1039/d0sm01078b>.
- (285) Alexandrova, A. V.; Shcherbina, M. A.; Repchenko, Y. L.; Selivantiev, Y. M.; Shokurov, A. V.; Arslanov, V. V.; Selektor, S. L. Structure Affinity of the Langmuir Monolayer and the Corresponding Langmuir-Blodgett Film Revealed by X-Ray Techniques. *Soft Matter* **2024**. <https://doi.org/10.1039/d4sm01050g>.
- (286) Ding, H.; Erokhin, V.; Ram, M. K.; Paddeu, S.; Valkova, L.; Nicolini, C. Physical Insight into the Gas-Sensing Properties of Copper (II) Tetra-(Tert-Butyl)-5,10,15,20-Tetraazaporphyrin Langmuir Blodgett Films. *Thin Solid Films* **2000**, *379* (1–2), 279–286.
- (287) Fuchter, M. J.; Beall, L. S.; Baum, S. M.; Montalban, A. G.; Sakellariou, E. G.; Mani, N. S.; Miller, T.; Vesper, B. J.; White, A. J. P.; Williams, D. J.; Barrett, A. G. M.; Hoffman, B. M. Synthesis of Porphyrazine-Octamine, Hexamine and Diamine Derivatives. *Tetrahedron* **2005**, *61* (25), 6115–6130. <https://doi.org/10.1016/j.tet.2005.03.090>.
- (288) Barbee, J.; Kuznetsov, A. E. Revealing Substituent Effects on the Electronic Structure and Planarity of Ni-Porphyrins. *Comput. Theor. Chem.* **2012**, *981*, 73–85. <https://doi.org/10.1016/j.comptc.2011.11.049>.
- (289) Okura, I. *Photosensitization of Porphyrins and Phthalocyanines*; CRC Press, 2017. <https://doi.org/10.1201/b22328>.

- (290) Nutting, G. C.; Harkins, W. D. Pressure-Area Relations of Fatty Acid and Alcohol Monolayers. *J. Am. Chem. Soc.* **1939**, *61* (5), 1180–1187.
- (291) Doan, V.; Koppe, R.; Kasai, P. H. Dimerization of Carboxylic Acids and Salts: An IR Study in Perfluoropolyether Media. *J. Am. Chem. Soc.* **1997**, *119*, 9810–9815. <https://pubs.acs.org/sharingguidelines>.
- (292) Kraack, H.; Ocko, B. M.; Pershan, P. S.; Sloutskin, E.; Tamam, L.; Deutsch, M. Fatty Acid Langmuir Films on Liquid Mercury: X-Ray and Surface Tension Studies. *Langmuir* **2004**, *20* (13), 5375–5385. <https://doi.org/10.1021/la049977y>.
- (293) Lelj, F.; Morelli, G.; Ricciardi, G.; Roviello, A.; Sirigu, A. Discotic Mesomorphism of 2,3,7,8,12,13,17,18-Octakis (Alkyl-Thio) 5,10,15,20 Tetraaza Porphyrin and Its Complexes with Some Divalent Transition Metal Ions Synthesis and Characterization. *Liq. Cryst.* **1992**, *12* (6), 941–960. <https://doi.org/10.1080/02678299208032810>.
- (294) Ricceri, R.; Ricciardi, G.; Lelj, F.; Martini, G.; Gabrielli, G. Monolayers and Langmuir–Blodgett Films of a Palladium(II)-Tetraazaporphyrin, *Thin Solid Films*, 1999342 (1–2), 277–281. [https://doi.org/10.1016/S0040-6090\(98\)01557-0](https://doi.org/10.1016/S0040-6090(98)01557-0).
- (295) Eichhorn, S. H.; Bruce, D. W.; Guillon, D.; Gallani, J. L.; Fischer, T.; Stumpe, J.; Geue, T. Metal Ion Mediated Mesomorphism and Thin Film Behaviour of Amphitropic Tetraazaporphyrin Complexes. *J. Mater. Chem.* **2001**, *11* (6), 1576–1584. <https://doi.org/10.1039/b100112o>.
- (296) Davison, A.; Holm, R. H.; Benson, R. E.; Mahler, W. Metal Complexes Derived from cis-1,2-dicyano-1,2-ethylenedithiolate and Bis(Trifluoromethyl)-1,2-dithiete. In *Inorganic Syntheses; Muettterties, E. L., Ed.; McGraw Hill, 1967; Vol. 10, pp 8–26.*
- (297) Eichhorn, H.; Rutloh, M.; Wohrle, D.; Stumpe, J. Synthesis and photochemical properties of octacinnamoylsubstituted tetraazaporphyrins. *J. Chem. Soc., Perkin Trans. 2* 1996, No. 9, 1801–1810.
- (298) Ghosh, A.; Yoshida, M.; Suemori, K.; Isago, H.; Kobayashi, N.; Mizutani, Y.; Kurashige, Y.; Kawamura, I.; Nirei, M.; Yamamuro, O.; Takaya, T.; Iwata, K.; Saeki, A.; Nagura, K.; Ishihara, S.; Nakanishi, T. Soft Chromophore Featured Liquid Porphyrins and Their Utilization toward Liquid Electret Applications. *Nat. Commun.* **2019**, *10* (1). <https://doi.org/10.1038/s41467-019-12249-8>.
- (299) Maruyama, S.; Saito, W. Liquid Porphyrin Derivative and Method for Producing the Same. EP2253634 A1, 2009.
- (300) Santini, E.; Krägel, J.; Ravera, F.; Liggieri, L.; Miller, R. Study of the Monolayer Structure and Wettability Properties of Silica Nanoparticles and CTAB Using the Langmuir Trough Technique. *Colloids Surf. A* **2011**, *382* (1–3), 186–191. <https://doi.org/10.1016/j.colsurfa.2010.11.042>.

Appendix A. Supplementary information for Chapter 3.

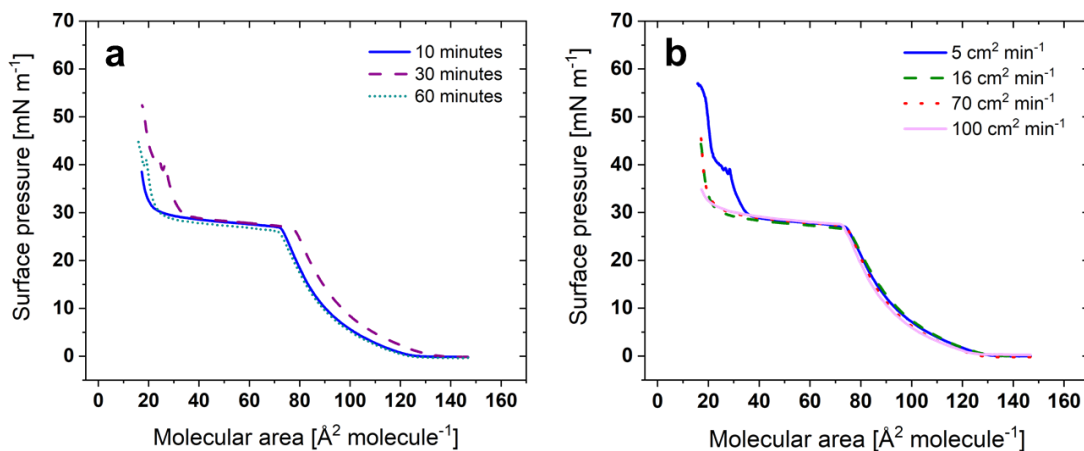


Figure A1 Surface pressure-molecular area isotherms of phosphole-lipids on ultrapure water subphase as a function of: (a) relaxation time prior to compression, and (b) compression rate.

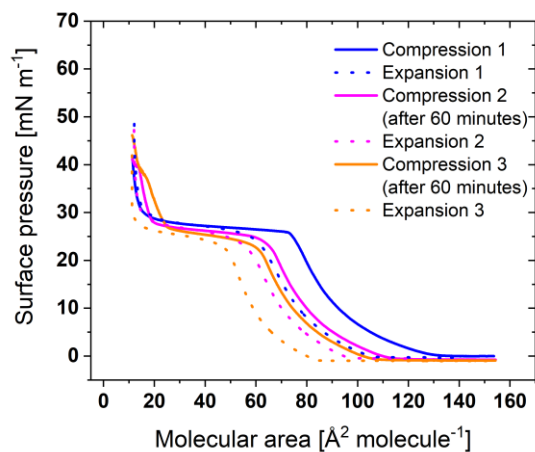


Figure A2 Repeated isotherm cycles for phosphole-lipids on ultrapure water as subphase with 60 minutes waiting time after each cycle.

Table A1 LB transfer ratio for AFM samples obtained at different surface pressures and from different NaBr concentrations in the subphase.

Surface pressure (mN m^{-1})	Transfer ratio values				
	Water	NaBr 1 μM	NaBr 1 mM	NaBr 10 mM	NaBr 100 mM
15	-	1.2	1.3	1.1	2.1
20	-	1.4	1.3	1.5	2.1
25	1.2	1.4	1.3	1.0	1.2
30	2.0	1.6	3.4	1.3	1.1
35	2.2	1.8	4.7	1.1	1.4
40	2.1	1.9	4.7	2.3	1.5
45	2.4	1.9	7.0	2.2	2.1

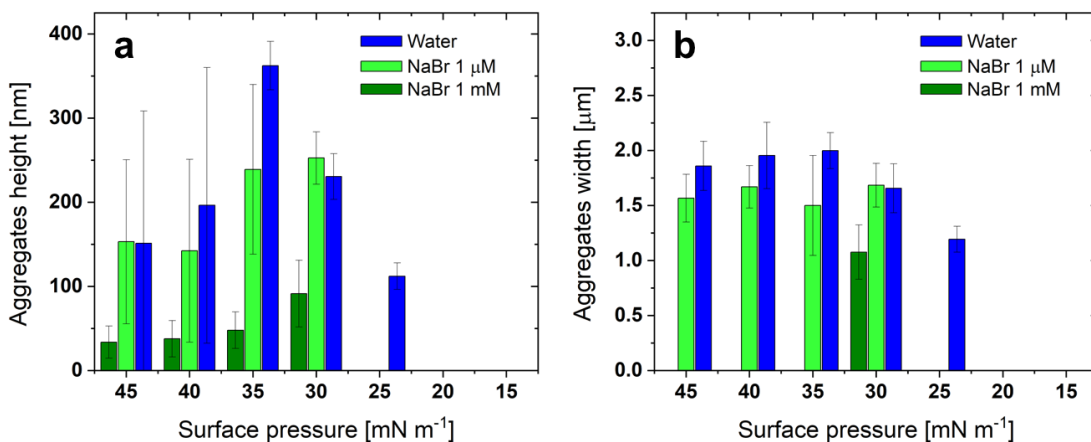


Figure A3 3D aggregates heights (a) width (b) measured from AFM images as a function of NaBr concentration in the subphase. At least three locations from each of two independently prepared samples were measured. For 1 mM NaBr, the 3D aggregate widths are too small at surface pressures above the plateau to be accurately measured and thus are not reported.

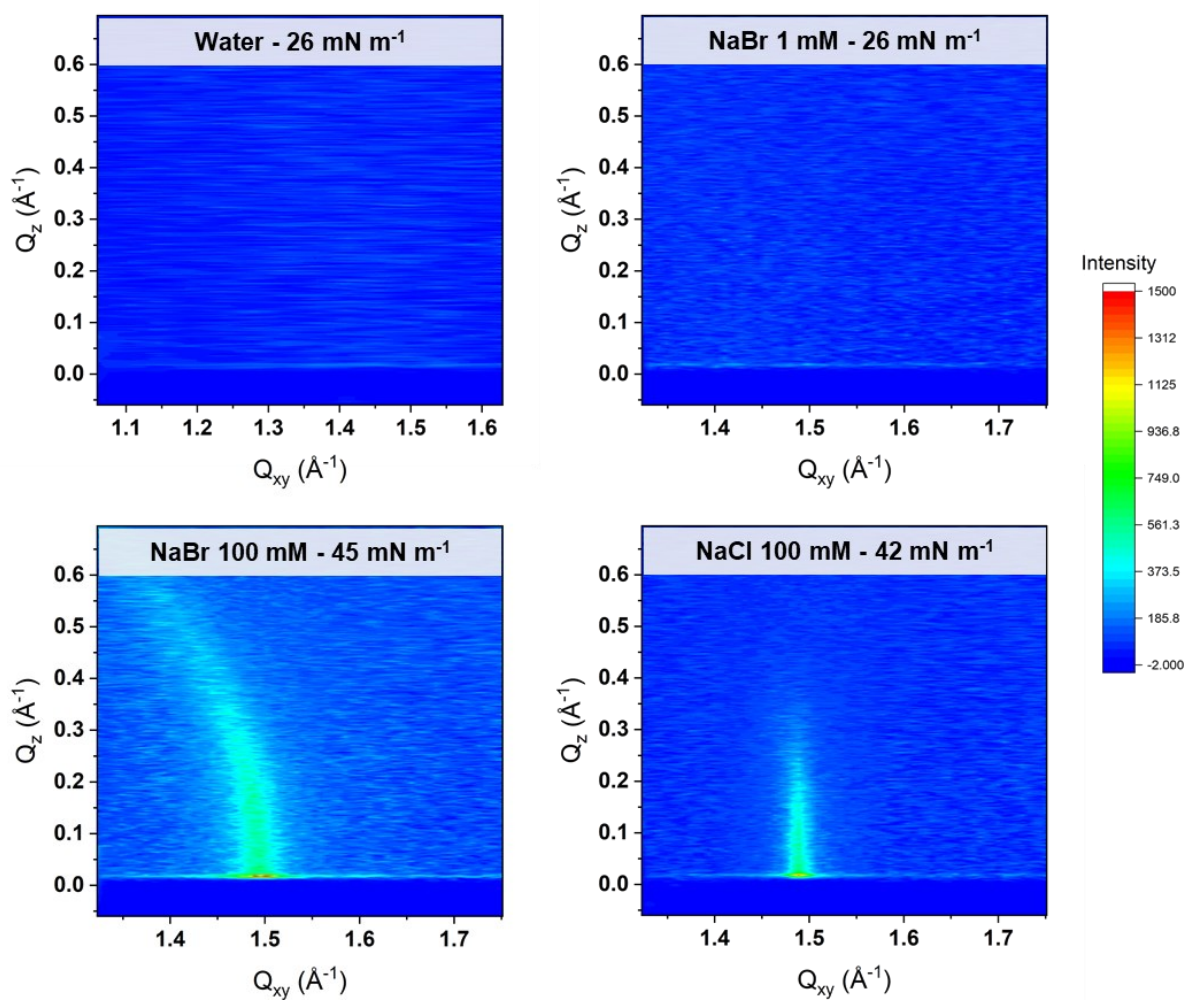


Figure A4 GIXD contour plot of X-ray diffraction intensity as a function of the Q_{xy} (in-plane) and Q_z (out-of-plane) vector components for phosphole-lipids on water at 26 mN m^{-1} (top left), 1 mM NaBr at 26 mN m^{-1} (top right), 100 mM NaBr at 45 mN m^{-1} (bottom left), and 100 mM NaCl at 42 mN m^{-1} (bottom right).

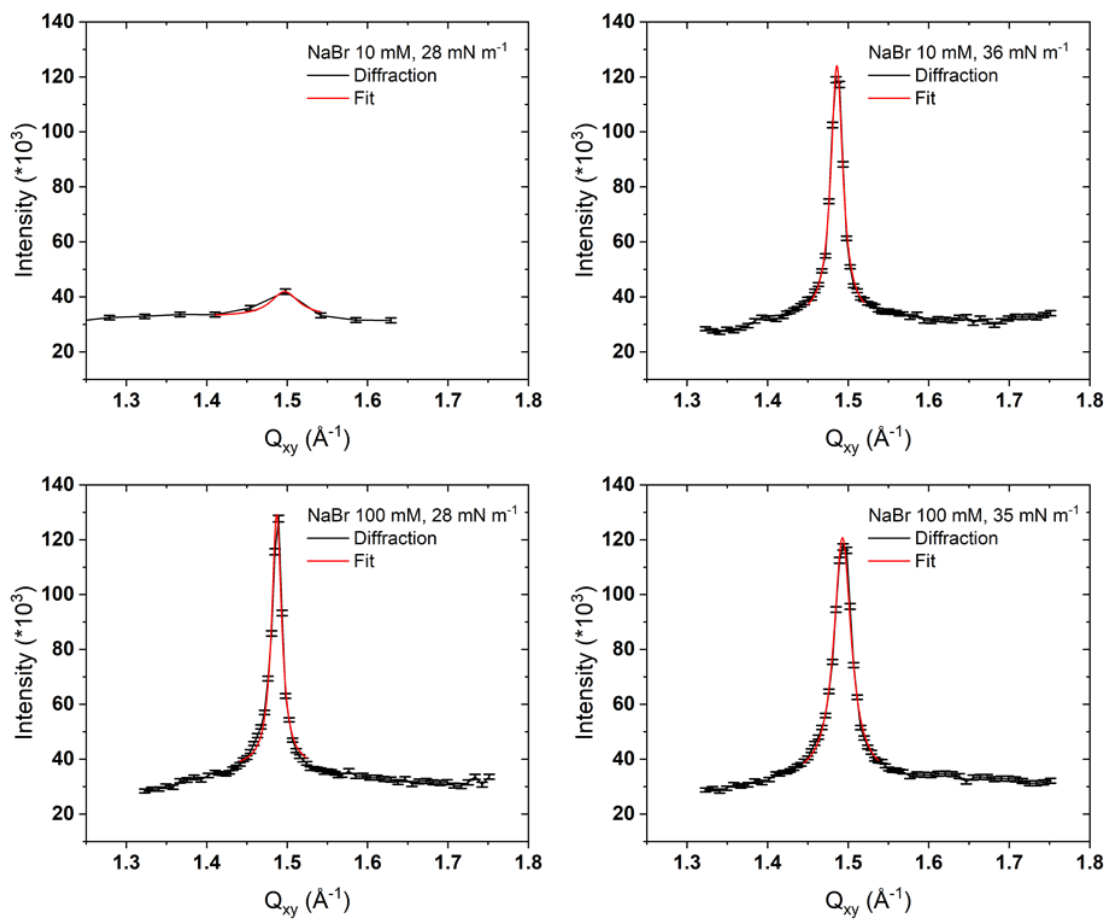


Figure A5 Bragg peak profile integrated over the full Q_z range, and corresponding Lorentzian fit. The fitting parameters are reported in Table A2.

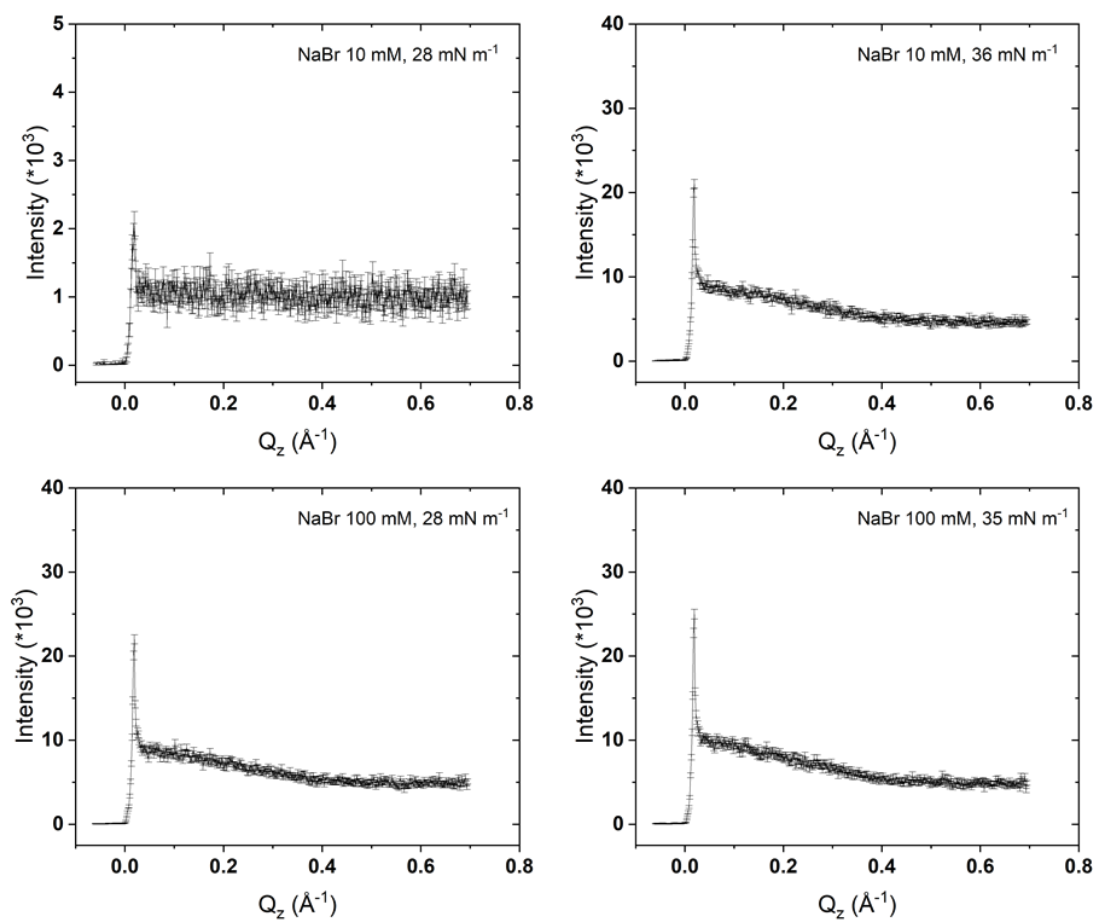


Figure A6 Bragg rod profile integrated over the full Q_{xy} range. The corresponding fits are shown in Figure A8.

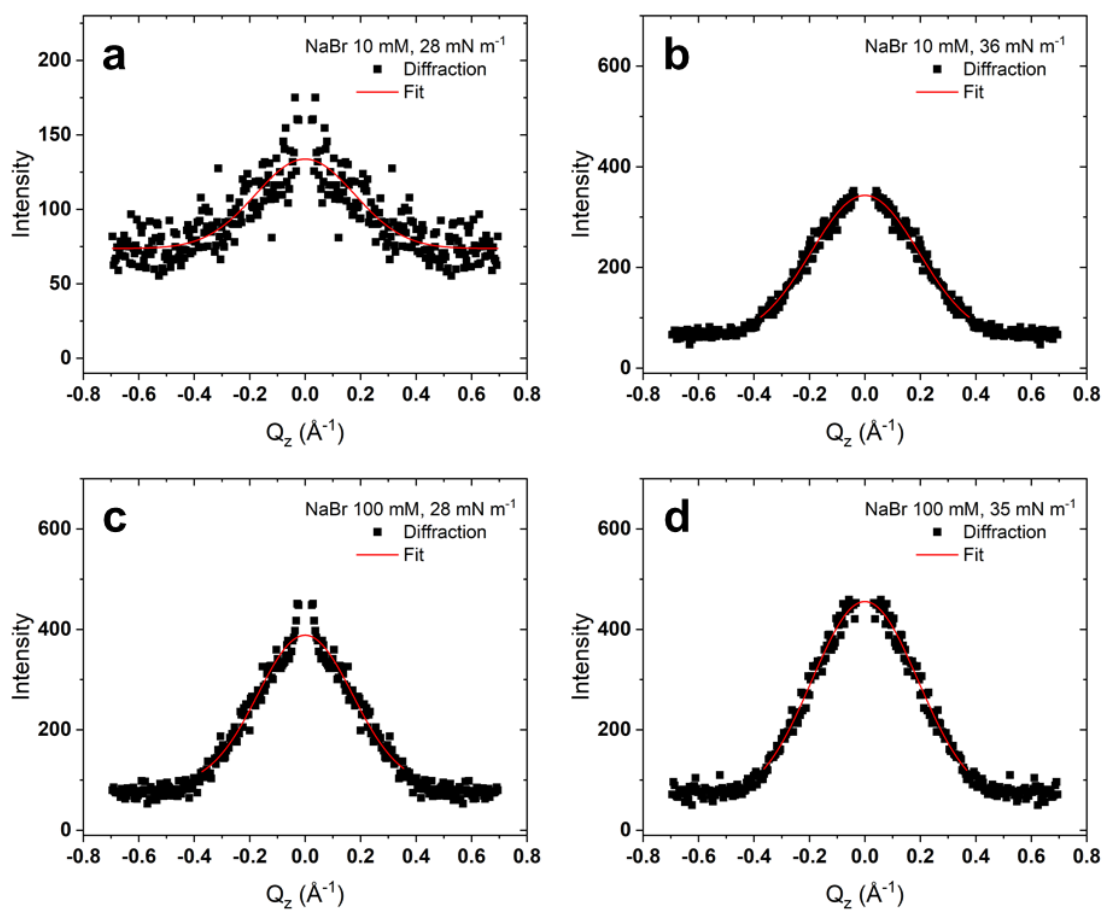


Figure A7 Bragg rod profiles from Figure A7 and corresponding Gaussian fits. The vineyard peak has been removed and the data mirrored for the fitting. The Q_{xy} integration ranges are: a) 1.475-1.505 \AA^{-1} , b) 1.436-1.536 \AA^{-1} , c) 1.470-1.510 \AA^{-1} , and d) 1.475-1.515 \AA^{-1} . The fitting parameters are reported in Table A9.

Table A2 Peak positions and best fit parameters obtained from GIXD for phosphole-lipids. Units: Surface pressure (π) in mN m^{-1} ; positions (Q_{xy} , Q_z), and FWHM values in \AA^{-1} ; a , d-spacing, lateral correlation length and vertical scattering length in \AA ; A_{xy} in \AA^2 ; γ and tilt angle in $^\circ$.

Surface pressure		Q_{xy}	Q_z	a	γ	Tilt angle	A_{xy}	d-spacing	Lateral correlation length	Vertical scattering length
NaBr 10 mM										
28	Position	1.489	0.000	4.87	120	0.0	20.58	4.22	182	13.5
	FWHM	0.011	0.419							
36	Position	1.486	0.000	4.88	120	0.0	20.64	4.23	111	12.4
	FWHM	0.018	0.457							
NaBr 100 mM										
28	Position	1.487	0.000	4.88	120	0.0	20.60	4.22	133	14.1
	FWHM	0.015	0.402							
35	Position	1.493	0.000	4.86	120	0.0	20.44	4.21	77	12.5
	FWHM	0.026	0.451							
45	Position	1.495	0.000	4.85	120	0.0	20.39	4.20	57	8.5
	FWHM	0.035	0.668							
NaCl 100 mM										
35	Position	1.489	0.000	4.87	120	0.0	20.55	4.22	83	10.4
	FWHM	0.024	0.545							

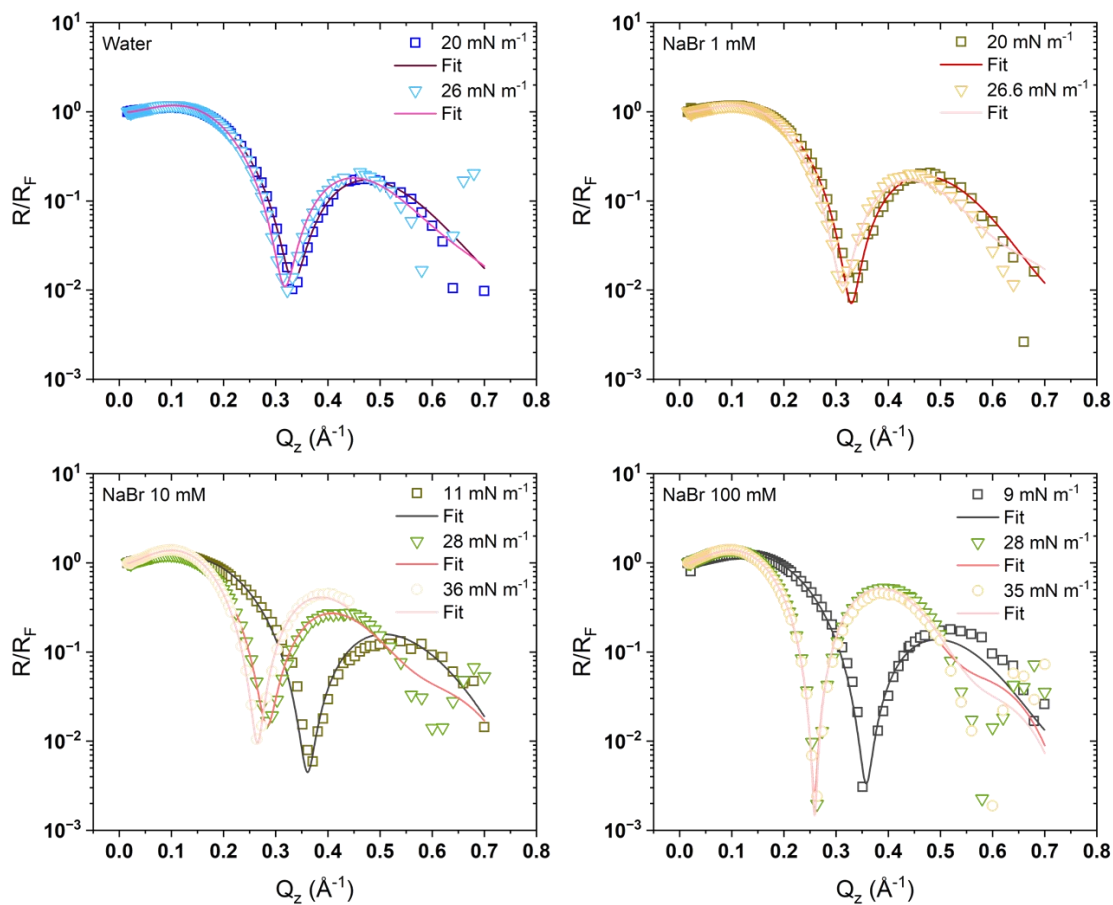


Figure A8 Normalized X-ray reflectivities and their fit model for phosphole-lipids on water and different concentrations of NaBr in subphase.

Table A3 Best fit X-ray reflectivity parameters using two box models for phosphole-lipids on different subphases and at different surface pressures. For water, 1 mM NaBr, 100 mM NaCl and 100 mM NaI, due to the shape of isotherm, we could not perform experiments at surface pressures above the plateau.

Surface pressure (mN m ⁻¹)	Chain region (top box)		Headgroup region (bottom box)	
	Thickness (Å)	ED (e/Å ³)	Thickness (Å)	ED (e/Å ³)
Water				
20	9.8	0.227	8.6	0.415
26	10.1	0.231	9.8	0.422
NaBr 1 mM				
20	9.9	0.236	8.8	0.425
26	10.1	0.267	10.5	0.406
NaBr 10 mM				
11	8.7	0.230	8.2	0.411
28	11.2	0.274	11.1	0.417
36	12.4	0.284	11.2	0.429
NaBr 100 mM				
9	8.8	0.286	8.9	0.423
28	12.6	0.275	11.1	0.439
35	12.3	0.268	11.5	0.440
NaCl 100 mM				
30	9.6	0.267	11.4	0.408
NaI 100 mM				
33	9.8	0.276	11.5	0.424
42	10.2	0.244	11.7	0.408

Appendix B. Supplementary information for Chapter 4.

Nomenclature used in the SI figures and tables:

PL1: phosphole-lipid with the core dithienophosphole headgroup

PL2: phosphole-lipid with the extended, benzo-fused dithienophosphole headgroup

C₁₂HB: dodecyl-4-hydroxybenzoate

Table B1 Transfer ratio values measured for LB deposition of **PL1** onto mica from phenol subphases.

Surface pressure (mN m ⁻¹)	Transfer ratio values			
	Phenol 1 μM	Phenol 1 mM	Phenol 10 mM	Phenol 100 mM
20	1.2	1.3	1.3	7.6
25	1.9	1.5	1.3	-
30	1.9	1.6	2.1	-
35	1.7	1.6	-	-
40	1.8	1.6	-	-
45	2.1	-	-	-

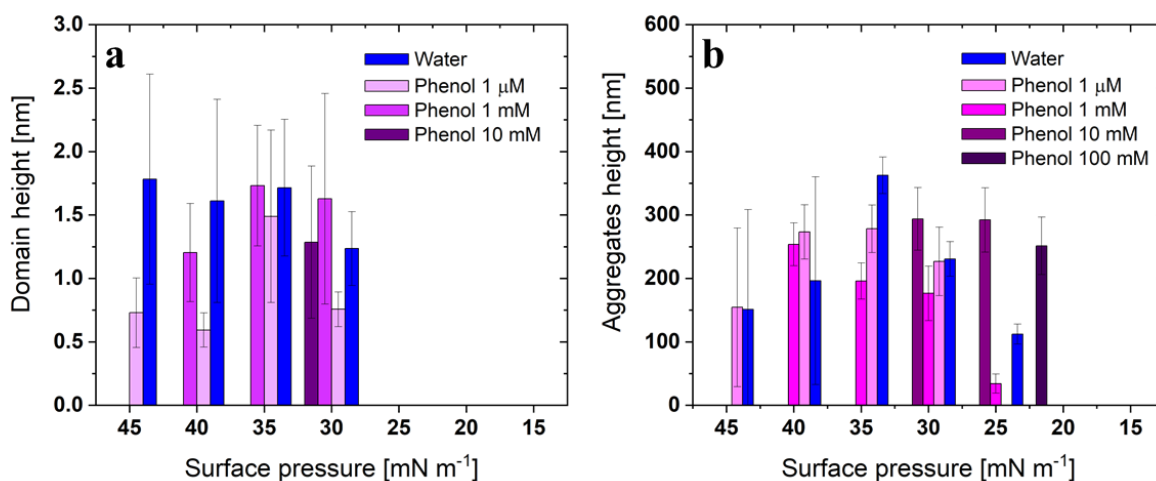


Figure B1 PL1 domain (a) and 3D aggregate (b) heights measured from AFM images as a function of phenol concentration in the subphase. The values and reported errors represent the combined data from at least three locations from each of two independently prepared samples were measured ($n > 100$ domains). The decrease in average aggregate height and increase in error bar for water and 1 μM phenol at high surface pressures reflect the emergence of a second population of aggregates with significantly decreased heights.

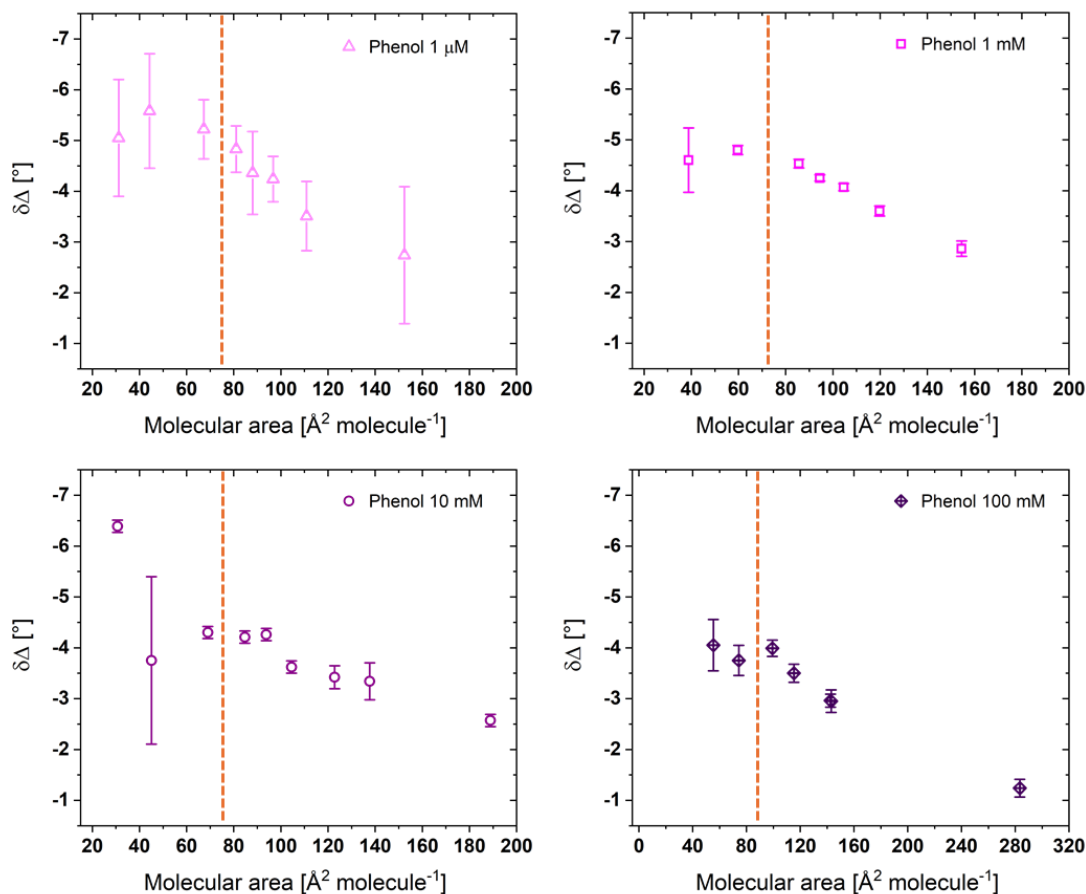


Figure B2 Ellipsometric measurements of PL1 at air-subphase interface as a function of phenol concentration in the subphase. The dashed line defines the molecular area where the phase transition plateau begins. Each value represents the average of measurements made on three independently formed films. For each independent film, the $\delta\Delta$ is the average of 10 measurements of the same monolayer film at constant surface pressure.

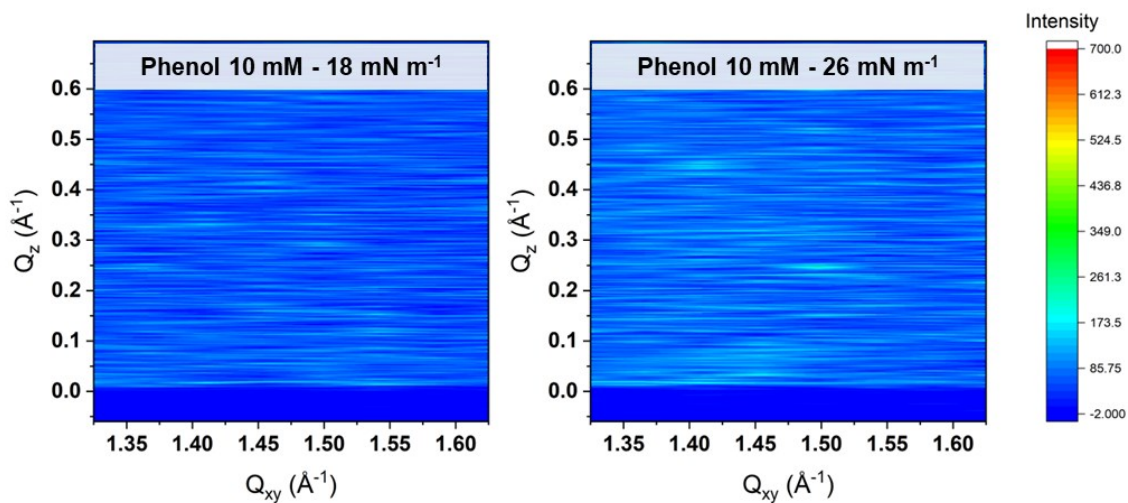


Figure B3 GIXD contour plot of X-ray diffraction intensity as a function of the Q_{xy} (in-plane) and Q_z (out-of-plane) vector components for the **PL1** on 10 mM phenol subphases at two surface pressures below (18 mN m⁻¹) and towards the end of the phase transition plateau (26 mN m⁻¹).

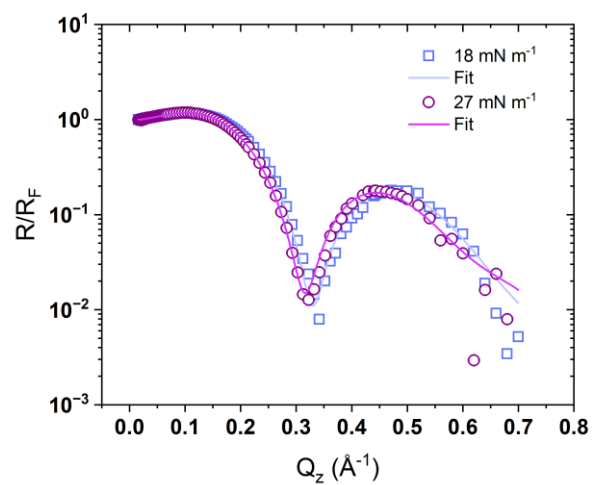


Figure B4 Normalized X-ray reflectivity and their fit model for **PL1** on 10 mM phenol subphase at different surface pressures.

Table B2 Best fit X-ray reflectivity parameters using a two-box model for **PL1** on water and on 10 mM phenol subphase, and **PL1:C₁₂HB** lipid mixture on water. Due to the shape of isotherm, experiments at surface pressures above the plateau could not be performed. The values for **PL1** on water were previously reported²³⁸ and provided here for comparison.

Surface pressure (mN m ⁻¹)	Chain region (top box)		Headgroup region (bottom box)	
	Thickness (Å)	ED (e/Å ³)	Thickness (Å)	ED (e/Å ³)
PL1 on Water				
20	9.8	0.227	8.6	0.415
26	10.1	0.231	9.8	0.422
PL1 on Phenol 10 mM				
18	9.9	0.277	8.8	0.410
27	10.0	0.222	10.3	0.419
PL1:C₁₂HB mixture (1:1 molar ratio) on Water				
17	10.0	0.275	8.5	0.417
25	10.4	0.232	9.9	0.429

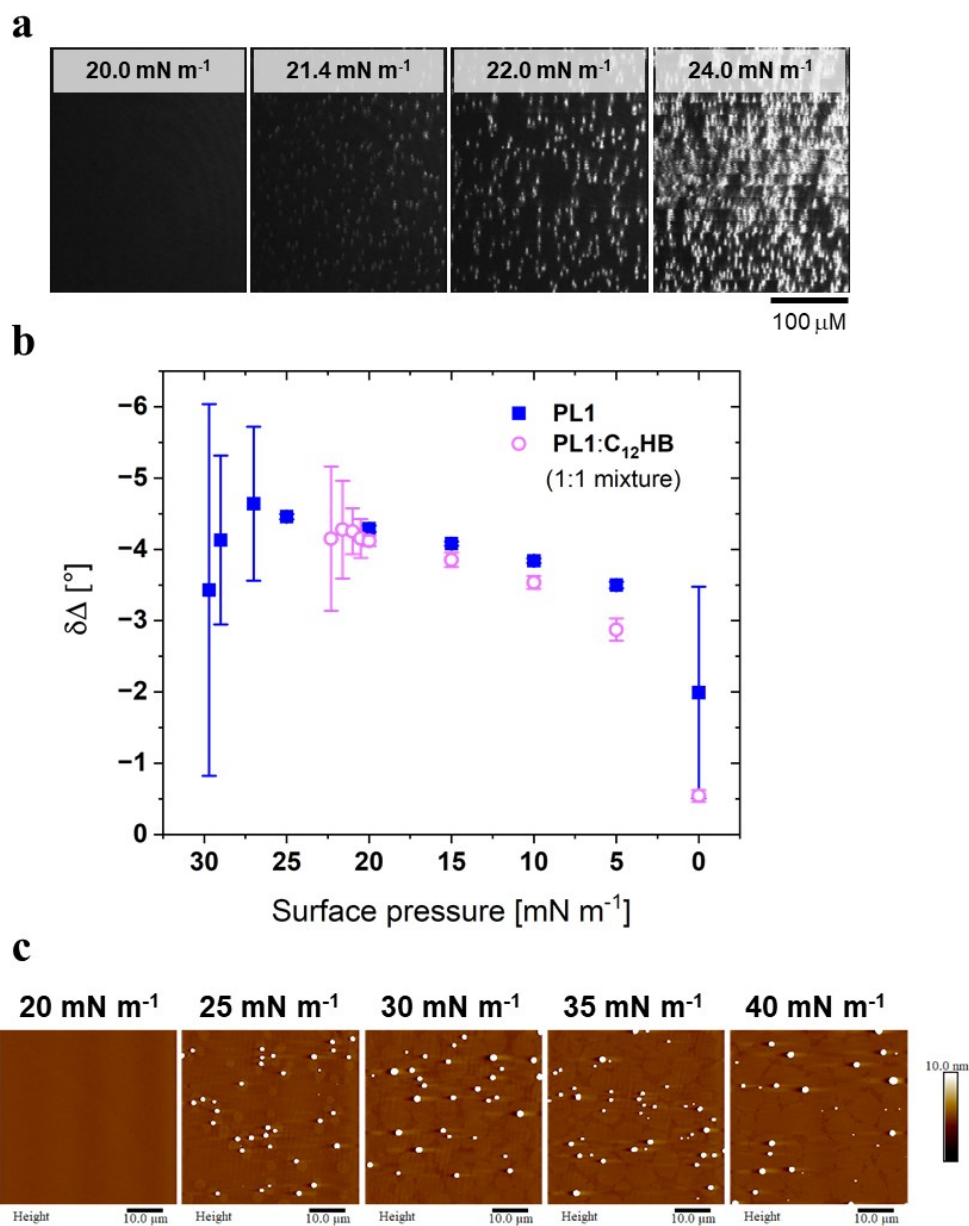


Figure B5 Representative BAM images (a), Ellipsometric measurements (b), and AFM images (c) of a 1:1 mixture of **PL1:C₁₂HB** (on ultrapure water subphase). The AFM images are obtained from the LB deposition of mixture film onto mica. For (b), each value represents the average of measurements made on three independently formed films. For each independent film, the $\delta\Delta$ is the average of 10 measurements of the same monolayer film at constant surface pressure.

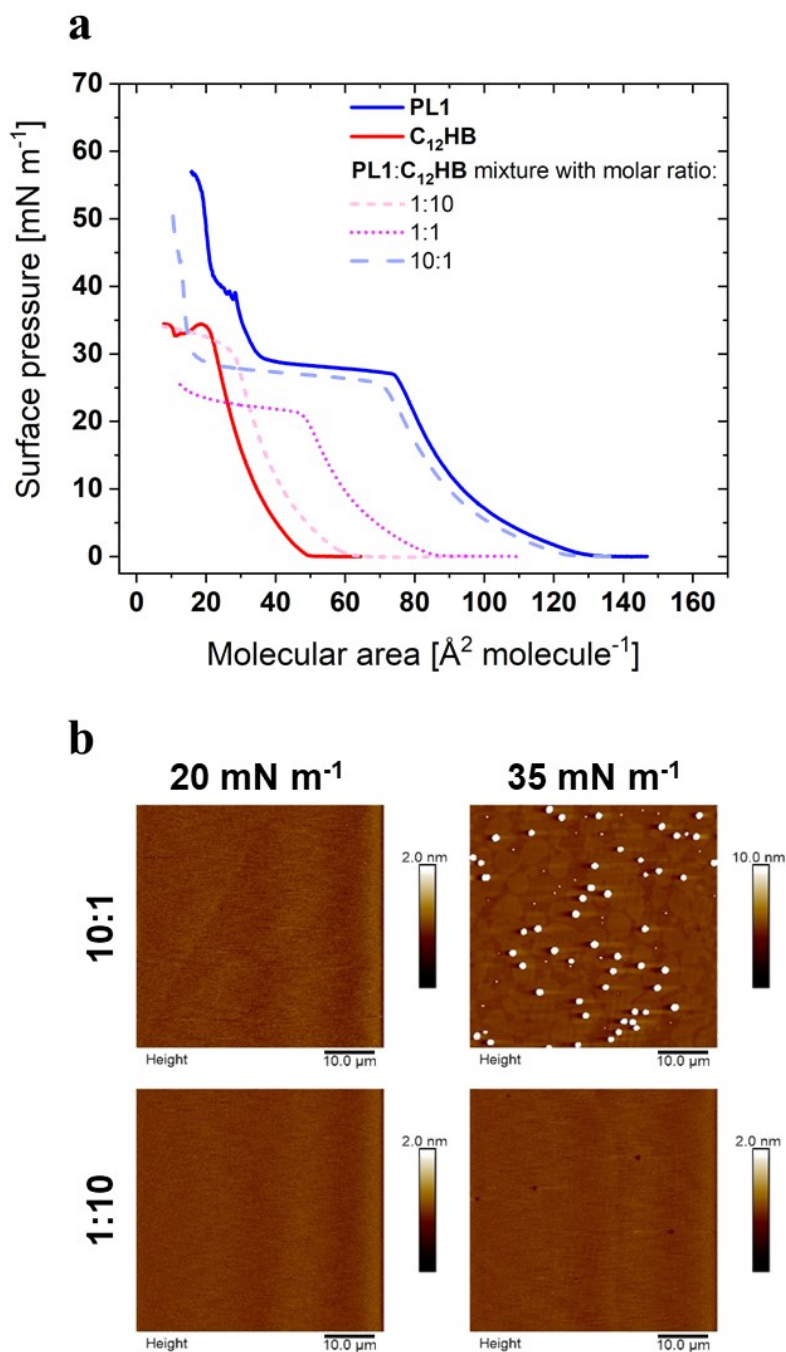


Figure B6 Surface pressure-molecular area of mixture of **PL1**:**C₁₂HB** with molar ratios of 1:10 and 10:1 on water subphase (1:1 mixture isotherm is shown for comparison) (a), and representative AFM images for these two mixtures deposited onto mica by LB at surface pressures of 25 mN m⁻¹ (below the plateau) and 35 mN m⁻¹ (beyond the plateau).

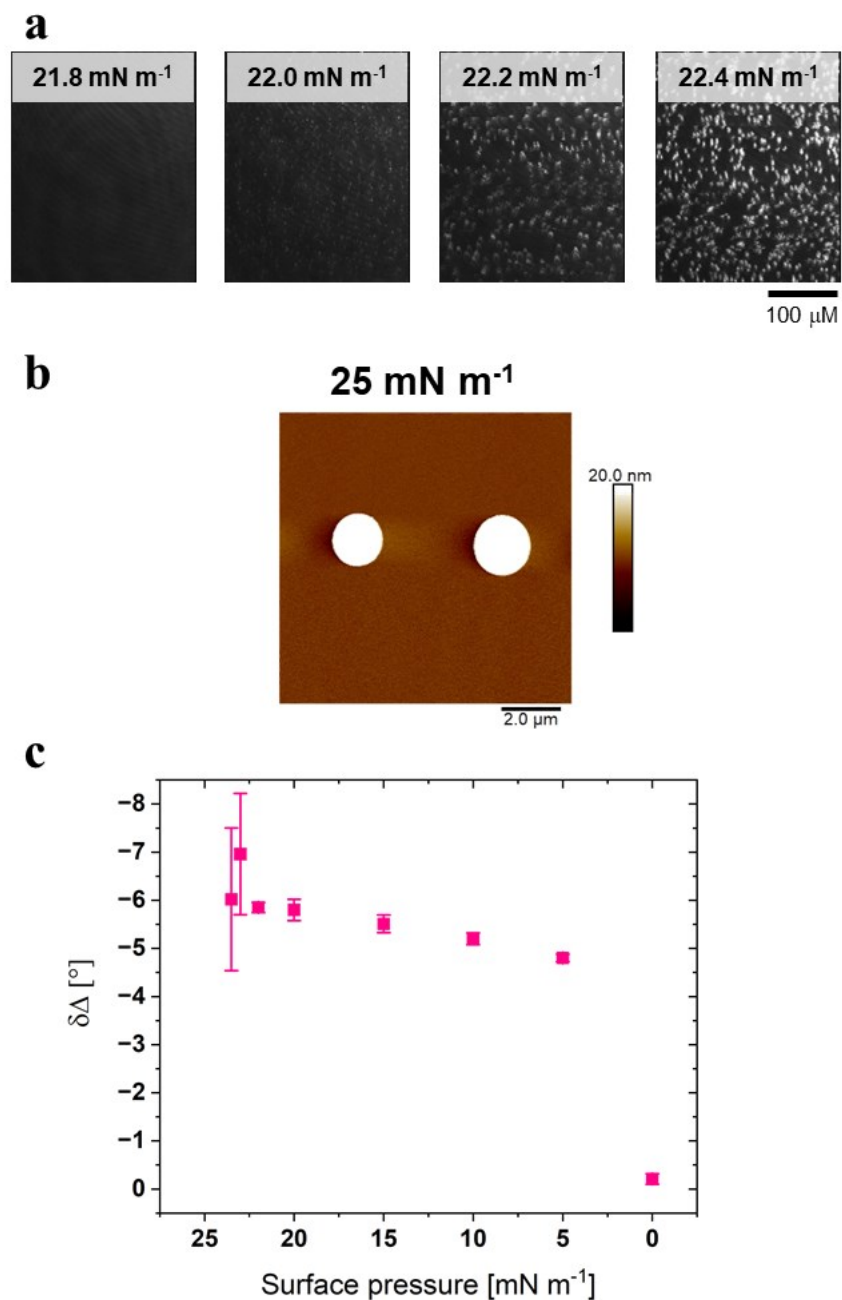


Figure B7 Representative BAM images (a), AFM image (b), and ellipsometric measurements (c) of **PL2** on water subphase. For (c), each value represents the average of measurements made on three independently formed films. For each independent film, the $\delta\Delta$ is the average of 10 measurements of the same monolayer film at constant surface pressure.

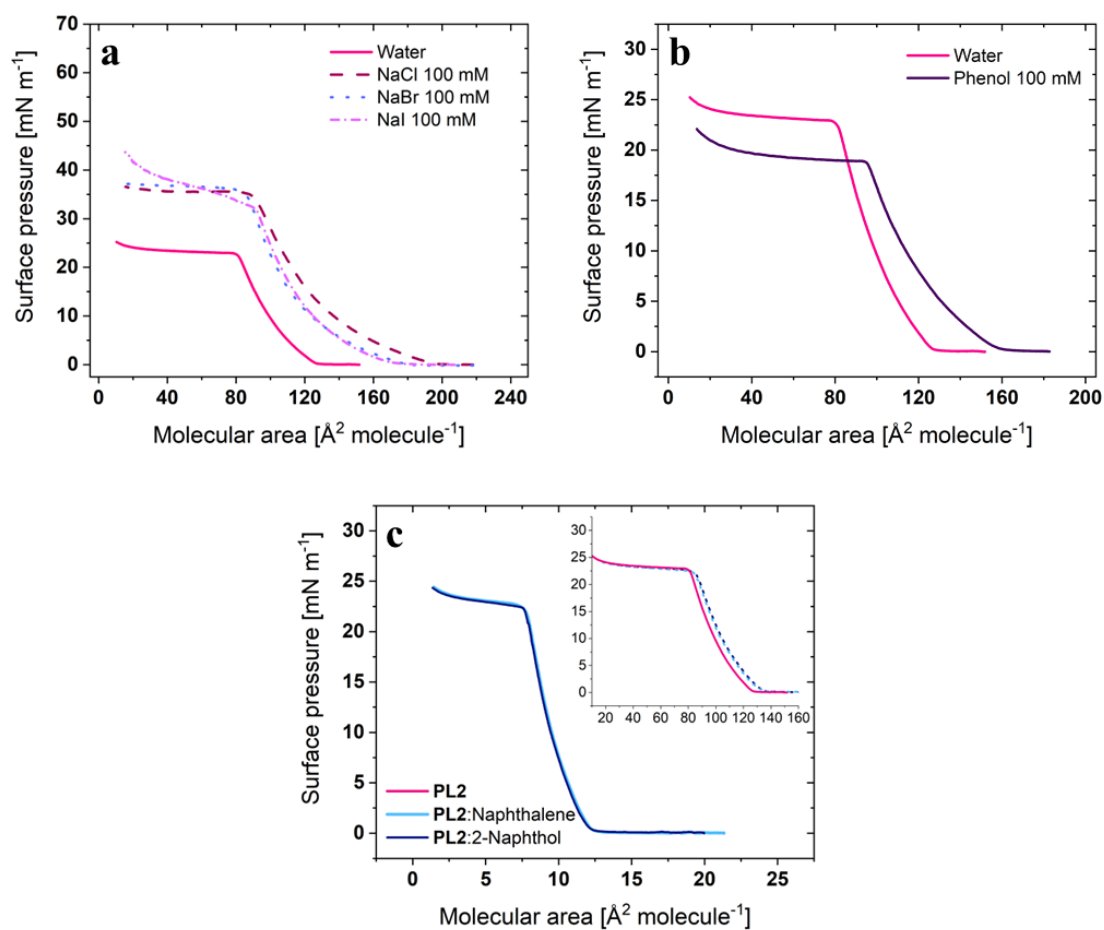
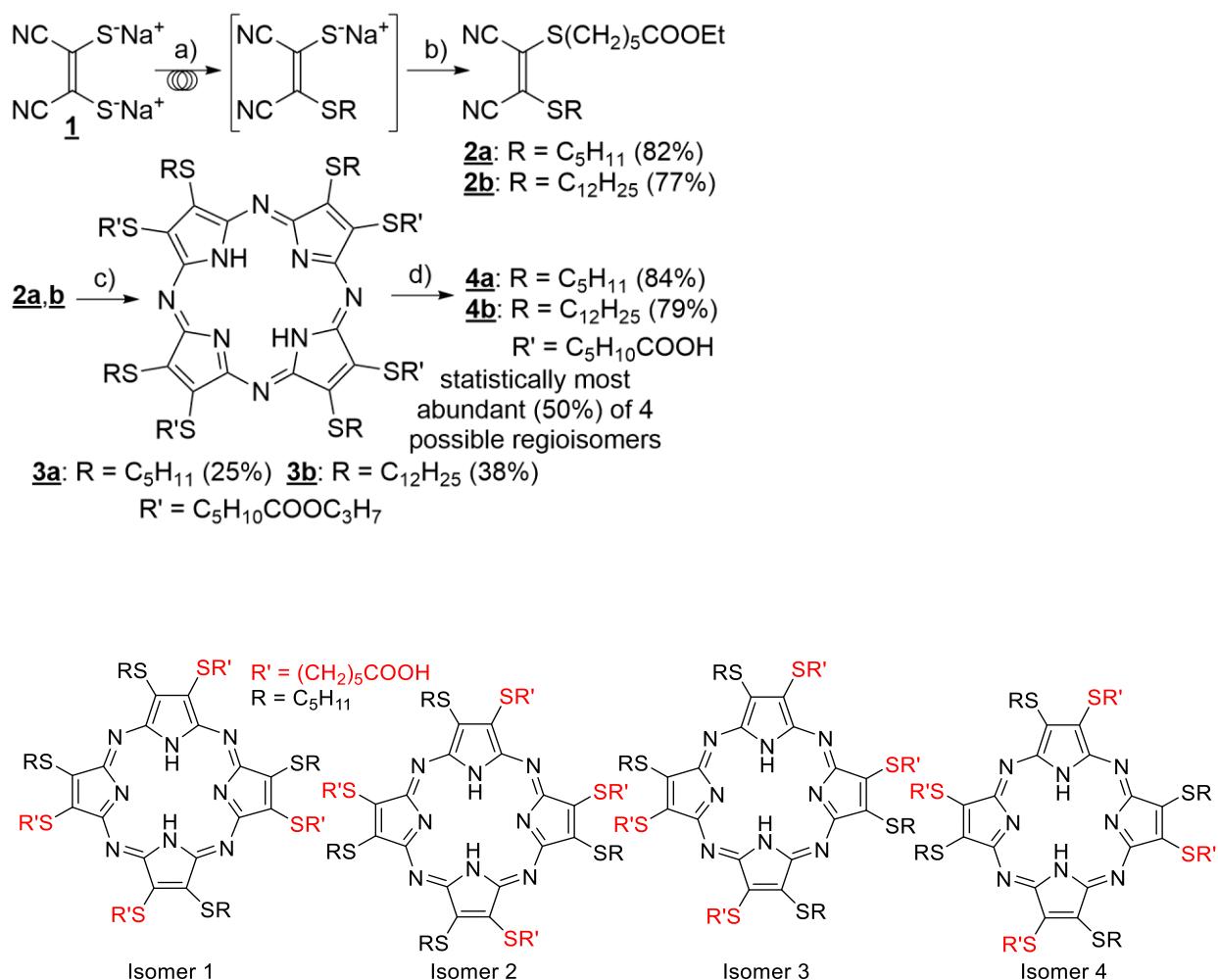


Figure B8 Surface pressure-molecular area isotherms of **PL2** a) with a subphase concentration of 100 mM halide counterions, b) with a subphase concentration of 100 mM phenol and c) co-spread in a 1:10 molar ratio with naphthalene and 2-naphthol (solid lines). For c) the dashed lines in inset represent the same isotherms replotted as a function of pure phosphole-lipid molecular area.

Appendix C. Supplementary information for Chapter 5.

Synthesis and Spectra



Scheme C1 Synthesis of TAPs as mixtures of 4 regioisomers. The statistical abundance of isomers 1-4 is 50%, 25%, 12.5% and 12.5%, respectively. No attempt was made to experimentally determine the actual isomer distribution and chromatographic purification may have altered the initial isomer ratios. Reaction conditions: a) flow reactor, diglyme, 1 equiv. BrC₅H₁₁ or BrC₁₂H₂₅, 0 °C, 6 hrs; b) diglyme, 1.1 equiv. BrC₅H₁₀COOEt, 0 °C, 12 hrs; c) 1. Mg(OC₃H₇)₂, 1-propanol, refl., Ar, 24 hrs; 2. THF/1 M HCl_{aq}, 0.5-1 hrs; d) THF/H₂O 95:5, 1 M NaOH_{aq}, refl., 24 hrs.

Chemicals and Materials. The starting reagent, disodium 1,2-dicyanoethylene-1,2-dithiolate **1**, was prepared according to literature procedures (see main text). 1-Propanol and methanol were dried over 4 Å and 3 Å molecular sieves, respectively, and dry and air-free dichloromethane, tetrahydrofuran, and diethyl ether were obtained from a solvent purification system (Innovative Technology Inc. MA, USA, Pure-Solv 400). All other reagents and solvents were used as received unless stated otherwise. Analytical thin-layer chromatography (TLC) and column chromatography were performed on aluminum-backed silica gel 60 plates and with SiliaFlash F60 silica gel, respectively, from Silicycle.

Characterization Methods. NMR spectra were recorded on Bruker Avance 300 and Bruker Avance III spectrometers operating at 300 MHz and 500 MHz, respectively. NMR data acquisition and processing were performed with the Topspin 2.1 software. Since the TAP compounds are mixtures of up to four different regioisomers, NMR spectra show more peaks than just for the most abundant regioisomer and the low symmetry of some regioisomers may also generate additional peaks. Infrared spectra (ATR) of neat samples were recorded on a Bruker Alpha FT-IR Spectrometer. Frequencies are given in reciprocal centimeters (cm⁻¹) for selected absorbance peaks. High-resolution mass spectra were obtained by matrix assisted laser desorption ionization (MALDI), chemical ionization, and atmospheric solids analysis probe ionization (ASAP) operated in positive modes. Solution UV-vis absorption spectra were recorded on a Varian Cary 50 spectrophotometer and corrected for solvent absorption. The flow reactor consisted of a dual syringe pump that injected into tubing with an inner diameter of 1 mm. Tubing of a total volume of 10 mL (1273 cm length) was coiled around a copper cylinder that was submerged in a heating or cooling bath

Synthesis of (Z)-ethyl 6-(1,2-dicyano-2-(pentylthio)vinylthio)hexanoate 2a and (Z)-ethyl 6-(1,2-dicyano-2-(dodecylthio)vinylthio)hexanoate 2b.

A basic flow reactor was used for the monoalkylation of disodium 1,2-dicyanoethylene-1,2-dithiolate **1**. Compound **1** (200 mg, 1.074 mmol) was dissolved in 10 mL of diethyl glycol dimethyl ether (diglyme) and loaded into a syringe (10 or 20 mL). Another syringe of the same size was filled with a solution of 1-bromopentane (162 mg, 1.074 mmol, 1.0 equiv.) or 1-bromododecane (268 mg, 1.074 mmol, 1.0 equiv.) in diglyme (10 mL). The reactor was cooled in an ice bath, and the reaction was run at a combined flow rate of 0.056 mL/min (20 mL are consumed in 6 hrs).

Both syringes were refilled with diglyme (10 mL each), and the solvent was injected at the same rate of 0.056 mL/min. The eluted reaction mixture was collected and stirred for 8 hrs at room temperature before ethyl-6-bromohexanoate (295 mg, 1.182 mmol, 1.1 equiv.) was added for the second alkylation. The reaction mixture was stirred for 8 hrs at room temperature, filtered, and the filtrate was evaporated in high vacuum (10^{-3} mbar) to give an orange oil. TLC analysis (silica, 1:7 ethyl acetate/hexanes) reveals the presence of small amounts of the symmetrically substituted side products with two alkyl chains and with two ester chains. The R_f values for **2a** and its dialkyl and diester side-products are 0.40, 0.60, and 0.20, respectively, and for **2b** and its dialkyl and diester side-products are 0.35, 0.70, and 0.20, respectively. The pure products were obtained by column chromatography (silica, 1:7 ethyl acetate/hexanes) as dark red oils in an average yield of 80%.

2a: ^1H NMR (300 MHz, CDCl_3) δ = 4.13 (q, J = 7.2 Hz, 2H, OCH_2), 3.11 (t, J = 7.5 Hz, 4H, SCH_2), 2.31 (t, J = 7.2 Hz, $2\text{HO}=\text{CCH}_2$), 1.8-1.6 (m, 6H, (CH_2)), 1.5-1.3 (m, 6H, (CH_2)), 1.25 (t, J = 7.2 Hz, 3H, $(\text{CH}_3, \text{ester})$), 0.91 (t, J = 6.9 Hz, 3H, CH_3). ^{13}C NMR (75 MHz, CDCl_3) δ = 173.50 ($\text{C}=\text{O}$), 121.63 and 120.92 ($\text{C}=\text{C}$), 112.31 and 112.27 ($\text{C}\equiv\text{N}$), 60.55 (OCH_2), 35.32 (SCH_2), 35.01 (SCH_2), 34.20 ($\text{CH}_2-\text{C}=\text{O}$), 30.77 (CH_2), 29.77 (CH_2), 29.75 (CH_2), 28.10 (CH_2), 24.49 (CH_2), 22.28 (CH_2), 14.46 CH_3 of ester, 14.04 (CH_3 of pentyl). FT-IR (ATR, neat, cm^{-1}) 2957, 2931, 2860 ($\text{C}-\text{H}$ stretches), 2224 ($\text{C}\equiv\text{N}$ stretch), 1732 ($\text{C}=\text{O}$ stretch). HRMS (TOF CI^+) m/z calcd for $\text{C}_{17}\text{H}_{26}\text{N}_2\text{O}_2\text{S}_2$ $[\text{M}]^+$ = 354.1436, found 354.1461.

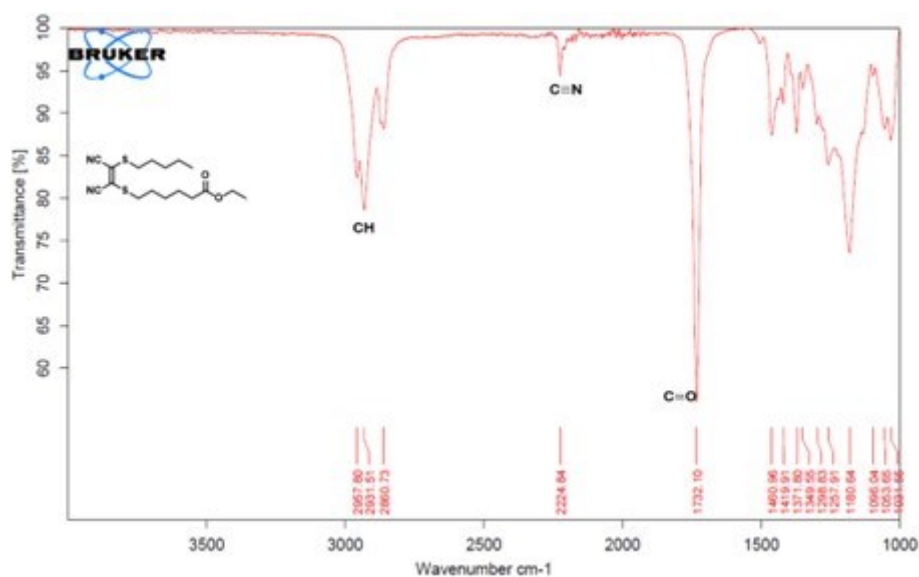


Figure C1 FT-IR (ATR) of neat **2a**.

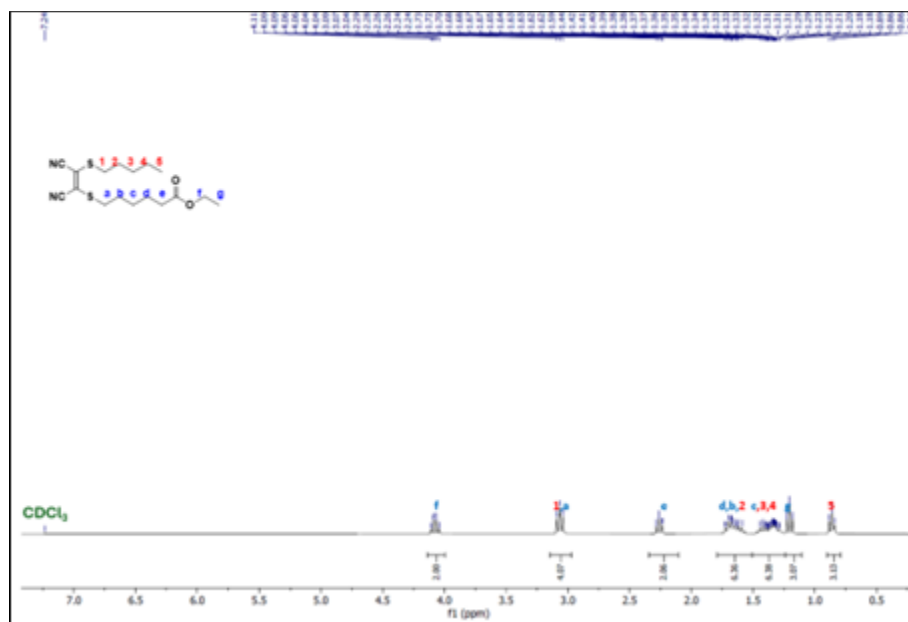


Figure C2 ^1H NMR of **2a** in CDCl_3 .

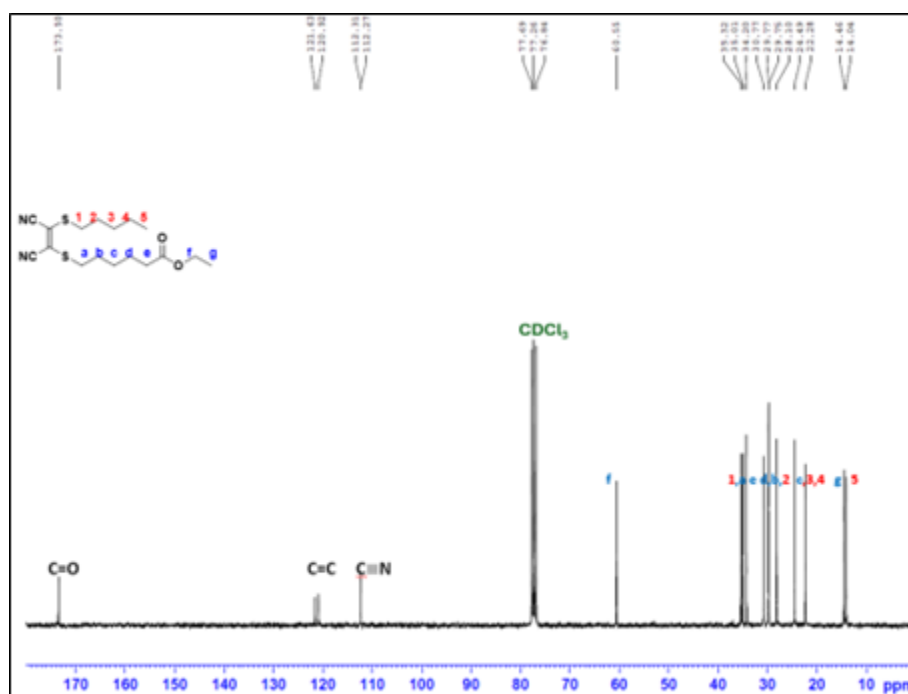


Figure C3 ^{13}C NMR of **2a** in CDCl_3 .

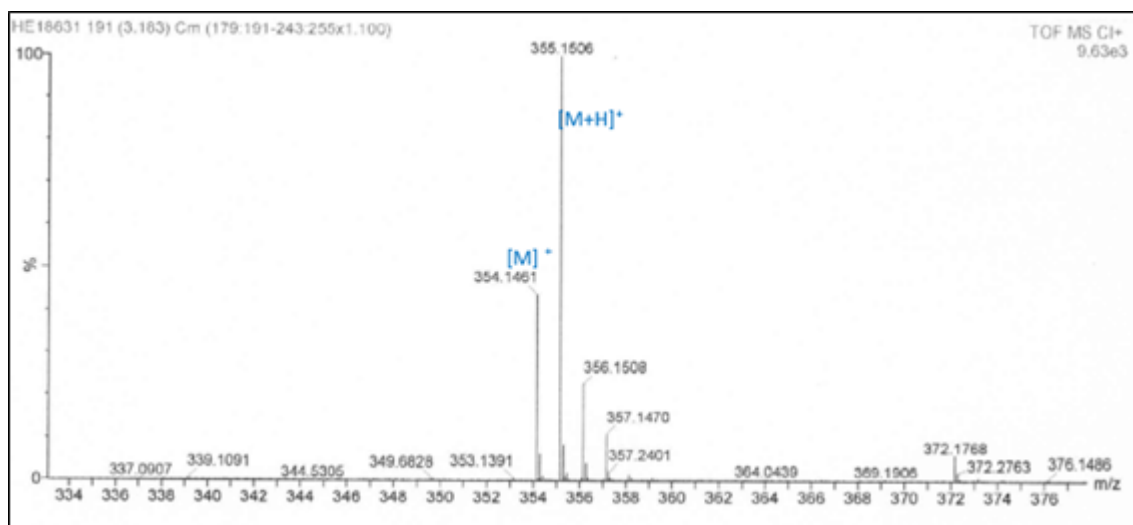


Figure C4 HRMS (TOF CI⁺) of **2a**.

2b: ¹H-NMR (CDCl₃, 300 MHz): δ (ppm) 4.12 (q, *J* = 6.9 Hz, 2H, OCH₂), 3.11 (t, *J* = 6.8 Hz, 4H, SCH₂), 2.31 (t, *J* = 6.8 Hz, 2H, O=CCH₂), 1.70 (m, 6H, CH₂), 1.44 (m, 4H, CH₂), 1.25 (m, 19H, CH₂), and 0.87 (t, *J* = 6 Hz, 3H, CH₃). ¹³C-NMR (CDCl₃, 75 MHz): δ (ppm) 173.09 (C=O), 121.26 and 120.60 (C=C), 112.00 and 111.97 (C≡N), 60.16 (O-CH₂), 35.01 (S-CH₂), 34.68 (S-CH₂), 33.85 (CH₂-C=O), 31.82 (CH₂), 29.76 (CH₂), 29.55 (CH₂), 29.52 (CH₂), 29.49 (CH₂), 29.43 (CH₂), 29.30 (CH₂), 29.24 (CH₂), 28.88 (CH₂), 28.35 (CH₂), 27.77 (CH₂), 24.17 (CH₂), 22.60, 14.17 (CH₃, ester), 14.04 (CH₃, dodecyl). FT-IR (ATR, neat, cm⁻¹): 2923, 2853 (C-H), 2212 (C≡N stretch), 1733 (C=O stretch). HRMS (TOF CI⁺) *m/z* calcd for C₂₄H₄₀N₂O₂S₂ [M]⁺ = 452.2531, [M+H]⁺ = 453.2604.

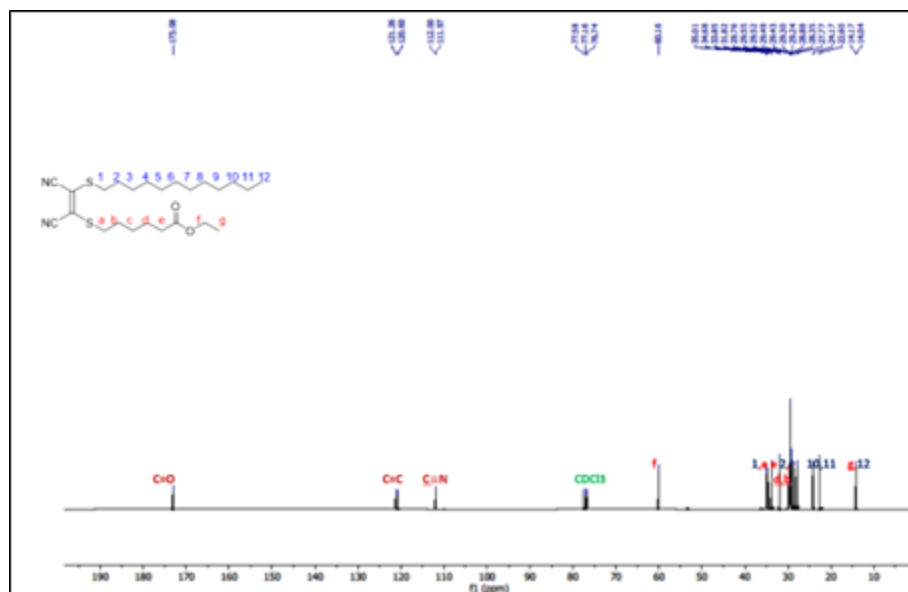


Figure C7 ^{13}C NMR of **2b** in CDCl_3 .

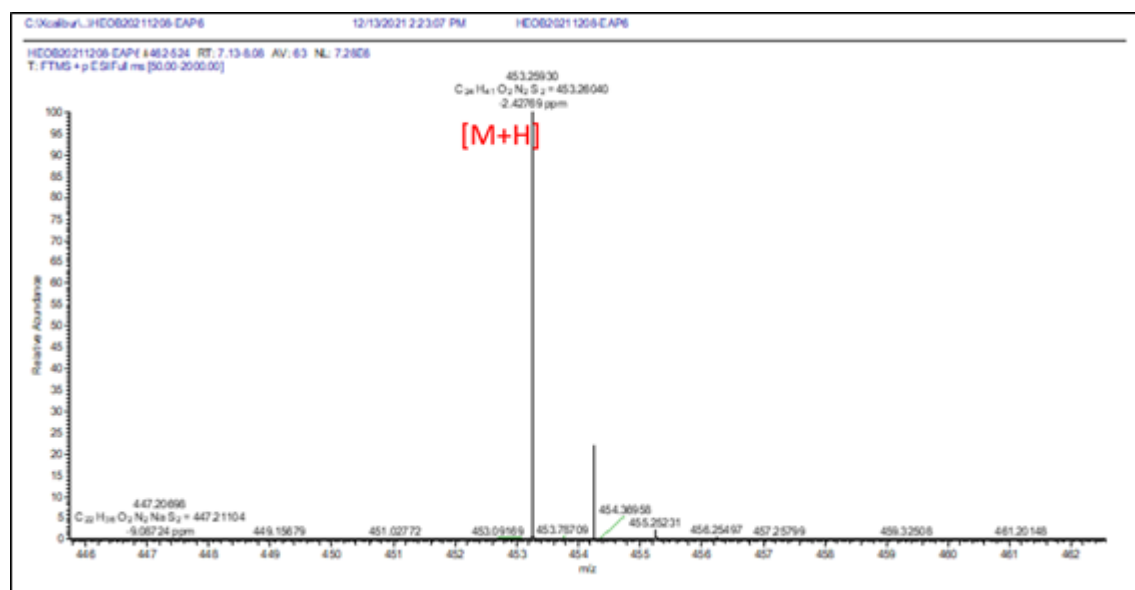


Figure C8 HRMS (ESI^+) of **2b**.

Syntheses of 2,7,12,18-tetrakis(6-oxo-6-propyloxyhexylthio)-3,8,13,17-tetrakis(pentylthio)-5,10,15,20-tetraazaporphyrin 3a and 2,7,12,18-tetrakis(6-oxo-6-propyloxyhexylthio)-3,8,13,17-tetrakis(dodecylthio)-5,10,15,20-tetraazaporphyrin 3b as the main regioisomer of four regioisomers in each mixture.

Mg turnings (100 mg, 4.11 mmol) were reacted with anhydrous 1-propanol (30 mL) at reflux under argon until all magnesium was converted to magnesium propanolate (about 24 hrs). The magnesium propanolate in propanol mixture (3 mL) was added to a dry flask under argon that contained compounds **2a** (100 mg, 0.28 mmol) or **2b** (210 mg, 0.46 mmol) and the reaction mixture was stirred under reflux for a total of 24 hrs. The appearance of a blue color after 1.5 hrs indicates a successful formation of the TAP macrocycle. Ethyl acetate (20 mL) was added at room temperature and the solution was extracted three times with deionized water to remove all remaining magnesium propanolate. Ethyl acetate was removed in vacuum to give the crude Mg²⁺ containing TAPs as residues which were not further isolated but demetallated to **3a** and **3b**. The residues were dissolved in THF (10 mL) and aqueous HCl (1 M, 10 mL) was added to the stirred solution at room temperature. Formation of the metal-free TAPs **3a** and **3b** was indicated by the immediate color change from dark blue to dark purple and progress was monitored by UV-vis spectroscopy to ensure a quantitative removal of Mg²⁺. Demetallation was quenched by the addition of aqueous HCl (1 M, 20 mL) that fully precipitated the metal-free TAPs **3a** and **3b** as dark purple solids after filtration. The crude products were purified by column chromatography on silica with EtAc/hexanes 1:6 as eluent to yield **3a** in 25% (103 mg) and **3b** in 37.6% (295 mg). TLC analysis (silica, 1:6 EtAc/hexanes) gives R_f values of 0.45 for **3a** and 0.50 for **3b**.

3a: ¹H NMR (300 MHz, CDCl₃) δ = 4.10-4.02 (m, 16H, SCH₂), 3.94 (m, 8H, OCH₂), 2.29 (m, 8H, OC), 1.88 (m, 16H), 1.62-1.52 (m, 24H, CH₂), 1.37-1.25 (m, 16H, CH₂), 0.93-0.83 (m, 24H, CH_{3,pentyl,ester}), -1.12 (s, 2H, NH). Some peaks are broadened by aggregation and overlapping peaks of regioisomers. ¹³C NMR (75 MHz, CDCl₃) δ = 173.7 (C=O), 153.4 (C=N), 141.0, 140.3 (C=C), 65.9 (OCH₂), 35.3 (SCH₂), 35.2 (SCH₂), 34.2 (CH₂-C=O), 31.2 (CH₂), 30.3 (CH₂), 29.8 (CH₂), 26.5 (CH₂), 24.8 (CH₂), 22.5 (CH₂), 22.3 (CH₂), 22.0 (CH₂), 14.1 (CH_{3,pentyl}), 10.4 (CH_{3,ester}). All peaks were labeled and listed although some belong to the less abundant regioisomers and the lower symmetry of some regioisomers may also generate peak splitting. FT-IR (ATR, neat, cm⁻¹) 3285 (N-H stretch), 2954, 2927, 2857 (C-H stretches alkyl), 1735 (C=O stretch), 1459 (aromatic C=C stretch), 1176 (C-O stretch). UV-vis (THF (10⁻⁵ M), λ_{max} (nm) / ε (10³ L mol⁻¹ cm⁻¹)): 351 (43.9), 521 (21.0), 634 (25.7), 730 (34.4). HRMS (TOF ASAP⁺) m/z calcd for C₇₂H₁₁₄N₈O₈S₈ [M+H]⁺ = 1475.6604, found 1475.6613.

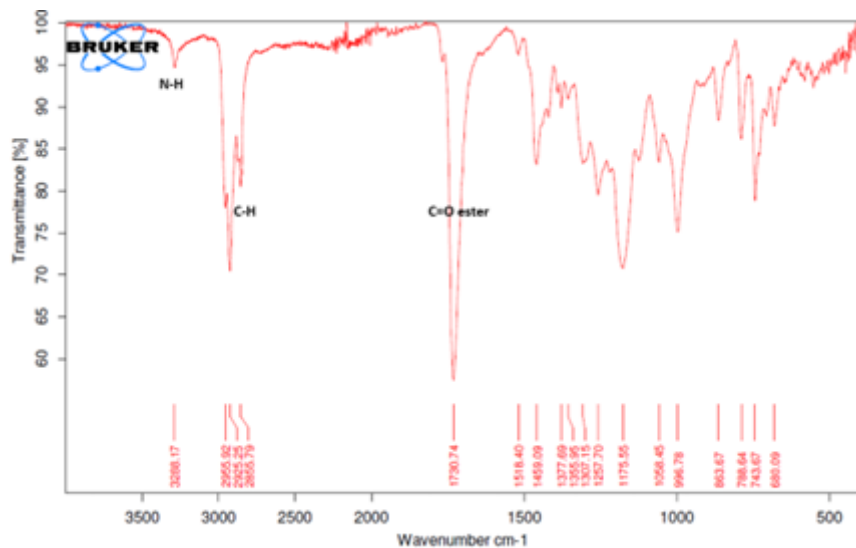


Figure C9 FT-IR (ATR) of neat **3a**.

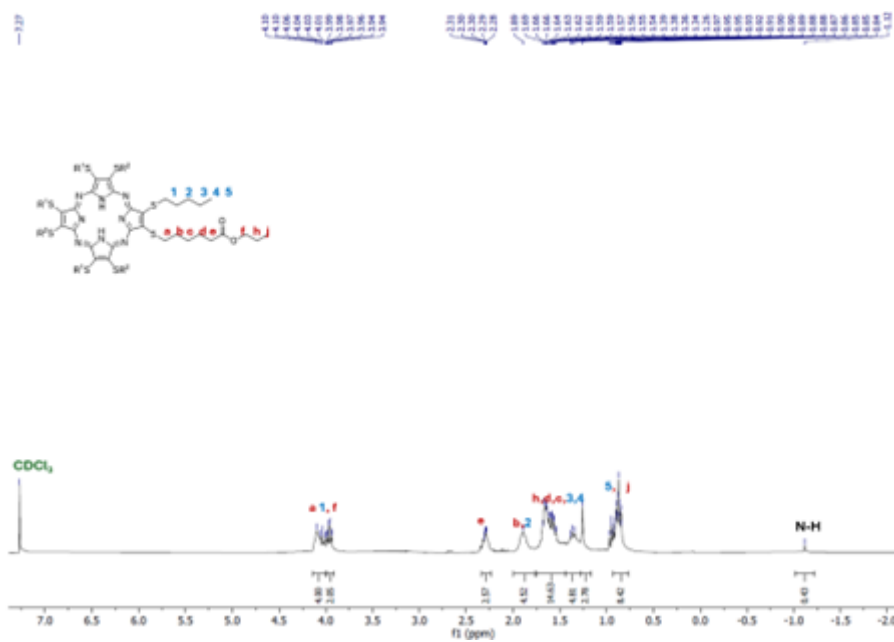


Figure C10 ^1H NMR of **3a** in CDCl_3 . Some peaks are broadened by aggregation and overlapping peaks of regioisomers.

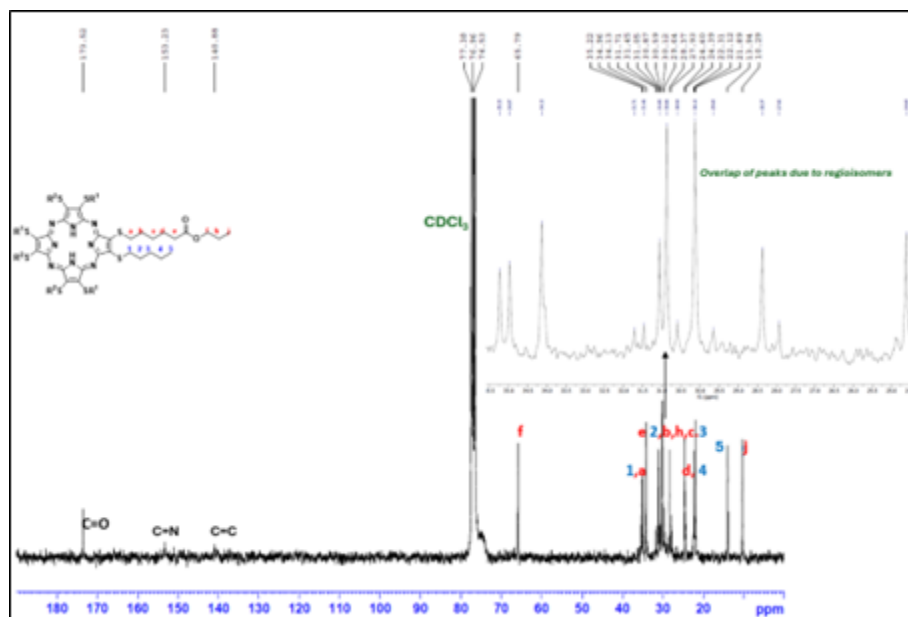


Figure C11 ^{13}C NMR of **3a** in CDCl_3 . All peaks were labeled and listed although some belong to the less abundant regioisomers and the lower symmetry of some regioisomers may also cause additional peaks.

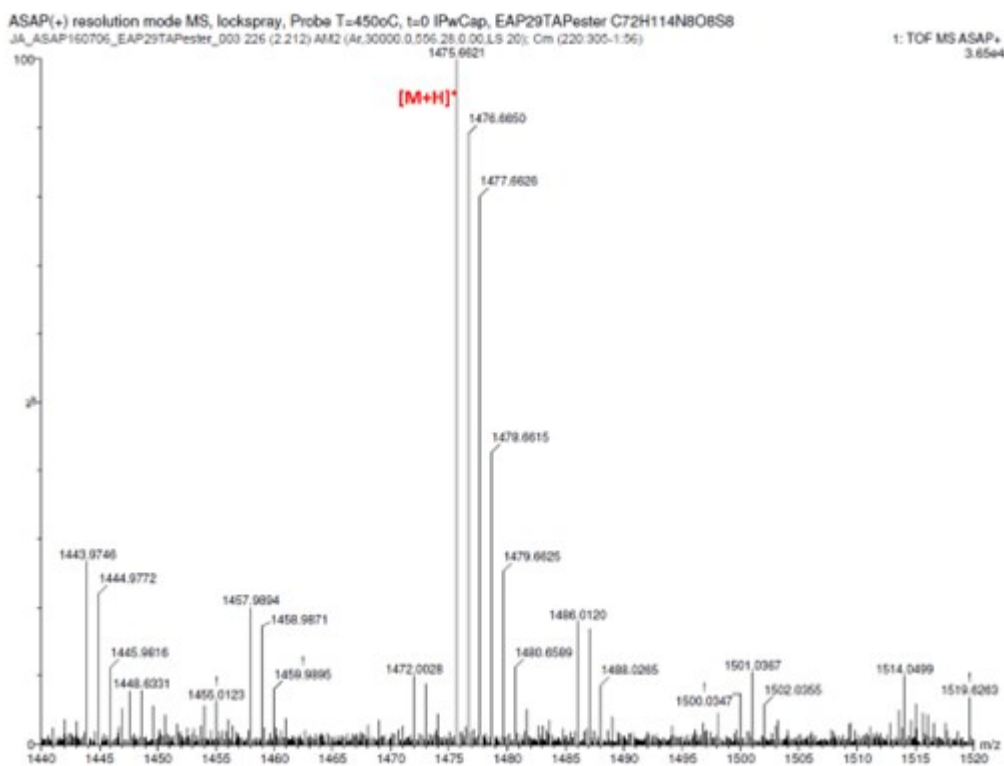


Figure C12 HRMS (ASAP⁺) of **3a**.

3b: ^1H NMR (300 MHz, CDCl_3) δ = 4.09 (m, 16H, SCH_2), 3.94 (t, J = 6.8 Hz, 8H, OCH_2), 2.28 (m, 8H, $\text{O}=\text{CCH}_2$), 1.89 (m, 16H, CH_2), 1.66-1.53 (m, 16H, CH_2), 1.28-1.25 (m, 24H, CH_2), 1.16 (m, 80H, CH_2), 0.90-0.81 (m, 24H, CH_3 ,_{ester,dodecyl}), -1.11 (s, 2H). Some peaks are broadened by aggregation and overlapping peaks of regioisomers. ^{13}C NMR (75 MHz, CDCl_3) δ = 173.71 (C=O), 153.43 (C=N), 140.33 (C=C), 65.99 (OCH_2), 35.4 (SCH_2), 35.1 (SCH_2), 35.1 (SCH_2), 34.3 ($\text{CH}_2\text{-C}=\text{O}$), 31.2 (CH_2), 30.8 (CH_2), 30.3 (CH_2), 29.8 (CH_2), 29.0 (CH_2), 28.9 (CH_2), 28.5 (CH_2), 28.1 (CH_2), 24.8 (CH_2), 24.7 (CH_2), 22.8 (CH_2), 22.5 (CH_2), 22.1 (CH_2), 22.0 (CH_2), 21.6 (CH_2), 14.1, 14.0 (CH_3 ,_{dodecyl}), 10.5, 10.4 (CH_3 ,_{ester}). All peaks were labeled and listed although some belong to the less abundant regioisomers and the lower symmetry of some regioisomers may also generate peak splitting. FT-IR (ATR, neat, cm^{-1}) 3292 (N-H stretch), 2927, 2923, 2853 (C-H stretches), 1732 (C=O stretch), 1458 (aromatic C=C stretch) 1178 (C-O stretch). UV-vis (THF (10^{-5} M), λ_{max} (nm) / ϵ ($103 \text{ L mol}^{-1} \text{ cm}^{-1}$)): 349 (58.7), 506 (22.0), 638 (29.2), 708 (35.7). HRMS (TOF ASAP⁺) m/z calcd for $\text{C}_{100}\text{H}_{170}\text{N}_8\text{O}_8\text{S}_8$ $[\text{M}+\text{H}]^+$ = 1868.0907, found 1868.0980.

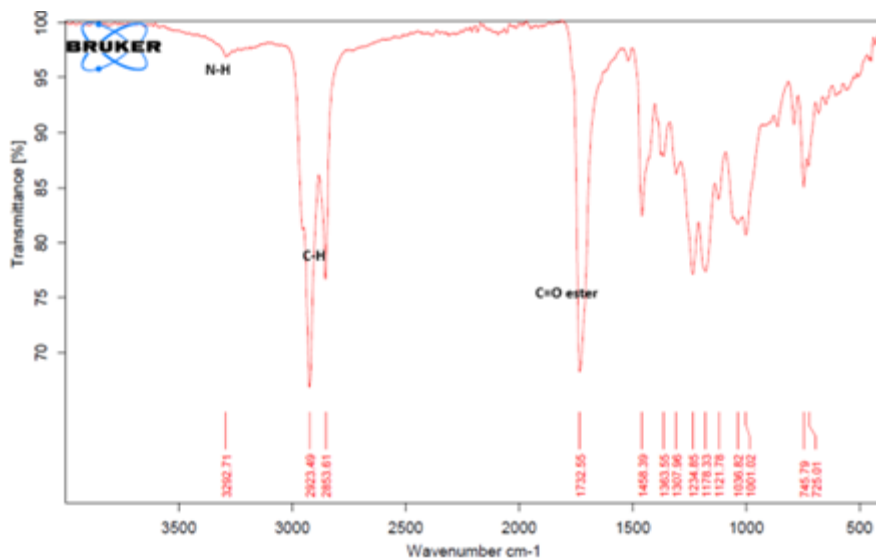


Figure C13 FT-IR (ATR) of neat **3b**.

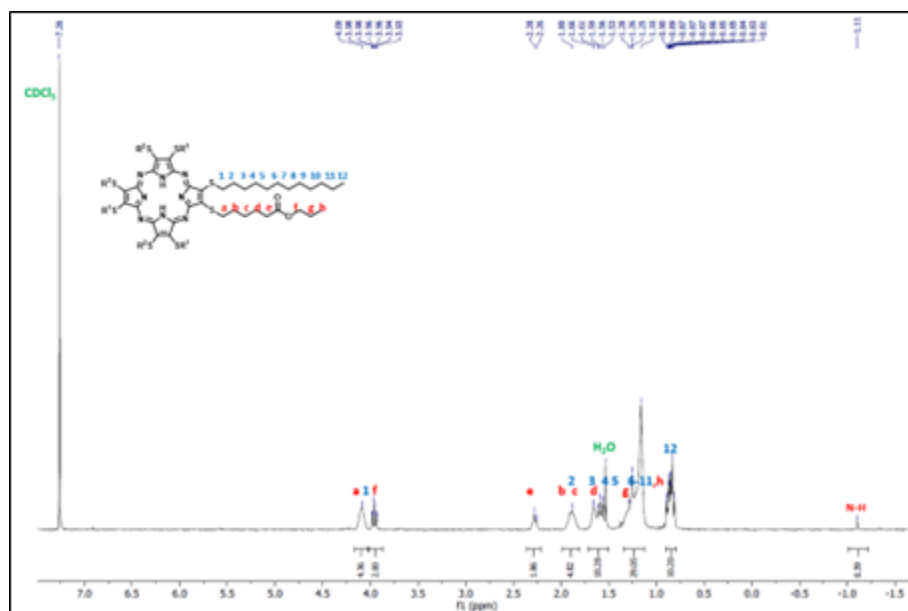


Figure C14 ^1H NMR of **3b** in CDCl_3 . Some peaks are broadened by aggregation and overlapping peaks of regioisomers.

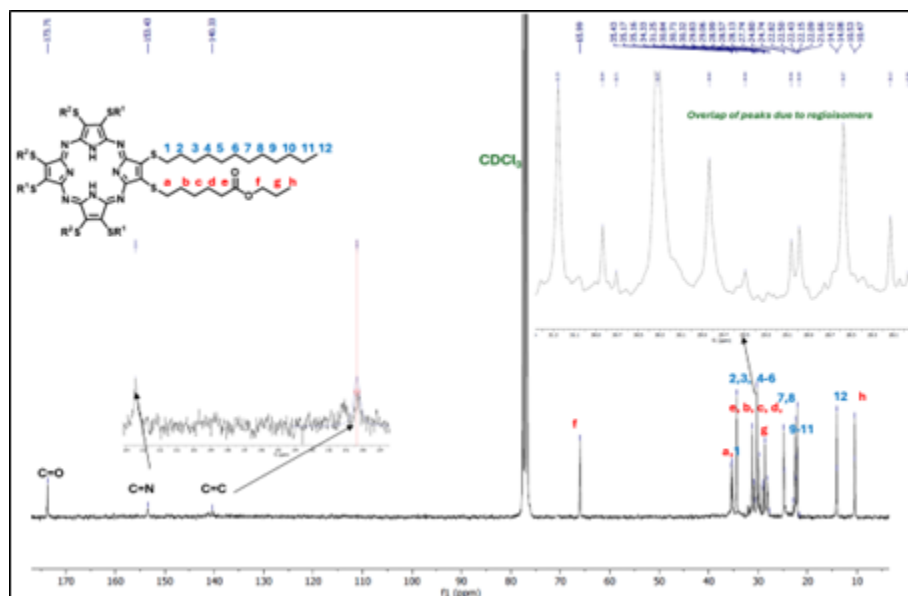


Figure C15 ^{13}C NMR of **3b** in CDCl_3 . All peaks were labeled and listed although some belong to the less abundant regioisomers and the lower symmetry of some regioisomers may also cause additional peaks.

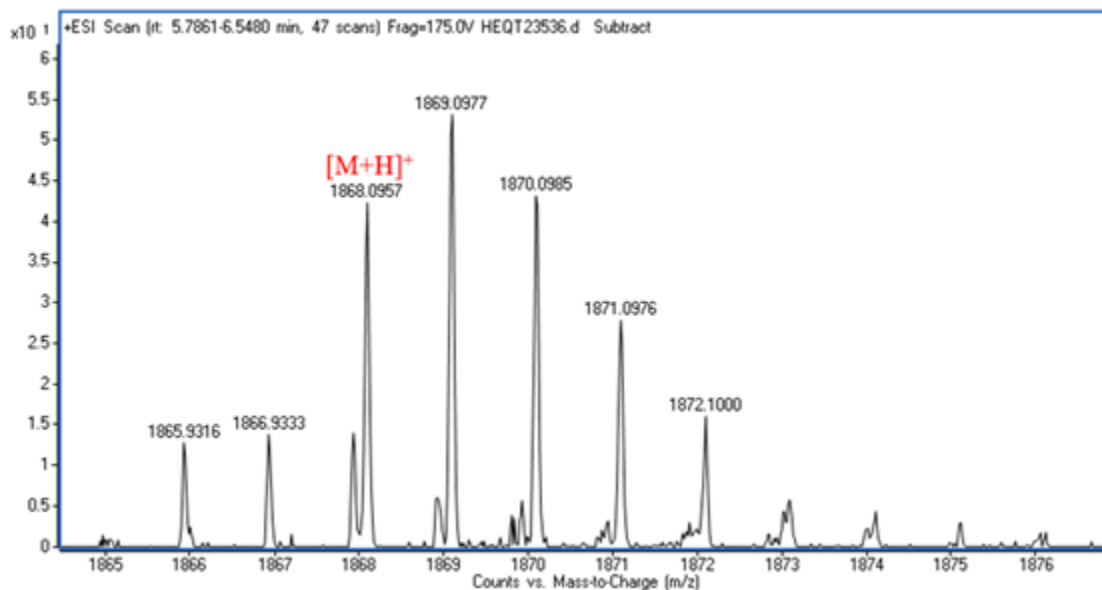


Figure C16 HRMS (ESI⁺) of **3b**.

Syntheses of 2,7,12,18-tetrakis(5-carboxypentylthio)-3,8,13,17-tetrakis(pentylthio)-5,10,15,20-tetraazaporphyrin 4a and 2,7,12,18-tetrakis(5-carboxypentylthio)-3,8,13,17-tetrakis(dodecylthio)-5,10,15,20-tetraazaporphyrin 4b as the main regioisomer of four regioisomers in each mixture.

An aqueous solution of NaOH (1 M, 5 mL) was added at a rate of 3 mL per hr to a stirred solution of TAP **3a** (70 mg, 0.047 mmol) or TAP **3b** (70 mg, 0.047 mmol) in a mixture of THF (10 mL) and methanol (2 mL) at reflux. The solution immediately changed color from dark purple to dark green, which is likely caused by a deprotonation of the TAP macrocycle. The progress of ester hydrolysis was monitored by TLC. When the reaction was completed after 12-24 hrs, the reaction mixture was acidified to a pH of 4 by the addition of aqueous HCl (1 M, 1 mL) and aqueous NH₄Cl (10 M, 0.5 mL) to buffer the dark purple solution. This mixture was extracted with ethyl acetate until the organic extracts were not purple anymore. The combined organic extracts were evaporated in vacuum to give the crude tetraacid products. Further purification of compounds **4a** and **4b** was achieved by precipitation from a solution of **4a** or **4b** in THF/EtAc 1:1 by the addition of CHCl₃/Hexane 1:1 for **4a** and the addition of methanol for **4b**. The precipitate was filtered off,

washed with the non-solvent, and finally dried in vacuum (10^{-2} mbar) at 70 °C to give the pure TAPs in yields of 85% (52 mg, 0.040 mmol) for **4a** and 81% (65 mg, 0.038 mmol) for **4b**).

4a: ^1H NMR (300 MHz, DMSO- d_6 , 50 °C) δ = 4.12 (m, 16H, SCH $_2$), 2,39 (*t*, J = 3 Hz, 8H, O=CCH $_2$), 1.88 (m, 16H), 1.62 (m, 16H, CH $_2$), 1.26 (m, 16H, CH $_2$), 0.88 (m, 12H, CH $_3$), -1.33 (s, 2H, NH). Some peaks are broadened by aggregation and overlapping peaks of regioisomers. ^{13}C NMR (75 MHz, DMSO- d_6 , 50 °C) δ = 174.2 (C=O), 151.5 (C=N), 138.7 (C=C), 35.3 (SCH $_2$), 34.9 (SCH $_2$), 34.5(CH $_2$ -C=O), 34.0 (CH $_2$ -C=O), 33.6 (CH $_2$), 31.2 (CH $_2$), 30.6 (CH $_2$), 29.5 (CH $_2$), 28.9 (CH $_2$), 27.9 (CH $_2$), 25.1 (CH $_2$), 24.2 (CH $_2$), 21.8 (CH $_2$), 13.8 (CH $_3$). All peaks were labeled and listed although some belong to the less abundant regioisomers and the lower symmetry of some regioisomers may also generate additional peaks. IR (ATR, neat, cm^{-1}) 3286 (N-H stretch), 2952, 2924, 2858 (C-H stretches alkyl), 1708 (C=O stretch), 1465 (aromatic stretch). UV-vis (THF (10^{-5} M), λ_{max} (nm) / ϵ (10^3 L mol $^{-1}$ cm $^{-1}$)): 356 (44.4), 521 (21.8), 642 (26.9), 720 (35.1). HRMS (TOF ESI $^+$) m/z calcd for C $_{60}$ H $_{90}$ N $_8$ O $_8$ S $_8$ [M+H] $^+$ = 1307.4725, found 1307.4681.

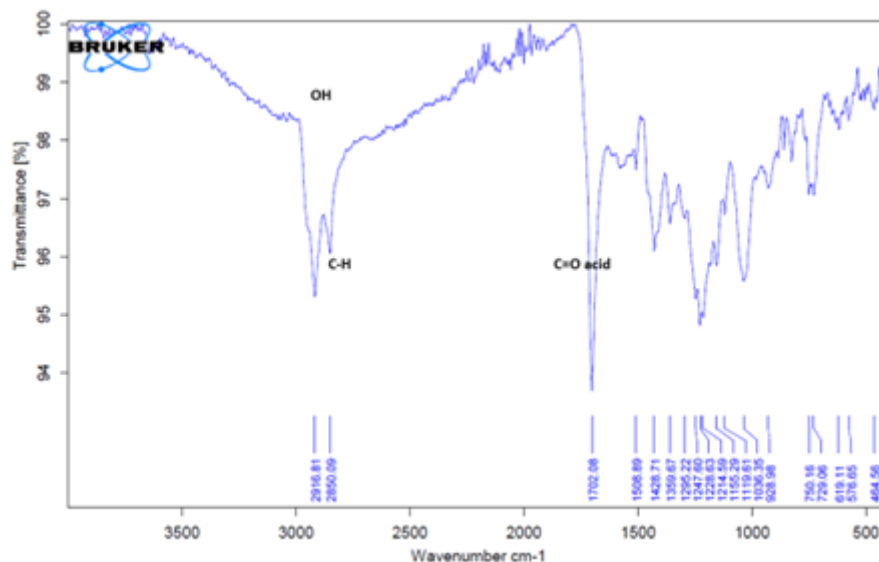


Figure C17 FT-IR (ATR) of neat **4a**.

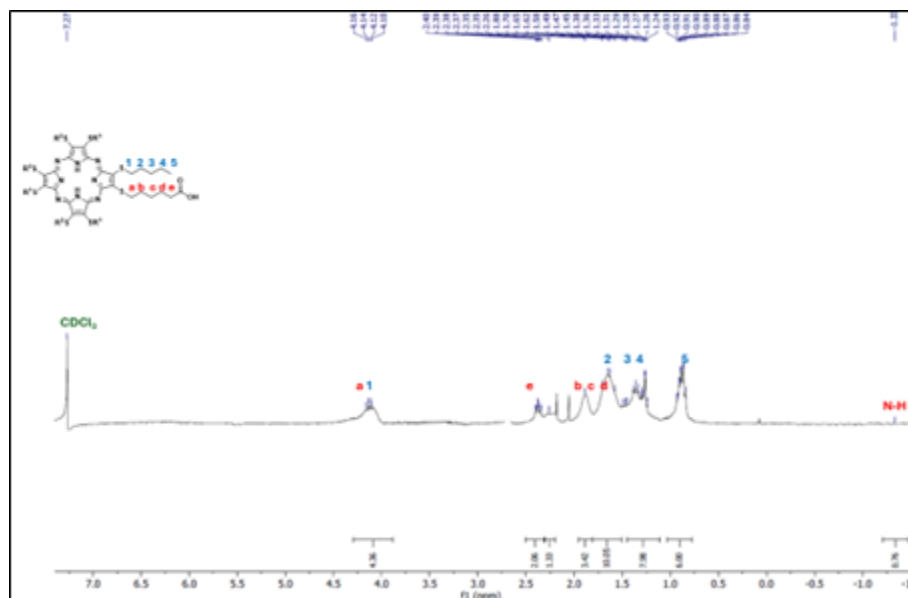


Figure C18 ^1H NMR of **4a** in CDCl_3 . Some peaks are broadened by aggregation and overlapping peaks of regioisomers.

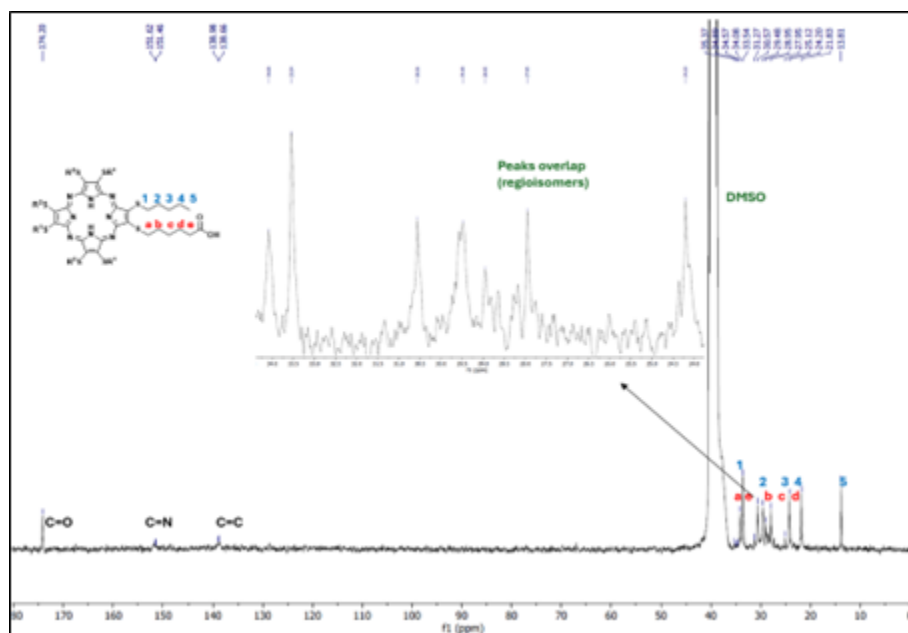


Figure C19 ^{13}C NMR of **4a** in DMSO-d_6 at $50\text{ }^\circ\text{C}$. All peaks were labeled and listed although some belong to the less abundant regioisomers and the lower symmetry of some regioisomers may also generate additional peaks.

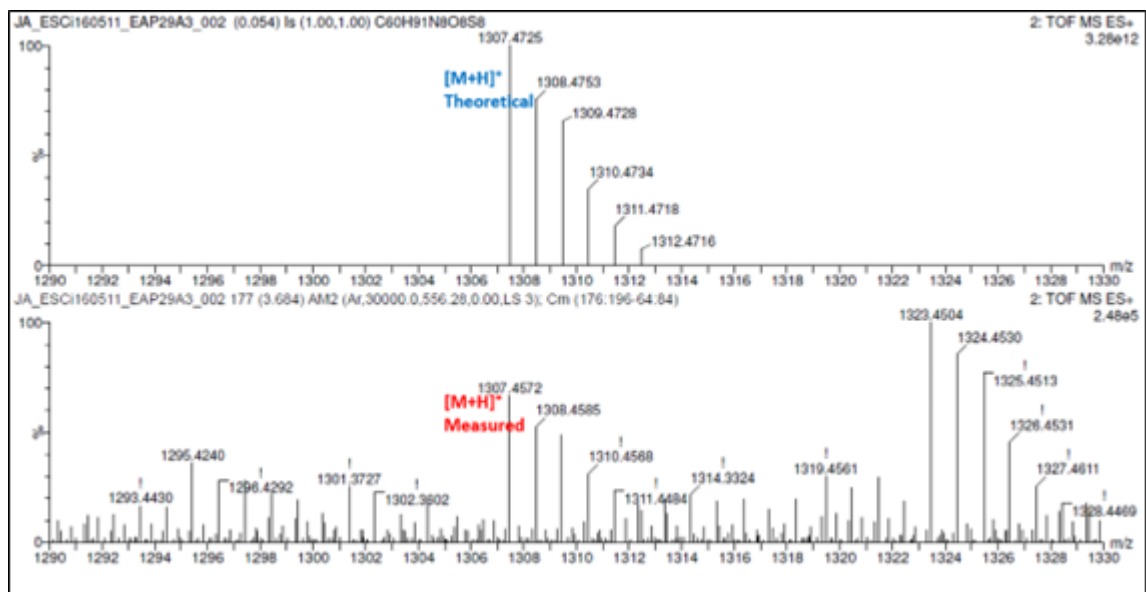


Figure C20 HRMS (ESI⁺) of **4a**.

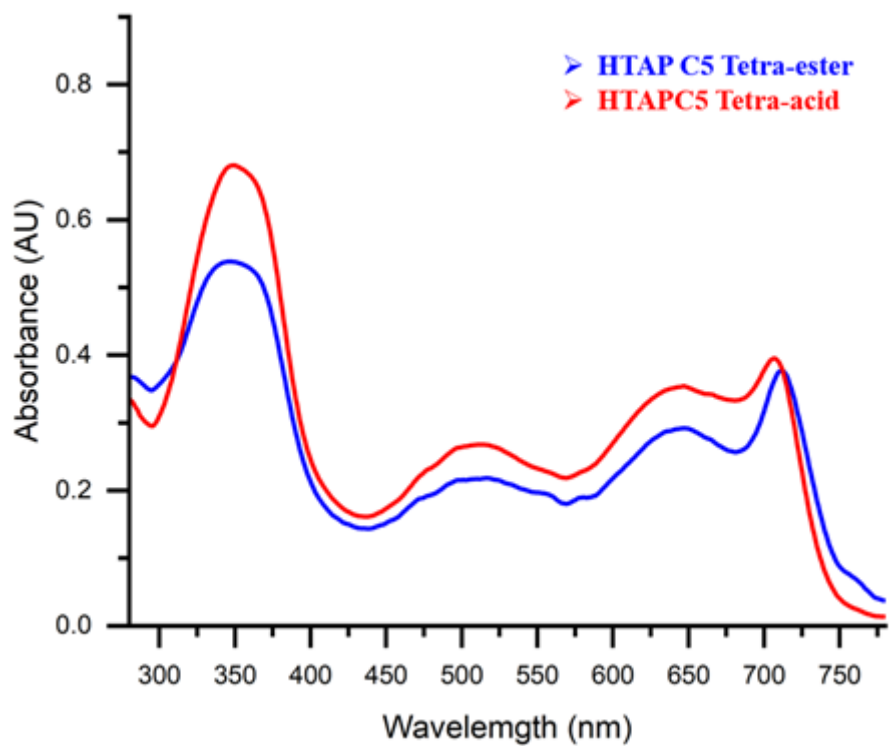


Figure C21 UV-vis Spectra of **3a** (ester) and **4a** (acid) in 10^{-5} M THF solution.

4b: ^1H NMR (300 MHz, 1,1,2,2-tetrachloroethane- d_2 , 60 °C) δ = 4.07 (m, 16H, SCH $_2$), 2.26 (m, 8H, O=CCH $_2$), 2.06 (m, 8H, CH $_2$), 1.87 (m, 12H, CH $_2$), 1.59 (m, 12H, CH $_2$), 1.42 (t, J = 6 Hz, 8H, CH $_2$), 1.20 (m, 56H, CH $_2$), 0.83 (t, J = 6 Hz, 12H, CH $_3$), -1.07 (s, 2H, NH). Some peaks are broadened by aggregation and overlapping peaks of regioisomers. ^{13}C NMR (300 MHz, DMSO- d_6 , 60 °C) δ = 174.9 (C=O), 154.3 (C=N), 137.5 (C=C), 35.1 (SCH $_2$), 34.9, 34.9 (SCH $_2$), 34.1 (O=CCH $_2$), 32.5 (CH $_2$), 31.7 (CH $_2$), 31.6 (CH $_2$), 29.6 (CH $_2$), 29.46 (CH $_2$), 29.42 (CH $_2$), 29.34 (CH $_2$), 29.31 (CH $_2$), 29.18 (CH $_2$), 29.15 (CH $_2$), 29.0 (CH $_2$), 28.9 (CH $_2$), 28.7(CH $_2$), 27.7(CH $_2$), 27.0(CH $_2$), 26.2 (CH $_2$), 24.9 (CH $_2$), 24.5 (CH $_2$), 22.57 (CH $_2$), 22.54 (CH $_2$), 22.51 (CH $_2$), 14.39 (CH $_3$). All peaks were labeled and listed although some belong to the less abundant regioisomers and the lower symmetry of some regioisomers may also generate additional peaks. FT-IR (ATR, neat, cm^{-1}) 3649 (N-H stretch), 3281 (O-H broad stretch), 2955, 2920, 2851 (C-H stretches alkyl), 1707 (C=O stretch), 1464 (aromatic stretch). UV-vis (THF (10^{-5} M), λ_{max} (nm) / ϵ (10^3 L mol $^{-1}$ cm $^{-1}$)): 350 (63.4), 509 (28.5), 645 (36.1), 713 (43.7). HRMS (TOF ESI $^+$) m/z calcd for C $_{88}$ H $_{146}$ N $_8$ O $_8$ S $_8$ [M+H] $^+$ = 1699.9029, found 1699.9039.

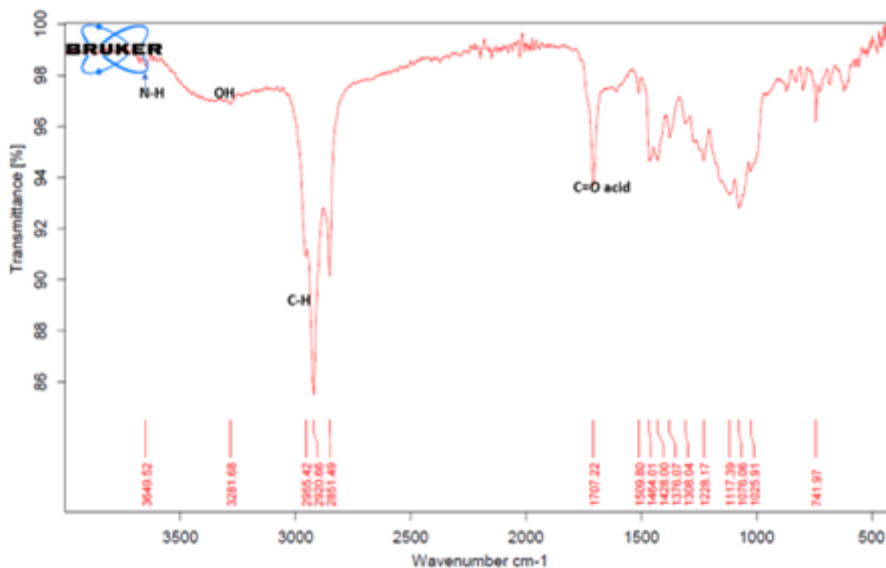


Figure C22 FT-IR (ATR) of neat **4b**.

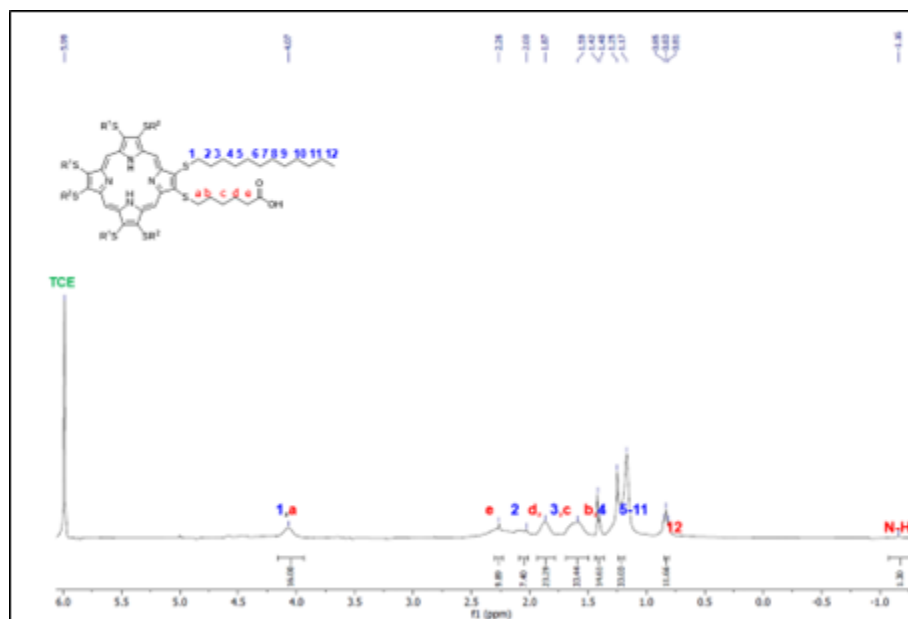


Figure C23 ^1H NMR of **4b** in tetrachloroethane- d_2 at 60 °C. Some peaks are broadened by aggregation and overlapping peaks of regioisomers.

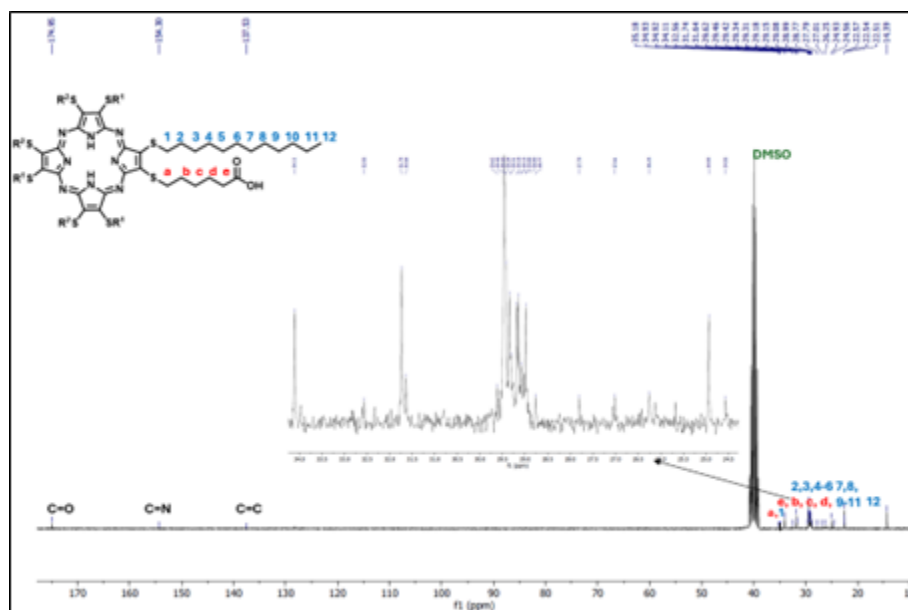


Figure C24 ^{13}C NMR of **4b** in DMSO- d_6 at 60 °C. All peaks were labeled and listed although some belong to the less abundant regioisomers and the lower symmetry of some regioisomers may also generate additional peaks.

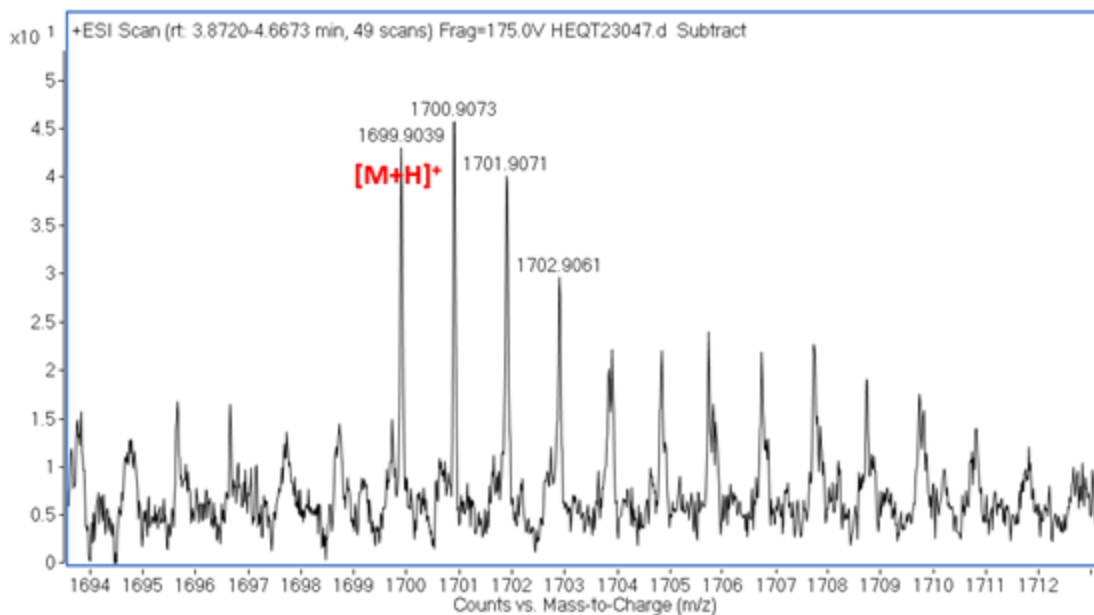


Figure C25 HRMS (ESI⁺) of **4b**.

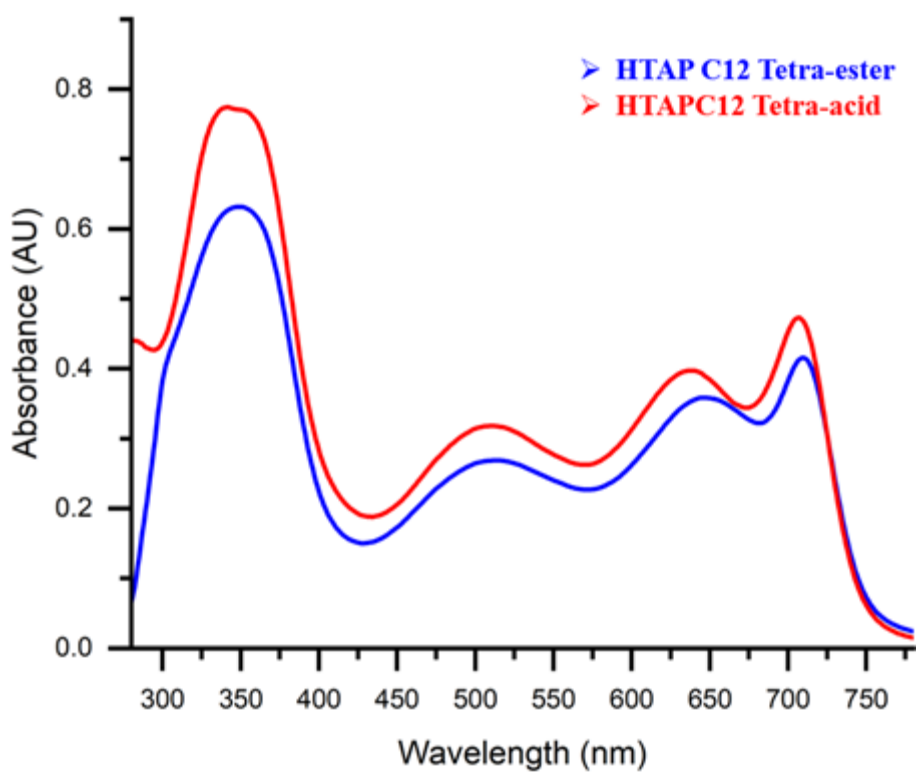


Figure C26 UV-vis spectra of **3b** (ester) and **4b** (acid) in 10⁻⁵ M THF solution.

Thermal Analysis Data and Polarized Optical Microscopy (POM) Images

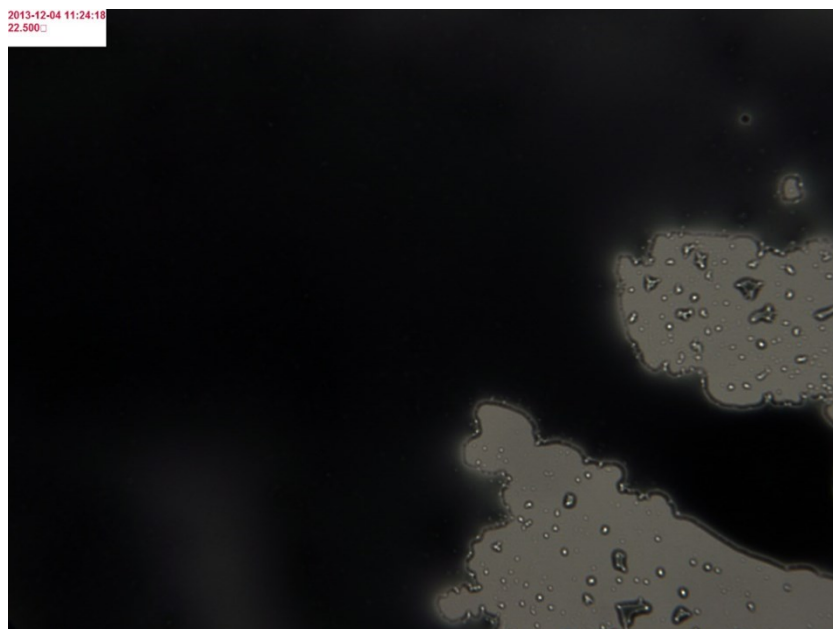


Figure C27 POM image of **3a** as a viscous isotropic liquid at 22 °C, polarizers at 80° crossing angle. The imaged area is 280 μm wide.

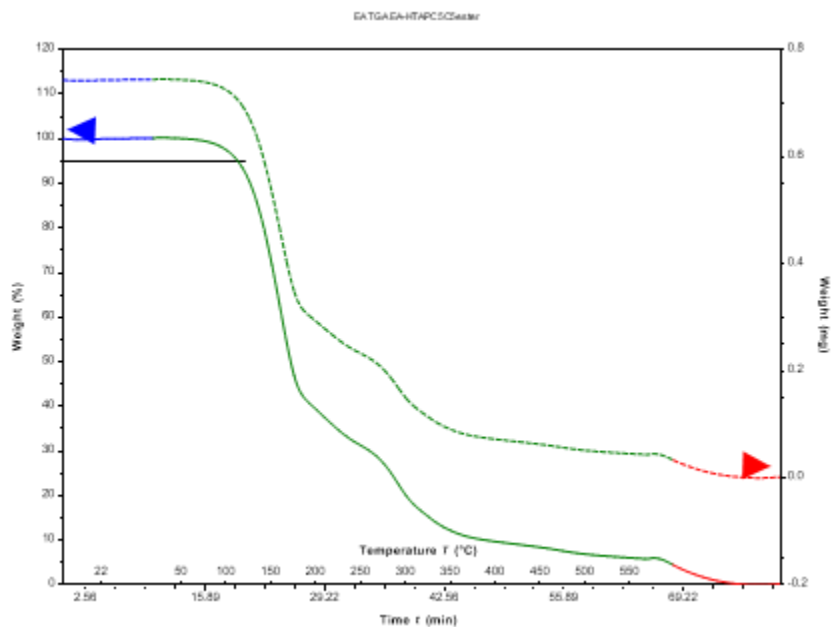


Figure C28 TGA of **3a** at 10 °C/min. The blue and red lines indicate isothermal segments at 20 °C and 600 °C, respectively. A mass loss of 5% was reached at 113 °C (black line).

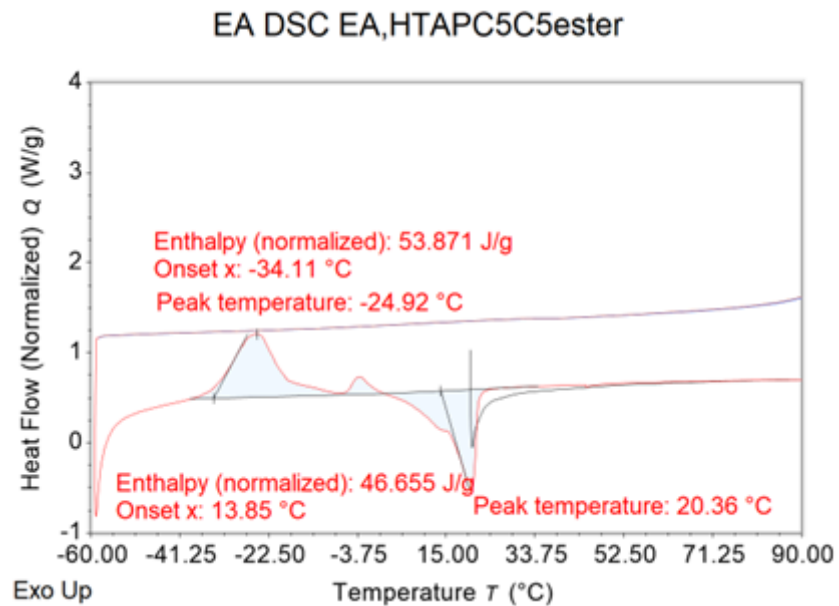


Figure C29 DSC of **3a** at 5 °C/min (1st (black) and 2nd heating (red) (bottom), 1st and 2nd cooling (top)). Cold crystallization on heating is followed by melting.

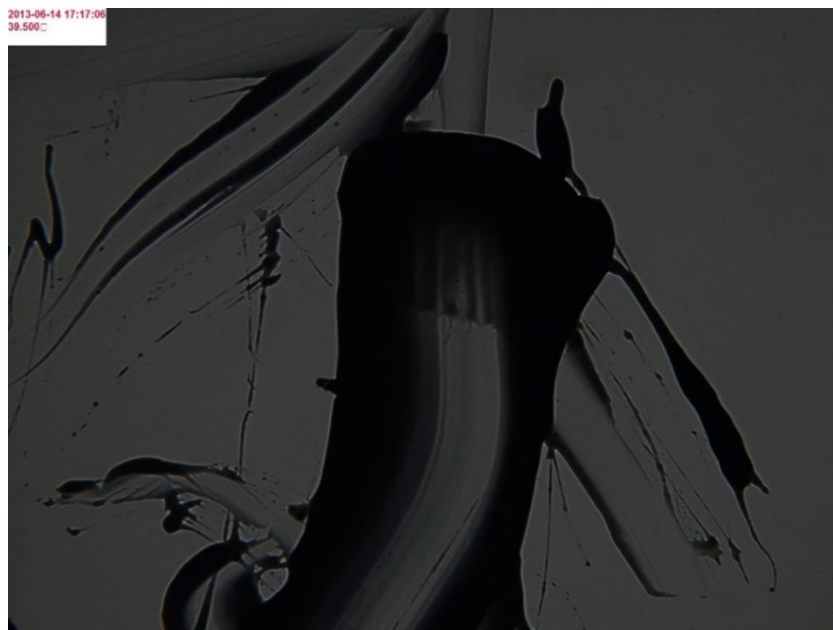


Figure C30 POM image of **3b** as a viscous isotropic liquid at 40 °C, polarizers at 80°. The imaged area is 280 μm wide.

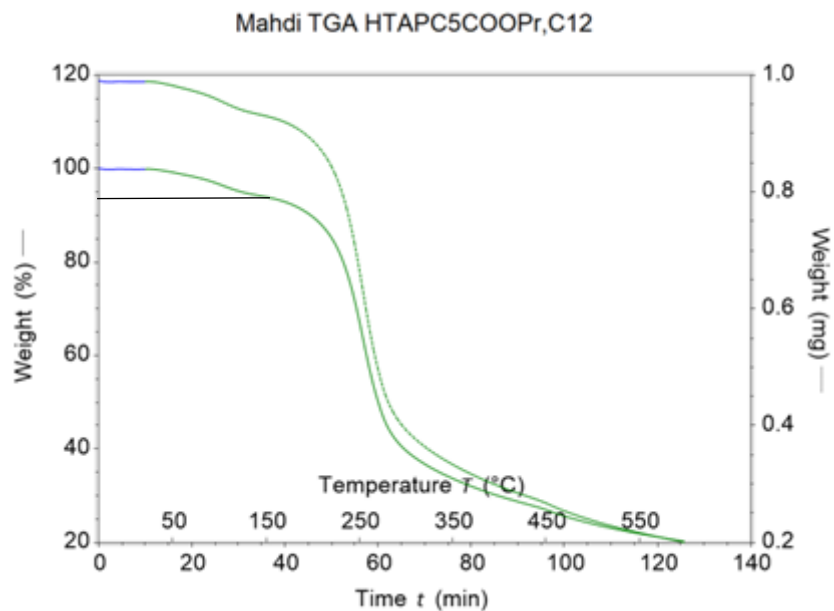


Figure C31 TGA of **3b** at 10 °C/min. The blue lines indicate isothermal segments at 20 °C. A mass loss of 5% was reached at 125 °C (black line).

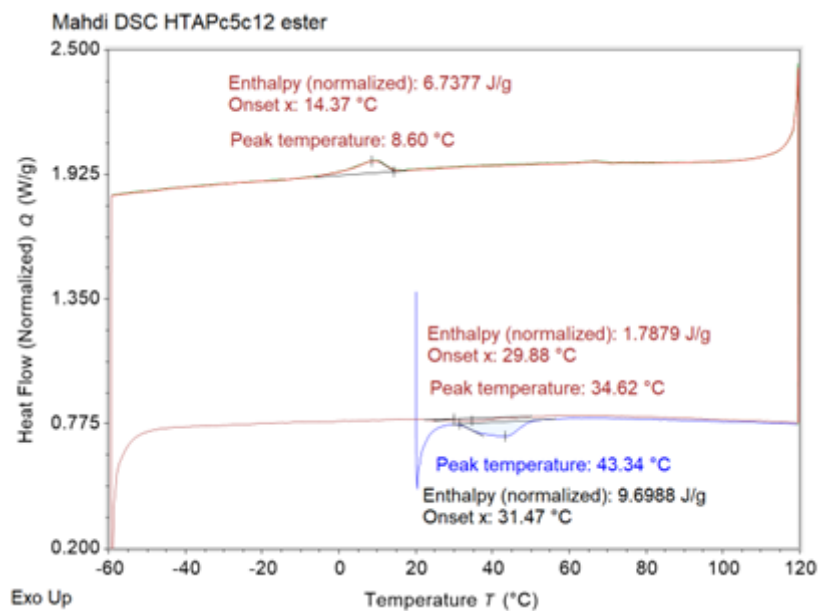


Figure C32 DSC of **3b** at 5 °C/min (1st and 2nd heating (bottom), 1st and 2nd cooling (top)). Onset of reversible melting and crystallization at 29.9 °C and 14.4 °C, respectively.

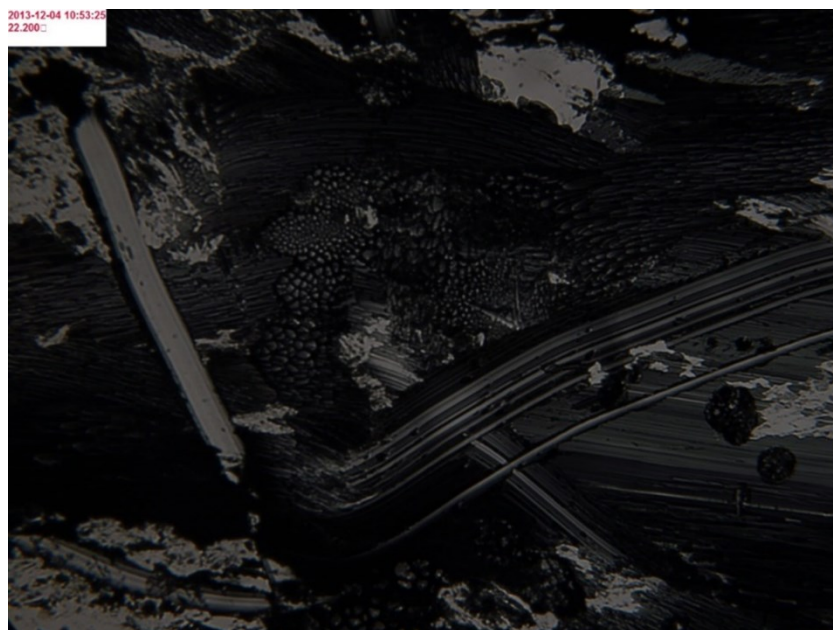


Figure C33 POM image of **4a** as a viscous isotropic liquid at 22 °C, polarizers at 80°. The brightest areas are uncoated glass. The imaged area is 280 μm wide.

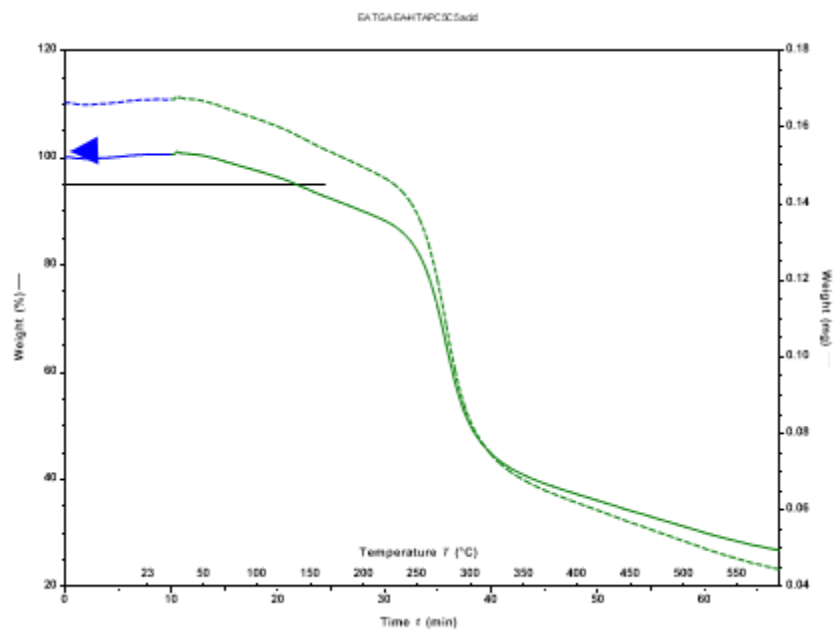


Figure C34 TGA of **4a** at 10 °C/min. A mass loss of 5% was reached at 138 °C (black line). The blue line indicates an isothermal segment at 20 °C.

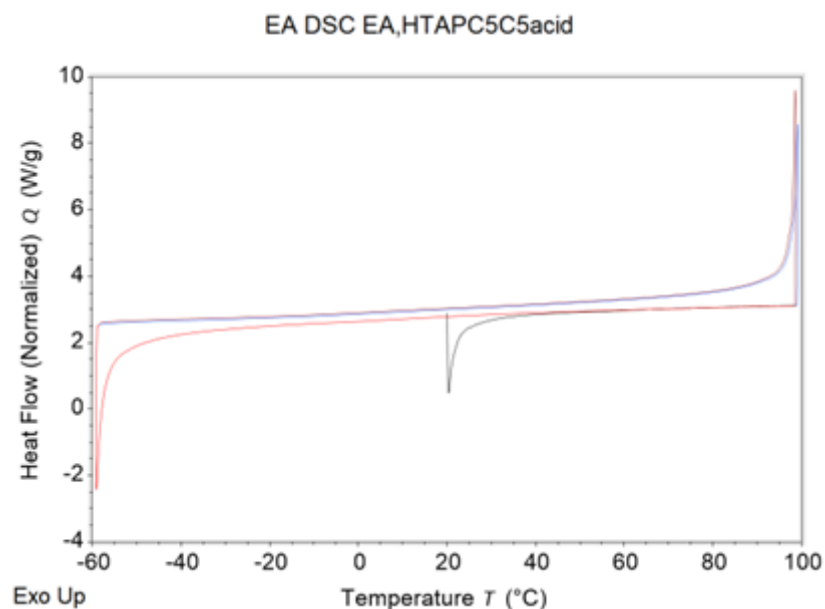


Figure C35 DSC of **4a** at 5 °C/min (1st heating (black), 1st cooling (purple), and 2nd heating and cooling (red)). No thermal transition was observed.

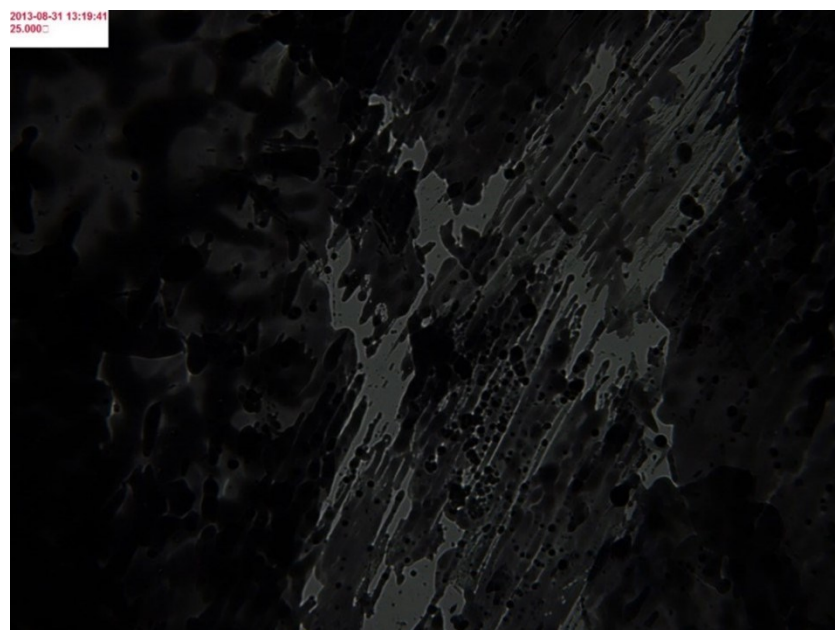


Figure C36 POM image of **4b** as a viscous isotropic liquid film on glass at 25 °C, polarizers at 80°, 1st heating. The brightest areas are the glass substrate without compound to show the difference. The imaged area is 280 μm wide.

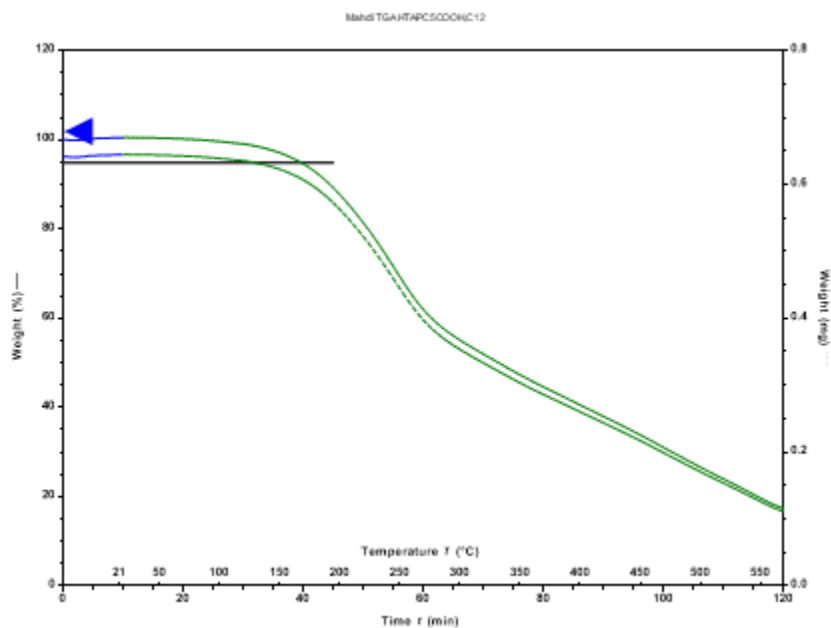


Figure C37 TGA of **4b** at 10 °C/min. The blue line indicates an isothermal segment at 20 °C. A mass loss of 5% was reached at 168 °C (black line).

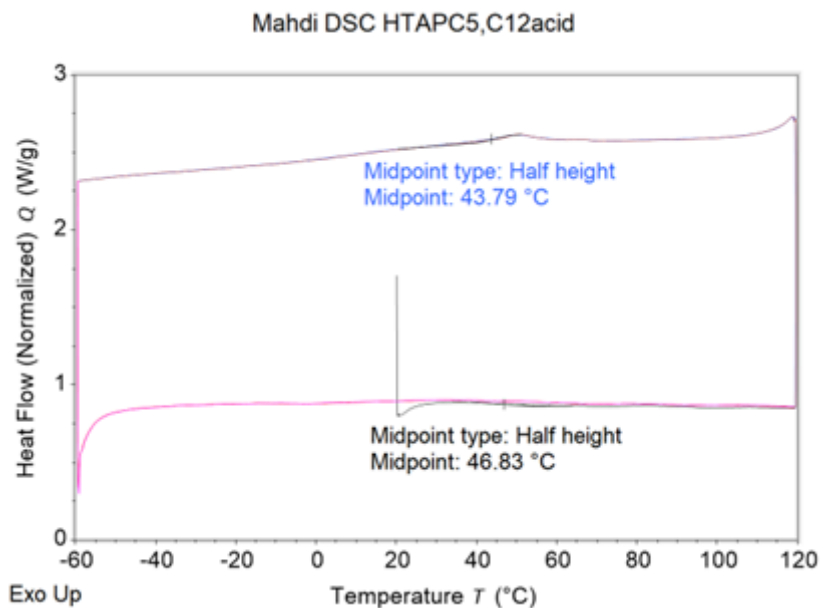


Figure C38 DSC of **4b** at 5 °C/min (1st and 2nd heating (bottom)), 1st and 2nd cooling (top). Glass transitions are observed on heating and cooling.

Film Characterization

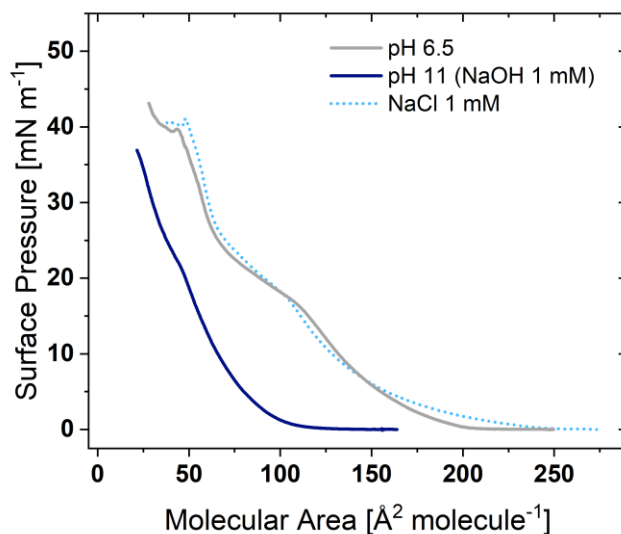


Figure C39 Surface pressure-molecular area isotherms of **4b** on pH adjusted, ultrapure water compared to a NaCl subphase with the same ionic strength as the pH 11 subphase.

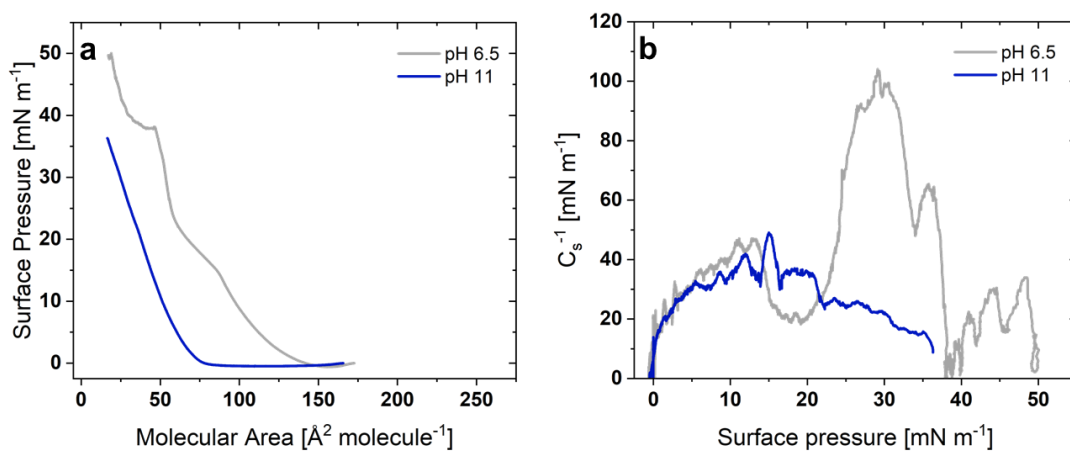


Figure C40 (a) Surface pressure-molecular area isotherm and (b) compressibility moduli plot of **4b** at different subphase pH (compression rate of 2 cm² min⁻¹, 22 °C).

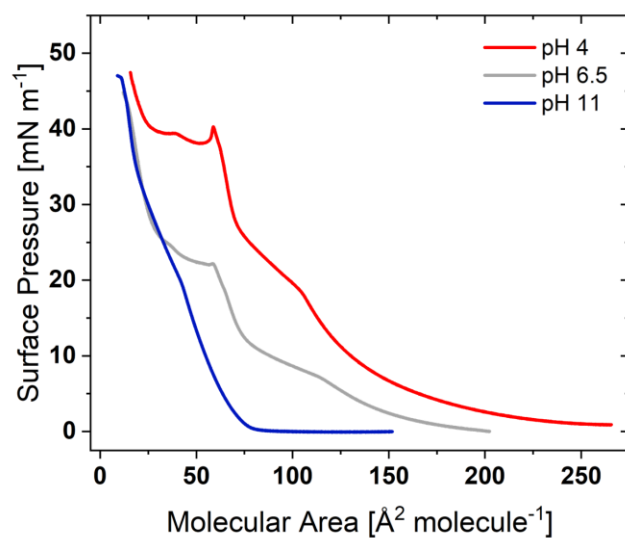


Figure C41 Surface pressure-molecular area isotherms of **4b** obtained for BAM imaging at compression rate of $7.5 \text{ cm}^2 \text{ min}^{-1}$ where the trough size is $7.5 \text{ cm} \times 73 \text{ cm}$.

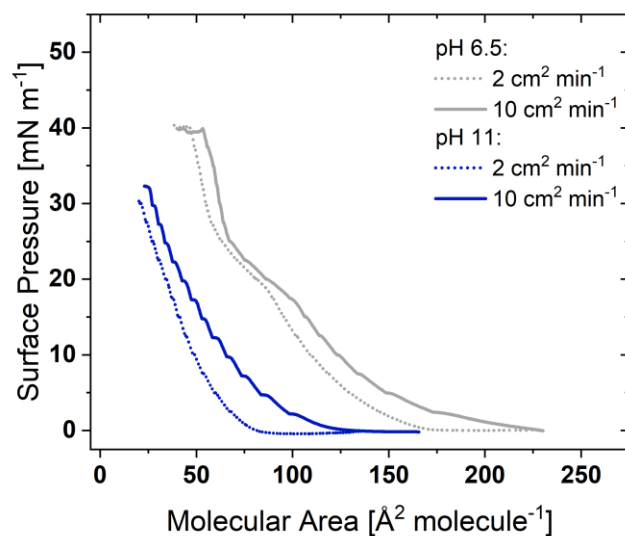


Figure C42 Surface pressure-molecular area isotherms obtained for ellipsometry measurements for **4b**.

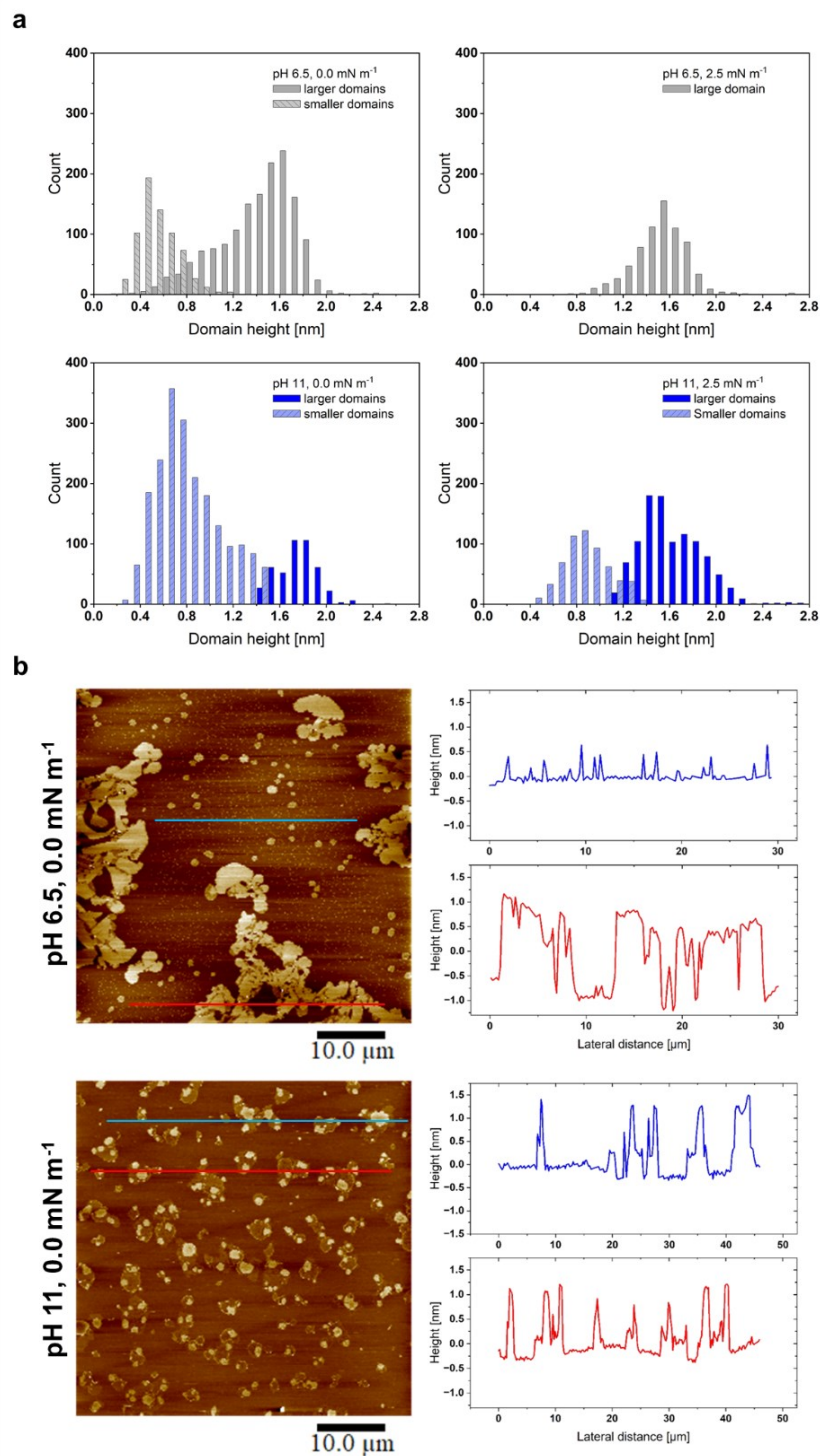


Figure C43 AFM images analysis for **4b** films deposited on mica; a) domain height histograms for the surface pressures of 0.0 and 2.5 mN m^{-1} at pH 6.5 and pH 11; b) sectional analysis showing domain populations with different heights.

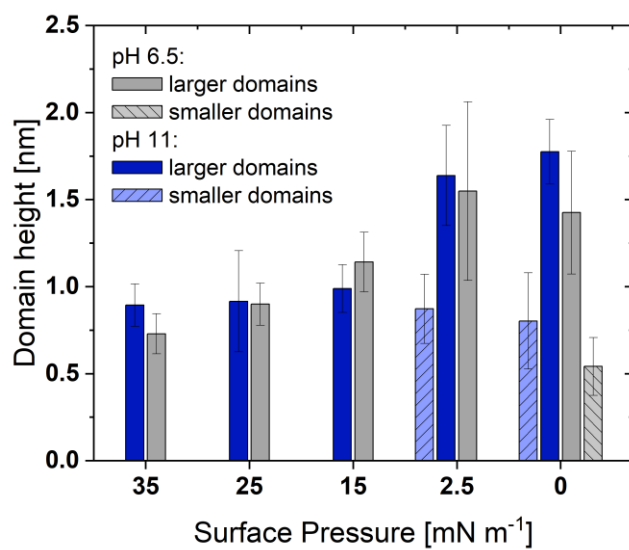


Figure C44 Domains' heights relative to the continuous phase measured from AFM images of **4b** as a function of subphase pH.

Table C1 Summary of GIXD best fitted parameters for **4b**. Units: Surface pressure (π) in mN m^{-1} ; positions (Q_{xy} , Q_z), and FWHM values in \AA^{-1} ; a, b, c, lateral and vertical correlation length in \AA ; A_{xy} , A_0 in \AA^2 ; α , β , γ , and tilt angle in $^\circ$. The vertical correlation length is calculated from the full width at half maximum (FWHM) in the Q_z direction. For comparison, the fully extended length (all trans conformations) of the C_{12} chains is 1.54 nm.

π		Q_{xy1}	Q_{z1}	Q_{xy2}	Q_{z2}	a	b	c	α	β	γ	Tilt angle	A_{xy}	A_0	d-spacing	Correlation length	
																Lateral	Vertical
pH 6.5																	
15	Position	1.489	0.326	1.500	0.000	4.88	4.85	4.85	119.5	120.2	120.2	14.2	20.5	19.8	4.2 – 4.2	67 – 77	14.9
	FWHM	0.030	0.380	0.026	0.380												
35	Position	1.513	0.000	-	-	4.79	-	-	120.0	-	-	0	-	19.9	4.1	67	17.0
	FWHM	0.030	0.332	-	-												
pH 11																	
15	Position	1.420	0.248	1.522	0	5.24	4.89	4.89	115.2	122.4	122.4	11.6	21.6	21.2	4.4 – 4.1	143 – 65	13.2
	FWHM	0.014	0.428	0.031	0.428												
31	Position	1.525	0	-	-	4.76	-	-	120.0	-	-	0	-	19.6	4.1	83	14.1
	FWHM	0.024	0.402	-	-												

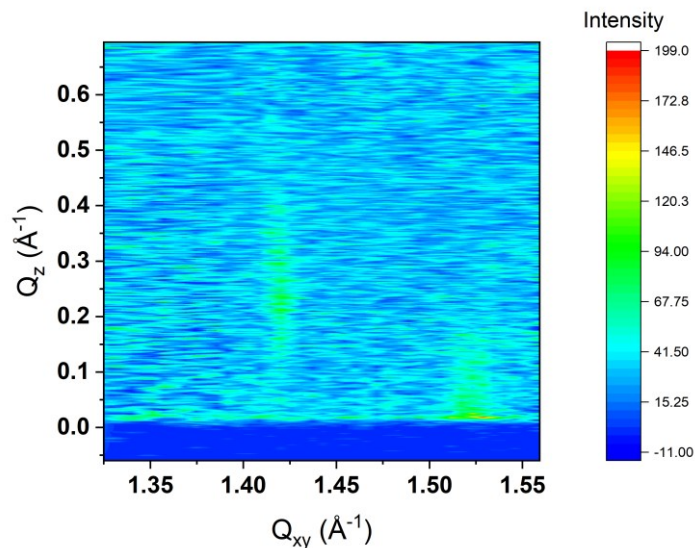


Figure C45 GIXD contour plot of X-ray diffraction intensity as a function of Q_{xy} (in-plane) and Q_z (out-of-plane) vector components for **4b** at pH 11 and surface pressure 15 mN m^{-1} , with modified intensity scale.

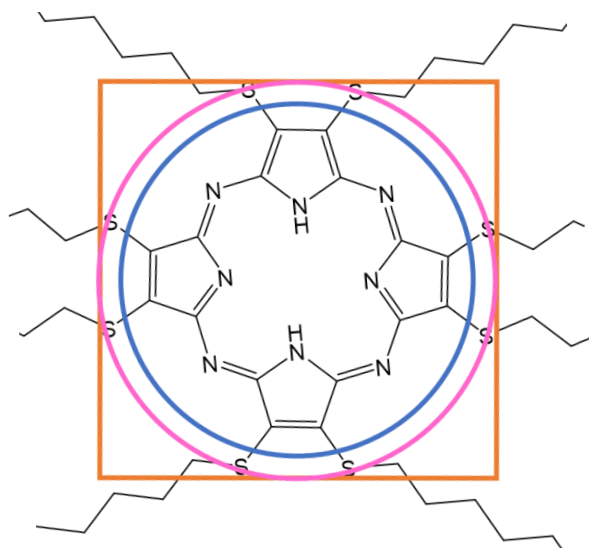


Figure C46 Estimations of porphyrin ring area. The orange square represents an area of 121 \AA^2 . The pink circle has the same diameter as the square length and yields an area of 95 \AA^2 . The blue circle corresponds to an area of 75 \AA^2 which is the pressure onset area from the isotherms. In actuality, the ring is neither a square nor a circle and these areas are estimated for comparison purposes only.

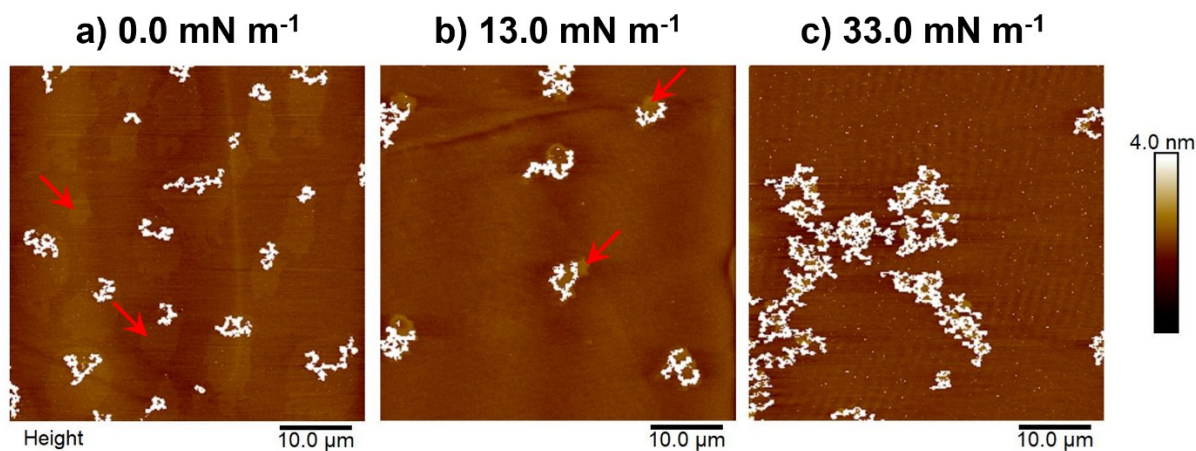


Figure C47 AFM images of **4a** deposited onto mica at different surface pressures and subphase pH 11. The measured height of the bright aggregates is a) 5.4 ± 0.7 , b) 5.9 ± 0.5 , and c) 6.3 ± 1.0 nm. The height of the condensed phase domains observed at 0 mN m^{-1} and 13 mN m^{-1} are ~ 0.2 - 0.3 and 0.5 nm high, respectively (red arrows), and the height of the tiny spots distributed across the AFM sample at 33 mN m^{-1} are ~ 1.3 nm.

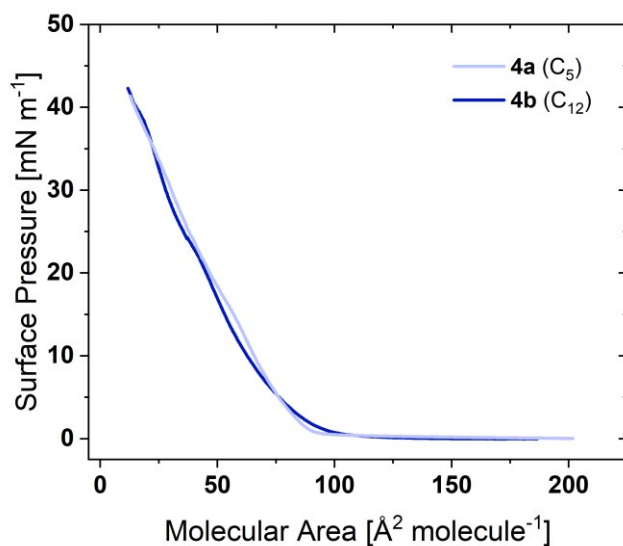


Figure C48 Surface pressure-molecular area isotherm of **4a** and **4b** on ultrapure water at pH 11.

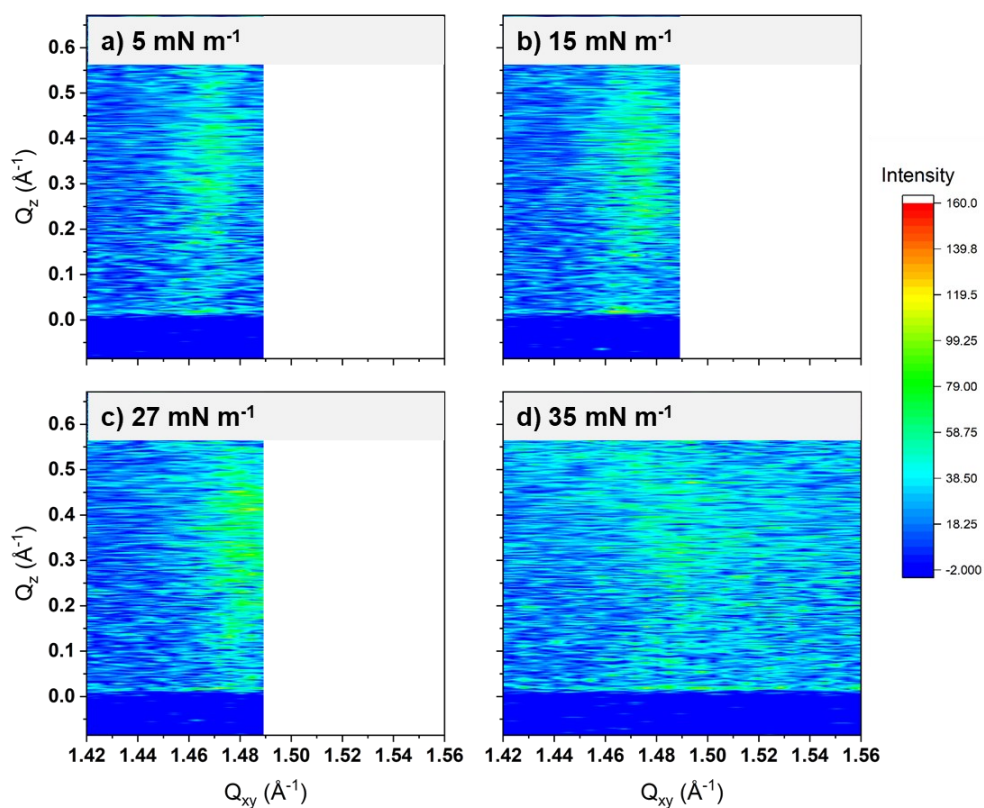


Figure C49 GIXD contour plots of X-ray diffraction intensity as a function of Q_{xy} (in-plane) and Q_z (out-of-plane) vector components for **4a** at pH 6.5. The plots are zoomed-in to show only the high Q_{xy} peaks: (a) 5 mN m^{-1} , (b) 15 mN m^{-1} , (c) 27 mN m^{-1} , and (d) 35 mN m^{-1} .

Table C2 Summary of GIXD best fitted parameters for **4a**. Units: Surface pressure (π) in mN m^{-1} ; positions (Q_{xy} , Q_z), and FWHM values in \AA^{-1} ; a, b, c, lateral and vertical correlation length in \AA ; A_{xy} , A_0 in \AA^2 ; α , β , γ , and tilt angle in $^\circ$.

π		Q_{xy1}	Q_z1	a=b=c	$\alpha=\beta=\gamma$	Tilt angle	$A_{xy} = A_0$	d-spacing	Correlation length	
									Lateral	Vertical
5	Position	0.369	0.000	19.6	120.0	0.0	334.1	17.0	111	8.1
	FWHM	0.018	0.695							
15	Position	0.371	0.000	19.6	120.0	0.0	331.6	16.9	111	10.2
	FWHM	0.018	0.554							
27	Position	0.373	0.000	19.4	120.0	0.0	327.4	16.8	105	12.4
	FWHM	0.019	0.457							
35	Position	0.376	0.000	19.3	120.0	0.0	322.7	16.7	77	11.2
	FWHM	0.026	0.505							

